

Improving Quality of Imaging Spectroscopy Data

Dissertation

zur

**Erlangung der naturwissenschaftlichen Doktorwürde
(Dr. sc. nat)**

vorgelegt der

Mathematischen-naturwissenschaftlichen Fakultät

der

Universität Zürich

von

Francesco Dell'Endice

aus

Italien

**Promotionskomitee
Prof. Dr. Klaus I. Itten (Vorsitz)
Dr. Jens Nieke
Prof. Dr. Michael Schaepman
Dr. Mathias Kneubuehler**

Zürich, 2010

“You begin saving the world by saving one person at a time; all else is grandiose romanticis or politics.”

Charles Bukowsky

Abstract

Imaging spectroscopy is moving into quantitative analysis of ecosystem parameters, which require high data quality. Thus, imaging spectrometers shall provide users with very accurate and low uncertainty measurements such that truthful products and reliable policies can be generated.

However, the quality of imaging spectroscopy data, which can be interpreted as the distance between the measurement and the true value, depends on a series of disturbance factors that can be divided into *instrument factors*, *environmental factors*, and *data processing factors*. Those factors lead to data non-uniformities and inconsistencies that, if not properly identified, quantified, and corrected for, can compromise the quality of the scientific findings.

This thesis investigates various techniques aimed to ensure the consistency of imaging spectroscopy data, namely in the spectral domain, throughout the data acquisition and specific data processing schemes, as for instance the calibration to radiances, with particular emphasis on instrument factors. The impact of data inconsistencies and non-uniformities on the quality of imaging spectroscopy data is first estimated. A scene-based technique for the characterization of keystone non-uniformity is then proposed. Moreover, a laboratory approach is established as the most reliable technique for the achievement of high accuracy calibration and characterization of imaging spectrometers. Last, an algorithm that identifies optimal sensor acquisition parameters for the retrieval of specific products in spectral regions of interest is presented.

It has been concluded that laboratory calibration and characterization procedures offer a higher degree of fidelity with respect to scene-based methodologies when non-uniformities and calibration parameters have to be determined and implemented into correction schemes.

A critical discussion of the main findings analyze advantages and drawbacks of the proposed techniques and suggests further improvements as well as future perspectives for the continuation of this work.

Zusammenfassung

Die abbildende Spektrometrie wird aufgrund ihres inhärenten Informationspotenzials in zunehmendem Masse für die Quantifizierung von Ökosystemparametern herangezogen. Ein entscheidendes Kriterium für die Ableitung exakter Produkte und verlässlicher Aussagen ist hierbei eine hohe Qualität der Spektrometerdaten.

Die Eigenschaften abbildender Spektrometer haben signifikanten Einfluss auf die Dateneigenschaften und -güte. Die Qualität dieser Instrumente manifestiert sich etwa in der Abweichung des gemessenen vom realen Wert und ist von verschiedenen Faktoren abhängig, speziell von *instrumentspezifischen*, *umweltspezifischen* und *datenprozessierungsspezifischen* Faktoren. Alleinstehend und in Kombination führen diese Einflussgrössen zu Unregelmässigkeiten in den, bzw. zur Inkonsistenz der aufgenommenen Daten. Die Identifikation, Quantifizierung und Korrektur dieser Effekte ist essentiell, um die Kontamination wissenschaftlicher Ergebnisse und abgeleiteter Produkte mit entsprechenden Instrumenten- und Datenfehlern zu minimieren.

In dieser Arbeit werden verschiedene Techniken untersucht, mit denen sich die spektrale Konsistenz der abbildenden Spektrometerdaten weitestgehend sicherstellen lässt. Im Fokus der Untersuchungen liegen Schritte der Datenaufnahme und -prozessierung, etwa die spezifische Kalibrierung von Instrumenteigenschaften zur Bereitstellung von Strahldichtenwerten.

Im ersten Schritt wird die Qualität der Spektrometerdaten auf mögliche Inkonsistenzen und Variabilitäten untersucht. Anschliessend wird eine szenenbasierte Technik vorgeschlagen, mit der eine spezifische Art der Dateninkonsistenz, der sog. *Keystoneeffekt*, charakterisierbar ist. Zudem wird ein Laboransatz entwickelt und aufgezeigt, der als zuverlässigste Technik zur Ableitung von hochgenauen Spektrometerkalibrationen und zur Charakterisierung von Spektrometereigenschaften angesehen werden kann. Im letzten Schritt wird eine Methode vorgestellt, mit der sensorspezifische Aufnahmeparameter indentifizierbar sind, die für eine optimale Ableitung spezifischer Produkte in relevanten Spektralbereichen erforderlich sind.

Als Ergebniss der Untersuchungen wird herausgestellt, dass laborbasierte Techniken mit Blick auf szenenbasierte Ansätze zur Ableitung von Kalibrationsparametern und Instrumentcharakterisierungen die höhere Genauigkeit bieten. Dies trifft speziell dann zu, wenn Datenunregelmässigkeiten und Kalibrationsparameter für Korrekturansätze zu quantifizieren, bzw. abzuleiten sind. Eine kritische Diskussion der Hauptergebnisse arbeitet Vor- und Nachteile der verschiedenen Techniken heraus und lässt Rückschlüsse auf notwendige Verbesserungen und zukünftige Arbeiten in diesem Themenbereich zu.

Table Contents

Abstract	I
Zusammenfassung	II
1 Factors influencing imaging spectroscopy data	2
1.1 Overview of past and current missions	2
1.2 Disturbance factors.....	3
1.3 Uncertainty types in imaging spectroscopy data.....	5
1.4 Data non-uniformities and the data quality problem.....	6
1.5 Uncertainty budget estimation	7
1.6 Research objectives	8
1.7 Structure of the dissertation.....	10
2 Observational requirements and instrument model	12
2.1 Earth-Sun Interactions.....	12
2.2 Some imaging spectroscopy applications	13
2.3 Observational requirements for imaging spectrometers.....	15
2.4 Instrument model and calibration requirements.....	20
3 Uncertainty impact on imaging spectroscopy products	27
3.1 Uniformity of Imaging Spectrometry Data Products	27
4 Detecting sensor properties through image data	40
4.1 Scene-based method for spatial misregistration detection in hyperspectral imagery	41
5 Laboratory calibration of imaging spectrometers	57
5.1 The generic calibration/characterization problem.....	58
5.2 The classic laboratory calibration approach.....	59
5.3 An innovative laboratory calibration/characterization strategy	60
5.4 Automatic Calibration and Correction Scheme for APEX.....	61
5.5 Calibration cube	71
5.6 A case study: the Airborne Prism Experiment (APEX)	71
5.7 Laboratory calibration and characterization of APEX	72

Table of Contents

6	Binning patterns for spectral regions of interest	95
6.1	Improving Radiometry by using Programmable Spectral Regions of Interest	96
7	Synopsis	106
7.1	Main findings	106
7.2	Discussion and conclusions.....	110
7.3	Future perspectives.....	114
	References	118
	Appendixes	130
	Acknowledgements.....	130
	Authored and Co-Authored Publications.....	131
	Conference Proceedings.....	132
	Curriculum	133

Factors influencing imaging spectroscopy data

1 Factors influencing imaging spectroscopy data

The purpose of this dissertation is to propose methodologies aiming at reducing the measurement uncertainty of imaging spectrometers. This chapter provides an overview on imaging spectroscopy and guides to the formulation of the main research questions.

1.1 Overview of past and current missions

In the last decades, Earth observation with optical remote sensing techniques has advanced the understanding of natural phenomena and led to relevant scientific progresses, thanks to the analysis of a large variety of geophysical and biochemical parameters. Spaceborne and airborne sensors have enabled the measurement of many key parameters, which are required to address the main Earth environmental challenges, e.g. climate change, water and carbon cycles and vegetation pattern changes.

These sensors operate in the solar ultra-violet (Wilson and Boksenberg 1969), visible, near-infrared (Ewing 1972; Low et al. 2007; Rieke 2007), shortwave-infrared radiation reflected by Earth's surface materials as well as in the spontaneously emitted thermal energy. Solar radiation that is incident on a material may be absorbed, transmitted or reflected. Dissimilar targets exhibit differing reflection, absorption and transmittance characteristics varying with wavelength. This implies that the reflectance spectrum of a material (i.e. reflected radiation versus wavelength) represents a unique signature for that target (Green 1998). Theoretically, a target is identifiable by its spectral signature if the sensing system has adequate spectral and radiometric resolution to properly resolve spectral and optical features. This physical principle posed the basis for spectroscopy. Similarly, imaging spectroscopy combines measurements along the spectral domain with spatial information such that a scene can be imaged (either by staring or moving platforms) and each pixel directly associated with its optical and biochemical properties. Hence, scenes can be mapped with respect to target properties. Imaging spectrometers collect spatial and radiometric information over a large spectral domain and the quality of these images depends mainly on spectral, radiometric, spatial, and temporal resolution of the instrument.

The growing interest in optical remote sensing data on one side and technology advances on the other one led to a first airborne hyperspectral mission in the early eighties. In fact, the Airborne Imaging Spectrometer (AIS) (Gross and Klemas 1986; Kruse and Taranik 1989) was operated by the NASA Jet Propulsions Laboratory for the identification of Earth surface materials between 900 nm and 2400 nm in 128 spectral bands. At the same time, an imaging spectroscopy program was carried out also in Canada and led to the Fluorescence Line Imager (FLI) (Gower et al. 1988), an airborne imaging spectrometer. FLI was used to measure naturally stimulated fluorescence emissions in near surface sea and lake water. Since then, several imaging spectroscopy missions, both airborne and spaceborne, have been successfully implemented (a selection is listed in Table 1).

Table 1: Non-comprehensive list of imaging spectroscopy missions

Instrument	Platform
CHRIS (Barnsley et al. 2004; Guanter et al. 2005; Duca and Del Frate 2008)	Spaceborne
MODIS (Barnes et al. 1998; Koziana et al. 2001; Descloitres et al. 2002),	Spaceborne
MERIS (Lobb 1994; Clevers et al. 2001),	Spaceborne
HYPERION (Goodenough et al. 2003)	Spaceborne
AVIRIS (Mouroulis et al. 2000)	Airborne
CASI (Babey and Anger 1993)	Airborne
PHILLS (Davis et al. 2002; Bowles et al. 2005)	Airborne
AISA (Makisara et al. 1993)	Airborne
DAIS (Krüger et al. 1998)	Airborne

Future airborne and spaceborne missions will soon be operational. For instance the Airborne Prism Experiment (APEX) imaging spectrometer (Itten et al. 2008), the Airborne Reflective/Emissive Spectrometer (ARES) (Muller et al. 2005), the Environmental and Mapping program satellite (EnMap) (Kaufmann et al. 2006), SENTINEL III (Nieke et al. 2009), and the Precursore Iperspettrale della Missioe Operativa (PRISMA) (Galeazzi et al. 2008). A more detailed historical background on imaging spectrometers is given in (Schaepman 2009).

The availability of imaging spectroscopy data is still considerably growing and accompanied by improvement of spectral, spatial, and radiometric resolutions of the scanning systems. Spectroscopy data provide an important contribution to the study of natural phenomena, and their derived products are used by policy makers (Kacenjara and Honvedel 2004) to develop strategies for environmental sustainability and to generate large series of social and economic benefits for the human kind. Hence, accurate imaging spectroscopy measurements are necessary to provide precise indications for natural resources management.

1.2 Disturbance factors

The accuracy of imaging spectroscopy data is affected by disturbances, which are described in this paragraph.

There are a certain number of factors that influence the quality or fidelity of imaging spectroscopy data. The core function of an imaging spectrometer is to perform *spectral measurements*. Low uncertainty products require low-uncertainty-high-accuracy spectral measurements. The quality of a measurement is expressed through its uncertainty, accuracy, and precision. *Uncertainty* (ISO 1993) is that range of values, which is likely to enclose the true value and it is usually indicated as standard deviation. *Accuracy* (ISO 1993) is the degree to which the result of a measurement conforms with the true value or standard. *Precision* (ISO 1993) expresses the degree of reproducibility of

the measurement. An imaging spectrometer should provide accurate, precise, and low uncertainty measurements. However, a series of elements interferes with both the data acquisition and data processing, hence influencing the accuracy and uncertainty of the data.

In fact, the quality of optical remote sensing data (i.e. the closeness of the measurement to the true value) depends on a series of disturbance factors that can be grouped into three main categories:

- *Instrument factors*: distortions (e.g. whiskbroom systems have less spectral distortion than pushbroom instruments), electronic disturbances (e.g. noise and saturation levels), and system parameters (e.g. spectral, geometric, and radiometric resolution).
- *Environmental factors*: adjacency effect, vibrations, external disturbances (e.g. turbulence, wind), illumination conditions.
- *Data processing factors*: acquired raw data are processed for corrections (e.g. atmospheric correction, geometric correction), calibrations (e.g. calibration to radiances, calibration to reflectances), dimensionality reductions, and product retrieval algorithms. Each data processing step introduces uncertainty.

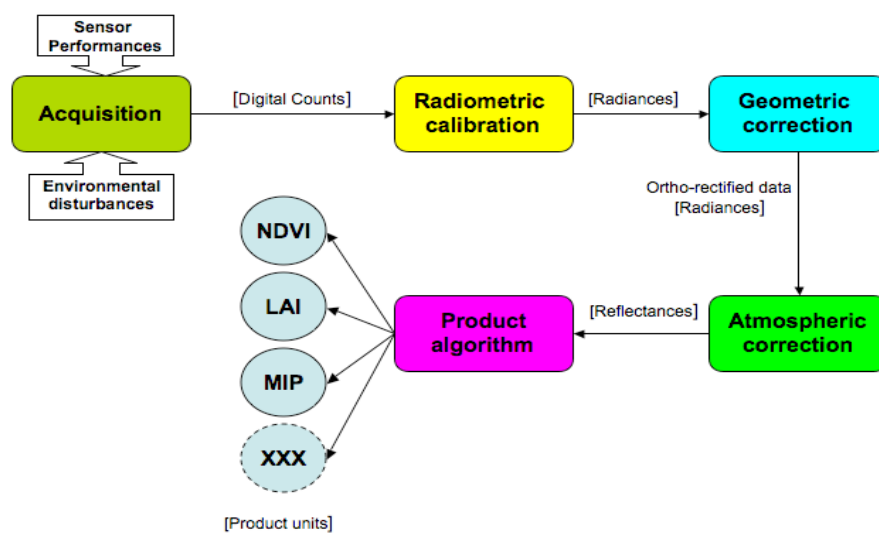


Figure 1: Basic imaging spectroscopy data processing scheme.

However, accuracy degradation due to data processing schemes can be evaluated as the comparison between the initial dataset and the corrected one. Imaging spectroscopy measurements are acquired under the influence of instrument and environmental disturbances (Figure 1).

test equipment is properly certified in terms of quality (e.g. if uncertainty, precision, repeatability error, stability error are given). In fact, if instrumentation accuracy and uncertainty are provided for each calibration/characterization instrumentation then the overall acquisition uncertainty can be quantified through an uncertainty propagation analysis (ISO 1993)

Data processing uncertainty is more difficult to evaluate because it depends on model assumptions and parameters. For example, atmospheric correction schemes contain several modeling parameters that are difficult to account for in the overall uncertainty analysis. Nevertheless, sensitivity analyses have been carried out for atmospheric correction algorithms (Seidel et al. 2005; Kotchenova et al. 2006; Kotchenova and Vermote 2007; Seidel et al. 2008) on single model parameters (e.g. zenith angle, aerosols); accuracy evaluation of atmospheric correction (Schlapfer et al. 2008) and comparison between the accuracy of atmospheric models have been also performed (Kotchenova et al. 2008). However, it is not possible to assess a general level of accuracy because a high number of inter-dependent model parameters need to be considered and this might be extremely complex and time-consuming.

Data processing uncertainty factors are not discussed in detail within this work. In the next paragraph, the influence of measurement uncertainty on imaging spectroscopy data is explained and an estimation of the uncertainty budget is provided.

1.4 Data non-uniformities and the data quality problem

The disturbance factors and their influence on the overall uncertainty have been described in the previous paragraphs. The effect of uncertainty on the data and the general data quality problem are described in this paragraph.

Measurement uncertainties result in data non-uniformities (e.g. punctual and linear defects) that have been extensively documented in the literature (Mouroulis et al. 2000; Mouroulis and McKerns 2000; Winter et al. 2003; Mouroulis et al. 2004; Schlapfer et al. 2007; Nieke et al. 2008). If these effects are properly modeled and detected, then the overall fidelity of the measurements is improved.

As spectral measurements influence the quality of the final products, the problem of increasing the accuracy of spectral measurements can be generally referred to as the *data quality problem* and formulated as follow:

How can high-quality imaging spectroscopy products be retrieved?

In order to identify the major contributors to the product uncertainty one shall (1) consider the entire disturbance factors (i.e. instrument, environmental, data processing factors), (2) perform a sensitivity analysis with respect to the desired product and (3) investigate the possibility of minimizing the errors. Here, particular emphasis is put on instrument factors.

Therefore, in order to attempt a solution, the problem shall be reformulated as follow:

What measurement uncertainty can lead to successful retrieval of products with given uncertainty?

Once the required product accuracy and uncertainty are defined, one shall identify the instrument performances whose related uncertainty can be properly estimated and possibly reduced or eliminated through optimization and/or correction schemes. Only a highly accurate spectral measurement can lead to the generation of a reliable imaging spectroscopy product. An estimation of the influence of instrument parameters on data uncertainty is given in the next paragraph.

1.5 Uncertainty budget estimation

The measurement uncertainty can be quantified and related to the overall uncertainty of imaging spectroscopy data. This paragraph gives an estimation of the imaging spectroscopy product uncertainties caused by acquisition uncertainty and data processing uncertainties of algorithms directly related to calibration and characterization processes. Data processing uncertainties of other correction schemes (e.g. atmospheric and geometric correction) as well as of product retrieval will not be considered here.

It has been estimated (Nieke et al. 2008) that imaging spectroscopy products are affected by an inherent uncertainty of about 10% connected with data non-uniformities and such errors can be reduced to less than 5% with currently available technology (e.g. calibration techniques and assimilation schemes). However, calibration and characterization uncertainties, related to other phenomena (e.g. radiometry, polarization, straylight) were not considered in this budget. (Chrien et al. 1990) performed an uncertainty calculation for the spectral and radiometric calibration of the Airborne Visible/Infrared Imaging Spectrometer (AVIRIS) instrument and it was found that (1) the uncertainty is wavelength dependent, (2) spectral calibration uncertainty can be as high as 20%, and (3) radiometric uncertainty is about 4%.

An estimated additional 10% stems from calibration and characterization procedures measuring the spatial and spectral distribution of instrument performances. Data correction schemes, based on instrument parameters, might contribute as much as 10% because of model assumptions. A 5% contribution has been included here to account for external sources, because the total acquisition uncertainty is the sum of environmental and measurement uncertainties.

A root-squared-sum (RSS) of these errors resulted in a total data uncertainty of about 27% (see Table 2).

Table 2: Uncertainty contributors on imaging spectroscopy data.

Source	Uncertainty
Data non-uniformities	10%
Radiometric calibration	4%
Spectral calibration	20%
Other calibration procedures	10%
Data processing factors	10%
Environmental factors	5%
Total RSS sum	≈ 27%

Data non-uniformities and calibration (i.e. first four entries of the Table 2) account for 73% of the total uncertainty budget (RSS sum). It is a matter of fact that sensor performance, sensor calibration and characterization (Chrien et al. 1990; Green 1998), as well as sensor optimization have a strong impact on the spectral consistency (i.e. accuracy) of the measurements. Investigating sensor calibration and

characterization can significantly reduce acquisition uncertainty (Chrien et al. 1990). An imaging spectrometer (namely pushbroom systems) consists of several spatial detectors (*samples*), each one associated with a high number of spectral channels. One of the assumptions of this work is that each sample can be considered as an independent spectrometer that has specific acquisition properties. Thus, calibrating and characterizing as many *sample-spectrometers* as possible increases the spectral consistency of the measurements (i.e. reduces measurement uncertainty) and the accuracy of the products.

1.6 Research objectives

Three main kinds of disturbance factors have been introduced in §1.2 and the data quality problem has been formulated in §1.4, where particular emphasis has been put on measurement uncertainty (§1.3). It has also been estimated that non-uniformities and calibration/characterization related issues (i.e. procedures and data schemes) account for 73% of the overall data uncertainty budget (i.e. 27%).

This thesis focuses on the investigation of techniques and methodologies aimed at reducing the uncertainty contribution of instrument factors, such that data uncertainty of less than 5% can be achieved.

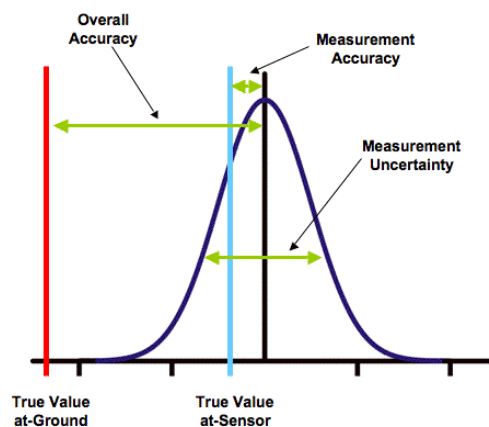


Figure 3: Quality of the spectral measurements.

The focus is namely on at-sensor measurements and corresponding uncertainty-accuracy budget (see Figure 3). The quality of an at-sensor measurement can be expressed through its accuracy (*measurement accuracy*), which can be defined as the distance between the measured value and the true-value at sensor. Furthermore, the *overall accuracy* can also be defined as the difference between the true-value at ground (ground-truth) and measured at-sensor values, which represents the unknown bias that remote sensing ultimately tries to minimize.

Factors influencing imaging spectroscopy data

Reaching 5% uncertainty by employing according calibration and characterization techniques would increase the measurement accuracy substantially. Such data could then be considered as a solid starting point for the application of data processing schemes aimed at either improving the overall accuracy or at retrieving accurate products.

Based on the uncertainty budget estimation of Table 2, the dissertation aims at reaching the following uncertainty goals:

Table 3: Uncertainty goals

Source	Uncertainty
Data non-uniformities	2%
Radiometric calibration	2%
Spectral calibration	2%
Other calibration procedures	2%
Data processing factors	2%
Environmental factors	5%
Total RSS sum	≈ 6.71%

Except for environmental factors (which are not discussed here), the overall objective is reaching a 2% uncertainty for every source such that the overall contribution of calibration/characterization factors is **4.47%** (RSS of sources 1-5 in Table 3).

The consistency of spectral measurements relies on the quality of the measuring device. Thus, the aim is to properly characterize instrument performances in such way that non-uniformities can be modelled and eventually eliminated from the image data. In order to accomplish this task, the overall uncertainty budget is first estimated (see §3) and the sensitive intervention areas of the data flow (see Figure 1) are identified. The possible investigation of non-uniformities directly in image data is also investigated as an alternative to direct assessment in laboratory (see §4). As it has been discussed in the previous paragraph, the measurement uncertainty can be quantified in laboratory. Therefore, a laboratory calibration and characterization strategy, namely developed for pushbroom spectrometers, is proposed (see §5). Finally, the potential of optimizing the sensor acquisition parameters for specific spectral regions of interest will be explored (see §6).

The research questions can be summarized as follows:

- Which impact do instrument factors have on the quality of imaging spectroscopy measurements and products? Is it possible to quantify the overall uncertainty of imaging spectroscopy products (see §3)?
- How can data non-uniformities be identified directly from the measured data? Is it possible to implement correction schemes based on this information (see §4)?
- How can the calibration and characterization process reduce the uncertainty of imaging spectroscopy products (see §5)?
- How can an imaging spectrometer be calibrated such that the measurement quality/fidelity

is improved? How can calibration and characterization techniques reduce the measurement uncertainty?

- How can instrument laboratory calibration be used to efficiently characterize non-uniformities (see §5)?
- How can high quality products be generated by optimizing the data acquisition for specific spectral regions of interest (see §6)?

The methodologies and techniques used to address and solve these research questions are described in the following paragraphs.

1.7 Structure of the dissertation

This paragraph outlines the structure of this dissertation and indicates how the research questions, described in §1.6, are analyzed through the next chapters.

In chapter 2, the sensing principles of imaging spectrometers are described. The observational requirements for a generic imaging spectroscopy mission and a general instrument model are introduced. By doing so, the uncertainty requirements can be transformed into instrument performance requirements.

Chapter 3 includes a co-authored publication (Nieke et al. 2008) where the uncertainty budget for imaging spectroscopy data has been estimated. In this publication, calibration, characterization, and assimilations schemes have been identified as potential intervention areas where to act in order the reduce data uncertainty.

Chapter 4 deals introduce a technique for the detection of non-uniformities directly on image data (Dell'Endice et al. 2007b). An edge detection algorithm for the quantification of spatial misregistration is proposed and discussed in this first-author publication.

Chapter 5 describes more in detail the laboratory calibration and characterization of imaging pushbroom spectrometers and justifies why laboratory is the ideal environment for the reduction of non-uniformities and their impact on the overall uncertainty. A conference proceeding (Dell'Endice et al. 2007a) outlines the laboratory infrastructure from a software and hardware point of view. The achievements of the laboratory calibration and characterization for the Airborne Prism Experiment APEX imaging spectrometer (Itten et al. 2008) are discussed in a first-author publication (Dell'Endice et al. 2009a).

Chapter 6 discusses the optimization of sensor acquisition parameters. A first-author publication (Dell'Endice et al. 2009c) introduces a methodology aiming at increasing information extraction from spectral regions of interest.

Chapter 7 summarizes the main scientific findings, discusses specific and question-related issues and outlines possible scenarios for the future continuation of this work.

Observational requirements and instrument model

2 Observational requirements and instrument model

This chapter briefly introduces the sensing principles of imaging spectrometers and lists some of the most common spectroscopy applications. Subsequently, observational requirements for a generic imaging spectroscopy mission are described. An instrument model is then outlined in order to allow the transfer of observational requirements into calibration and characterization goals. An explanation of the most frequent terms and expression in this thesis is also given.

2.1 Earth-Sun Interactions

The driving energy for physical and chemical processes on Earth is the solar radiation. The solar energy flux incident on a surface is called *irradiance* (I [W m^{-2}]). *Spectral radiance* (L [$\text{W m}^{-2} \text{sr}^{-1} \text{nm}^{-1}$]) is the power projected per unit area, per unit solid angle and per unit wavelength. The ratio between the radiant exitance (M [W m^{-2}]) (i.e. the radiant flux reflected from a surface) to the irradiance (I) is called *reflectance* (Schaeppman-Strub et al. 2006). Each material reflects and absorbs solar energy according to its atomic structure such that it can be characterized through its reflectance profile, referred to as *spectral signature*.

Before reaching the Earth's surface, the Sun energy has to travel through the atmosphere. Particles, aerosols and gases in the atmosphere affect the incoming light and radiation. These effects are caused by the mechanisms of scattering and absorption.

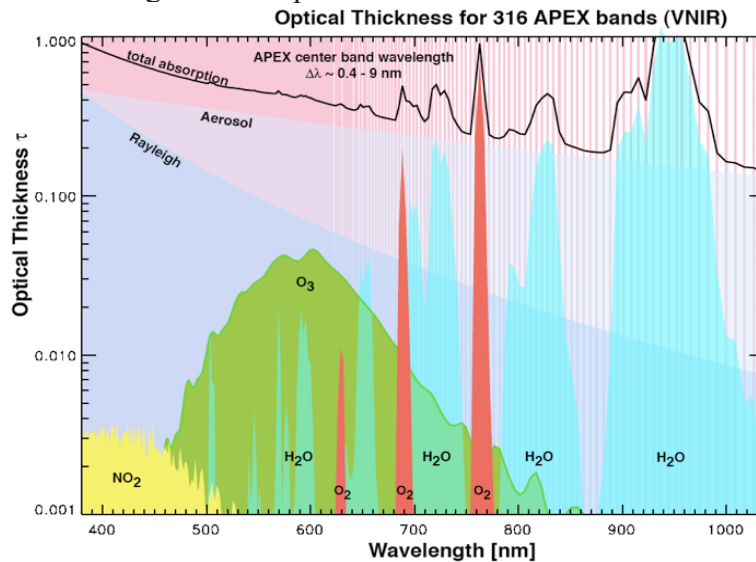


Figure 4: Atmospheric windows in the VNIR spectral region.

Scattering occurs when particles or large gas molecules suspended in the atmosphere interact with and cause the solar electromagnetic radiation to deviate from its original path. The quantity of scattering depends on several factors including abundance of particles of gases, wavelength dependence, and the distance that photons travel through the atmosphere. Absorption is the process by which radiant energy is absorbed and converted into another form of energy. An absorption band is a range of wavelengths (or frequencies) in the electromagnetic spectrum within which radiant energy is absorbed by substances such as water (H_2O), carbon dioxide (CO_2), oxygen (O_2), ozone (O_3), and nitrous oxide (N_2O). Ozone, carbon dioxide, and water vapor are the three main atmospheric constituents that absorb radiation. Absorption is restricted to only certain wavelength regions of the solar electromagnetic energy (Ångström 1930). The wavelength ranges in which the atmosphere is particularly transmissive for energy are named *atmospheric windows* (Figure 4 and Figure 5).

Sun energy that is neither absorbed nor scattered by the atmosphere reaches the Earth's surface where it can be further transmitted, absorbed or reflected. The proportion of each interaction depends on the material chemical composition (Hollander and Shirley 1970), the material geometry and the wavelength of the incident energy. Optical remote sensing measures the solar radiation reflected from target materials (a) through the UV, VIS, and Near-Infrared atmospheric windows, i.e. between 380 nm and 2500 nm and, (b) in the thermal window; in fact the level of reflected solar energy in those regions is such as can be detected by passive instruments.

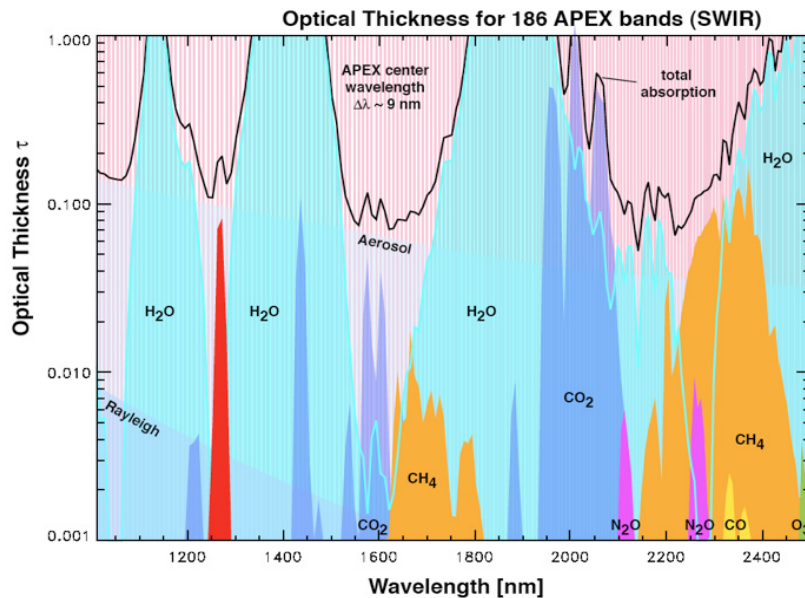


Figure 5: Atmospheric windows in the SWIR spectral region.

2.2 Some imaging spectroscopy applications

The measured solar-reflected energy is used to retrieve remote sensing products. A list of some applications and products that are based on imaging spectroscopy data is given in this paragraph. As mentioned earlier, the imaging spectroscopy era started in 1982 with the deployment of the Airborne Imaging Spectrometer (AIS) (Gross and Klemas 1986). Since then, a large number of applications based on imaging spectroscopy data have been implemented (a non-exhaustive list is given in Table 4). For instance, remote sensing data have also been useful in developing genetic algorithms for retrieval of vegetation equivalent water thickness (EWT) (Li et al. 2008) or in managing transportation and asses road quality (Gomez 2002). The increase of imaging spectroscopy platforms has gone in parallel with the development of estimation and predictions models. These models try to simulate the structure of natural species in order to understand the interaction mechanisms between Sun radiation and cells. Vegetation has been one of the most investigated fields. Models have been implemented in order to retrieve data on plant pigment (Ustin et al. 2006) and leaf biochemistry (Kokaly and Clark 1999), to understand leaf optical properties and canopy bidirectional reflectance (Govaerts et al. 1995; Jacquemoud et al. 2006), to study the variation of optical properties in leaf and litter (Asner et al. 1998), to estimate water content (Zarco-Tejada et al. 2003), chlorophyll content (Zarco-Tejada et al. 2004; Haboudane et al. 2008), and nitrogen content (Coops et al. 2003) in plants.

Table 4: Selected applications based on imaging spectroscopy data and their related instruments and platforms.

Application	Instrument	Platform
Maps of minerals (e.g. sulfides, calcite) and metals (e.g. iron) (Clark et al. 2006)	AVIRIS (Vane et al. 1993)	Airborne
Maps of native and invasive plants (Asner et al. 2008),	AVIRIS	Airborne
Maps of canopy nitrogen concentration (Townsend et al. 2003; Martin et al. 2008),	AVIRIS	Airborne
Analysis of spectral and chemical composition of tropical forests (Asner and Martin 2008),	AVIRIS	Airborne
Analysis of mixture of soil and vegetation (Datt and Paterson 2000)	AVIRIS	Airborne
Cirrus cloud detection (Gao et al. 1993)	AVIRIS	Airborne
Estimation of chlorophyll concentration in conifer trees (Moorthy et al. 2008)	CASI (Babey and Anger 1993)	Airborne
Analysis of vascular plant (Lucas and Carter 2008)	HyMap	Airborne
Mapping of sea ice extent and ice surface temperature (Hall et al. 2004),	MODIS (Barnes et al. 1998)	Spaceborne
Monitoring of seasonal changes in vegetation indexes (Hao et al. 2008)	MODIS	Spaceborne
Snow cover mapping (Hall et al. 2000)	MODIS	Spaceborne
Atmosphere properties (clouds, aerosols, precipitable water vapor (King et al. 1992)	MODIS	Spaceborne
Classification algorithms for forest (Goodenough et al. 2003; Thenkabail et al. 2004)	HYPERION (Folkman et al. 2001)	Spaceborne
Land cover of ecosystems (Pignatti et al. 2009)	HYPERION	Spaceborne
Prediction of larval mosquito presence (Brown et al. 2008)	HYPERION	Spaceborne
Characterization of spatial structure of invasive plants (Walsh et al. 2008)	HYPERION	Spaceborne
Study the forest biomass (le Maire et al. 2008)	HYPERION	Spaceborne
Measure of temporal variability of vegetation patterns in low canopy (Foster et al. 2008)	HYPERION	Spaceborne
Estimation of radiant flux from a lava lake (Wright and Pilger 2008)	HYPERION	Spaceborne
Generation and validation of characteristic spectra (Ramsey et al. 2005)	HYPERION	Spaceborne
Study about the dependency of vegetation indexes on angular effects, such as BRDF (Verrelst et al. 2008)	CHRIS (Barnsley et al. 2004)	Spaceborne

2.3 Observational requirements for imaging spectrometers

The accuracy of imaging spectroscopy products strongly depends on the fidelity of the spectral measurements and on how the imaging sensor is conceived. In fact, the performances of imaging spectrometers are the result of an elaborate trade-off process between several observational requirements. These mission specific prerequisites can be various and some of them are illustrated in Figure 6.

One of the main challenges in imaging spectroscopy is the generation of reliable and accurate spectral signatures, because a multitude of products and models is based on these. For instance, several ecosystem models (Ustin et al. 2004; Ustin et al. 2006) make regular use of imaging spectroscopy data to analyze biophysical properties or to predict the trend of environmental variables.

Observational requirements for imaging spectroscopy missions must be defined in any data dimension, i.e. spatial, spectral, radiometric and temporal with the ultimate aim of serving several application domains with the same dataset.

This means that imaging spectrometers are designed in such a way that a high number of output products can be generated with a high degree of liability and low uncertainty.

It is obvious that the uncertainty is a relative quantity: it is usually defined as the deviation between the quantity measured at-sensor level and the same quantity measured and the same quantity measured at-ground level (e.g. in-field measurement, primary or secondary laboratory standard).

An imaging spectroscopy mission

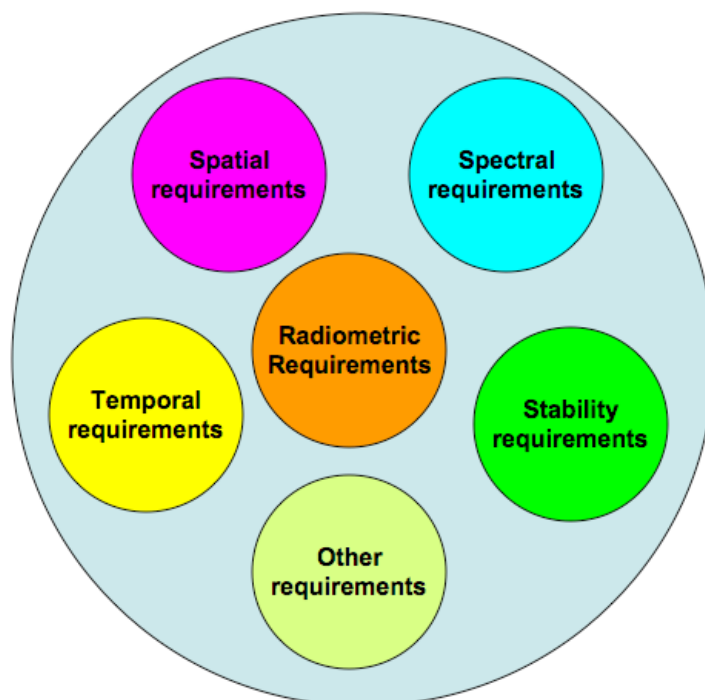


Figure 6: Observational requirements for an imaging spectroscopy mission.

The purpose of the next subparagraphs is to quantify the requirements depicted in Figure 6 (i.e. spatial, spectral, radiometric, temporal, stability, and other requirements) in terms of resolution.

2.3.1 Spatial requirements

Airborne and spaceborne imaging spectrometers offer a wide range of spatial resolution. This parameter mainly depends on the optical system (i.e. lenses, mirrors and dispersing elements) and it is proportional to the field-of-view (FOV) of the sensor, the height and the speed of the moving platform as well as the integration time.

In order to define an optimal spatial resolution (i.e. the minimum detectable spatial separation) for imaging spectroscopy products, one must consider the issue from the spectral point of view. The larger the pixel size, the larger the quantity of spectral information comprised by it. In the case of a non-homogeneous target, this would mean that the spectral signatures of different materials would somehow mix; the sensor will then record an impure spectrum, correctly referred to as an *incoherent* spectrum, being the result of an interaction between several adjacent signals. As stated before, one of the main goals of imaging spectroscopy is to create reliable spectral libraries. A low spatial resolution can seriously compromise the efficiency of spectral differentiation and spectral unmixing algorithms. Such algorithms aim at separating the different materials that compose a pixel. Usually, airborne scanners have a higher spatial resolution (from a few centimeters to a few meters) compared to spaceborne instruments (from half a meter to few kilometers). Besides the constraints dictated by the sensor technology and application domain, there are other aspects related to data volume and data download, namely for satellite missions, that act as boundary conditions for such a parameter.

It is then understood that a high spatial resolution is strongly recommended because it can lead to successful material classifications and maps. Nevertheless, this requirement can be relaxed for a certain range of applications that focus on homogenous targets only.

The spatial quality of imaging spectroscopy data can be degraded by spatial non-uniformities (e.g. the full-width-at-half-maximum (FWHM) variation of the across-track and along-track spatial point-spread-function (PSF) along the FOV); a sensitivity analysis is therefore recommended in order to solve the trade-off decision process. Those data inconsistencies are due to the imaging system and result in non-uniform spatial responses in the focal plane pixels (Hayat et al. 1999; Kavaldjiev and Ninkov 2001). These defects have to be restricted to a certain threshold (Dell'Endice et al. 2007b; Schlapfer et al. 2007; Nieke et al. 2008) or the error data budget can seriously increase.

2.3.2 Spectral requirements

The use of the same imaging spectrometer data set for heterogeneous purposes manifests one of the main advantages of this technology; it means that an imaging spectrometer shall potentially be able to produce variable spectral bandwidths (see §2.4.3) in different portions of the covered spectral domain. Consequently, the usual wavelength interval of imaging spectrometers goes from 380 to 2500 nanometers. Within this domain, it is then possible to define application-dependent spectral regions of interest (SROI) (Dell'Endice et al. 2009b), each one coming with its own spectral requirements. The determination of an optimal spectral resolution (see §2.4.3) is governed by several considerations, strictly connected to the application domain. Nevertheless, this parameter depends on the sensor technology as well, namely on how the incoming light flux is separated into its composing wavelength. Generally, every application can dictate its own spectral requirements. Specific spectral bandwidths have been established for some applications (Green 1998; Schläpfer and Schaepman 2002). Nowadays, the spectral bandwidths of imaging scanners can be re-programmed using field-programmable-gate-arrays (FPGA) (Kuusilinna et al. 1999) to adapt the mission to specific spectral needs.

In order to correctly identify materials, to distinguish distinct spectrum features like absorption lines, and to precisely determine other spectrum characteristics, it is preferred to sense a target by using

narrow spectral bands (see §2.4.3); in this way, spectral unmixing algorithms have a better chance of success. However, narrower bands receive less energy and therefore, obtaining good signal-to-noise ratio (SNR) is a technical challenge.

Therefore, it is desirable to achieve very narrow spectral bandwidths. It has been demonstrated that a bandwidth larger than 5-10 nanometers can dangerously affect the purity of the recorded spectra (Green 1998) and jeopardize the success of unmixing, classification, and mapping methods. Spectral uncertainty and spatial uncertainty are inter-correlated; the choice of the right limits is the result of a trade-off process based on a sensitivity analysis.

Another topic that needs to be discussed in this paragraph is the absolute spectral uncertainty, i.e. the difference between the measured centre wavelengths (see §2.4.3) and absolute centre wavelengths of certified primary calibration standards (see §2.4.5). Institutes for calibration standards provide absolute centre wavelengths for a series of well-known targets. Efficient calibration and characterization are mandatory in order to quantify this error in a precise manner. Namely, imaging spectroscopy pushbroom scanners have a high number of detector elements; therefore, a full calibration is time consuming. One of the main topics of this work is to recommend an efficient calibration concept that allows an almost complete sensor characterization; such a concept has been structured in a way that absolute uncertainty would be lower than 3%.

2.3.3 Radiometric requirements

Radiometric uncertainty and resolution are crucial requirements for imaging spectrometers but they are also the most complex to determine for the simple reason that nature is extremely heterogeneous and imaging spectrometers are designed to cover a large portion of such a variety. Radiometric requirements are usually indicated as signal-to-noise ratio (SNR), i.e. the ratio between the signal and the unwanted disturbances that degenerate the signal itself. As mentioned earlier, SNR is application dependent; generally, a strong SNR is needed for weak spectral features while a low SNR is fine with strong spectral feature. The establishment of SNR requirements is the result of an elaborate trade-off between several variables. Apart from the intensity of the incoming spectral signal, this ratio depends as well on the interference of the atmosphere (e.g. absorption features, aerosols), on the sensor optical chain (e.g. shape of the response functions) and on the electronics at the end of the data acquisition stream (e.g. quantization, saturation level). The other difficulty concerning this parameter is that it is not constant and its value may vary accordingly to other parameters as, for instance, weather and illumination conditions. Therefore the goal of a sensor manufacturer is to ensure a minimal level of SNR corresponding to the worst scenario, not neglecting the overall mission objectives. It is possible to model this ratio by using a typical SNR equation if the levels of incoming radiance, as well as the noise sources are known (Dell'Endice et al. 2009b); this way the levels of SNR can be predicted. SNR can be evaluated also from imagery data. In fact, users estimate it by taking a spectral uniform target extending over a few pixels (e.g. a desert, a lake), calculating an average radiance value and dividing it by its standard deviation. This approach usually underestimates the SNR but it represents a baseline indication for the user in order to understand the quality of the foreseen product.

2.3.4 Temporal requirements

Many natural targets change their properties over time as is e.g. well known for vegetation, water, and soil (Foster et al. 2008; Hao et al. 2008). The incoming solar radiation is also time dependent (i.e. change of illumination conditions). For ecosystem models to accurately predict the evolution of biophysical and chemical properties, a temporal series of measurement data would be necessary. Every application can dictate the necessary revisiting frequency: spaceborne instruments are more suitable for this purpose mainly because of programmed revisiting periods. The same is not true for airborne sensors; those instruments fly over a target only once or sporadically at best.

The target observation frequency is referred to as *temporal resolution*, and it may coincide with the overpass frequency in the case of satellites. Generally, this parameter can be specifically associated with spaceborne sensors that fly over the same geographical coordinates with certain repeatability. On the other side, airborne imaging spectrometers do not usually fly over the same target. Nevertheless, the increased number of available airborne sensors grants the access to different datasets of a same Earth's scene. However, comparing datasets acquired by different sensors arises a number of additional issues that have to be considered as, for instance, different spatial and spectral resolution. These obstacles can be overcome if resampling techniques are adopted. Nevertheless, resampling must be carefully weighted, particularly in the spectral domain. In principle, the inter-comparison is not straightforward and care must be taken to ensure consistency between datasets generated by different sensors. Some sensors are also able to emulate the uncertainties of other instruments thanks to spectral binning re-programming (Dell'Endice et al. 2009b). The inter-comparison of data is one of the main subjects of vicarious calibration, which will not be extensively considered in this work.

Generally, in order to compare spectroscopy data of a target at two different dates, it is necessary to ensure data consistency from the radiometric, spectral and spatial point of view. In order to achieve this goal, the target must be flown with the same platform (e.g. speed, altitude) and sensor (e.g. integration time, frame period) conditions. Validation of data should be used before any inter-comparison.

However, the repeatability of the measurements is affected from many factors like illumination and atmospheric conditions, sensor degradation over time, stability of the flight pattern; these parameters are discussed in the next paragraph.

2.3.5 Stability requirements

Consistency of the measurements as well as comparison between datasets acquired at different times can be ensured if, and only if, the imaging spectrometer can be considered stable. The spectral, radiometric, and spatial stability requirements of imaging spectrometers depend mainly on the (1) *stability of the platform* and the (2) *stability of the sensor*. Both refer to the group of variables that might affect the quality of the data over time; adequate temporal resolutions without a stable instrument might be useless unless frequent re-calibration or validation of the instrument is possible.

The platform stability includes disturbances of the flight pattern either due to platform movement (e.g. roll, pitch, and yaw movements) or by atmospheric factors (e.g. wind, snow). The flight pattern of a space platform is easier to control than an airborne one. In airborne spectrometers, geometric and bore-sight resampling techniques are applied in order to correct these effects. These perturbations can be controlled also through a stabilizing inertial platform that interfaces the instrument with the airplane.

The stability of the sensor, also referred to as internal stability, includes mechanical, electrical,

thermal and optical aspects. The motion of the platform, either airborne or spaceborne, can influence the assembly of the instrument components (e.g. lenses, detectors, mirrors). If, due to any reason, the alignment of optical parts changes then the imaging quality of the system will be compromised. This can result in unwanted blurring or image defocusing. Some systems use specific solutions in order to correct for instability effects; for instance, geometrical stability is monitored in the Airborne Prism Experiment (APEX) by measuring the projection of two wires, mounted perpendicularly to the entrance slit, over time. Spectral and radiometric stability can be monitored using onboard calibration facilities. Detector ageing plays also its role, i.e. the number of detector bad pixels (i.e. pixels with anomalous responsivity) can change over time.

One main advantage of airborne imaging spectrometers over spaceborne instruments is the possibility to re-calibrate and re-characterize the instrument in laboratory and to identify instabilities and eventually correct for them. Generally, a 5% requirement for stability is a threshold that should not be exceeded to ensure high data quality. This figure might drop to 2-3% for more demanding products.

2.3.6 Other requirements

Imaging spectrometers require specific software and hardware configurations. The high number of both spectral channels and spatial pixels result in a vast data volume; therefore, huge storage capacity is required to cope with the amount of data. The downlink acquisition chain is also subjected to frequency transmission constraints, namely for spaceborne sensors. Other issues are related to integration time (also referred to as exposure time), data compression, quantization, etc. Imaging spectral scanners require specific and customized software packages in order to process, calibrate and store the recorded images along with their corresponding metadata. Solutions have been implemented and successfully applied to several sensors (Makisara et al. 1993; Hueni et al. 2008).

Part of this thesis discusses the issues described above. For this reason, an instrument model is introduced to explain how the above requirements can be met.

2.4 Instrument model and calibration requirements

At this point, an instrument model must be introduced in order to understand how to transfer observational requirements into calibration and characterization objectives.

Imaging spectrometers measure the solar spectral radiance reflected from ground targets. A spectral measurement represents the spectral signature of the pixel under investigation.

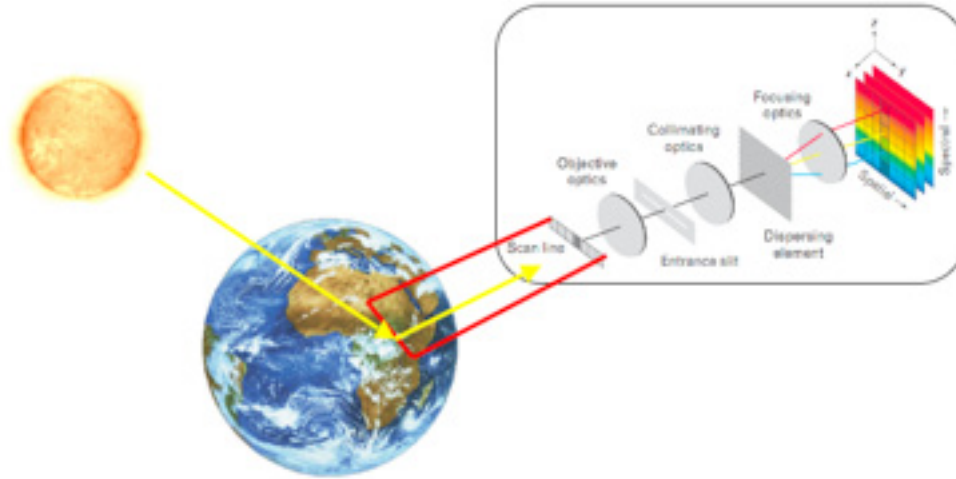


Figure 7: Acquisition principle of an imaging spectrometer (Dell’Endice et al. 2009b).

The general acquisition scheme of an imaging spectrometer is illustrated in Figure 7. The solar reflected spectral radiance passes through an entrance slit and then collimating optics projects light beams onto a dispersing element (e.g. prism, grating) or a dispersing mechanism (e.g. interferometer). The incoming spectral signature is so decomposed in its wavelength constituents and projected on a focal plane (i.e. light-sensitive detector) by means of focusing optics.

2.4.1 Scanning devices

There are different optical designs that can be used to provide spectral separation. *Dispersion systems* (Vane et al. 1993; Mouroulis et al. 2000; Barnsley et al. 2004; Itten et al. 2008; Schaepman 2009) use a prism, a grating, or a combination of them, to separate the incoming radiation. *Fourier Transform Spectrometers* (Doyle et al. 1980; Carlson et al. 1988; Fetterman 2005; Hopey et al. 2008) generally use a moving (Michelson interferometer) or static (Sagnac interferometer) mirror to split the input energy and reconstruct its spectrum through the inverse Fourier transform of the interference pattern of the light. *Filter spectrometers* (Wang et al. 2007; Chang and Lee 2008; Schaepman 2009) separate the light by means of a rotating wheel holding several spectral filters.

Targets sensed by an imaging spectrometer are displayed in three-dimensions: two spatial dimensions (x and y) and one spectral dimension (λ). An example of such a data format is given in Figure 8 and is generally referred to as *image cube*. The image cube comprises several slices (i.e. xy planes) each acquired at a different wavelength; in other words, a xy slice is a monochromatic view of the sensed scene. The y direction (also referred to as *across-track*) is perpendicular to the forward motion of the platform while the x dimension (also referred to as *along-track*) is parallel to it. The forward movement of the platform generates the along-track direction (see Figure 7). The width of the across-track dimension corresponds to the sensor field of view (FOV).

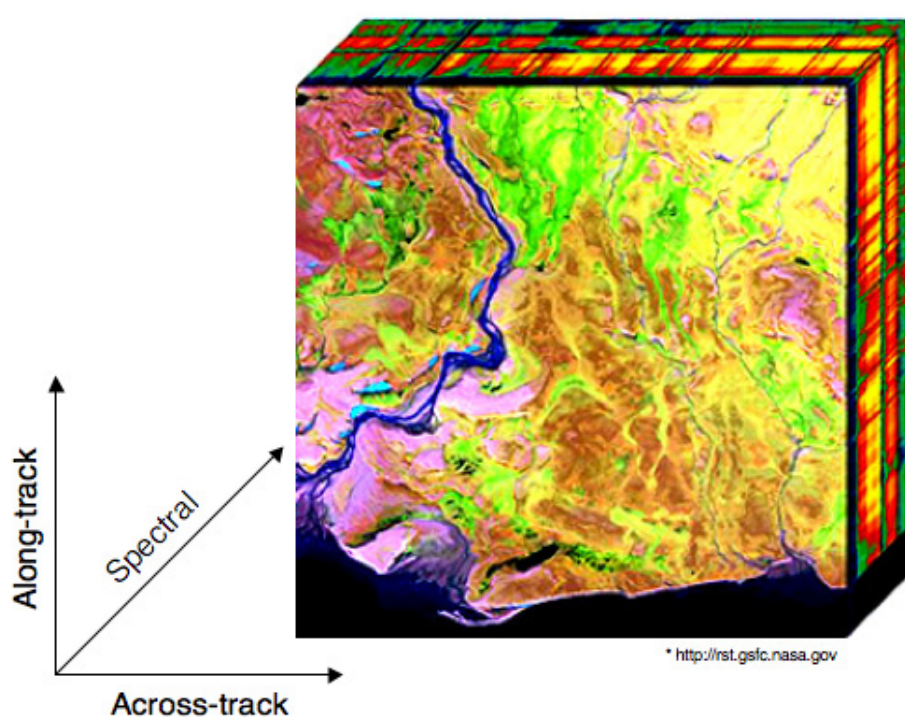


Figure 8: An image cube.

The across-track dimension can be scanned in different ways. In this work, we refer to airborne and spaceborne systems only; systems used for terrestrial or astronomical applications record the x and y dimensions simultaneously and they are usually referred to as *stare* instruments. They are not discussed in this thesis.

2.4.2 Whiskbroom and pushbroom systems: a comparison

The most common imaging spectroscopy sensors are either pushbroom or whiskbroom. A comparison between these two types of scanning devices is made hereafter and a quantification of the corresponding calibration effort is given.

Whiskbroom scanners (Vane et al. 1993; Schaepman 2009) use linear array technology and rotating mirrors to scan the landscape in across-track direction (Figure 9 left). The pixels that constitute the instrument's FOV are recorded sequentially. *Pushbroom* scanners (Babey and Anger 1993; Barnsley et al. 2004; Itten et al. 2008; Schaepman 2009) use instead two-dimensional array technology (Figure 9 right); the across-track swath (i.e. y dimension) is captured at once without the need for a sweeping mechanism. Both scanning systems image the x dimension using the forward (i.e. along-track) motion of the platform (e.g. airplane, satellite).

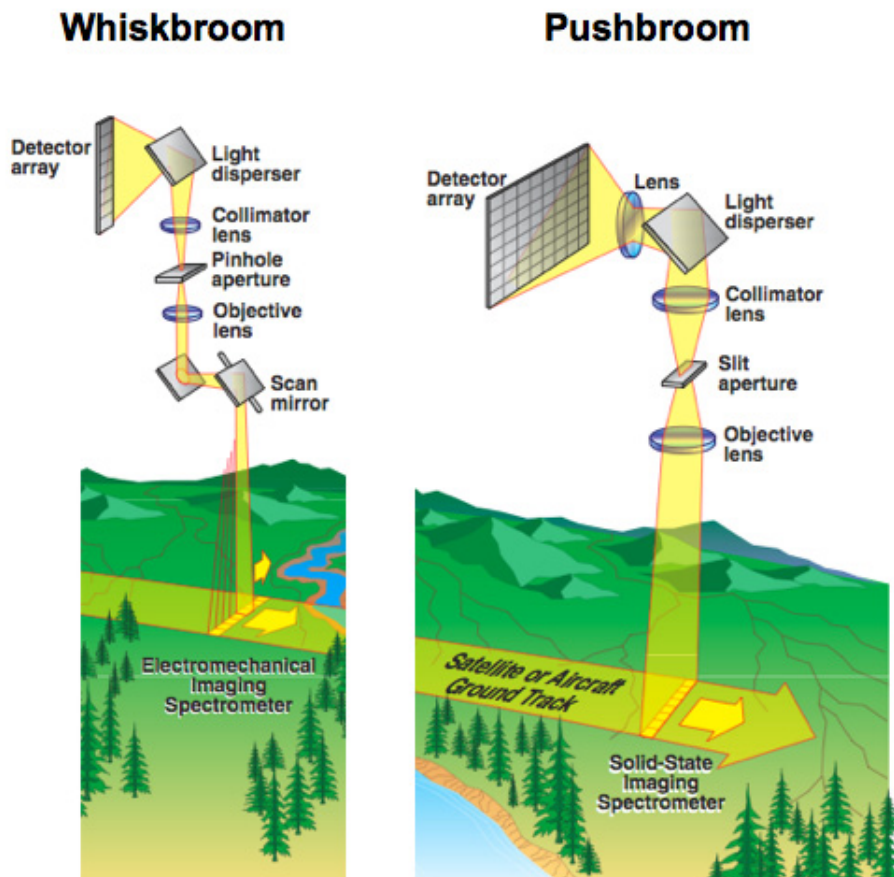


Figure 9: Whiskbroom (Left) and Pushbroom (Right) scanners (Vural 1987).

Whiskbroom and pushbroom systems differ for various reasons, mainly related to (1) the achievable SNR level, (2) the optical design, and (3) the calibration and characterization effort.

The *Signal-To-Noise Ratio (SNR)* describes how the signal is comparable with the noise level. It is the ratio between the number of electrons composing the incoming signal and the number of electrons that characterize the noise (Nieke et al. 1998; Nieke et al. 1999). A high SNR enables a high level of information extraction from spectroscopy data. A lower SNR suffices for strong spectral features while a higher SNR is needed for weak features (Aspinall et al. 2002). The SNR level is strictly dependent on various parameters, e.g. the scanner technology, the acquisition chain, the detectors, and on the spectral regions. In order to combine the motion of the platform with the across-track scan, the angular velocity of the mirror mechanism in whiskbroom systems is relatively high; this restricts the achievable integration times (e.g. limited number of collectable photons) to lower values. It thus defines the upper limit of the maximum achievable SNR. Pushbroom systems allow much higher integration times due to static mechanical elements and, consequently, higher SNR levels can be reached. Higher levels of SNR can considerably increase the level of information extraction from imaging spectroscopy data.

The optical design of a whiskbroom system is less complex because only 1-dimensional (1-D) light sensitive detectors are needed; pushbroom systems, instead, employ a 2-dimensional (2-D) detector requiring more elaborated focusing and collimating optics as well as a more sophisticated reading electronics. This results in greater calibration and characterization effort needed for pushbroom systems in order to characterize the several optical distortions introduced from the 2-D imaging

optics. *Calibration* refers to the process of quantitatively defining the system responses to know and controlled signal inputs. Generally, imaging spectroscopy instrument should undergo the following calibration processes:

1. *Spectral calibration*: defining the center wavelength of a detector spectral channel.
2. *Geometric calibration*: defining the spatial response of a detector pixel.
3. *Radiometric calibration*: defining the relationship between the recorded digital number and the measured spectral radiance.

Characterization is the process of defining the influence of detector parameters (e.g. integration time, temperature, pressure, pixel location) on the spectral, geometric and radiometric properties.

Whiskbroom instruments require less effort in calibration and characterization as only a single line detector is used; additionally, optical distortions may be neglected in several cases. Nevertheless, the movement of the mirrors may cause spatial distortions that should be carefully taken into account during data processing. Pushbroom systems have a more complex optical design because a bi-dimensional detector is needed. This introduces relevant optical distortions, which are not exhibited by whiskbroom systems. Thus, more effort is needed during the calibration and characterization. A complete characterization (e.g. the variation of optical properties on the focal plane) is necessary and time consuming. The comparison between pushbroom and whiskbroom systems is summarized in Table 5.

Table 5: Comparison between whiskbroom and pushbroom systems

	Advantages	Drawbacks
Whiskbroom	<ul style="list-style-type: none"> • Simple optical design • Small optical distortions • 1-D detector • Less complex laboratory calibration • Reading electronics 	<ul style="list-style-type: none"> • Complex mechanical design • Low integration time • Low SNR • Spatial distortions caused by the movement of the mirrors
Pushbroom	<ul style="list-style-type: none"> • High integration time • High SNR • No moving optical elements 	<ul style="list-style-type: none"> • Complex optical design • Relevant optical distortions • Complex optical design • 2-D detector • Reading electronics

Furthermore, the calibrated data should be also validated. Validation refers to the process of assessing, by independent means, the quality of the data products derived from the system outputs.

An overview about the most relevant calibration and characterization procedures as well as about the most used technical terms on this dissertation are given in the next paragraphs.

2.4.3 Spectral calibration

Spectral calibration consists of defining the center wavelength of a detector spectral channel. The spectral sensitivity of a detector pixel to the incoming light is called *spectral response function* (SRF). The SRF is the image on the focal plane of a monochromatic light source after spectral separation or dispersion (Brown et al. 2006). In many imaging spectrometers the SRF can be approximated by a Gaussian function (Vora et al. 2001); such a function is completely defined by its center and its Full-Width-at-Half-Maximum (see Figure 10).

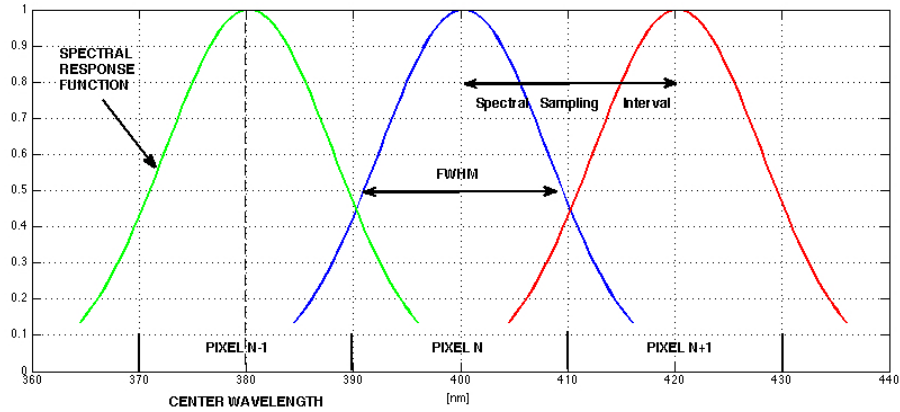


Figure 10: Spectral Response Function and Spectral Sampling Interval.

The main goal of the spectral calibration is to (1) measure the spectral response function, to (2) fit this function to a known curve (i.e. a Gaussian if possible), and to (3) define the response through representative parameters (i.e. center wavelengths and FWHM for a Gaussian function). In the case of pushbroom systems, this process must be carried out for several pixels. The FWHM of a Gaussian SRF can be considered as being the *spectral resolution* (also referred to as *bandwidth*), which represents the spectral selectivity of each spectral channel of the system. It depends on the characteristics of the dispersive element and coincides with the minimal detectable spectral range that a single pixel can detect. It can also be referred to as the bandwidth of the spectral channel (Green 1998; Soares and Costa 1999; Brown et al. 2006; Dell'Endice et al. 2009b).

The distance between the center wavelengths of two consecutive pixels is defined as the *spectral sampling interval*. Imaging spectrometers can offer a spectral resolution as good as 0.1 nanometers. A narrow (Du and Voss 2004) spectral bandwidth provides more details about the physical, and biochemical properties of the sensed targets. The aim of the spectral characterization is to determine the distortions in the spectral direction.

2.4.4 Geometric calibration

An imaging spectrometer resolves spatial features and therefore its spatial responsivity must be defined. The *point spread function* (PSF) is the image of a point source onto the focal plane of an imaging system (Marchand 1964; Du and Voss 2004). Such an image is not a point but it is a blurred spot extending in two spatial dimensions (Marchand 1964), also referred to as the Airy disk. The dispersion of the input energy is therefore described by the spatial point spread function (PSF). The PSF of imaging spectrometers (Schlapfer et al. 2007) can be usually described by a Gaussian function (Vora et al. 2001), completely defined by center position and FWHM. The Gaussian assumption works fine for several imaging spectrometers but must always be assessed upon calibration activities. Airborne or spaceborne imaging spectrometer feature across-track PSF and along-track PSF. The

goal of the geometric calibration is to define these properties and to characterize them over the focal plane. *Spatial selectivity* refers to the measurement error that is introduced when sampling spatial information at a certain angular position in the instrument field-of-view; it is also the minimum detectable spatial distance in metric or angular units that a single system pixel can resolve allowing a sharp and clear identification of the sensed target. Spatial selectivity can also be considered as the minimum detectable area (Schlapfer et al. 2007). If the spatial PSF of the instrument is represented with a Gaussian function, then the spatial uncertainty can be defined as the FWHM of such a curve. It is a measure of the measurement dispersion. The *spatial resolution* is the angular difference between two adjacent across-track pixels or, in other terms, the difference between the peaks of two consecutive spatial PSF. Airborne and spaceborne scanners spatial resolution may range from a few centimeters to a few meters.

If the spatial selectivity is higher than the spatial resolution then the imaging spectrometer is operating in spatial oversampling. Geometric calibration shall also provide the characterization of distortions along the spatial domain(s).

2.4.5 Radiometric calibration and calibration standards

Radiometric calibration consists of defining the relationship between the recorded digital number and the measured spectral radiance. The calibration curve is found correlating the digital output of the imaging spectrometer with the light stimulus provided by a certified light source. There are different types of certified light sources:

- *Primary standard*: it represents a physical unit established by some authority (e.g. institutes of standards) against which all other instruments (secondary standards) are calibrated.
- *Secondary standards* are calibration equipments (e.g. lamps) calibrated against primary standards and provided to users along with a calibration certificate. These are usually the common reference during the calibration of imaging spectrometers.

Radiometric resolution (Green 1998; Du and Voss 2004) is the sensitivity of a sensor to differences in spectral radiance levels and determines the smallest difference in signal intensity that can be identified by the instrument. In other words, it is the amount of energy necessary to increase a pixel value by one digital count. On the other hand, radiometric resolution is commonly also described by the number of bits used to represent such a signal, which can mean that although the electron count is still sensitive to radiance difference, such information that may be lost during the digitization process. *Radiometric uncertainty* can be defined as the calculated standard deviation when repeating the measurement of the same light source in the same measuring conditions; it is also referred to as *Noise-Equivalent-Delta-Radiance*. Finally, *radiometric accuracy* defines how well a system may approximate the true value of the radiation source

Uncertainty impact on imaging spectroscopy data

3 Uncertainty impact on imaging spectroscopy products

This chapter focuses on the estimation of the imaging spectroscopy data uncertainty budget. Imaging spectroscopy data are intrinsically affected by a series of uncertainty factors. The uncertainty of imaging spectroscopy products depends also on data non-uniformities, which are caused by instrument defects and the result in radiometric instabilities, geometric and spectral artefacts, and spectral inconsistencies. Earth-looking optical sensors suffer from these anomalies and removing non-uniformities can improve the quality of the spectral measurements. Improving quality of the measurements can improve the quality of the products. Determining the quantitative distribution of non-uniformities over the detector arrays can improve measurement accuracy and this can be achieved with (1) a full laboratory sensor calibration and characterization or with (2) scene-based detection algorithms.

The impact of some non-uniformity on imaging spectroscopy data has been quantified in the literature. (Green 1998) defined an upper limit for spectral calibration requirements and concluded that a spectral calibration error between 5% and 10% causes relevant errors in the measured radiances. (Schlapfer et al. 2007) investigated the effects of spatial non-uniformities during interpolation schemes and concluded that these influence directly the radiometric data accuracy.

The following manuscript (1) quantifies the intrinsic product uncertainty level caused by data non-uniformities (i.e. the uncertainty contribution of several factors has been estimated), (2) derives an upper limit to product uncertainty for optimal information retrieval, and (3) outlines a calibration and characterization strategy aimed at improving the measurement accuracy.

The discussed research question is:

Which impact do instrument factors have on the quality of imaging spectroscopy measurements and products? Is it possible to quantify the overall uncertainty of imaging spectroscopy products?

3.1 Uniformity of Imaging Spectrometry Data Products

Nieke, J., Schläpfer, D., Dell'Endice, F., Brazile, J., & Itten, K.I. (2008). Uniformity of Imaging Spectrometry Data Products. *IEEE Transactions on Geoscience and Remote Sensing*, 46, 11

Uniformity of Imaging Spectrometry Data Products

Jens Nieke, Daniel Schläpfer, Francesco Dell'Endice, Jason Brazile, and Klaus I. Itten, *Senior Member, IEEE*

Abstract—The increasing quantity and sophistication of imaging spectroscopy applications have led to a higher demand on the quality of Earth observation data products. In particular, it is desired that data products be as consistent as possible (i.e., ideally uniform) in both spectral and spatial dimensions. Yet, data acquired from real (e.g., pushbroom) imaging spectrometers are adversely affected by various categories of artifacts and aberrations including as follows: singular and linear (e.g., bad pixels and missing lines), area (e.g., optical aberrations), and stability and degradation defects. Typically, the consumer of such data products is not aware of the magnitude of such inherent data uncertainties even as more uncertainty is introduced during higher level processing for any particular application. In this paper, it is shown that the impact of imaging spectrometry data product imperfections in currently available data products has an inherent uncertainty of 10%, even though worst case scenarios were excluded, state-of-the-art corrections were applied, and radiometric calibration uncertainties were excluded. Thereafter, it is demonstrated how this error can be reduced ($< 5\%$) with appropriate available technology (onboard, scene, and laboratory calibration) and assimilation procedures during the preprocessing of the data. As a result, more accurate, i.e., uniform, imaging spectrometry data can be delivered to the user community. Hence, the term uniformity of imaging spectrometry data products is defined for enabling the quantitative means to assess the quality of imaging spectrometry data. It is argued that such rigor is necessary for calculating the error propagation of respective higher level processing results and products.

Index Terms—Calibration, data processing, imaging, spectroscopy.

I. INTRODUCTION

SINCE the first airborne hyperspectral imagers (HSIs) were developed in the 1980s, significant effort has been devoted to increase the quality of the resulting hyperspectral data cube. Today, it can be stated that the use of hyperspectral data found its way from prototyping to commercial applications resulting in an increasing demand on highly accurate measurements to satisfy the needs of hyperspectral data user community [1]. In general, a hyperspectral data cube is typically generated by a pushbroom- or whiskbroom-type imaging spectrometer in order to enable the registration in the three dimensions of the cube, i.e., spectral, first spatial (across-track), and second

spatial time (along-track) domains [2]. Examples for selected currently operational [3]–[8] and soon-to-be-available HSI [9]–[11] are given in the Table I.

Even though HSI instrument development and its data application have long history, error estimations for the entire data cube were not established so far—mainly due to the lack of detailed performance specifications on the manufacturer side and the nescience of the consequence of relaxed (or nonexistent) requirements on the user side.

In order to better understand the quality of the HSI data products, a thorough understanding of nonuniformities of the data and their corresponding correction schemes needs to be elaborated.

This is why this paper specifically performs the following:

- 1) addresses the HSI instrument model, which was developed at Remote Sensing Laboratories (RSL) in order to account for the error contributions of data nonuniformities appropriately;
- 2) describes the source and impact of uniformities artifacts on the HSI data products quality;
- 3) outlines possible characterization, calibration, and correction schemes;
- 4) summarizes the overall impact on the HSI product and gives estimates on anticipated errors.

II. INSTRUMENT MODEL

An appropriate HSI instrument model F is introduced for serving as a forward model in order to solve the inverse problem of data processing as well as that of instrument calibration.

The instrument model must reproduce the instrument's behavior accurately. This is why, first, the common equation of signal transformations is provided. The transformation converts the digital numbers C inside the instrument to the radiance field L_s

$$C = F * L_s \quad (1)$$

where the symbol $*$ represents the convolution operator.

Due to the higher transformation complexity of a pushbroom-like HSI, only this kind of instrument is addressed in this paper. In an HSI optical system, the photons of the radiance at sensor L_s are distributed among the pixels of the detector in both the spectral and the across-track directions. The forward movement of the instrument over the scene and the detector's integration time—together with high frequency read-out—allows generation of a hyperspectral data cube.

The instrument model consists of the system's pixel response function $R_{\text{sys}}^{\text{PRF}}$ and various other calibration and characterization parameters (such as polarization sensitivity, ghost and

Manuscript received June 4, 2007; revised September 29, 2007. Current version published October 1, 2008.

J. Nieke is with the European Space Agency (ESA), European Space Research and Technology Centre, 2200 Noordwijk, Netherlands.

D. Schläpfer is with the Remote Sensing Laboratories (RSL), University of Zurich, 8057 Zurich, Switzerland, and also with Kantonsschule Wil, 9501 Wil, Switzerland.

F. Dell'Endice, J. Brazile, and K. I. Itten are with the Remote Sensing Laboratories (RSL), University of Zurich, 8057 Zurich, Switzerland.

Color versions of one or more of the figures in this paper are available online at <http://ieeexplore.ieee.org>.

Digital Object Identifier 10.1109/TGRS.2008.918764

0196-2892/\$25.00 © 2008 IEEE

TABLE I
SPECIFICATIONS AND DESIGN PARAMETERS FOR CURRENT AND FUTURE HYPERSPECTRAL IMAGERS

HSI [manufacturer, country/agency]	Year of 1 st operations	No. of Spectr. Bands	Spectr. Range (μm)	Spectr. Resolution ($\lambda/\Delta\lambda$)	FOV [deg] IFOV [mrad]	Imaging Technique
Airborne IS						
AVIRIS [JPL, US]	1987	224	0.4 - 2.5	40-200	30° 1 mrad	1D whisk., grating
CASI [ITRES, CA]	1990	288	0.4 - 1.0	200	40° 1.5 mrad	2D push., grating
HYMAP [Intergrated Spectronics, AU]	1994	128	0.4 - 2.5	30-125	65° 2 mrad	1D whisk., grating
AISA Eagle [SPECIM, FI]	2005	244	0.4 - 0.97	200-300	39.7° 1 mrad	2D push., prism
ARES [Intergrated Spectronics, AU/DLR]	from 2007	128 (VIS-SWIR); 308 (TIR)	0.4-2.5 0.8-12	30-125 64-100	65° 2 mrad	1D whisk., grating
APEX [RUAG, ESA/CH/BE]	from 2008	313-500	0.38 - 2.5	1000-277	28° 0.5 mrad	2D push., prism
Spaceborne IS						
HYPERION [Northrop Grumman, NASA]	2000	200	0.4 - 2.5	40-250	7.5 km, 30 m	2D push., grating
CHRIS [SSTL, ESA]	2001	18-62	0.4 - 1.0	300-90	13km, 17-34 m	2D push., prism
EnMAP [Keyser Threde, GFZ, DLR]	from 2012	220	0.43 - 2.5	43-250	30km, 30m	2D push., prism

straylight effects, and the absolute radiometric accuracy) combined in the variable K_{sys}

$$F = R_{\text{sys}}^{\text{PRF}} * K_{\text{sys}}. \quad (2)$$

Assuming a linear system, the $R_{\text{sys}}^{\text{PRF}}$ can be expressed as a multiple convolution of point spread functions (PSFs), each associated with one of the system components (e.g., the optics, detectors, and signal and data processing).

In the case of a pushbroom imaging spectrometer, the image of one line is redistributed at the detector level in the spectral (λ) and first spatial (θ) domains. Together with the along-track movement (given by the time t) of the sensor (second spatial domain), we define two spatial PSFs ($R_{\text{AC}}^{\text{PSF}}$ and $R_{\text{AL}}^{\text{PSF}}$) and the spectrometer-inherent spectral response function (SRF) (R_{λ}^{SRF}). The convolution of the normalized PSFs (in a way that the 2-D integral over the two-orthogonal distance variables is equal to one) and the R_{λ}^{SRF} results in the pixel response function ($R_{\text{IS}}^{\text{PRF}}$)

$$R_{\text{IS}}^{\text{PRF}} = R_{\text{AC}}^{\text{PSF}} * R_{\text{AL}}^{\text{PSF}} * R_{\lambda}^{\text{SRF}} \quad (3)$$

where $R_{\text{AC}}^{\text{PSF}}$ and $R_{\text{AL}}^{\text{PSF}}$ correspond to the across-track (indices AC) and along-track (indices AL) PSFs.

Hence, $R_{\text{IS}}^{\text{PRF}}$ is the spatial map of sensitivity across a pixel as well as the information about the crosstalk between neighboring pixels over the entire detector at a certain wavelength λ .

Now, the relation for the HSI needs to be expressed mathematically. In contrast to classical camera design models [12], [13], an HSI model must also account for the spectral domain, resulting in an incident image intensity distribution represented by $f(x, y, z)$, with the pixel response function $r(x, y, z)$ and the signal $s(t, \lambda, \Theta)$ being detected by the pixel (i, j, k) and given as

$$s(i, j, k) = \iiint_{-\infty}^{+\infty} L_s(t, \lambda, \theta) F_{i,j,k}(t, \lambda, \theta) dt d\lambda d\theta \quad (4)$$

on the level of the detector.

The data are already influenced by the optics, and therefore, the different equation based on the image density function $f(x, y, z)$ applies

$$s(i, j, k) = \iiint_{-\infty}^{+\infty} R_{\text{sys}}^{\text{PRF}}(x, y, z) f(x, y, z) dx dy dz \quad (5)$$

where the coordinate system is defined with reference to the detector.

The R^{PRF} resulting from the convolutions in the two spatial and the spectral domains is a good basis to assess the quality of HSI data. Here, the shape, the size, and the diameter of the central lobe are not only related to the spectral and spatial resolutions but also to the sharpness in 3-D of the image cube produced. An ideal R^{PRF} would have a constant value within the boundaries of a pixel (i.e., uniform pixel sensitivity) and

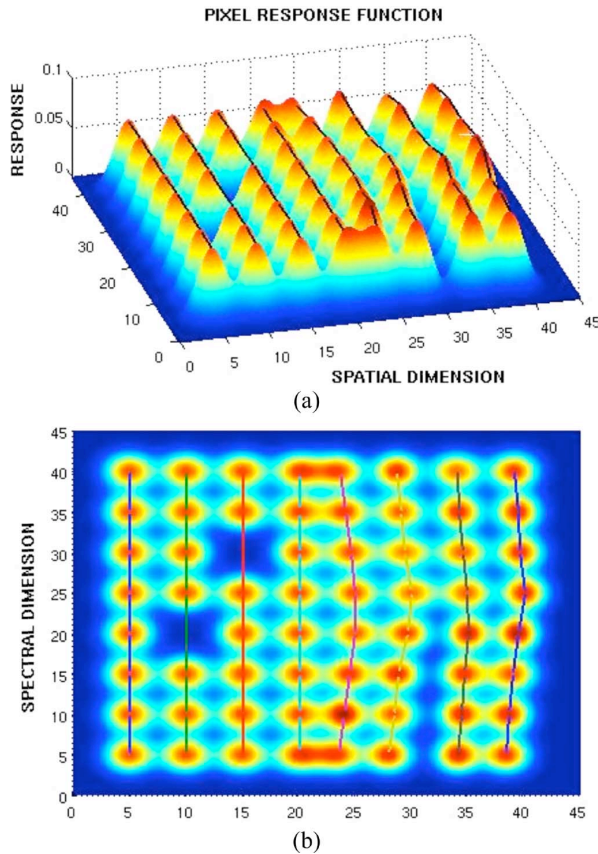


Fig. 1. 3-D view (a) and top view (b) of PRF for eight across-track pixels and eight spectral bands before the 2-D detector array. On the left side, 4×8 PRFs are uniform except of two bad pixels. In contrast, keystone (or spatial misregistration) as nonuniformity is affecting the image quality of 4×8 PRFs on the right side.

zero outside (i.e., no crosstalk or oversampling). However, in practice, instrument data show intrapixel sensitivity variations and nonuniformities in the detector domains (see Figs. 1 and 2). This is why real sensors' PRFs are, in general, simplified as Gaussian functions and not as boxcar functions—the Gaussian distribution more closely matches the description of real sensors. However, we have to keep in mind that the Gaussian PSF is still a simplification. The differences to a real PSF can be estimated comparing the function shapes in Fig. 1 for Gaussian and Fig. 2 for real system distributions.

For the components of R^{PRF} to be measured, various techniques can be applied. Whereas monochromators, tunable lasers, echelons, or absorption filters can be used for R^{SRF} determination, the characterizations of $R_{\text{AC}}^{\text{PSF}}$ and $R_{\text{AL}}^{\text{PSF}}$ are more complex. A favorable way is to characterize the PSF via a line spread function (LSF) (R^{LSF}) or an edge spread function (R^{ESF}). In contrast to the PSF, which can be regarded as a two-dim response to an input point source, the one-dim LSF is determined by a line that is infinitely long and narrow. However, either an R^{LSF} or R^{ESF} exists for each line or edge orientation. Assuming that $R_{\text{AC}}^{\text{PSF}}(y, z)$ represents the response at a point of the spatial coordinate (y, z) and that $R_{\text{AC}}^{\text{LSF}}(y')$

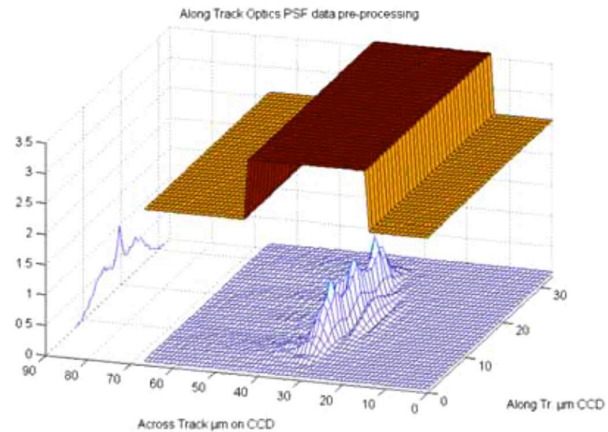


Fig. 2. Typical PSFs as an $R_{\text{AC}}^{\text{PSF}} * R_{\text{AL}}^{\text{PSF}}$ convolution for an imaging spectrometer at $\text{FOV} = 14^\circ$ and $\lambda = 400 \text{ nm}$.

represents the LSF for a line of orientation z' , where y' is orthogonal to z' , then the LSF is the integral of the $R_{\text{AL}}^{\text{PSF}}$ in the z' -direction

$$R^{\text{LSF}}(y') = \int_{-\infty}^{+\infty} R_{\text{AC}}^{\text{PSF}}(y, z) dz'. \quad (6)$$

The straightforward consequence of (1)–(6) is that $R_{\text{IS}}^{\text{PRF}}$ should be exactly known in order to decompose the measured data C into a sum of point sources with known spatial and spectral profiles, i.e., the quantitative assessment of the quality of HSI data.

To better understand the influence of possible imperfections of a homogenous or uniform distribution of equal $R_{\text{IS}}^{\text{PRF}}$, it is important to define the artifacts and aberrations in HSI data and their consequences more precisely.

III. IMPACT OF UNIFORMITY DEFECTS ON IMAGING SPECTROMETRY DATA PRODUCTS

A. Uniformity Definition

Two uniformity terms are commonly used for the description of artifacts in electronic imaging, i.e., spatial uniformity and temporal uniformity.

- 1) Spatial uniformity: For spatial uniformity, the radiometric response is defined as equality within a (spatial) frame detector. This term primarily stems from frame imaging, e.g., in digital photography. It includes effects such as striping or spectrally variable radiometric response related to varying quantum efficiency within a detector array.
- 2) Temporal uniformity: The temporal uniformity describes the temporal radiometric response stability of a detector element. This term is common in video analysis and is used synonymously with “radiometric stability” in imaging spectroscopy.

In contrast to those definitions, pushbroom imaging spectrometry consists of one image frame registering the spectral and

the spatial dimension simultaneously. Any nonuniformity in the system PSF (i.e., the PSF nonuniformity) leads therefore to nonuniformities of the data products in both the spectral and spatial dimensions [14]. Such nonuniformities are commonly termed smile and keystone, respectively. This is why the term uniformity of imaging spectrometry data products must be introduced.

B. Uniformity of Imaging Spectrometry Data Products

In order to reduce the R_{IS}^{PSF} nonuniformity of HSI data, major efforts on data preprocessing and analysis have to be taken into account. The following types of imperfections are defined as nonuniformities, assuming the pixel as a point.

- 1) Singular defects, where the R_{IS}^{PSF} of a single pixel is significantly lower (e.g., 50%) than the mean response of the surrounding detector pixels (e.g., “bad pixels”). Also, all intrapixel nonuniformities are singular defects that are not to be neglected for HSI data preprocessing.
- 2) Linear defects, where the response of an entire line is affected (e.g., “striping,” missing lines) or smear [15].
- 3) Area defects, where the entire frame has imperfections, which are mainly formed by optical aberrations and sampling inconsistencies in the spectral and the first spatial domain. The result is a PSF nonuniformity through spectral and spatial misregistrations which correspond to smile and keystone within one detector array [16].
- 4) Stability defects, where the entire image cube (including the temporal dimension) is affected by, e.g., nonstability of an instrument. These defects typically result in deviations in the second spatial (along-track) domain during the flight.
- 5) Discontinuity defects are caused through the degradation of the HSI through stepwise deteriorations in the optics and/or electronics of the instrument. This defect may cause misinterpretations of temporal effects and time series.

C. Impact of Nonuniformity

After defining the nonuniformity of imaging spectrometry data, it is important to quantify the impact of the PSF nonuniformity on data processing. The most prominent effects have been analyzed recently, i.e., R_{AC}^{PSF} variation, coregistration, and spectral stability, using test data, which were systematically convolved to standard R_{AC}^{PSF} values. The root mean square (rms) of the radiance difference between deviating PSFs and an ideal PSF was derived from such simulated data, which resulted in relative error percentages. As test data, various spectral data cubes were used, such as artificial data cubes derived from the SPECCHIO spectral database [17], [18], where a wide range of more than 4000 natural and simulated surface reflectance spectra had been modeled to at-sensor radiance data using the MODTRAN radiative transfer code [19], or a number of real imaging spectrometry (e.g., from AVIRIS) test data sets. The results from the different analyses [14], [20] are summarized in the following.

1) *Singular and Linear Defects*: The correction of singular pixel defects was tested by linear interpolation of missing

pixels from neighboring pixels. The average error of the bilinear interpolation method to the original pixel value was between 11% and 19% for the replacement of individual pixels, dependent on the wavelength and the interpolation method. If the interpolation was done in the spectral domain, this error was reduced below 5% for spectrally highly resolved instruments. The deviations with nearest neighbor processing were stable at about 17.5%. Bilinear interpolation performed better than nearest neighbor replacement techniques by a factor of up to two if only individual pixels have to be replaced. Singular defects could not be corrected by interpolation beyond a distance of two to three pixels for high-resolution imagery [20].

2) *Area PSF Defects*: For HSI, the spatial PSF width is ideally 1.0 and, typically, is slightly blurred to higher values assuming a contiguous sampling. A variation of the PSF width of 1–1.6 pixels in the across-track direction and 1.2–1.6 pixels in the along-track dimension across the full spectral range was investigated. The influence on the data is in the range of 1%–4% [14]. The results for PSF variations showed that higher resolution of low altitude imagery increases the errors significantly—this indicates that the highest resolution imagery will be even more critical.

Spatial coregistration between the two detectors (e.g., for a visible and infrared channel) can be defective due to pressure- or temperature-dependent misregistrations. In fact, this is a special case of area defects and may be treated by similar procedures. The misregistration effect is quantified as the standard deviation of the difference between resampled imagery using ideal and distorted sensor models. Relative differences of at-sensor radiance reaching 10% were observed between the two sensor models for an arbitrary collection of spectra. To improve the situation, across-track linear interpolation was applied to distorted data (at the same spatial resolution) in order to recover the original image positions. The linear interpolation reduced the error to a level of 2% [20].

3) *Stability Defects*: The stability of HSI is mainly driven by pressure/temperature dependencies resulting from flight level variations from airborne systems and solar heat forcing on the sensor during a single orbit for spaceborne systems. Deviations from uniformity may be observed in the data up to a corresponding estimated level of 10% (compare Table V). The quantification of this defect is technically feasible using an onboard characterization means and the HSI instrument model. A relative accuracy (i.e., stability) level of 2% is achievable by onboard characterization and subsequent data calibration—in case these instabilities are actually encountered [21], [22].

4) *Discontinuity Defects*: Discontinuities of system performance are by nature unforeseeable (e.g., degradation of optical performances) in their impact on system performance. It is assumed that laboratory or in-flight performance monitoring will allow tracing the system performance after a discontinuity has been encountered, e.g., after an unexpected shift of the system parameters. Except for a short transition phase, laboratory or in-flight calibration will allow a complete update of the system characterization. Depending on the performance of in-flight monitoring, a 2% error level can be reached, at the latest after a new laboratory characterization [20].

TABLE II
ESTIMATED IMPACT IN TERMS OF RMS DEVIATIONS DUE TO NONUNIFORMITIES FOR THE APEX INSTRUMENT

Non-Uniformity	Maximum Error	Corrected Error
Point / Line	16%	5%
Area: spatial PSF	4%	1%
Area: spectral PSF	5%	1%
Shortterm Stability	10%	2%
Longterm Discont.	50%	2%
Total RMS	52.90%	6.3%

TABLE III
TYPICAL TECHNICAL REQUIREMENTS FOR STATE-OF-THE-ART HSI [23], [24]

Dimension	Technical Requirement	EnMAP	APEX
Spectral	Spectral Misregistration	< 0.2 pixels	< 0.2 pixels
	Spectral Stability	< 0.5 nm	< 0.1 nm
Spatial	Spatial Misregistration	< 0.2 pixels	< 0.16 pixels
	Coregistration error (VNIR-SWIR)		< 0.16 pixels
General	Relative radiometric stability		< 2%

5) *Error Budget*: Such derived relative errors due to the different nonuniformity effects can be scaled to the actual performance of a specific HSI using a linear relationship between nonuniformity value and expected error. Given the expected radiometric performance of current systems (e.g., those mentioned in Table I), a residual inaccuracy in the range of 2% [21] is achievable for short-term stability only and remains a challenging goal for operational long-term use of the instrument.

In Table II, the impact of nonuniformities is summarized for the most prominent effects in terms of relative data errors as worst case maximum error and corrected error estimates. The residual error is large even after corrections are applied. It only falls below 4% if bad pixels are not part of the error budget or if considerably improved correction schemes are developed for all kinds of nonuniformities.

D. Typical Uniformity Requirements for HSI Data Products

The state of the art of technical requirements for PSF-related issues for HSI is quite difficult to determine since these values were not discussed in detail within the HSI user community so far. This is why just some state-of-the-art requirements can be summarized resulting from two exemplary sensors (Table III). Those values combined with the values retrieved from existing instruments using scene-based characterization methods (Section IV) will be used in Section V as average performance values.

IV. INSTRUMENT AND DATA CALIBRATION

Since the early steps of HSI calibration, important steps in the quantification of HSI nonuniformities have been performed [25], [26]. In order to deliver high-quality data products, it is necessary to quantify the defect and, thereafter, calibrate the flight data appropriately. These steps are called instrument calibration and data calibration. The realization is carried out during various calibration cycles and a processing of the flight data using the retrieved calibration parameters. In the following, an exemplary approach is described on how HSI instrument

and data calibration is performed [22], [27] and the subsequent processing [28] is provided. This approach has been tested with various HSI data sets; it is also generic, i.e., can be used for different HSI sensors.

A. Calibration Measurements

First, the HSI instrument model F and the related parameters have to be described appropriately. Therefore, it is necessary to perform a large variety of calibration and characterization measurements applying different methods, e.g., onboard characterization, frequent laboratory characterization, and vicarious calibration. The retrieved parameters allow data calibration in a processing and archiving facility (PAF). The data calibration includes the calculation of the required time-dependent calibration coefficients from the calibration parameters and, subsequently, the radiometric, spectral, and geometric calibrations of the raw data. Because of the heterogeneity of the characterization measurements, the optimal calibration for each data set is achieved by using a special assimilation algorithm. In order to demonstrate state-of-the-art calibration technology, the characteristics of the recently developed calibration facilities are summarized in the following sections. Serving as examples are the APEX in-flight characterization (IFC) [22], [29] and the APEX calibration home base (CHB) facilities, which were recently developed and allow accurate PRF characterization measurements for providing input for the subsequent processing and assimilation scheme.

1) *Onboard Performance Monitoring*: As an integral part of an HSI, an onboard performance monitor can be used to perform characterization measurements using a filter wheel consisting of various filters, which permits spectral and radiometric characterization. The spectral filters are a rare-earth filter and three bandpass filters at 694, 1000, and 2218 nm. IFC design and performance were described recently [22], and it was shown that the IFC is capable of characterizing the spectral band center with an accuracy of < 1 nm together with a radiometric stability of < 0.5% as relative error. IFC measurements are performed before and after each run (flight

line with continuous uninterrupted data acquisition) and during the CHB calibration measurements.

2) *CHB*: The CHB with dedicated spectral, radiometric, and geometric calibration facilities allows full laboratory characterization and calibration of HSI. The CHB is located at DLR in Oberpfaffenhofen near Munich (Germany).

The CHB consists of a large integrating sphere (1.6-m diameter) to enable radiometric calibration and an optical bench for the spatial and spectral calibrations of APEX. The entire setup makes use of a highly stable design mechanism, such as a rigid granite optical bench, a perfectly isolated foundation (seismic block), and special air bearings. This is why high positioning accuracy in the range of micrometers and arc seconds can be guaranteed. Details on the special design realized for the calibration bench, the integrating sphere, and the interfaces, as well as the large variety of possible spectral, geometric, radiometric, polarimetric, and straylight-related characterization measurements, are given in [29]. For the determination of APEX's PRF, the following measurements are performed: SRF and across/along-track LSF characterization.

For the SRF, a two-step procedure is applied. In the first step, the stimulus from a monochromatic source is geometrically centered on a detector column by equalizing the signal from neighboring elements. In the second step, the SRFs of the elements in this column are scanned by the stepwise increase or decrease of the wavelength of the stimulus. For each element, the integration time should be individually optimized by APEX to suppress noise and achieve best possible results.

Spatially, the characterization will be performed in along- and across-track directions by measuring the R^{LSF} simultaneously using the panchromatic beam of the collimator. For the characterization of the entire matrix detector, the measurements have to be performed for different angular positions across the swath.

For the along-track R_{AL}^{LSF} , the measurement will be accomplished by shifting a vertical slit (perpendicular to the one used for the across-track R_{AC}^{LSF}) in the focal plane of the collimator slightly left and right, i.e., in along-track direction. This movement will be realized by a rotating slit wheel, as the rotational component of such a small shift is negligible. The LSF for the across-track characterization is measured in steps of 1° , i.e., performing 29 steps from -14° to $+14^\circ$.

It has been recently shown [29] that the resulting accuracies of R^{LSF} and R^{SRF} characterizations are in the range of < 0.1 pixels leading to very small uncertainties with regard to spectral (± 0.1 nm) and geometric (± 0.007 mrad) calibrations.

3) *Vicarious or Scene-Based Calibration*: In-orbit vicarious or scene-based calibration is an important tool for monitoring an instrument's performance throughout the mission's duration. Along with the measurement of radiometric features, spectral R^{SRF} and spatial PSF characterizations and/or refinement can be performed as well. In support of the aforementioned uniformity goals, the latter two (R^{SRF} and R^{PSF}) are more critical and, therefore, led to a more detailed investigation. Based on proofs of concept, it has been shown that both R^{SRF} (i.e., band center, bandwidth, and R^{SRF} shape) and spatial misregistration (i.e., keystone) characterizations are possible in most cases. This is of special interest for addressing HSI

nonuniformity issues, particularly for those instruments where characterization is only performed once throughout the entire mission duration, i.e., during the prelaunch calibration activities.

a) *Spectral misregistration*: While the scene-based retrieval of band center and bandwidth is well described in literature [30]–[34], recently, the discernibility of per-band SRF parameters has been explored using imaging spectroscopy data [34]. It was demonstrated that various instrument R^{SRF} shapes could be discerned from a scene by measuring the difference between HSI data and various theoretical R^{SRF} (Gaussian, Bartlett, cosine, Welch, and box).

In particular, to establish discernibility, feature windows for comparison of 75 MODTRAN-4 cases (five target reflectances \times three visibilities \times five R^{SRF}) were selected from among candidate Fraunhofer lines determined to have prominent features: K (Ca), H (Ca), G (Fe), C (H), B (O_2), and A (O_2) (see Fig. 3). For each candidate feature, all window sizes ranging from two to five bands on each side of the feature were iteratively evaluated to choose the "best" window. The window size was then fixed for that particular feature, and an iterative window selection procedure allowed tuning the selection of features that are most suitable for a particular instrument.

In this investigation, it was shown that the Bartlett R^{SRF} is generally the least discernible from the Gaussian R^{SRF} ; the A (O_2) and B (O_2) features seem to have the lowest signal-to-noise (SNR) requirements for discernment; the seemingly very similar cosine and Welch R^{SRF} appear to be easily discernible when compared against the Gaussian; and finally, differing visibility and target reflectance values have mostly minor influences on discernibility.

Based on the establishment of discernibility under these conditions, a method for direct R^{SRF} retrieval was then developed assuming less theoretical R^{SRF} shapes and tested over a wider variety of instrument performance characteristics [35]. Promising results were seen under simulation conditions, allowing variation of parameters over hundreds of permutations based on models of three currently available imaging spectrometers.

Promising results were seen under simulation conditions, allowing variation of parameters over hundreds of permutations based on models of the CHRIS, Hymap, and Hyperion imaging spectrometers, even though their realization of the feature window sizes and locations relative to the actual feature centers varied greatly. Many features proved usable with SNR performance as low as 5000 : 1, which is easily achievable by averaging samples of topologically invariable homogeneous targets, since SNR is improved by the square root of the number of samples taken. Even in its currently primitive form, the described method could be used to obtain SRF estimates better than the typically used Gaussian for the not-uncommon case in which bands are created by summing up to tens of subchannels.

In summary, an instrument's R^{SRF} shape can now be added along with the already established bandwidth and band center in the list of spectral characteristics that can be retrieved or at least refined from the spectroscopy data.

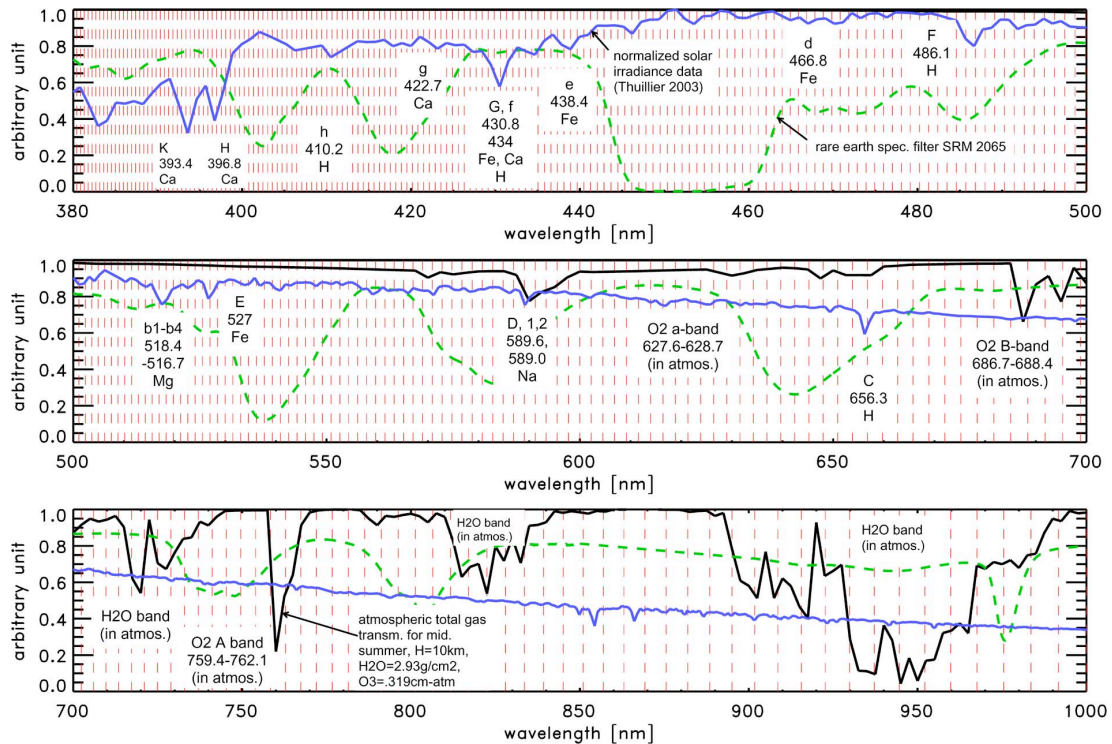


Fig. 3. SRF characterization is integral part of the APEX design using absorption information of the atmosphere (black line), solar light (blue line), and the spectral filters within the IFC. The rare-earth filter is indicated as dashed green line. In the figure, the center wavelength of 312 VNIR spectral bands (before binning) is shown as vertical dashed red lines.

This is particularly true in scenes with characteristics commonly encountered in applications where homogenous areas with high SNR are required, e.g., mining, snow, and agriculture targets.

b) Discernibility of spatial misregistration: Spatial misregistration is an artifact caused either by quadratic optical aberrations and/or misalignments between the components of the scanning system, and it concerns pushbroom spectrometers. Spatial misregistration, if more than 5% of a pixel size, acts in such a way that two spectra, corresponding to two neighboring ground pixels, cannot be distinguished completely.

Recently, a scene-based procedure has been implemented in order to detect spatial misregistration: Edges are first identified on the acquired data, and the variation of their orientation in both wavelength and across-track pixels is then calculated [36].

More in detail, the method recognizes prominent edges within the image and sharpens them in order to increase the contrast. The maxima in the sharpened image are a first good guess on the indication of where the edges can be located. A weighted sum around the maxima, decreasing linearly with the distance from them, is applied in order to achieve subpixel precision. As spatial misregistration depends on the sensed scene, an ideal edge is used as a reference in order to allow correction for such an artifact.

The results demonstrated that spatial misregistration is not constant within the focal plane; it depends quadratically on wavelengths and linearly on across-track positions. This artifact

is constant for all the pixels with nadir view (i.e., 0°), and it changes quadratically along the pixels corresponding to other view angles. At a given spectral wavelength, spatial misregistration varies linearly along the pixels corresponding to different view angles. This scene-based procedure has been applied to several hyperspectral sensors, and the analysis (see Table IV) shows that, on average, spatial misregistration is within the requirements for most of the sensors. The table also gives a comparison of keystone in different sensors and the average amount of spatial misregistration in three significant positions along the across-track dimension.

Spatial misregistration as determined by this procedure has also been compared, when possible, with laboratory measurement: Such a comparison gives confidence that this algorithm can be used in a potential correction scheme. Furthermore, the results allow identification of misalignments between the optical components of the sensor.

B. Data Processing

In general, the processing of imaging spectrometers is divided into two basic steps: 1) the retrieval of the calibration and characterization parameters describing the spectral, spatial, and radiometric performance of the instrument; and 2) the processing of calibrated image data products generated by the same instrument using the calibration parameters retrieved during the first step.

TABLE IV
SPATIAL MISREGISTRATION FOR VARIOUS IMAGING SPECTROMETERS, EXPRESSED IN FRACTION OF A PIXEL SIZE AT NADIR AND TWO OFF-NADIR POSITIONS (\pm FOV/2)

	-FOV/2	NADIR	+ FOV/2
AISA	-0.0343	0.0014	0.0841
AVIRIS VIS	0.0281	0.0112	-0.0184
AVIRIS NIR	0.0188	-0.0099	-0.0054
AVIRIS SWIR1	0.0507	0.0045	-0.0639
AVIRIS SWIR2	0.0452	0.0112	-0.0305
CASI3	0.1004	0.0098	-0.1015
CHRIS	-0.2002	0.0381	0.2569
HYPERION SWIR	0.0511	-0.0028	-0.0232
HYPERION VNIR	0.2261	-0.0046	-0.2296
HYSPEX	0.0629	-0.0025	-0.1039
PHILLS	-0.1405	-0.0029	0.2269

1) *Calibration Data Assimilation and Processing*: In general, the HSI instrument is calibrated by using different sources such as measurements from the CHB, the IFC, and vicariously retrieved calibration information. For each method, a slightly different set of calibration parameters will be delivered at various times throughout the duration of the mission. For example, the effect of the R_{AC}^{PSF} width variation is modeled by convolving the photon flux at detector with a 2-D normalized Gaussian distribution $\sigma_{j,k}$ taking the at-detector coordinates (y_j, z_k) corresponding to continuous pixel indices. Thus, the PSF of the detector pixel (j, k) is calculated as

$$PSF_{j,k}(y_i, z_k) = \frac{1}{2\pi\sigma_j\sigma_k} \exp\left(-\frac{(y_i - j)^2}{2\sigma_j^2} - \frac{(z_k - k)^2}{2\sigma_k^2}\right). \quad (7)$$

It is characterized by its widths j and k in the two dimensions of the detector. These two parameters are assumed to be constant for columns j, k for the standard forward modeling case.

In addition, the accuracy of the results is not constant, depending on the uncertainties of the measurements. This means that the retrieved calibration parameters must be analyzed in a way to reflect the situation of the HSI instrument at a given time. To find adequate parameters, the time evolution of the parameters from the heterogeneous calibration measurements is retrieved by using a data assimilation technique. This flexible data assimilation algorithm was implemented in the PAF in order to combine the information from all of the heterogeneous calibration measurements, as well as from the system insight. In the data assimilation, a Kalman filter combines the past observations in an optimal way at every instance in time. Under the assumption that the system behaves linearly and that the measurement uncertainty is Gaussian, the Kalman filter performs the conditional probability density propagation as described in [37].

The data assimilation algorithm is pursued during the operational phase of the HSI instrument, monitoring possible upgrades or degradations of the system. The open architecture

of the processor allows enhancements to the processor to be done on a regular basis in response to the increasing knowledge of the HSI system's stability and performance.

2) *Processing of Image Data*: In general, a PAF manages the data from acquisition and calibration to processing and dissemination [28]. The processing chain is based on analyzing in-flight acquired image data, housekeeping information (e.g., navigation data and temperature), and onboard calibration data. Frequent laboratory measurements allow the characterization and calibration of the geometric, radiometric, and spatial sensor parameters. By using the outcome of the sensor calibration, the raw image data are converted to at-sensor radiance, traceable to a certified standard.

By using state-of-the-art technology, a large amount of data (100's of GB) are expected during HSI flight campaigns. Hence, data will undergo an offline chain of data correction and characterization processes based on previously acquired laboratory and in-flight calibration parameters. This processing chain includes conversion of raw data values into SI units, bad pixel replacement, and corrections of smear, straylight, smile, and keystone anomalies. A simplified block diagram of the processing is shown in Fig. 4. The data acquisition process produces the top four components on the left side in the "raw data" column. The lower two components are produced during intermission characterization measurements of the instrument which take place in the laboratory during the flight or vicariously. The analysis of the characterization measurements will result in calibration parameter files consisting of required calibration parameters for L1 processing and quality control. All parameters are accompanied by variances that quantify their uncertainties. In addition, any correlation between the parameters' errors, which may be induced by the instrument characterization procedure, is quantified.

V. SUMMARY AND CONCLUSION

Summarizing the results of the nonuniformity studies from Section III, it is possible to generalize the influences for the HSI assuming the following preconditions: 1) exclusion of worst

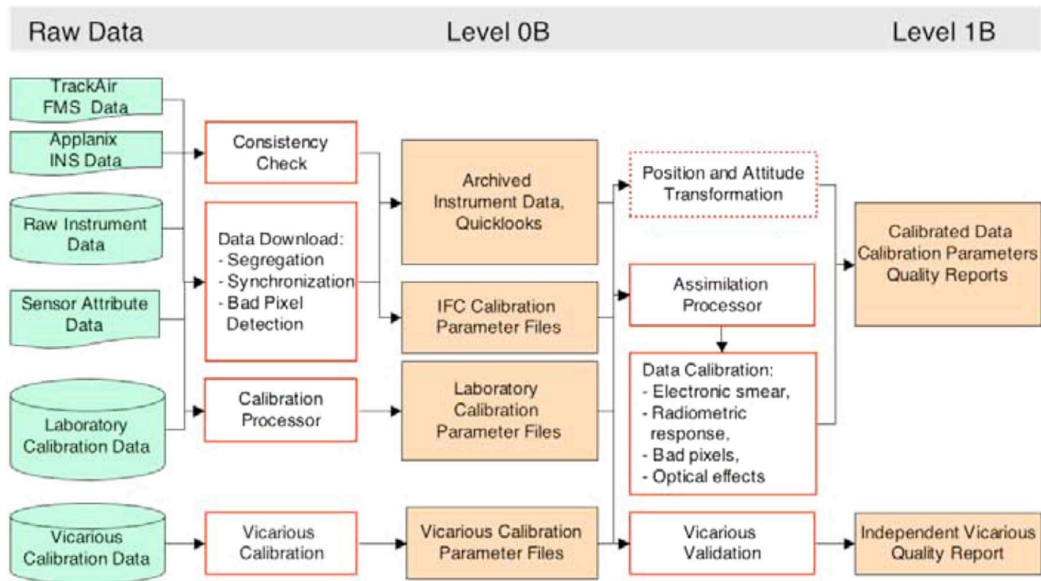


Fig. 4. Generalized processing data flow from raw data until a calibrated at-sensor Level 1B data product.

TABLE V
ESTIMATED AVERAGE IMPACT DUE TO NONUNIFORMITIES IN TERMS OF RMS DEVIATIONS AND ANTICIPATED ERRORS FOR UPCOMING SENSOR GENERATIONS

Defect	Average performance	Average error	Resulting cube error	Anticipated error	Anticipated cube error
Punctual defects			0.1 %		0.1 %
punctual	100 bad pixels/frame	5 %		5 %	
line	1 missing line/frame	5 %		5 %	
Area			1.4 %		0.7 %
spatial	0.2 pixel	1 %		0.5 % (0.1 pixel)	0.5 %
spectral	0.2 pixel	1 %		0.5 % (0.1 pixel)	
Stability	2 % / flight line	2 %	2 %	1 %	1 %
Degradation	4 % / year	8.9 %	8.9 %	2 % (with CHB)	4.5 %
Total error (RMS)			~9.2 %		~4.6 %

case scenarios, such as spectral bands located in absorption band and in the near-UV or far-SWIR; and 2) state-of-the-art correction through raw data preprocessing, such as bad pixel replacement.

Thereafter, it is possible to calculate rms uncertainties for the entire cube (see Table V, column 4), taking the following values for the relevant variables: An HSI provides an imaging cube in the across-track \times spectral \times along-track dimensions with

altogether $1000 \times 300 \times 15000 = 4.5$ Gpixels; the lifetime of the sensor should be five years.

As a result, the total rms error of the image cube was calculated reaching the 10% level after five years, even though worst case scenarios were excluded and state-of-the-art correction was applied.

Clearly, uncertainties in the magnitude of 10% for the delivered data are unacceptable, particularly when considering that

these calculations are only true for those uncertainties outlined in Section III. Further uncertainties resulting from radiometric (absolute and relative) performance, polarization sensitivities, straylight, and pointing instabilities are not considered in this analysis. Since these errors very much depend on the selected radiance standard and the chosen optical design, these values have not been reflected in the current analysis elaborating the influence of nonuniformities of HSI data products. However, it can be concluded that the magnitude of a resulting absolute-total-cube error could easily approach 15%—also without taking worst case scenarios into account.

In the right part of Table V (column 6), the anticipated image cube error was summarized with the following assumptions:

- 1) Improvement on the number of bad pixels is detector technology driven and not considered for the improvement of overall data accuracy.
- 2) Improved optical design will also reduce the spatial and spectral misregistrations to about 0.1 pixel on average, resulting in an improved cube error of 0.7%.
- 3) The short-term stability of hyperspectral data will be improved by using enhanced monitoring and correction schemes, leading to the 1% limit for a single flight line.
- 4) Long-term monitoring using further laboratory and scene-based calibration methodologies (as described in Section IV) will allow further reduction to the 2% level per year (or 4.5% over the five-year lifetime).

This table shows an overall error of 4.6% which is mainly driven by the sensor degradation (i.e., the temporal nonuniformity). If the degradation is monitored accurately by calibration means to a level of 2%, the overall error can apparently be reduced to a level below 3%.

In anticipation of the future pushbroom imaging spectrometer missions (e.g., APEX and EnMAP) and its expected applications, this paper has shown the importance of a coordinated method for achieving a maximum of uniformity in data products. This investigation addresses the increasing demand for more reliable data products generated by current and future imaging spectrometer data providers. The data user is able to better understand the impact of a deviation from the perfect data cube, i.e., a nonuniformity of imaging spectroscopy data products. This directly leads to the fact that the science community will now be able to quantify the quality of imaging spectroscopy data and predict (via error propagation) the uncertainty of their respective higher level processing results and products.

REFERENCES

- [1] J. Nieke and I. Reusen, "A new method to retrieve the data requirements of the remote sensing community—Exemplarily demonstrated for hyperspectral user needs," *Sensors*, vol. 7, pp. 1545–1558, Aug. 2007.
- [2] J. Nieke, H. Schwarzer, A. Neumann, and G. Zimmermann, "Imaging spaceborne and airborne sensor systems in the beginning of the next century," *Proc. SPIE*, vol. 3221, pp. 581–592, Dec. 1997.
- [3] M. A. Folkman, J. Pearlman, B. L. Liao, and P. J. Jarecke, "EO-1/Hyperion hyperspectral imager design, development, characterization, and calibration," *Proc. SPIE*, vol. 4151, pp. 40–51, Feb. 2001.
- [4] M. A. Cutter, "A small satellite hyperspectral mission," in *Proc. 4S Symp. Small Satell., Syst. Services*, La Rochelle, France, Sep. 20–24, 2004, SP571.
- [5] S. K. Babey and C. D. Anger, "Compact airborne spectrographic imager (CASI): A progress review," *Proc. SPIE*, vol. 1937, pp. 152–163, Sep. 1993.
- [6] T. G. Chrien, R. O. Green, and M. L. Eastwood, "Accuracy of the spectral and radiometric laboratory calibration of the Airborne Visible/Infrared Imaging Spectrometer (AVIRIS)," in *Proc. SPIE—Imaging Spectroscopy of the Terrestrial Environment*, 1990, vol. 1298, pp. 37–49.
- [7] R. Bärs, L. Watson, and O. Weatherbee, "AISA as a tool for timely commercial remote sensing," in *Proc. 4th Int. Airborne Remote Sens. Conf. Exhib., Ottawa, ON, Canada*. Ann Arbor, MI: ERIM, 1999, vol. I, pp. 239–246.
- [8] T. Cocks, R. Janssen, A. Stewart, I. Wilson, and T. Shields, "The Hymap airborne hyperspectral sensor: The system, calibration and performance," in *Proc. 1st EARSeL Workshop Imaging Spectrosc.*, Zurich, Switzerland, 1998, pp. 37–42.
- [9] J. Nieke, K. I. Itten, and W. Debruyn, "The airborne imaging spectrometer APEX: From concept to realization," in *Proc. 4th EARSeL Workshop Imaging Spectrosc.*, Warsaw, Poland, 2005.
- [10] A. Müller, R. Richter, M. Habermeyer, H. Mehl, S. Dech, H. J. Kaufmann, K. Segl, P. Strobl, P. Haschberger, and R. Bamler, "ARES: A new reflective/emissive imaging spectrometer for terrestrial applications," *Proc. SPIE*, vol. 5574, pp. 120–127, Oct. 2004.
- [11] H. Kaufmann, K. Segl, S. Chabrilat, S. Hofer, T. Stuffer, A. Mueller, R. Richter, G. Schreier, R. Haydn, and H. Bach, "EnMAP a hyperspectral sensor for environmental mapping and analysis," in *Proc. IGARSS*, 2006, pp. 1617–1619.
- [12] I. E. Abdou and N. J. Dusaussay, "Survey of image quality measurements," in *Proc. Fall Joint Comput. Conf.*, Dallas, TX, Nov. 2–6, 1986, pp. 71–78.
- [13] D. Kavaldjiev and Z. Ninkov, "Influence of nonuniform charge-coupled device pixel response on aperture photometry," *Opt. Eng.*, vol. 40, no. 2, pp. 162–169, Feb. 2001.
- [14] D. Schläpfer, J. Nieke, and K. I. Itten, "Spatial PSF non-uniformity effects in airborne pushbroom imaging spectrometry data," *IEEE Trans. Geosci. Remote Sens.*, vol. 45, no. 2, pp. 458–468, Feb. 2007.
- [15] J. Nieke, M. Solbrig, and N. Neumann, "Noise contributions for imaging spectrometers," *Appl. Opt.*, vol. 38, no. 24, pp. 5191–5194, Aug. 1999.
- [16] P. Mouroulis, R. O. Green, and T. G. Chrien, "Design of pushbroom imaging spectrometers for optimum recovery of spectroscopic and spatial information," *Appl. Opt.*, vol. 39, no. 13, pp. 2210–2220, May 2000.
- [17] S. Bojinski, M. Schaepman, D. Schläpfer, and K. Itten, "SPECCHIO: A spectrum database for remote sensing applications," *Comput. Geosci.*, vol. 29, no. 1, pp. 27–38, Feb. 2003.
- [18] A. Hüni, J. Nieke, J. Schopfer, M. Kneubühler, and K. I. Itten, "The spectral database SPECCHIO for improved long term usability and data sharing," *Comput. Geosci.*, 2007, to be published.
- [19] A. Berk, L. Bernstein, G. Anderson, P. Acharya, D. Robertson, J. Chetwynd, and S. Adler-Golden, "MODTRAN cloud and multiple scattering upgrades with applications to AVIRIS," *Remote Sens. Environ.*, vol. 65, no. 3, pp. 367–375, 1998.
- [20] D. Schläpfer, M. Schaepman, and P. Strobl, "Impact of spatial resampling methods on the radiometric accuracy of airborne imaging spectrometer data," in *Proc. 5th Int. Airborne Remote Sens. Conf. Exhib.*, San Francisco, CA, 2001, p. 8. CD-ROM.
- [21] D. Schläpfer, J. Nieke, and K. I. Itten, *APEX Performance Assessment*, p. 52, 2006. Internal ESA Report APEX_RSL_CON05.
- [22] J. Nieke, J. Kaiser, D. Schläpfer, J. Brazile, K. Itten, P. Strobl, M. Schaepman, and G. Ulbrich, "Calibration methodology for the airborne dispersive pushbroom imaging spectrometer (APEX)," *Proc. SPIE*, vol. 5570, pp. 445–452, 2004.
- [23] H. Kaufmann, S. Chabrilat, S. Mannheim, N. Richter, K. Segl, M. Dees, R. Haydn, M. Lautner, A. Müller, R. Richter, S. Hofer, I. Chorus, P. Hostert, F. Jung-Rothenhäusler, F. Kühn, and M. Sommer, *EnMAP, Environmental Mapping and Analysis Program—User Requirements Document*, 2005. Third Issue (21.06.2005) by GeoForschungsZentrum Potsdam (GFZ), Gesellschaft für Angewandte Fernerkundung AG (GAF), Deutsches Zentrum für Luft- und Raumfahrt (DLR).
- [24] G. Ulbrich, *APEX SoW for Phase C/D*, Apr. 5, 2002. ESA document, EOP-FI/2002-04-631/GU/gu.
- [25] B.-C. Gao, K. B. Heidebrecht, and A. F. H. Goetz, "Derivation of scaled surface reflectances from AVIRIS data," *Remote Sens. Environ.*, vol. 44, no. 2/3, pp. 165–178, Jun. 1993.
- [26] K. Staenz, J. Secker, B.-C. Gao, C. Davis, and C. Nadeau, "Radiative transfer codes applied to hyperspectral data for the retrieval of surface reflectance," *ISPRS J. Photogramm. Remote Sens.*, vol. 57, no. 3, pp. 194–203, Dec. 2002.

[27] D. Schläpfer, M. Schaepman, S. Bojinski, and A. Börner, "Calibration and validation concept for the airborne prism experiment (APEX)," *Can. J. Remote Sens.*, vol. 26, no. 5, pp. 455–465, 2000.

[28] A. Hueni, J. Biesemans, K. Meuleman, F. Dell'Endice, D. Odermatt, D. Schläpfer, M. Kneubuehler, S. Adriaensen, S. Kempenaers, J. Nieke, and K. Itten, "Structure, components and interfaces of the Airborne Prism Experiment (APEX) processing and archiving facility," *IEEE Trans. Geosci. Remote Sens.*, 2008, to be published.

[29] P. Gege, J. Fries, P. Haschberger, P. Schötz, H. Schwarzer, P. Strobl, B. Suhr, G. Ulbrich, and W. J. Vreeling, "Calibration facility for airborne imaging spectrometers," *ISPRS J. Photogramm. Remote Sens.*, 2007, to be published.

[30] B.-C. Gao, M. J. Montes, and C. O. Davis, "Refinement of wavelength calibrations of hyperspectral imaging data using a spectrum-matching technique," *Remote Sens. Environ.*, vol. 90, no. 4, pp. 424–433, Apr. 2004.

[31] R. A. Neville, L. Sun, and K. Staenz, "Detection of spectral line curvature in imaging spectrometer data," *Proc. SPIE*, vol. 5093, pp. 144–154, Sep. 2003.

[32] D. Ramon, R. P. Santer, and P. Dubuisson, "MERIS in-flight spectral calibration in O₂ absorption using surface pressure retrieval," *Proc. SPIE*, vol. 4891, pp. 505–514, Apr. 2003.

[33] D. G. Goodenough, A. Dyk, O. Niemann, J. S. Pearlman, H. Chen, T. Han, M. Murdoch, and C. West, "Processing Hyperion and ALI for forest classification," *IEEE Trans. Geosci. Remote Sens.*, vol. 41, no. 6, pp. 1321–1331, Jun. 2003.

[34] J. Brazile, R. A. Neville, K. Staenz, D. Schläpfer, L. Sun, and K. I. Itten, "Scene-based spectral response function shape discernibility for the APEX imaging spectrometer," *IEEE Geosci. Remote Sens. Lett.*, vol. 3, no. 3, pp. 414–418, Jul. 2006.

[35] J. Brazile, R. A. Neville, K. Staenz, D. Schläpfer, L. Sun, and K. I. Itten, "Toward scene-based retrieval of spectral response for hyperspectral imagers using Fraunhofer features," *Can. J. Remote Sens.*, vol. 34, pp. S43–S58, 2008, Supplement 1.

[36] F. Dell'Endice, J. Nieke, D. Schläpfer, and K. I. Itten, "Scene-based method for spatial misregistration detection in hyperspectral imagery," *Appl. Opt.*, vol. 46, no. 15, pp. 2803–2816, May 2007.

[37] J. W. Kaiser, D. Schläpfer, J. Brazile, P. Strobl, and M. E. Schaepman, "Assimilation of heterogeneous calibration measurements for the APEX spectrometer," *Proc. SPIE*, vol. 5234, pp. 211–220, Feb. 2003.



Jens Nieke received the M.Eng. degree in aeroc and astronautical engineering from the Technical University of Berlin, Berlin, Germany, and National Institute of Applied Sciences (INSA), Lyon, France, and the Ph.D. degree on an advanced satellite mission study for regional coastal zone monitoring from the Technical University of Berlin in 2001.

In 1995, he joined the MOS-IRS Team, German Aerospace Center, Berlin, which launched a spaceborne imaging spectrometer in 1997. From 2000 to 2003, he was a Visiting Scientist with the Earth Observation Research Center, Japan Aerospace Exploration Agency, Tokyo, Japan, involved in the calibration and validation of the ADEOS-II GLI mission. From 2004 to 2007, he was with the Remote Sensing Laboratories, University of Zurich, Zurich, Switzerland, as a Senior Scientist, Lecturer, and Project Manager of the Airborne Prism Experiment (APEX) project of the European Space Agency (ESA). Since 2007, he has been with the ESA at the European Space Research and Technology Centre, Noordwijk, Netherlands, where he is member of the Sentinel-3 team.



Daniel Schläpfer received the M.Sc. degree in geography, the Ph.D. (Dr.sc.nat.) degree, and the teaching degree in physics and geography from the University of Zurich, Zurich, Switzerland, in 1994, 1998, and 1999, respectively.

He is currently a Research Associate with the Remote Sensing Laboratories, University of Zurich, and a Consultant to and a Processing Scientist with the European Space Agency's Airborne Prism Experiment. In addition, he holds a physics teaching position at Kantonsschule Wil, Wil, Switzerland. His current scientific work focuses on the implementation of sophisticated tools for the processing and validation of imaging spectrometry data. He owns and runs the company ReSe Applications Schläpfer, Wil, which is a company focused on the development and distribution of the imaging spectroscopy software packages PARGE, MODO, and ATCOR. His major fields of research are atmospheric and geometric preprocessing of hyperspectral data.



Francesco Dell'Endice received the master's degree in aerospace engineering from the Politecnico di Milano, Milano, Italy, the Dipl.Ing. degree in spacecraft and vehicles from the Ecole Supérieure de l'Aéronatique et de l'Espace (SUPAERO), Toulouse, France, and a graduate certificate in applied science (space studies) from the International Space University (Strasbourg, France)–University of South Australia (Adelaide, Australia). He is currently working toward the Ph.D. degree in remote sensing at the Remote Sensing Laboratories, University of

Zurich, Zurich, Switzerland, with a special interest in the calibration of hyperspectral imaging spectrometers.

He is a member of the Airborne Prism Experiment (APEX) Team, responsible for the calibration concept.



Jason Brazile received the B.A. degree in computer science from the University of North Texas, Denton, in 1991, the M.S. degree in computer science from the University of Texas, Austin, in 1994, and the Ph.D. degree in natural sciences from the University of Zurich, Zurich, Switzerland, in 2008.

He joined the Airborne Prism Experiment (APEX) Team, Remote Sensing Laboratories, University of Zurich, in 2002, where he worked on the parallel and distributed implementation of calibration and preprocessing algorithms in support to the production of APEX imaging spectrometer data products.



Klaus I. Itten (M'82–SM'97) received the M.Sc. and Ph.D. degrees in geography from the University of Zurich, Zurich, Switzerland, in 1969 and 1973, respectively.

Since 1982, he has been a Professor in geography and remote sensing with the University of Zurich. As the Head of the Remote Sensing Laboratories, his research and teaching interests are remote sensing and image processing for natural resources inventory and monitoring. In particular, the application of optical remote sensing and high-spatial- and high-spectral-resolution image data and analysis are the focus of his research. As the Principal Investigator for the APEX project, imaging spectroscopy and spectroradiometry have become important parts of his endeavors.

Detecting sensor properties through image data

4 Detecting sensor properties through image data

This chapter described a scene-based detection algorithm for spatial misregistration, which is a kind of non-uniformity that affects mainly pushbroom sensors and it answer to the following research questions:

How can data non-uniformities be identified directly from the measured data?

Is it possible to implement correction schemes based on this information?

Detector non-uniformities represent a main source of product uncertainty in imaging spectroscopy (Nieke et al. 2008). Several studies (Green 1998; Mouroulis and McKerns 2000; Schlapfer et al. 2007; Nieke et al. 2008) have demonstrated how non-uniform sensor behaviors (Piterman and Ninkov 2002) can significantly influence the quality of imaging spectroscopy products. Such non-uniformities are caused either by sensor defects or by intrinsic instrument properties.

Spectral misregistration (also referred to as *smile*) and *spatial misregistration* (also referred to as *keystone* or *frown*) are some of these non-uniformities. Non-uniformities might also be caused by mechanical parts altering the preferred light path of the incoming light beams inside the instrument as, for instance, vignetting (Seon Joo and Pollefeys 2008), non-uniform entrance slit-width, variable pixel responsivity, imprecise alignment of optical elements (lenses, mirror or dispersive elements). Internal straylight (Coleman 1947; Busch et al. 2000; Brown et al. 2003; Zong et al. 2006) and polarization (Tanzi and Aben 1999; Böttger et al. 2006) also introduce additional disturbance to the ideal spectral and geometrical response of the instrument to light stimuli.

Laboratory calibration is the most accurate way of (1) measuring the instrument optical properties, (2) characterizing the distribution of non-uniformities over the focal plane, and (3) establishing the basis for the implementation of correction schemes. Optimized instrument optical designs (Mouroulis and McKerns 2000) can considerably reduce such effects. If laboratory calibration and characterization cannot be performed, then alternative approaches must be implemented as, for instance, scene-based algorithms. A few correction schemes based on scene-based algorithms have been used so far; for example, (Hayat et al. 1999) corrects non-uniformities adopting a statistical approach; (Ruyten 1999; Winter et al. 2003) developed a scene-based smear correction algorithms; (Zong et al. 2006) and (Brown et al. 2003) proposed methodologies to correct for the straylight.

Scene-based algorithms aiming at the detection of smile and keystone effects were implemented by (Neville et al. 2003, 2004), while a scene-based method for the retrieval of the sensor spectral response function was proposed by (Brazile et al. 2006). (Neville et al. 2004) implemented a scene-based keystone detection scheme that assumes that there is a special point on the instrument detector array where keystone can be considered as zero. The reference point is chosen considering that the least affected pixels are the ones along the nadir. Keystone was then quantified with respect to this point by means of an edge detection algorithm.

The following manuscript proposes an alternative for the choice of the optimal reference by investigating the root causes of keystone. It has been demonstrated that this non-uniformity depends (1) on optical aberrations and (2) on misalignments between optical elements (e.g. lenses, mirror, and detector). The identification of the root causes allows the implementation of model such that scene-based results can be compared with. Several datasets from some several imaging spectrometers have been analyzed and the results are presented in the following publication.

4.1 Scene-based method for spatial misregistration detection in hyperspectral imagery

Dell'Endice, F., Nieke, J., Schläpfer, D., & Itten, K.I. (2007). Scene-based method for spatial misregistration detection in hyperspectral imagery. *Applied Optics*, 46, 14

Scene-based method for spatial misregistration detection in hyperspectral imagery

Francesco Dell'Endice, Jens Nieke, Daniel Schläpfer, and Klaus I. Itten

Hyperspectral imaging (HSI) sensors suffer from spatial misregistration, an artifact that prevents the accurate acquisition of the spectra. Physical considerations let us assume that the influence of the spatial misregistration on the acquired data depends both on the wavelength and on the across-track position. A scene-based method, based on edge detection, is therefore proposed. Such a procedure measures the variation on the spatial location of an edge between its various monochromatic projections, giving an estimation for spatial misregistration, and also allowing identification of misalignments. The method has been applied to several hyperspectral sensors, either prism, or grating-based designs. The results confirm the dependence assumptions on λ and θ , spectral wavelength and across-track pixel, respectively. Suggestions are also given to correct for spatial misregistration. © 2007 Optical Society of America

OCIS codes: 080.1010, 100.6890, 120.6200, 300.6190.

1. Introduction

Spatial misregistration (SM) is an artifact that mainly affects pushbroom systems,¹ where contiguous ground pixels are recorded at the same time by an array-based detector, e.g., a CCD, in comparison to whiskbroom scanners,¹ which scan one ground pixel at a time, recording its spectral components. The study of this artifact is relevant to understand the quality degradation of the acquired data. The basic element in hyperspectral imaging (HSI) is the image cube² [Fig. 1(a)], which contains two spatial dimensions, and one spectral dimension. An x - y section of the cube is the monochromatic view of the sensed scene (also called the layer), while the y - z section represents one frame [Fig. 1(b)], which can be identified with either the sensor focal plane, or the image plane, i.e., the CCD. The pixels in one array line, i.e., the across-track dimension, correspond to the sampled ground spots. The spectrum of each ground spot is dispersed along one array column. In airborne and spaceborne applications the second spatial dimension (x axis), i.e., the along-track dimension, is provided by

the motion of the platform, while in terrestrial sensors the two spatial dimensions are recorded temporally. Each pixel is then characterized by three indices (i, j, k) . The hyperspectral image cube contains millions of picture elements (pixels), providing a rich source of information for identifying and classifying objects^{3,4} with as much accuracy as possible. Nevertheless, there are a number of artifacts that degrade the image quality,⁵ and result in nonuniformities in the acquired data. Uniformity can be intended as whatever makes the recorded data consistent with the actual data.

SM, one of these artifacts, is mainly investigated in this paper. The upwelling radiance, reflected by one ground pixel, should be decomposed in all its spectral components, along the same array column, at least in an ideal situation. SM alters this uniformity allowing the upwelling energy to decompose itself along more than one array column. It means that if two neighboring ground pixels contain two different target materials, with different spectra, then the spectrum measured by the sensor in one column will result in a mixture of the spectra of the two different materials. The objective of this work is to demonstrate that SM varies quadratically with wavelength and linearly with across-track position. First the physical causes for SM are analyzed, and later on a detection method is proposed.

2. Physical Reasons for Spatial Misregistration

SM is the sum of a high-order aberration and misalignments; the former refers to a distortion term in

The authors are with the Remote Sensing Laboratories (RSL), the Department of Geography, University of Zurich, CH-8057, Switzerland. F. Dell'Endice's e-mail address is fradel@geo.unizh.ch.

Received 6 October 2006; revised 5 December 2006; accepted 4 January 2007; posted 19 January 2007 (Doc. ID 75827); published 1 May 2007.

0003-6935/07/152803-14\$15.00/0

© 2007 Optical Society of America

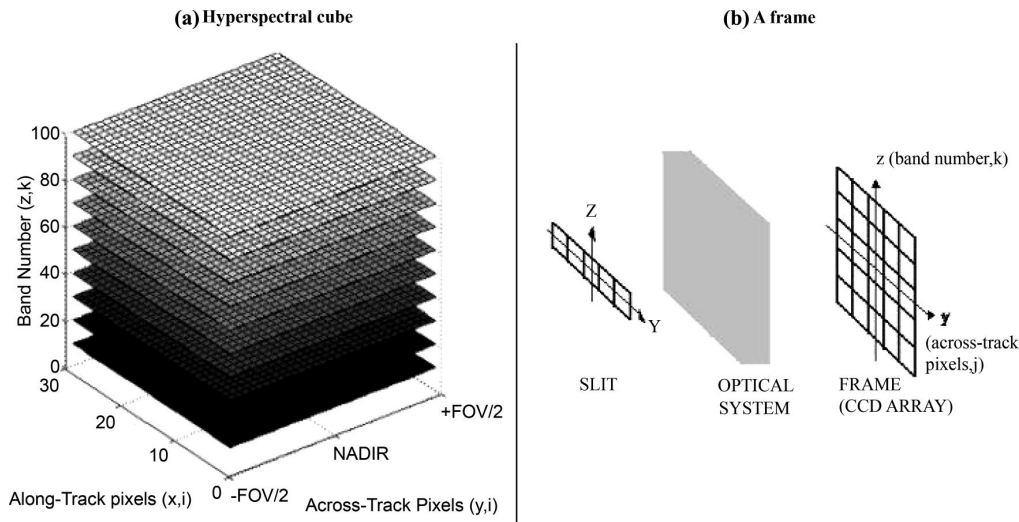


Fig. 1. (a) Various layers in a hyperspectral cube, (b) basic elements in a hyperspectral scanner. The yz plane is the main reference of this work.

the wave aberration function, while the latter refers to the arrangement of the sensor components. The distortion term is called keystone, which is sometimes erroneously used to address SM, as it gives the main contribution to this artifact. We want to point out that hereafter keystone is intended as an optical aberration only, and not as SM.

Keystone, as it is the case for the smile distortion,⁶ acts in such a way that a straight line is not imaged in a straight line but rather in a curve.^{6–8} The main contribution to keystone is given by the quadratic distortion II wave aberration (QAII).⁹ An expression for this aberration, in the case of a prism is given in Eq. (1), while that for a plane grating is given in Eq. (2), as analyzed analytically in Ref. 8. (We used the formulas and notation of Ref. 8):

$$W_{QAII} = -\frac{(1-n^2)}{n^2} \bar{u} \left[\bar{u}(\sin I_1 - \sin I_2')y - \frac{1}{2}(\sin I_1 + \sin I_2')\frac{ut}{n} - \Psi(\sin I_1 - \sin I_2') \right], \quad (1)$$

$$W_{QAII} = -\bar{u}^2 \left(\frac{m\lambda}{d} \right) y + \bar{u} \Psi \left(\frac{m\lambda}{d} \right). \quad (2)$$

This distortion is called quadratic because it depends quadratically on the field,^{8,10,11} which we can identify with the focal plane. If we assume that the CCD pixel coordinate system (y, z) is centered on the focal plane [Fig. 1(b)], which applies to most of the available sensors, we can derive the following relationship:

$$\beta(y, z) = d(y, z)W_{QAII}, \quad (3)$$

$$d(y, z) = y(c_1 z^2 + c_2), \quad (4)$$

where $\beta(y, z)$ is the keystone at position (y, z) , $d(y, z)$ is the dependency coefficient in the same position, c_1 and c_2 are two proportionality constants, and y and z are the across-track, and the spectral dimensions, respectively. The expression for d suggests that keystone depends quadratically on wavelength [Fig. 2(a)] and linearly on the across-track pixel [Fig. 2(b)]. The quadratic dependence is symmetrical with respect to the y axis (i.e., changing of the parabola curvature sign), and increases when we move away from it. The whole keystone profile over the entire focal plane is shown in Fig. 2(c).

Misalignments between optical components influence the keystone profile, altering the position of the dispersed ray on the focal plane¹² and acting as an offset for it. The paraboloid [Fig. 2(c)] can be shifted either along the spectral axis, resulting in a vertical misalignment m_V [Fig. 3(a)], and/or rotate around the focal plane center, resulting in a rotational misalignment m_R [Fig. 3(b)].

We can now derive an expression for the SM, indicated with the variable s :

$$s(y, z) = \beta(y, z) + m_V + m_R, \quad (5)$$

where m_V , and m_R take in account for the offset, introduced by the two misalignments. Given a sensor, these two values are constant for all the focal plane elements. The SM can increase if two or more detector arrays are used to cover, for instance, a predefined spectral range: The overlapping regions generate the so-called coregistration.

We can also explain the spatial misregistration evaluating the detector response to the electromagnetic stimuli. Every pixel of the CCD is characterized by its spectral response function (SRF), and its point-spread function (PSF), the latter representing the sensor spatial response. If we assume that both the

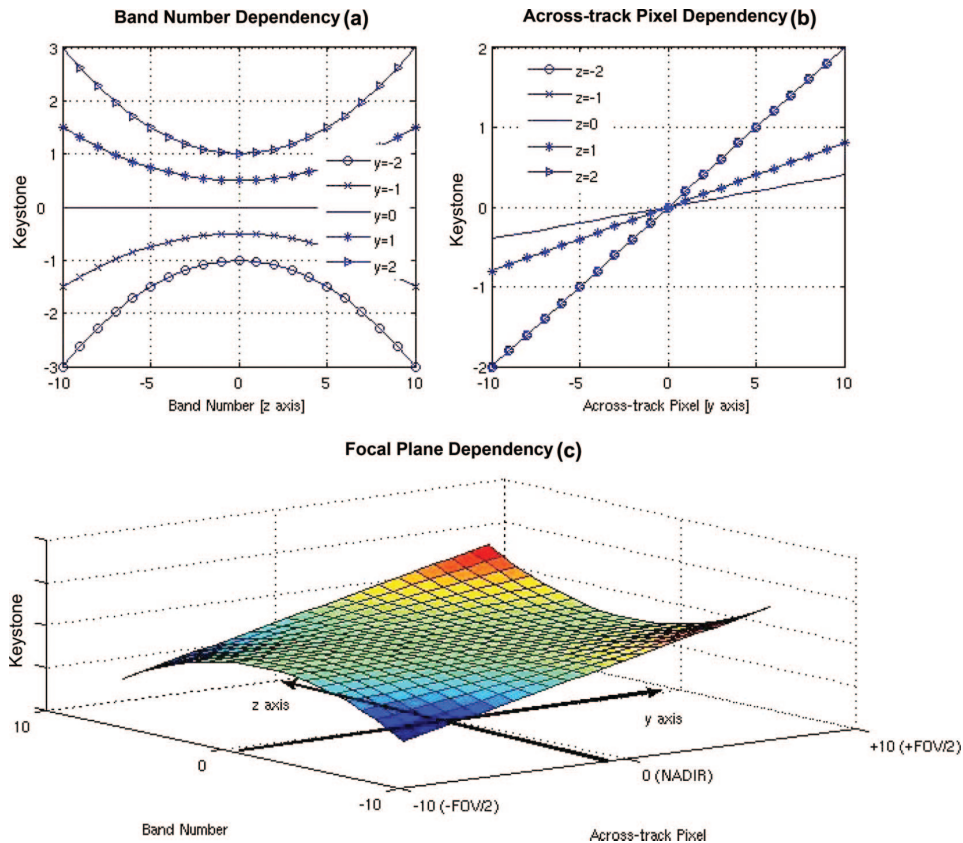


Fig. 2. (Color online) (a) Keystone variation with wavelength: Each curve corresponds to one spatial location. (b) Keystone variation with across-track position: Each curve corresponds to one band number. (c) The whole keystone variation over the focal plane.

SRF and the PSF are Gaussian-like functions, they can be distinctly identified by the FWHM and the peak location.¹³ The combination of these two responses makes up the pixel response function (PRF), which, in an ideal system, has a 2D Gaussian shape (Fig. 4). Spatial uniformity¹³ means that both the FWHM and the peak location of the PSF are constant over the spectrum (z direction), if they refer to the same across-track pixel. Generically, PSF nonuniformities correspond to variations of the FWHM and a peak location for each sort of response function, either spectral or spatial¹⁴ (Fig. 4). In spite of that, hyperspectral imaging systems that have a SRF of nonuniform FWHM can efficiently gather information about a scene with a minimal corruption.⁴

3. State of the Art

SM affects the data in a manner that depends on the shape of the spectra to be recovered, and this makes it difficult to fix a requirement for such an artifact. Nevertheless, the maximum keystone has to be less than 5% of the pixel size.^{6,14,15} This requirement is very stringent, but it is compulsory if we want spectral signatures useful for the science community. Strategies are then needed both to detect and to correct for it.

To avoid image distortions, new optical designs have been investigated, especially based on concentric optics,^{6,16} to make both grating-based and prism-based sensors as accurate as possible. Concentric optics has been used for the Compact High Resolution Imaging Spectrometer (CHRIS)¹⁷; by introducing a field prism near the image plane, the image distortions can be corrected.¹⁸ Moreover, if the optical system is plane symmetric (also called bilateral symmetric), the main dependence of aberrations as a function of system parameters has been established by a set of approximate aberration coefficients.⁹ Conditions to make the optical system free from aberrations, which have quadratic dependence on the focal plane position, have also been studied.¹¹

A pushbroom is usually preferred to a whiskbroom scanner because it offers a higher signal-to-noise ratio (SNR),^{14,19} even if it experiences a few nonuniformities, which can be removed by means of careful calibration.⁶ Nevertheless, whiskbroom sensors can present a constant SM, because of misalignments. Laboratory measurements are performed to quantify the SM. A pinhole, illuminated by a white source,²⁰ is imaged onto a CCD column (z axis), for a few spatial positions along the y axis. The gravity centers of the pinhole blurred images onto the pixel elements cor-

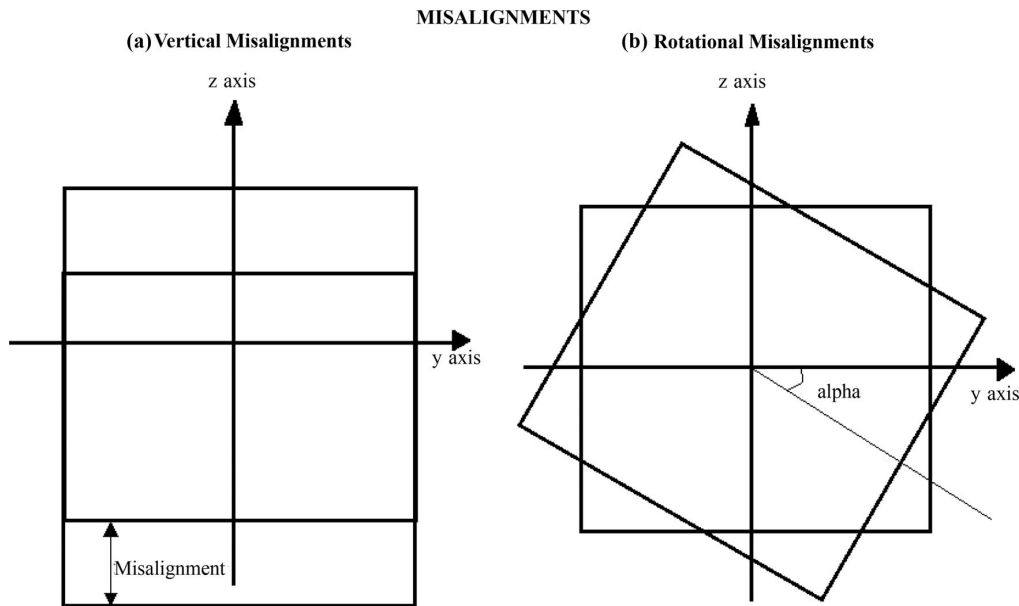


Fig. 3. (a) Vertical misalignment m_V , (b) rotational misalignment m_R .

respond to the PSF centers; their alignment gives a measure for SM. However, this procedure is time consuming; it implies that only a few locations along the field of view (FOV) can be measured. A complete analysis of the whole focal plane is not possible. Additionally, the laboratory calibration is usually performed once or twice per year. As each instrument may suffer from temporal instability (i.e., a changing of the calibration parameters with time), a few labo-

ratory calibrations per year can be inadequate to characterize properly the instrument during its operational life (i.e., flight campaigns). On the other hand, several laboratory calibrations per year will continuously interrupt the flight sessions.

Data processing can be used then to improve the characterization of the sensor. Resampling, for instance, has been applied to the airborne hyperspectral imager (AHI), via a statistical approach, called "kriging,"²¹ a correction procedure that transforms the actual radiance values to the desired ones. The desired values are computed on pixel basis using a weighting coefficient, which depends both on the expected error and on a set of calibration parameters. A detection method is also available and is based upon the edge detection.²² It relies on the sensed scene, and it uses a Sobel filter to detect edges in each layer of the scene. One monochromatic view of an edge is chosen as a reference (e.g., zero SM), and a correlation analysis is then performed between this reference and the other monochromatic views of the same edge. This technique measures a series of subpixel shift values, which are an estimation for SM; such values are relative because they depend on the band chosen as reference. An invariant measure can be recovered by calculating a rms deviation of the shifts for each across-track pixel over all the spectral bands, but this will bring only one value for the whole frame. In the next section, we propose an improved version of this method, whose results are independent of the layer chosen as a reference.

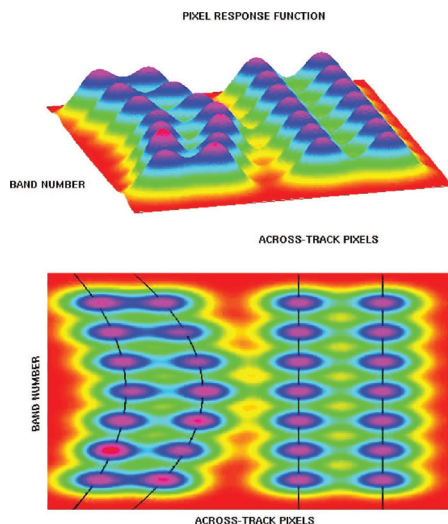


Fig. 4. (Color online) Two views of a CCD with 4 across-track pixels and 7 bands. The 2 across-track pixels at the right of the image do not have any SM because the peaks are all aligned. In the left-side pixels, there is some SM: In fact, the peaks are not aligned, but they are located on a curved line.

4. Method

The following procedure analyzes the acquired scenes. Let us consider an image cube matrix \mathbf{C} . We assume

that edges are present in the acquired scene, and for sake of easiness, we analyze only one of them, which extends for several along-track pixels, and for a few across-track pixels. If the sensor suffers from SM, both the orientation, and location of the edge will vary both with the wavelength and with the across-track pixel. The aim of the procedure is indeed to find the edge location, at subpixel level, in a given spectral band, and retrieve the same parameter for all the bands, and this will be estimation for SM. As the sampled image of an edge is blurred, by edge location we mean a point within this transition region whose exact position will be specified afterwards. In the notation, matrices are capitalized, while their elements are in lower case. The method can be summarized as follows:

1. *Selection*: If there is a noticeable edge, a subset of the image cube \mathbf{C} is then selected manually, by means of visualization software. This can be accomplished observing a quick look of the scene. This produces a 3D matrix subset \mathbf{B} , with p along-track pixels, q across-track pixels, and r spectral bands, and each \mathbf{B} element will be indicated as $b(i, j, k)$.

2. *Desaturation*: Digital number values equal to the upper limit of the sensor dynamic range need to be changed to zero to avoid discontinuities during the edge sharpening. This step will generate the desaturated subset \mathbf{D} with same dimensions as \mathbf{B} :

$$\begin{aligned} \text{If } b(i, j, k) = u, \text{ then } d(i, j, k) &= 0 \\ \text{else } d(i, j, k) &= b(i, j, k), \end{aligned} \quad (6)$$

where u is the dynamic range upper limit.

3. *Sharpening*: The edge is sharpened using a first-derivative kernel, applied only in the across-track dimension (y direction), for the entire r layer. The gradient we used has the following expression:

$$\mathbf{G} = \begin{pmatrix} 1 & 1 & 1 & 0 & -1 & -1 & -1 \\ 1 & 2 & 2 & 0 & -2 & -2 & -1 \\ 1 & 2 & 3 & 0 & -3 & -2 & -1 \\ 1 & 2 & 3 & 0 & -3 & -2 & -1 \\ 1 & 2 & 3 & 0 & -3 & -2 & -1 \\ 1 & 2 & 2 & 0 & -3 & -2 & -1 \\ 1 & 1 & 1 & 0 & -1 & -1 & -1 \end{pmatrix}. \quad (7)$$

The filtered cube \mathbf{T} will then be the convolution between the kernel gradient and the selected subset:

$$\mathbf{T} = \mathbf{G} * \mathbf{D}, \quad (8)$$

where $*$ denotes the convolution operation.

4. *Squaring*: The filtered cube is then squared in order to obtain positive maxima only:

$$\mathbf{F} = \mathbf{T}^2. \quad (9)$$

5. *Locating maxima*: For a given band \bar{k} the pixel number corresponding to the derivative maximum in each i th line of the layer is found:

$$m(i)_{\bar{k}} = \max_j f(i, j, \bar{k}) \quad \forall i = 1, 2, \dots, p. \quad (10)$$

$\mathbf{M}_{\bar{k}}$ is a column vector with p elements. The number of $\mathbf{M}_{\bar{k}}$ vectors will be equal to r . Locating an ideal edge is equivalent to finding the point where the derivative has a maximum (for a rising edge with positive slope) or a minimum (for a falling edge with negative slope). We can assume, without loss of generality, that the derivative has maxima only.

6. *Weighting*: For a give spectral band \bar{k} , a weighted sum around the maximum position is carried out for all the q lines:

$$v(i)_{\bar{k}} = \frac{\left[\sum_{u=i-3}^{i+3} \sum_{j=m(i)_{\bar{k}}-3}^{m(i)_{\bar{k}}+3} c(j) \cdot (f(e, j, \bar{k})) \right]}{\left[\sum_{u=i-3}^{i+3} \sum_{j=m(i)_{\bar{k}}-3}^{m(i)_{\bar{k}}+3} (f(e, j, \bar{k})) \right]}, \quad (11)$$

where $f(e, j, \bar{k})$ is the derivative value for the pixel $u(i, j, \bar{k})$ in the k th band, and $c(j)$ is a weighting factor for the pixel $u(i, j, \bar{k})$ whose value is linearly decreasing with the distance from the maximum position $m(i)$ along the across-track direction, being e a temporary index for i . The summation is taken over an odd number of columns and rows (usually 3, 5, or 7). The outcome of this operation will be r subpixel edge position vectors $\mathbf{V}_{\bar{k}}$, each one of them containing p elements.

7. *Averaging*: The mean across-track edge position, for each spectral band, is the averaging of the all p subpixel locations for that spectral channel:

$$z(k) = \frac{\left[\sum_{i=1}^p v(i)_{\bar{k}} \right]}{p} \quad \forall k = 1, 2, \dots, r. \quad (12)$$

The next two steps are optional: They are useful for visualization (step 8), and analysis (step 9) purposes.

8. *Fitting*: The r elements of the \mathbf{Z} vector are fitted using a second-order polynomial against the r bands.

9. *Comparison*: \mathbf{Z} is compared with the available laboratory SM measurements.

It is apparent, that applying the method to several across-track pixels will provide the $s(y, z)$ profile.

There are different arguments that lead to the aforementioned procedure. In the literature there are several first-derivative kernels; some of them (i.e., Sobel,²³ Frei and Chan,²⁴ Prewitt²⁵) are not suitable in the sense that they are not able to detect edges in a high-noise environment.²³ As the SNR is not uniform over the spectral range, this should be taken into account using an adequate detecting operator. A kernel, which performs well in such a case, is the Abdou²⁶ kernel that gives a linearly decreasing weighting to pixels away from the center of the edge. Obviously, one can use the kernel that better satisfies its requirements, but this has to be chosen attentively in accordance with the sensor characteristics. Second-derivative kernels have not been employed because they produce two-pixel-thick

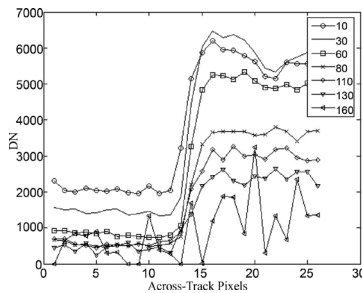


Fig. 5. An edge at different wavelengths, from the HYSPEX sensor. The edge is prominent from band 1 to band 110. In the last bands the derivative maximum disappears, and the edge is not detectable anymore.

edges, and they are extremely sensitive to noise. Besides, not all the spectral bands can be employed for the edge detection. The distinction between certain features can be clear, or at least evident in some region of the spectrum and blurred, or completely absent in other portions; this is because the spectral signature of the edge changes over the wavelength range (Fig. 5), and so the derivative maximum can be more significant in certain bands, and either less significant or completely absent in other bands. Edge detection is also influenced by the sensor performances, as is the SNR. The consequence is that in these bands the method fails. Bypassing this difficulty is achievable by selecting only the spectral channels with an acceptable contrast. Such a selection is done automatically by the method, in the sense that noisy bands will produce discontinuities in the \mathbf{Z} vectors. Interpolation can be done afterwards to infer about the missing spectral information, but the interpolated value does not have any physical meaning unless we have some *a priori* knowledge.

The reason for a weighted sum is because in reality the maximum position is not corresponding to the exact edge location, but is rather an indication of where the edge center probably will be. This is for diffraction, aberrations, and optical issues that smooth the sampled image of the edge. Basically, we do not know *a priori* which band gives the absolute edge position to be used as a standard reference for all the spectral bands; it implies that there is an offset somewhere. If we assume that SM has a quadratic

dependence on wavelength, then there will be a point (i.e., a band) where SM is the lowest. Ideally, this point will coincide with the band number located on the y axis [Fig. 1(b)]. We assume that the values measured in this spectral band will be the offset that we have been looking for, i.e., the minimal spatial misregistration values. In a real application, this reference point will be along an axis parallel to the y axis because of misalignments for instance.

5. Results and Discussion

The detection method has been applied to several pushbroom sensors, where AVIRIS²⁷ is the only whiskbroom scanner considered (Table 1). For each sensor, by means of various image cubes, several across-track positions have been analyzed, but in the next figure only three spatial positions are shown: $-\text{FOV}/2$, NADIR, and $+\text{FOV}/2$, which correspond to across-track pixels close respectively to $j_1 = 1$, $j_2 = q/2$, and $j_3 = q$, where q is the number of across-track pixels. The y axis, and the z axis are oriented as in Fig. 1(a). To improve the results, the data corresponding to neighboring across-track pixels have been averaged together, and standard deviation is the discriminant criteria in removing misregistration values out of the interval of confidence. The vertical axis corresponds to the spectral range while the horizontal axis corresponds to SM in a fraction of a pixel size [Fig. 1(b)].

Our objective will be to show that SM depends quadratically on wavelength and linearly on across-track position: Namely, we expect no SM along the j_2 column, and SM, equal in absolute value but opposite in sign, along j_1 (i.e., $-\text{FOV}/2$), and j_3 (i.e., $+\text{FOV}/2$).

As other artifacts and detector misalignments prevent this ideal behavior, we expect the SM variation to be slightly different and, in other words, the minimal linear variation to be along the NADIR direction, and a symmetrical variation on the rest of the focal plane. For a few sensors, SM laboratory measurements were available, and they will be used to validate the method.

A. HYSPEX

HYSPEX is a series of compact, high-resolution imaging spectrometers that is being developed by Norsk Elektro Optik AS, (NEO, Norway).²⁸ The instrument is modular and consists of three different spec-

Table 1. List of the Analyzed Sensors

Sensor	Scanner	Bands	Spectral Range [nm]	FOV [°]	Across Track Pixels	Dispersing Element	Image Acquisition Date
HYSPEX	Pushbroom	160	400–2500	17	1600	Grating	2005
PHILLS	Pushbroom	128	386–1003	30	1024	Grating	2004
AISA Eagle	Pushbroom	126	400–990	36.7	941	Prism-Grating-Prism	2005
HYPERION	Pushbroom	220	357–2576	0.63	256	Grating	2004
CHRIS	Pushbroom	37	440–1020	0.66	383	Prism	2005
CASI 3	Pushbroom	288	380–1050	39	1490	Prism	2006
AVIRIS	Whiskbroom	224	400–2500	34	677	Grating	2003

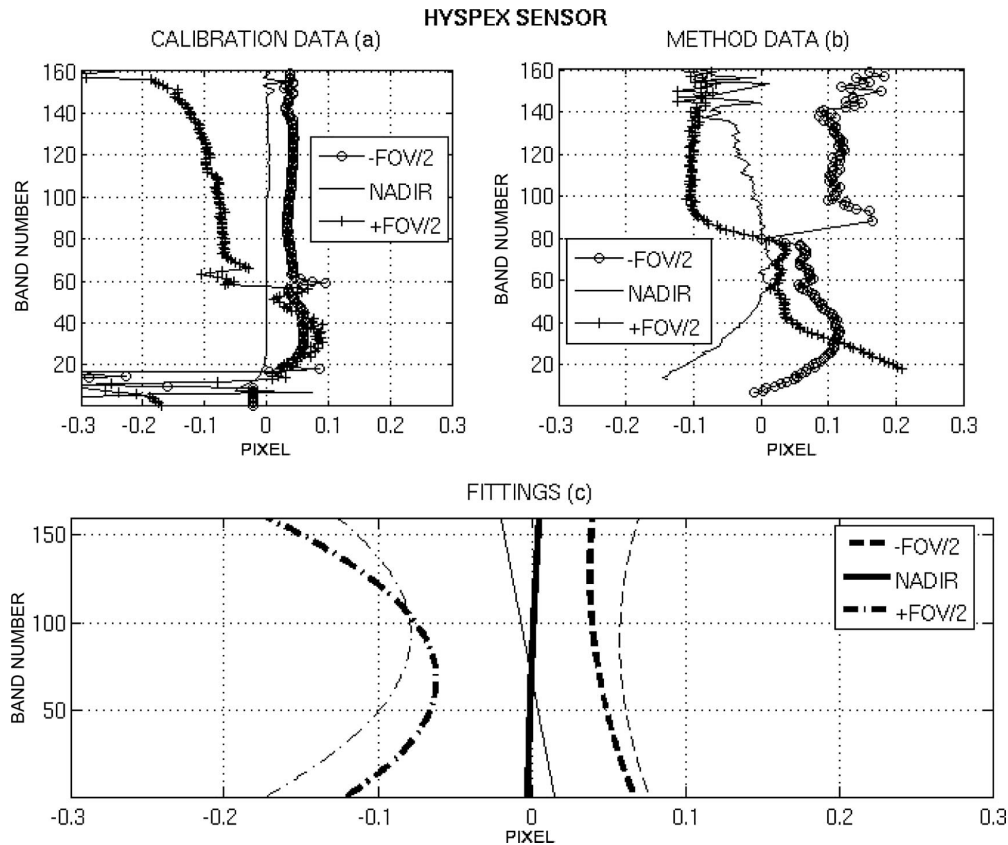


Fig. 6. (a) HYSPEX laboratory measurements: the three curves, starting from the left side, represent the spatial misregistration at +FOV/2, NADIR, and -FOV/2, respectively. (b) HYSPEX method analysis: plotting of the spatial misregistration data retrieved using the proposed procedure. (c) HYSPEX fittings: the thicker fittings represent laboratory data. The +FOV/2 curves have been plotted not considering the step attributable to the filter mask. The method overestimates the spatial misregistration.

trometer modules. We considered a prototype of the VNIR-1600 module. The latest release of the VNIR instrument has similar general specifications but improved optical quality.

The HYSPEX team provided a set of laboratory SM measurements [Fig. 6(a)], acquired using a broadband point source, which was located at three positions along the FOV at 1 m object distance. A simple singlet lens was inserted in the entrance aperture to achieve a good focus at this distance. It is important to notice that this lens slightly changes the optical image quality, which can explain discrepancies between the laboratory and airborne results. Furthermore, it should also be noted that the point source used was not perfect, as it had a size of approximately $\frac{1}{3}$ of a pixel, and the lamp available at the time of the measurements had a very low response in the blue range. For the laboratory measurements, SM is almost zero along the nadir direction; it becomes positive at -FOV/2 and negative at +FOV/2. Quantitatively, SM ranges from -6.63% to +2.24%. In the two sets of data, corresponding to the borders of the FOV, there is a step around band number 60, which is more prominent at +FOV/2. The step could arise

because the PSF is of the order of only 1 pixel. For band numbers below 60, most of the energy is contained within one pixel column, and a signal level close to 0 is measured in the adjacent spatial pixel row. Above band 60, because of the small amount of the SM effect, the signal level in the adjacent pixel row gets large enough to shift the center of gravity of the energy distribution. The sudden shift can thus be viewed as a kind of quantization noise, and the position of this sudden shift can be altered by moving the point source in the along-track direction. The second-order filter mask could partly cause this shift, as the shift is located around the spectral bands at the border of the filtered region. The next figure [Fig. 6(b)] shows the data we obtained using the proposed scene-based method. The data out of the interval of confidence have been removed after filtering. In general, the variations are close to those described in the laboratory set: There is almost no SM along the nadir, and positive and negative SM at -FOV/2, and +FOV/2, respectively. In this case, a step is also present but it occurs at approximately band number 80 instead of being at approximately band number 60. The measurements related to the first 16 bands

are missing because the SNR in this part of the spectral range is low. The method, as expected, gives higher values owing to the not standard conditions experienced during the flight; in fact, SM, on average, ranges from -10.39% to 6.29% . There is an overestimation at approximately 4% , in absolute value, of the pixel size. We fit both the laboratory data, and the results of the proposed method with a quadratic polynomial [Fig. 6(c)]. In this plot, the thicker curves correspond to laboratory data while the thinner curves correspond to the results. Even if the fitting curves at both $-\text{FOV}/2$ and $+\text{FOV}/2$ exhibit a quadratic shape, we cannot infer about the SM quadratic dependence on wavelength, because of the mentioned step, but we can see at least a linear dependence on the across-track pixel between band number 90 and band number 160. The NADIR fitting is tilted around the focal plane center, and it implies a rotational misalignment. It should be noted that the VNIR-1600 has a physical pixel size of only $7.4 \mu\text{m}$, corresponding to a FOV of 0.187 mrad , so the misalignment is

very small; the vertical misalignment is almost absent, being the fitting lines symmetrical around the y axis. As the minimal SM is around band number 80, we can therefore assume this channel as the offset to be removed from the SM values corresponding to the other spectral channels. To measure quantitatively the similarity between these curves, we compare, in each of the three FOV positions, the excursion range, which is defined in absolute value, as the difference between the maximum and the minimum value for each fitting. The difference is approximately 0.01 pixels at $-\text{FOV}/2$, approximately 0.03 pixels at NADIR, and approximately 0.02 pixels at $+\text{FOV}/2$; it implies that the agreement is high, if we also consider that we are working at a very subpixel level.

B. PHILLS

The Ocean Portable Hyperspectral Imager for Low-Light Spectroscopy (Ocean PHILLS)²⁹ is used mainly for imaging the coastal ocean. We analyzed two versions of this instrument: The first has a focal length

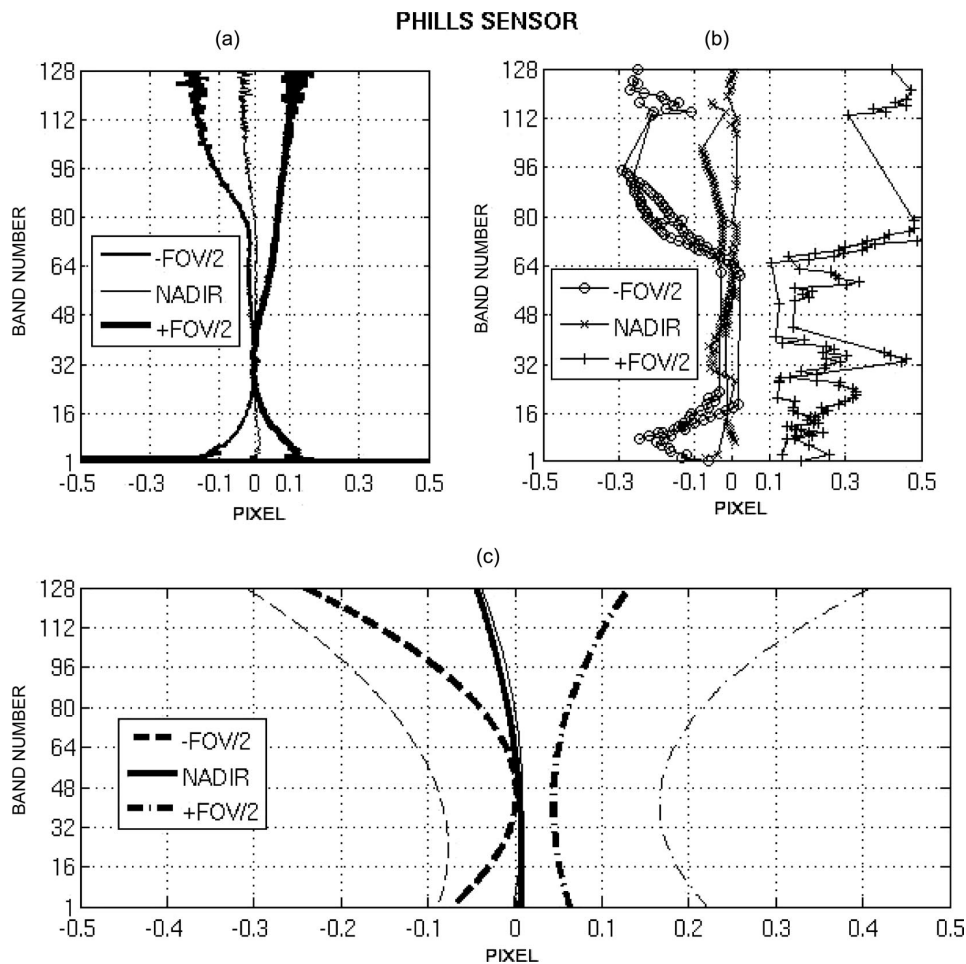


Fig. 7. (a) The sets of laboratory measurements: The blocking filter influence is evident after band number 64. (b) The data retrieved from the method: spatial misregistration at $+\text{FOV}/2$ is higher than that at $-\text{FOV}/2$. (c) Comparison between fittings.

of 12 mm, and the second has a focal length of 17 mm. PHILLS could provide up to 512 spectral channels, but our data have been binned by 4, and this leads to 128 bands.

A set of laboratory SM measurements was available [Figure 7(a)]; they were taken placing the sensor at the output of a collimator, a large off-axis parabola, which projects a geometric image of approximately 0.1 pixel. The aperture image on the CCD plane is wavelength dependent, and this gives a measure of SM. The data show how SM is almost absent along the NADIR direction, positive at $+FOV/2$, and negative at $-FOV/2$. SM is, in absolute value, under 10% of a pixel size, except beyond band number 96. Basically, SM becomes more evident after band number 64. The reason for this is because a blocking filter has been used: in fact, second-order diffractions, coming from the lower spectral range (between 380 and 500 nm) are falling between 760 and 1000 nm; a filter has been mounted behind the spectrometer, and it blocks wavelengths below 530 nm. In reality, the filter adds an offset in the bands where it is present. It should also be noticed that SM toward $+FOV/2$ is higher than that around the $-FOV/2$ pixels, and this could be attributable to some straylight. The SM values, retrieved applying our method to the PHILLS acquired scene [Fig. 7(b)], are slightly higher than those obtained in the laboratory. As from laboratory investigations, the SM increases after band number 60. The SM is negative at $-FOV/2$, below 2% around the NADIR direction, and positive at $+FOV/2$. We also notice here that SM is higher at $+FOV/2$. The fitting lines [Fig. 7(c)] make clear how the method overestimates SM; the bold curves represent the laboratory data. Even if after band number 64, the SM values seem to change in a quadratic way, we cannot prove a quadratic dependency on wavelength; we can claim a linear dependence on across-track pixels between band number 50 and band number 128. There is no symmetry around the y axis, and this lets us assume a vertical misalignment. Anyway, this sensor has an optical design where the lenses and the spectrometer do not share the same optical axis. In fact, the NADIR direction is at approximately pixel 460 nm, and it means that the optical axis does not intersect the focal plane in its center (i.e., along band number 64). This can be clearly identified from the fitting curves, which have a change in their first-derivative slope not around band number 64, but between band number 16 and band number 48. It implies that the layer at 460 nm can be used as the SM offset for the other spectral channels. Considering the fitting curves related to the method, we note a SM, on average, going from -14.05% up to 22.69% .

C. AISA Eagle

The Airborne Imaging Spectrometer (AISA)³⁰ uses a prism-grating-prism (PGP) as a dispersing element. There were no laboratory measurements available for this sensor. The data out of the interval of confidence, which we set equal to two mean deviations, have been removed. The SNR was good enough to let

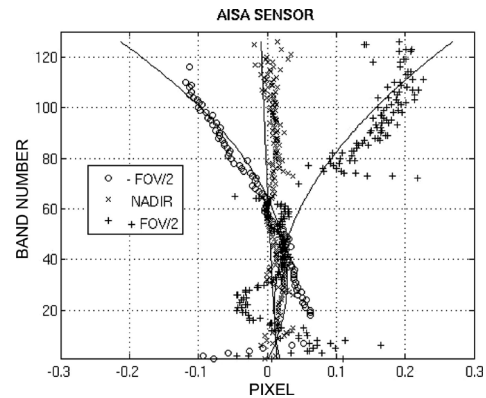


Fig. 8. AISA analysis. The plot shows a quadratic dependence of keystone on the focal plane and symmetry around the nadir axis. The focal plane has no rotational misalignment, but a slightly negative vertical misalignment.

us apply the method almost over all the spectral range.

The SM (Fig. 8) is almost zero in the middle of the focal plane; then it becomes negative when we move toward the $-FOV/2$, and it ranges from -1% to -11.5% . The SM is positive on the right side of the CCD, but it goes up to 19% .

Both the data and fitting lines show this time a quadratic variation with wavelength and a linear variation with across-track pixels. The symmetry around the z axis is apparent, meaning that there is no rotational misalignment. The fitting first-derivative sign is changing at approximately band number 30; there is no symmetry around the z axis, which supposes to pass by band 63, implying that there is little vertical misalignment. The optical axis does not pass by the CCD center, but it intersects the focal plane slightly below it. This behavior also suggests that the offset band should be taken from the first bands of the spectral range.

D. HYPERION

Hyperion,³¹ in orbit since 2000, consists of a visible near-infrared detector (VNIR), and a shortwave infrared detector (SWIR). The instrument has a spatial resolution of 30 m for all bands. Laboratory data were not available.

The SWIR detector [Fig. 9(a)] has no SM along the NADIR direction; the artifact is positive at $-FOV/2$, and negative at $+FOV/2$, respectively. On average, the SM varies between 5.11% (at $-FOV/2$) and -2.32% (at $+FOV/2$). The SWIR fitting lines [Figure 8(a)] show that this detector has no rotational misalignment; in fact the NADIR SM line is parallel to the z axis. The symmetry that these lines have around the axis passing by band number 150 implies that the focal plane center is almost on the optical axis itself, which means no vertical misalignment. Band number 150 then exhibits the lowest SM. In this case, the quadratic variation with wavelength is

HYPERION SENSOR

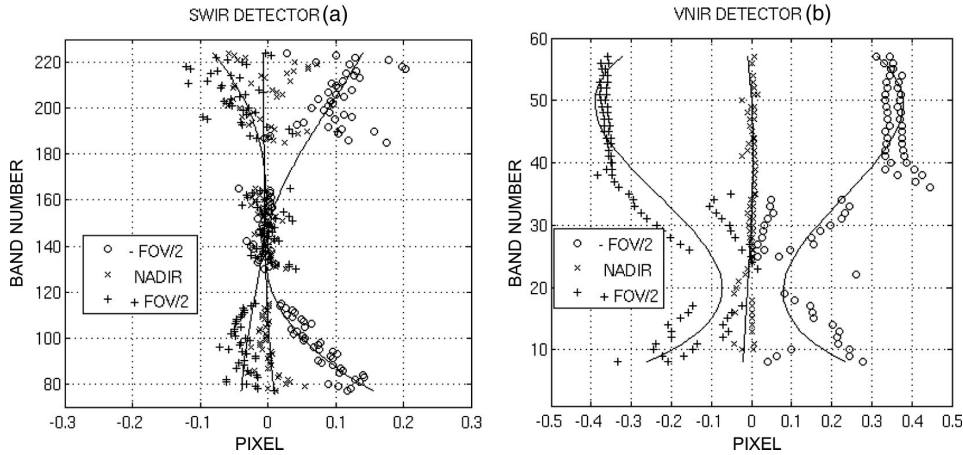


Fig. 9. (a) HYPERION SWIR analysis: SM is positive toward $-FOV/2$, and negative toward $+FOV/2$. The SWIR detector is well aligned, and also centered. Some bands are missing because of a low SNR. (b) HYPERION VNIR analysis: Spatial misregistration is higher than in the HYPERION SWIR detector. This detector has no rotational misalignment.

apparent even if few bands are missing because they were too noisy.

The VNIR detector shows a different situation [Figure 9(b)]. In general, the SM is negative at $+FOV/2$, approaching zero around the NADIR direction, and positive at $-FOV/2$. In this case, the method produces higher values than those obtained for the SWIR detector: on average, the SM goes from -22.96% up to 22.61% . We also notice that in the last 20 bands, SM is almost constant, and approximately 38.2% in absolute value; the main SM excursion (from 10% to 40% in absolute value) occurs before band number 40, and this is probably attributable to the SNR of the VNIR detector, which is low on the first spectral wavelengths. We decided to break down the spectral range to use two different fittings, the first going from band number 0 to band number 40, and the second for

the other bands. The NADIR fitting line is parallel to the z axis, and once again it implies that the NADIR axis is perpendicular to the optical axis. There is no symmetry around the y axis; because of the reasons explained before, we suggest using band number 40 as the offset for all the other VNIR spectral channels.

E. CHRIS

CHRIS¹⁸ is a spaceborne scanner, which has been in orbit since 2001. It can be used with different acquisition modes, and our data have been collected in MODE V. As we mentioned before, CHRIS uses curved prisms, but the surfaces are all spherical, and only one material is used for all the prisms. There are no laboratory data available, but the method results are worth discussing because the prism used is curved.

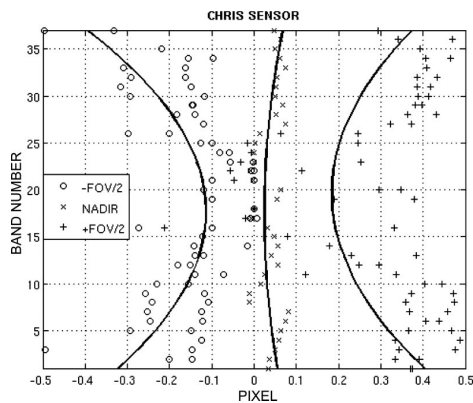


Fig. 10. CHRIS analysis: Nadir line does not coincide with the nadir direction, but it is slightly shifted aside; we may suppose that the instrument is slightly misaligned with the other optical components.

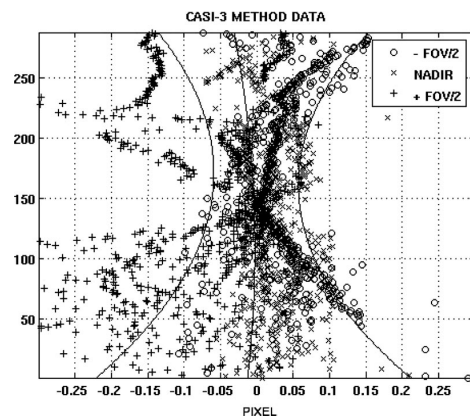


Fig. 11. CASI-3 analysis: Spatial misregistration profile shows a symmetry, which implies that the sensor is well aligned to the other optical parts, with no misalignments.

The SM profile (Fig. 10) shows the following behavior: The SM is constant along the NADIR direction, positive for pixels located at $+FOV/2$, and negative for pixels located at $-FOV/2$. The SM is slightly higher on the right side of the focal plane: The mean value in this side is approximately 26% of a pixel, while on the opposite side it is approximately 20%. The average SM along the nadir is approximately 4% of a pixel size. The fitting lines have symmetry at approximately both the z axis, and the y axis, passing by band number 18; this implies that the focal plane has neither vertical misalignment nor rotational misalignment. The focal plane center lies on the optical axis. This also means that the values corresponding to the 18th band can be used as an offset for all the other channels. Nevertheless, the NADIR fitting curve does not coincide, within a really low percentage, with the NADIR line, and it may be because the CCD center is a little bit aside from the optical axis.

F. CASI-3

The Compact Airborne Spectrographic Imager³² (CASI) is a VNIR sensor manufactured by ITRES Research Ltd., Canada. The SNR profile allows all the spectral range to be explored, and only a few results have been removed from the interval of confidence. The analysis has been conducted over several subsets, extracted from the available hyperspectral cubes.

The SM profile (Fig. 11) exhibits a quadratic dependence on the CCD array positions. The SM is constant, and close to zero, along the z axis; it becomes positive if we move toward pixels at approximately $-FOV/2$, while it is negative in the opposite direction. On average, the SM varies between 10.04% (at $-FOV/2$) and -10.15% (at $+FOV/2$), being 0.98% along the NADIR direction. The SM is higher at both limits of the spectral range, and this is attrib-

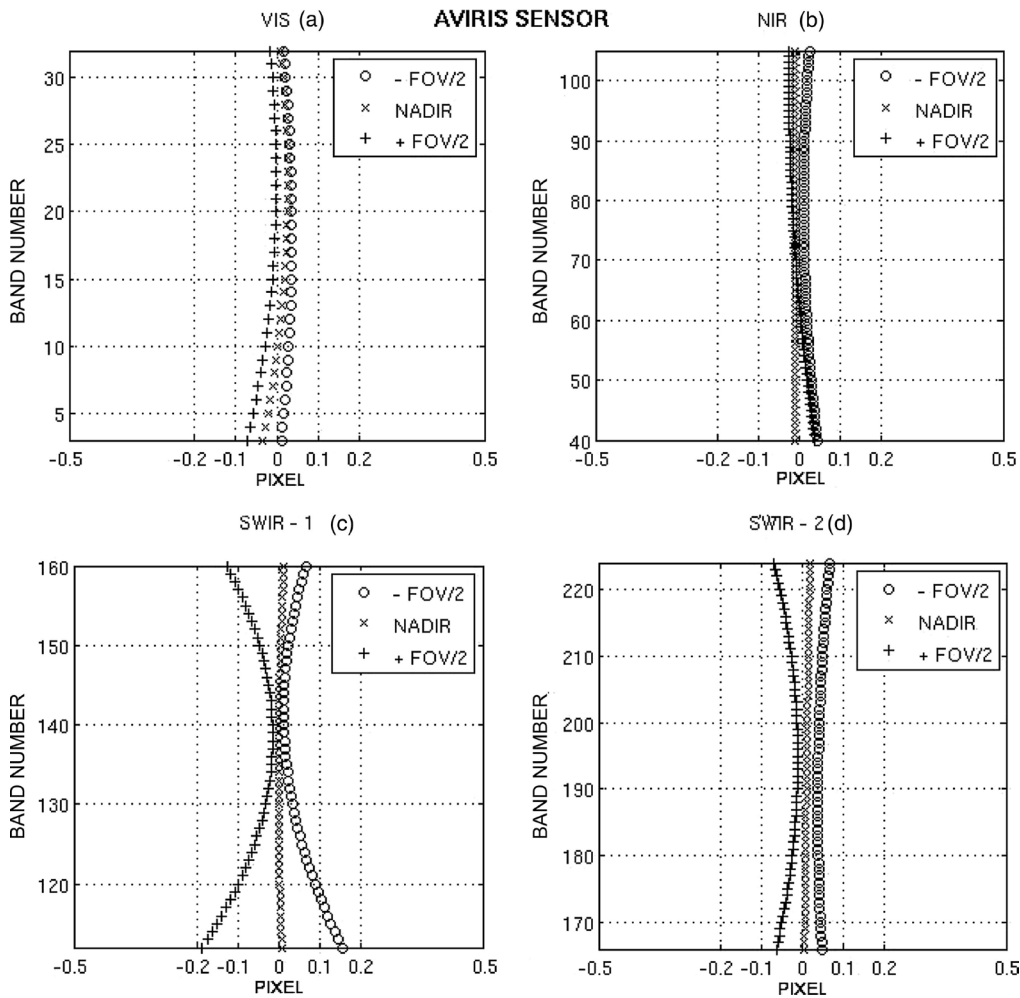


Fig. 12. AVIRIS analysis: Spatial misregistration in this whiskbroom detector is very low, namely under 3% both in the VNIR and in the NIR detectors. The two SWIR detectors present some curvature especially in the positive part of the field of view, and this is probably attributable to some instability. SM is also very low in these two detectors.

utable to the sensor SNR. The fitting lines are symmetrical with respect to both the y axis and the z axis; this means that there are no misalignments within this sensor, i.e., the focal plane center is on the optical axis. These properties let us assume that band number 144 can be used as an offset for the whole SM profile, and, second, that the alignment procedure applied to CASI has been really precise. In any case, this sensor confirms our assumptions concerning the variation relationships.

G. AVIRIS

AVIRIS²⁷ flew for the first time in 1988. There are four detectors: one in the visible range (VIS), one in the near-infrared (NIR), and two detectors in the shortwave infrared region (SWIR1, and SWIR2). This sensor has a very good SNR profile, and thus all the bands have been considered during this analysis. The scanning method should not provide any kind of SM, and thus it can be used as a benchmark because each ground pixel is recorded separately. The detection procedure produces values that almost superimpose themselves to the fittings lines, and so we decide to show only the fitting curves.

The VIS detector [Fig. 12(a)] exhibits an almost constant SM (i.e., the fitting lines have no curvature) in all the three selected locations along the across-track direction, and it is less, in absolute value, of 2.81% of a pixel size. It is actually what we expected because of the whiskbroom scanning system. The SM is very low, but if we would like to correct for it, we have to take a channel at approximately band number 16, as an offset for the whole array. The NIR detector [Fig. 12(b)] shows the same behavior as the VIS detector. The SM is even less than before: it is lower, in absolute value, than 1.88%. One can also assume that the SM is absent in this sensor. The two SWIR detectors have a spatial misregistration performance, which is a little bit different from the two previous detectors [Figs. 12(c) and 12(d)]. They show, except for the NADIR position, fitting lines that have a certain amount of curvature; this is probably because these two sensors suffer more from airplane instability. Another reason could be the spectral transmittance that is low (approximately 10%) in the last bands of these two detectors, in comparison to the other part of the spectrum. The fittings at $-FOV/2$, and $+FOV/2$ have symmetry both around the z axis, and the y axis: this implies that SWIR-1 and SWIR-2 are both aligned and centered with the optical axis; in other words, there are no misalignments. The SM values are higher than before but they are within a very low threshold. The SM for the SWIR-1 detector is, in absolute value, below 6.39% of a pixel size, while for the SWIR-2 detector it is below 4.52%. In general, AVIRIS has the lowest SM if we compare it with the other tested instruments; this confirms our assumptions, and it also gives validity to the proposed scene-based method.

6. Conclusion

Spatial misregistration has been analyzed, and its effect on the quality of data has been shown: If it is higher than 5%–10% of a pixel size then the physical meaning of the recorded spectra can be compromised. Therefore a scene-based detection method has been proposed. SM is mainly detected with laboratory measurements for a few positions along the FOV because it is time consuming. The proposed method allows several locations to be analyzed, provided that edges are apparent within the acquired image cubes. The main advantage of the method is that we do not have to choose any *a priori* reference. The average edge position in a monochromatic view is calculated with respect to an ideal edge. The average position profile has a minimum at a given band, and this can be used as an offset for the position values corresponding to the other bands.

The SM profile is then relative to the lowest SM, which corresponds to one spectral band. If we consider this minimal value as being zero misregistration, a correction scheme can be implemented. The method can be adapted with only a few modifications (e.g., number of across-track pixels and file format) to most of the hyperspectral sensors, such as pushbroom or whiskbroom.

The results show that SM depends both on wavelength, and across-track position: We have been able to identify a quadratic dependence on wavelength for some of the analyzed sensors, while the linear dependence is more or less apparent in each one of them. It is important to notice that SM changes the sign when we cross the z axis.

The fitting lines can be used as a tool to check the alignments within the sensor components; basically they show if vertical and/or rotational misalignments are affecting the focal plane. Laboratory SM measurements were available for two sensors, and when compared them with our results, they suggest that the method can be useful for SM detection.

Most of the analyzed pushbroom sensors use a grating as a dispersing element and often filters to remove high-diffraction orders. When the filter does not cover all the spectral range, a sort of discontinuity appears in the SM profile. This step is located exactly around the band number corresponding to the transition between the filtered and the unfiltered spectral region of the spectrometer.

The tested whiskbroom sensor (AVIRIS) provides a further validation to the procedure. In this case, the SM profile does not follow the same quadratic dependence with wavelength as in the pushbroom scanners. Furthermore, the values are much lower because it records one ground pixel at once, which keeps the interference between the adjacent spectra extremely modest.

A comparison table (Table 2) shows the average SM values for all the tested instruments: The values are expressed as a fraction of the pixel size. It is easy to see that almost all the checked sensors have a very low SM. Generally, it is not higher than 5%,

Table 2. Spatial Misregistration in Different Sensors Expressed as Fraction of a Pixel Size

	-FOV/2	NADIR	+FOV/2
HYSPEX	0.0629	-0.0025	-0.1039
PHILLS	-0.1405	-0.0029	0.2269
AISA	-0.0343	0.0014	0.0841
HYPERION SWIR	0.0511	-0.0028	-0.0232
HYPERION VNIR	0.2261	-0.0046	-0.2296
CHRIS	-0.2002	0.0381	0.2569
CAS3	0.1004	0.0098	-0.1015
AVIRIS VIS	0.0281	0.0112	-0.0184
AVIRIS NIR	0.0188	-0.0099	-0.0054
AVIRIS SWIR1	0.0507	0.0045	-0.0639
AVIRIS SWIR2	0.0452	0.0112	-0.0305

which is supposed to be the operational demanded requirement for SM in hyperspectral sensors. Further developments of the implemented methodology include automatic selection of the subsets needed for SM detection and integration of the procedure in a processing software chain that brings the acquired data from Level-0 to Level-1. This will be fully included in the Airborne Prism Experiment (APEX)³³ data-processing chain.

This work has been supported by the European Space Agency/European Space Research and Technology Centre. The authors thank Ivar Baarstad from the HYSPEX team, Daniel Korwan from the Ocean PHILLS team, and Reno Choi from the UK Environmental Agency for providing data and information about the respective sensors. The authors also thank Pantazis Mouroulis (Jet Propulsion Laboratory), Robert Neville (CCRS), and Andrea Sacchetti (Eidgenössische Technische Hochschule) for the fruitful discussions.

References

- J. Nieke, H. Schwarzer, A. Neumann, and G. Zimmermann, "Imaging spaceborne and airborne systems in the beginning of the next century," in *Sensors, Systems and Next-Generation Satellites*, H. Fujisada, ed., Proc. SPIE **3221**, 581–592 (1997).
- J. Fisher, M. Baumbach, J. Bowles, J. Grossmann, and J. Antoniadis, "Comparison of low-cost hyperspectral sensors," in *Imaging Spectrometry IV*, M. Descour and S. Shen, eds., Proc. SPIE **3438**, 23–30 (1998).
- R. B. Gomez, "Hyperspectral imaging: a useful technology for transportation analysis," Opt. Eng. **41**, 2137–2143 (2002).
- S. E. Reichenbach, L. Cao, and R. M. Narayanan, "Information efficiency in hyperspectral imaging system," J. Electron. Imaging **11**, 347–353 (2002).
- Christophe, D. Léger, and C. Mailhes, "Quality criteria benchmark for hyperspectral imagery," IEEE Trans. Geosci. Remote Sens. **43**, 2103–2113 (2005).
- P. Mouroulis, R. O. Green, and T. G. Chrien, "Design of pushbroom imaging spectrometers for optimum recovery of spectroscopic and spatial information," Appl. Opt. **39**, 2210–2220 (2000).
- W. Mao and Y. Xu, "Distortion of optical wedges with a large angle of incidence in a collimated beam," Opt. Eng. **38**, 580–585 (1999).
- J. M. Sasian, "Aberrations from a prism and a grating," Appl. Opt. **39**, 34–39 (2000).

- J. M. Sasian, "How to approach the design of a bilateral symmetric optical system," Opt. Eng. **33**, 2045–2061 (1994).
- W. S. S. Blaschke, "Field aberrations in wide aperture optical systems," Proc. Phys. Soc. London Sect. B **67**, 801–810 (1954).
- C. Zhao and J. H. Burge, "Conditions for corrections of linear and quadratic field-dependent aberrations in plane-symmetric optical systems," J. Opt. Soc. Am. A **19**, 2467–2472 (2002).
- W. Mao, "Error and adjustment of reflecting prisms," Opt. Eng. **36**, 3367–3371 (1997).
- D. Schläpfer, J. Nieke, and K. I. Itten, "Spatial PSF non-uniformity effects in airborne pushbroom imaging spectrometry data," IEEE Trans. Geosci. Remote Sens. (to be published).
- P. Mouroulis, D. A. Thomas, T. G. Chrien, V. Duval, R. O. Green, J. J. Simmonds, and A. H. Vaughan, "Trade studies in multi/hyperspectral imaging systems final report," Jet Propulsion Laboratory files (29 October 1998).
- R. O. Green, "Spectral calibration requirement for Earth-looking imaging spectrometers in the solar-reflected spectrum," Appl. Opt. **37**, 683–690 (1998).
- D. R. Lobb, "Theory of concentric designs for grating spectrometers," Appl. Opt. **33**, 2648–2658 (1994).
- M. J. Barnsley, J. J. Settle, M. A. Cutter, D. R. Lobb, and F. Teston, "The PROBA/CHRIS mission: A low-cost smallsat for hyperspectral, multi-angle, observations of the Earth surface and atmosphere," IEEE Trans. Geosci. Remote Sens. **42**, 1512–1520 (2004).
- D. R. Lobb, "Imaging spectrometers using concentric optics," in *Imaging Spectrometry III*, M. R. Descour and S. S. Shen, eds., Proc. SPIE **3118**, 339–347 (1997).
- J. Nieke, M. Solbring, and A. Neumann, "Noise contributions for imaging spectrometers," Appl. Opt. **38**, 5191–5194 (1999).
- P. Mouroulis and M. M. McKerns, "Pushbroom imaging spectrometer with high spectroscopic data fidelity: experimental demonstration," Opt. Eng. **39**, 808–816 (2000).
- M. E. Winter, P. G. Lucey, T. Williams, and M. Wood, "Calibration of the University of Hawaii's airborne hyperspectral imager," in *Imaging Spectrometry IX*, S. S. Shen and P. E. Lewis, eds., Proc. SPIE **5159**, 370–379 (2003).
- R. A. Neville, L. Sun, and K. Staenz, "Detection of keystone in imaging spectrometer data," in *Algorithms and Technologies for Multispectral, Hyperspectral, and Ultraspectral Imagery X*, S. Shen and P. Lewis, eds., Proc. SPIE **5425**, 208–217 (2004).
- J. C. Russ, *The Image Processing Handbook*, 4th ed. (CRC Press, 2002).
- W. Frei and C. Chen, "Fast boundary detection: A generalization and a new algorithm," IEEE Trans. Comput. **10**, 988–998 (1977).
- J. M. S. Prewitt, "Object enhancement and extraction," in *Picture Processing and Psychopictorics*, B. S. Lipkind and A. Rosenfeld, eds. (Academic, 1970).
- I. Abdou, *Quantitative Methods of Edge Detection*, USCIRI Report 830, Image Processing Institute (University of Southern California, Los Angeles, 1973).
- T. G. Chrien, R. O. Green, and M. L. Eastwood, "Accuracy of the spectral and radiometric laboratory calibration of the airborne visible/infrared imaging spectrometer (AVIRIS)," in *Imaging Spectroscopy of the Terrestrial Environment*, G. Vane, ed., Proc. SPIE **1298**, 37–49 (1990).
- I. Baarstad, T. Løke, and P. Kaspersen, "ASI-A new airborne hyperspectral imager," in *Proceedings of the Fourth EARSel Workshop on Imaging Spectroscopy—New Quality in Environmental Studies* (Warsaw, 2005), pp. 107–110.
- C. O. Davis, J. Bowles, R. A. Leathers, D. Korwan, T. V. Downes, W. Snyder, W. Rhea, W. Chen, J. Fisher, P. Bissett, and R. A. Reisse, "Ocean PHILLS hyperspectral imager: design, characterization, and calibration," in Opt. Express **10**, 210–221 (2002).

30. R. Bärs, L. Watson, and O. Weatherbee, "AISA as a Tool for Timely Commercial Remote Sensing," in *Fourth International Airborne Remote Sensing Conference and Exhibition (ERIM, 1999)*, Vol. I, pp. 239–246.
31. M. A. Folkman, J. Pearlman, B. L. Liao, and P. J. Jarecke, "EO-1/Hyperion hyperspectral imager design, development, characterization, and calibration," in *Hyperspectral Remote Sensing of the Land and Atmosphere*, W. L. Smith and Y. Yasuoka, eds., Proc. SPIE **4151**, 40–51 (2001).
32. S. K. Babey and C. D. Anger, "Compact airborne spectrographic imager (CASI): a progress review," in *Imaging Spectrometry of the Terrestrial Environment*, G. Vane, ed. Proc. SPIE **1937**, 152–163 (1993).
33. J. Nieke, K. I. Itten, W. Debruyn, and the APEX team, "The Airborne Imaging Spectrometer APEX: from concept to realization," in *Proceedings of the Fourth EARSeI Workshop on Imaging Spectroscopy—New Quality in Environmental Studies* (Warsaw, 2005), pp. 47–53.

Laboratory calibration of imaging spectrometers

5 Laboratory calibration of imaging spectrometers

Laboratory calibration is the most accurate way of defining the acquisition properties of an imaging spectrometer. This chapter introduces an optimal laboratory strategy that aims at reducing the overall acquisition measurement uncertainty.

The following research questions will be answered:

How can the calibration and characterization process reduce the uncertainty of imaging spectroscopy products?

*How can an imaging spectrometer be calibrated such that the measurement quality/fidelity is improved?
How can calibration and characterization techniques reduce the measurement uncertainty?*

How can instrument laboratory calibration be used to efficiently characterize non-uniformities?

The error budget of imaging spectroscopy products has been estimated in (Nieke et al. 2008) taking into account only the impact of non-uniformities. Radiometric calibration uncertainties, other optical performances (e.g. polarization and straylight effects), as well as the uncertainty of a relative radiometric calibration (i.e. calibration with respect to secondary standards) were not accounted. Nevertheless, it was demonstrated that a well-established calibration and characterization strategy could reduce the measurement uncertainty. A laboratory assessment of the spectral, spatial and radiometric performances of an imaging spectrometer is more accurate than detection algorithms, which are applied directly to the imaged scene. Precise laboratory procedures and methodologies provide the most accurate estimation of the non-uniformities and open the horizon to reliable correction schemes. *Calibration* refers to determining the relation between detector readouts (e.g. digital counts) and measurement standards, while *characterization* defines instead the influence of sensor parameters (e.g. pixel location, integration time, temperature, pressure) on the spectral, geometric, and radiometric properties, that have been determined during calibration. A customized calibration and characterization approach can improve the measurement accuracy and it represents the first step towards the retrieval of low uncertainty imaging spectroscopy products.

Calibration consists of converting measured digital readings (also referred to as digital numbers (DN) or digital counts (DC)) into physical units as, for example, radiance (L) (Schaepman-Strub et al. 2006). Characterization refers instead to experiments aimed at defining the behavior of the sensor with respect to spectral, radiometric and geometrical properties. The outcome of characterization is use to increase the accuracy of the calibration by reducing the negative influence of sensor non-uniformities.

There are different types of calibrations:

1. *Laboratory calibration/characterization* (Chrien et al. 1990; Chrien et al. 1994; Barnes et al. 1998; Nieke et al. 2000; Folkman et al. 2001; Davis et al. 2002; Murakami et al. 2003; Winter et al. 2003; Kohler et al. 2004; White et al. 2004; Dell'Endice et al. 2009a)
2. *In-flight calibration/characterization* (Biggar et al. 2001; Jarecke et al. 2001; D'Odorico et al. 2009)
3. *Vicarious calibration* (Koepke 1982; Soares and Costa 1999; Nieke et al. 2003; Brazile et al. 2006; Gambhir and Erives 2006; Guanter et al. 2006; Dell'Endice et al. 2007c, b).

Laboratory calibration offers the highest degree of accuracy because measurements are taken under well-known and stable environmental conditions and because the reference light stimuli (e.g. integrating spheres, monochromators, emission-line lamps, lasers) are directly traceable to calibration standards (usually secondary standards). In-flight and vicarious calibration are valid alternatives to laboratory but their accuracies are lower; nevertheless, namely in space missions, these approaches are the only ones that might be used to monitor the post-launch performance of the instruments. Vicarious calibration is also used as a validation technique, which consists of comparing the sensor data with established ground-truths.

Instrument calibration can be based on reflectance, irradiance, or radiance standards. The latter is the most common approach because it allows the direct retrieval of the calibration coefficients. In fact, a reflectance approach would also require the measurement of other light sources (e.g. sun) that is performed by independent means and this may increase the overall error budget.

5.1 The generic calibration/characterization problem

Each calibration and characterization procedure can be represented by means of equations. This paragraph formally describes the whole calibration problem. Calibration and characterization are formalized and expressed as functions of the most relevant sensor performance parameters. Let assume that a detector with B spectral bands and T spatial pixels has to be calibrated and characterized in a laboratory environment. A single detector pixel has a b coordinate, corresponding to its spectral row, and a t coordinate, corresponding to its spatial location along the field-of-view (FOV).

Laboratory calibration/characterization aims at defining the following position-dependent parameters:

- Centre wavelengths $\lambda(b,t)$
- FWHM of spectral response functions $f(b,t)$
- Radiometric gains $g(b,t)$
- Radiometric offsets $d(b,t)$

This scheme leads to the determination of the following non-uniformities:

- Smile $s(b,t)$
- Keystone $k(b,t)$
- Spatial FWHM variations across-track $a(b,t)$
- Spatial FWHM variations along-track $l(b,t)$

It is apparent that the assessment of the non-uniformities distribution requires a specific calibration strategy. Furthermore, not all parameters have been considered here. The measurement and/or retrieval of additional parameters may lead to complex calibration approaches. For instance, straylight from inside and outside the FOV, smear, polarization effects, and non-linearities shall be also accounted for.

The parameters listed above are generally not considered being dependent on two variables (i.e. b and t) but only on one variable (usually b). The next paragraphs outlines the difference between the classical calibration approach and the one proposed in this dissertation.

5.2 The classic laboratory calibration approach

Imaging spectroscopy data (Chrien et al. 1990; Chrien et al. 1994; Barnes et al. 1998; Nieke et al. 2000; Folkman et al. 2001; Davis et al. 2002; Murakami et al. 2003; Winter et al. 2003; Kohler et al. 2004; White et al. 2004; Dell'Endice et al. 2009a) are usually distributed with a calibration file that includes the following parameters:

- Center wavelengths
- FWHM of the spectral response functions
- Radiometric gains and offsets
- Uncertainty values

Users of imaging spectroscopy data generally accept the following assumption:

The calibration coefficients are the same for all the instrument spatial pixels.

This introduces the classical calibration problem that is formulated as follows:

Equation 1: the classical laboratory calibration approach.

$$\begin{array}{l} \lambda(b) = \lambda \quad \forall t \\ f(b) = f \quad \forall t \\ g(b) = g \quad \forall t \\ d(b) = d \quad \forall t \end{array} \quad \text{with} \quad \begin{cases} s(b,t) = 0 & \forall b, \forall t \\ k(b,t) = 0 & \forall b, \forall t \\ a(b,t) = 0 & \forall b, \forall t \\ l(b,t) = 0 & \forall b, \forall t \end{cases}$$

It is implicitly assumed that the calibration parameters are constant over the spatial direction of the detector array. In other words, it implies that the calibration file applies to all pixels in the detector FOV. It is then assumed that the detector is not affected by any kind of non-uniformities. Hence, a calibration measurement of the sensor performances along a preferred FOV spatial location is enough to characterize and calibrate the whole detector.

While the variations of radiometric coefficients are usually compensated during raw image data processing (i.e. vignetting correction), other non-uniformities are considered zero and not corrected. The calibration and characterization approach as stated in Equation 1 is suitable for whiskbroom imaging spectrometers but not for pushbroom imaging spectrometer. In fact, non-uniformities can be considered minimal in whiskbroom systems because only one detector pixel is used to reconstruct the final image. Whiskbroom systems can be considered as being *one-spatial pixel systems*. Pushbroom systems, which can be referred to as *multiple-spatial pixels systems*, use a bi-dimensional detector technology and therefore the level of non-uniformities may be high and the calibration approach of Equation 1 may be not valid anymore. Theoretically, every pixel of a pushbroom imaging spectrometer should be considered as an independent spectrometer, which needs to be independently characterized and calibrated.

The scanning mechanism (i.e. moving mirror) of whiskbroom systems significantly reduces characterization and calibration efforts to a single pixel, which is considered to have stable performances when scanned over the entire swath. This is true for spatial and spectral properties depending on optical aberrations, as it was demonstrated for the keystone effect (Dell'Endice et al. 2007b), but this

may not hold true for other properties (e.g. straylight, polarization, radiometric performances).

Pushbroom sensors, on the other end, require a higher effort because a plurality of pixels is simultaneously used to scan the scene. Airborne and spaceborne pushbroom imaging spectrometers are mainly based on light sensitive elements such as a charge-coupled-device (CCD) (Amelio et al. 1970; Janesick and Putnam 2003) or a complementary-metal-oxide-semiconductor (CMOS) (Hendry and Massingham 1992; Chorier and Tribolet 2001; Janesick and Putnam 2003). These devices are composed of a high number of detector elements or pixels, usually in the range of hundred thousands or so. Only a few out of those pixels are generally characterized and calibrated because of time and budget constraints. Nevertheless, non-uniformities might not be correctly characterized because they change over the detector and they depend on the type of optical system. The distribution of non-uniformity over the focal plane may also depend on the dispersing setup. For example, a prism-based imager (Itten et al. 2008) might have a smile profile, which differs substantially from a prism-grating-prism (Makisara et al. 1993) system.

(Nieke et al. 2008) indicated that most of the product uncertainty comes from the fact that the imaging spectrometers are not characterized in depth, which results in a lack of knowledge about the non-uniformities distribution over the focal plane. A calibration approach for these systems is proposed in the next paragraphs.

5.3 An innovative laboratory calibration/characterization strategy

The classical calibration approach of Equation 1 is suitable for whiskbroom imagers but it is not recommendable for pushbroom imaging spectrometers if the consistency of the spectral measurements has to be ensured. The measurement accuracy of pushbroom systems can be improved if a proper system characterization of the instrument optical properties is carried out (e.g. smile and keystone distributions have to be determined). The calibration parameters of Equation 1 cannot be considered constant over the focal plane. (Neville et al. 2003, 2004; Brazile et al. 2006; Dell'Endice et al. 2007b) demonstrated how scene-based methodologies can be used to detect non-uniformities. However, accurate assessment of the variability of calibration parameters over the detector array is possible only in laboratory because of the controlled measurement setup.

The calibration problem is now reformulated as follows:

Equation 2: a calibration approach for pushbroom systems.

$$\begin{aligned}\lambda &= \lambda(b,t) \\ f &= f(b,t) \\ g &= g(b,t) \\ d &= d(b,t) \\ s &= s(b,t) \\ k &= k(b,t) \\ a &= a(b,t) \\ l &= l(b,t)\end{aligned}$$

The optical performances of the detector have to be measured in several spatial positions, in order to characterize the variation of non-uniformities in the most accurate way.

This calibration and characterization approach, which will be outlined in the following manuscripts, is specialized for pushbroom imaging spectrometers. If optical performance parameters are varying, a customized laboratory approach for the measurement of non-uniformity distributions over the focal plane is implemented and discussed.

One of the main challenges is to establish a precise measurement setup that allows such a complex calibration and characterization strategy that otherwise would not be possible. The input to such an approach is a state-of-the-art calibration lab, called Calibration Home Base (CHB), located in the German Aerospace Center (DLR, Munich, Germany), because it allows automatic operation of the main calibration instrumentation (Suhr et al. 2005). Calibration equipment (e.g. monochromator, integrating spheres, collimator assembly) can be operated automatically and, the characterization of detector performances along the FOV is accomplished by using (1) a moving motor-driven folding mirror and (2) a turret holding a series of six rotating imaging slits. The main advantage of the CHB laboratory equipment is that it can be operated automatically and continuously. Its key elements are the engine-driven folding mirror, moving slits used for geometrical experiments, a monochromator covering the range between 350 and 2500 nm, two integrating spheres (one is a primary calibration standard) for radiometric purposes and large series of neutral density and polarizing filters. For more details refer to (Suhr et al. 2005).

By means of such a calibration setup, the problem stated in Equation 2 can be directly solved through a sequence of well-established measurement procedures. Several algorithms have been implemented and coded into the Calibration Test Master (CTM). The CTM consists of a twofold software package:

- Controller Unit: it interfaces the sensor with the calibration equipment.
- Processor Unit: it processes the measurement data and derives calibration and characterization coefficients.

Once the sensor and the CHB parameters are optimized, the calibration and the characterization can take place in an automatic manner in all selected detector pixel locations. This approach minimizes manual intervention, increases the number of calibrated and characterized pixels, and provides a complete and accurate understanding of the detector spectral, geometrical and radiometric performances. Nevertheless, optimization of the measurement setup requires a preliminary effort in order to adapt the measurement equipment to the measurement strategy. The features of the CTM, as well as its advantages and drawbacks are outlined in the next publication (Dell'Endice et al. 2007a).

5.4 Automatic Calibration and Correction Scheme for APEX

Dell'Endice, F., Nieke, J., Brazile, J., Schläpfer, D., Hueni, A., & Itten, K.I. (2007). Automatic Calibration and Correction Scheme For APEX (Airborne Prism EXperiment). In, *Proceedings of 5th EARSeL Workshop on Imaging Spectroscopy* (p. 9). Bruges

AUTOMATIC CALIBRATION AND CORRECTION SCHEME FOR APEX (AIRBORNE PRISM EXPERIMENT)

*Francesco Dell'Endice¹, Jens Nieke¹, Jason Brazile¹, Daniel Schlöpfer¹, Andreas Hueni¹
and Klaus Itten¹*

1. Remote Sensing Laboratories, University of Zurich, Department of Geography, Zurich, Switzerland; fradel@geo.unizh.ch

ABSTRACT

Hyperspectral sensors provide a large amount of both spatial and spectral information. Calibration plays an important role in the efficient use of such a rich data source. However, calibration is extremely time consuming if undertaken with traditional strategies. Recent studies demonstrated that various non-uniformities, and detector imperfections drastically affect the hyperspectral data quality if not known and corrected for. The APEX (Airborne Prism Experiment) spectrometer adopts an automatic calibration and characterization strategy with the ultimate goal of providing scientific products of very high accuracy. This strategy relies on the control test master (CTM), an advanced software/hardware equipment able to control independently the instrumentation, and to process online or offline the large amount of data acquired to characterize such a sophisticated instrument. Those data, once processed by the master processor, will generate several coefficients that in turn will feed the processing and archiving facility (PAF), a software module that calibrates the acquired scenes, and corrects for artefacts and non-uniformities.

INTRODUCTION

Hyperspectral sensors provide a large amount of both spatial and spectral information. Calibration plays an important role in order to use efficiently such a rich data source. Hyperspectral scanners are calibrated by means of various techniques, which are usually applied both in a laboratory and/or during the acquisition itself via on-board instrumentation. However, calibration is extremely time consuming if undertaken with traditional strategies, i.e. by manual laboratory measurements at a few selected pixels over the detector area. Thus a compromise is necessary: only the compulsory measurements are performed, namely those concerning the spectral and the radiometric calibration (1); nevertheless these measured parameters can be sufficient to reach an acceptable accuracy of the hyperspectral products delivered to the scientific community. On the other hand, measuring several calibration parameters for all the detector pixels implies the production of a large amount of data, which would need a dedicated hardware/software environment (2,3) able to exploit such information. If calibration data are acquired also during the acquisition phases, i.e. on-board, the situation becomes even more challenging, due to the increased amount of information.

Recent studies (4,5,6) demonstrated that various non-uniformities, and detector imperfections will drastically affect the hyperspectral data quality if not known and corrected for. Thus better detector characterization and calibration are recommended. Such a goal can only be achieved if both laboratory and in-flight calibration data are acquired at several pixels on one side, and if other parameters are introduced and measured in the calibration strategy on the other side, as for instance misregistration (5,6), co-registration, and stability.

For this to be feasible in terms of both time and precision, the APEX (Airborne Prism Experiment) spectrometer adopts an automatic calibration and characterization strategy with the ultimate goal of providing high accuracy scientific products. The concept is illustrated in the further sections.

THE CALIBRATION TEST MASTER

The APEX calibration strategy focuses on the measurement of several calibration and characterization parameters at selected pixels within the detector area. For this purpose, a calibration test master (CTM) is used. The CTM is a hardware/software facility that optimizes the time needed for the calibration by automatic generation of optical stimuli. Thus no manual action is required, apart from some secondary settings, e.g. switching on/off the light sources. The CTM interfaces APEX with both a laboratory ground facility, i.e. the Calibration Home Base (CHB) (7) in Oberpfaffenhofen (Germany), and an In-Flight Calibration facility (IFC) (2). The instrumentation in both the CHB and the IFC can be controlled remotely via a computer interface, thus enabling automatic measurements.

The CTM consists of three main elements (**Figure 1**):

- *The controller* that is the core unit of the CTM.
- *The storage unit*, which is partly embedded in APEX and partly located on an external desktop.
- *The processor*, whose function is to process all the calibration data.

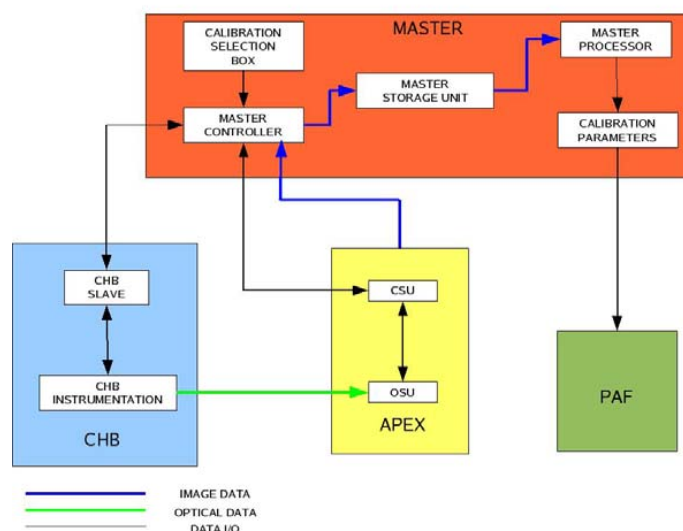


Figure 1: CTM logical working flow. The CTM interfaces APEX, the CHB, and the PAF.

The CTM controller is embedded in the APEX instrument and sets up all the necessary parameters, i.e. APEX settings (e.g. integration time) and calibration facility settings (e.g. monochromator wavelength, integrating sphere lamp intensity), for a particular calibration procedure to be performed. Once the setting is completed, the calibration measurements take place, and the acquired data are stored in the storage unit. The CTM processor is a complementary software utility, installed on a dedicated external hardware, whose goal is to generate the calibration parameters, necessary to calibrate the acquired raw data by processing all the data in the CTM storage unit. The Processing and Archiving Facility (PAF) (2) utilizes the calibration parameters provided by the CTM for the level 0 to level 1 processing.

For automated procedures a certain number of sequential sub-requests for both the CHB (e.g. folding mirror height, scan angle, lamp voltage, etc.) and APEX are generated. For each sub-request to be processed by the hardware the controller generates a well-formatted file, which in turn will be transformed into an electric and/or mechanic signal. The measurements are carried out once the sub-requests have been executed by the relevant hardware. The time needed to process

every sub-request has been estimated to be about 5s but this can be reduced if no drastic changes on the setup are needed. The overall calibration phase therefore requires about one week time.

Several units of the laboratory facility can be controlled remotely, e.g. the folding mirror (i.e., height, linear position, and angular position), the monochromator (e.g., voltage, current, wavelength), the collimator and the integrating sphere (e.g. lamp combination) thus facilitating the automated approach chosen for the CTM.

CALIBRATION AND CHARACTERIZATION PARAMETERS

Several calibration and characterization procedures are applied to APEX in order to better characterize and calibrate the sensor. Procedures are applied both in laboratory and on board by means of a dedicated instrumentation or by using special methodologies on the acquired scenes, the so-called scene-based vicarious calibration algorithms.

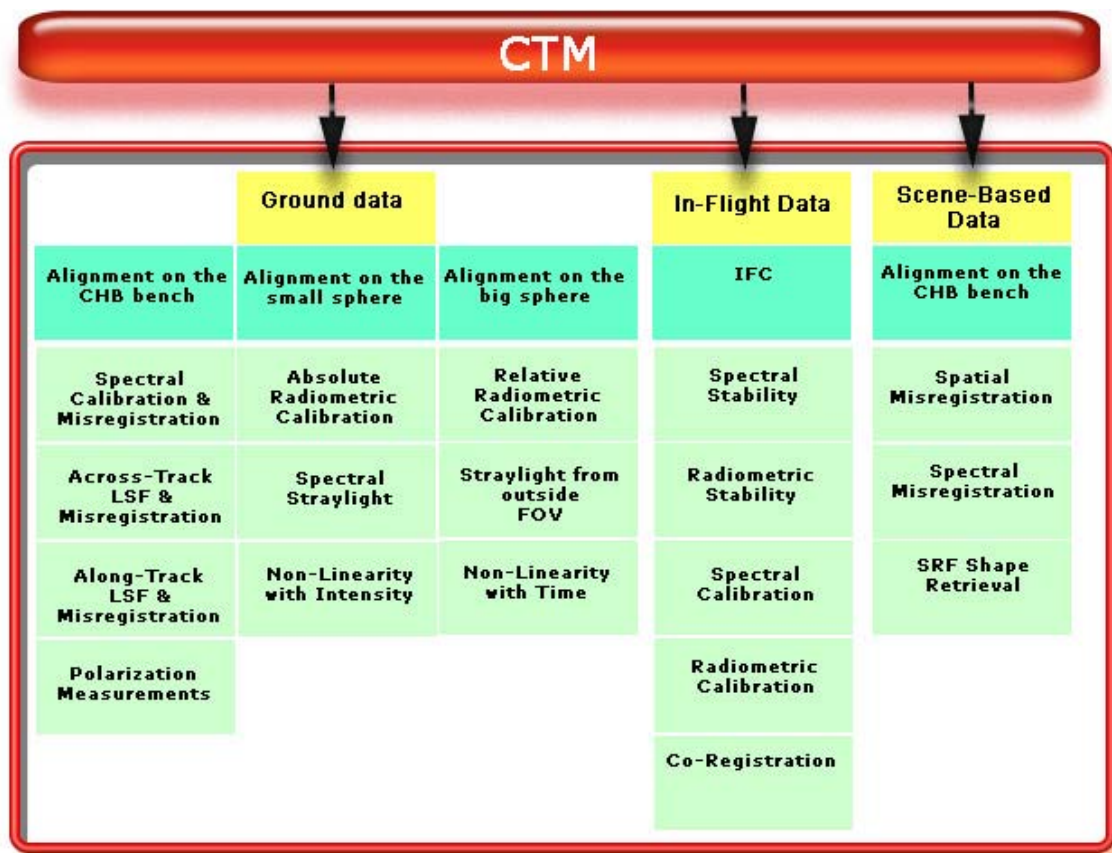


Figure 2: Data acquired by means of the Calibration Test Master (CTM), using the CHB, the IFC, and scene-based algorithms.

These procedures produce several parameters that can be grouped as follows (**Figure 2**):

- *Ground parameters*: generated by processing the data acquired by the laboratory facility, i.e. the CHB.
- *In-Flight parameters*: generated by processing the data acquired by the on-board calibration facility, i.e. the IFC.
- *Scenes parameters*: generated by processing the recorded real scenes.

As mentioned earlier, the CHB can be controlled remotely by the CTM. This is mainly possible because an engine-driven folding mirror with two degrees of freedom is used in order to redirect the illumination source beams on a specified detector position. Thus, the time saved in performing the common hyperspectral calibration procedures (i.e. spectral calibration and radiometric calibration) is employed to increase the number of characterized pixels, but it is also used to perform additional characterization measurements such as straylight from inside and outside the field of view (FOV), point spread function (PSF) across as well as along track, polarization measurements and so on. PSF measurements are important in order to understand both the spectral and spatial resolution performances of the detector. Besides the folding mirror, two integrating spheres of different sizes allow the absolute and the relative radiometric detector calibration as well as the measurement of non-linear detector behaviours with time and light intensity in order to model the sensor when close to saturation limits.

On the other side the IFC facility performs other characterization measurements that further increase the amount of information at detector level, e.g. co-registration in across-track, along-track and spectral dimensions, radiometric stability and spectral stability. Co-registration, meant to measure the change on detector performances with temperature and pressure, starts actually at laboratory level, where a first set of calibration data is acquired at standard environment conditions. The IFC plays also another important role on the decision-making process for the calibration strategy. The degradation of the detector performances is constantly monitored and compared with the laboratory results. If the difference between the on-board results and the laboratory results is such that the best detector performances cannot be guaranteed, then the operational phase has to be stopped and APEX has to be characterized and calibrated once again in the CHB.

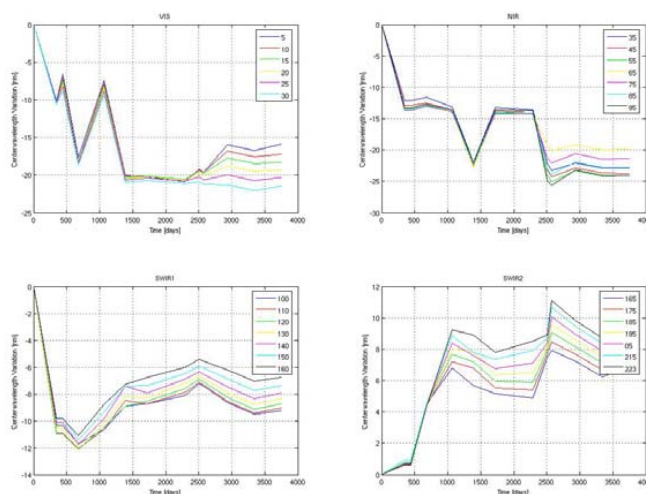


Figure 3: Absolute centre wavelength variation vs. time for the AVIRIS sensor, as measured in the laboratory.

A stability analysis has been performed on the AVIRIS (1) calibration data over a period of almost ten years for both the centre wavelength (**Figure 3**) and the spectral sampling interval. For instance, the centre wavelengths change constantly. Abrupt variations correspond to substitutions of optical detector elements and these cases necessitate a new laboratory characterization phase. On the other hand, smoother changes correspond to a degradation of the detector performances. However, if such degradation can still guarantee a satisfying performance then the operational phase could continue. The APEX strategy foresees an on-board monitoring of the most significant calibration parameters to check whether a significant degradation took place and performances are compromised. If multi-temporal analysis, also called change detection, has to be performed for a

ground target, then these monitoring parameters can be used in order to compare the scenes acquired at different times.

In order to measure spectral stability, the IFC is equipped with a set of four different filters:

- A standard reference SRM material 2065 filter from NIST.
- A bandpass 694 nm filter.
- A bandpass 1000 nm filter.
- A bandpass 2218 nm filter.
- A NG4 filter.

These elements are mounted on a rotating filter wheel. The NG4 filter is used to avoid detector saturation at maximum radiance level in the VNIR channel. The 1000 nm bandpass filter is used in order to measure the APEX properties in the overlapping region between the VNIR and SWIR detectors. The radiance coming out of the IFC lamp will pass through one of the aforementioned filters and it will reach the detector. By comparing different measurements over time is possible to quantify the spectral stability as well as the radiometric stability. These measurements are performed before and after every flight section and will be represented by dedicated parameters. These filters are also used for in-flight spectral calibration, namely by using the rare Earth materials filter, which has predefined absorption characteristics.

Recently, it has become feasible to retrieve and/or refine instrument characteristics by analyzing acquired scene data as opposed to synthetic laboratory data acquisitions. This is achieved by the (a) the acquisition and maintenance of precise reference databases of known physical phenomena, (b) increasing sophistication of engineering techniques for the juxtaposition of calibration references (e.g. cross-hairs of known angle and thickness) within the image data, (c) decreasing effort needed to run scores of model simulations permuted over varying parameters for the purpose of inverse data fitting and (d) sophistication of algorithms for retrieving various characteristics. Among the first instance of scene-based hyperspectral instrument characterization was the use of a spectrum-matching technique for improving wavelength calibration (8), that was later refined (9). A process for the detection of spectral line curvature including bandwidth as well as band centre shifts was refined by Neville (10). The APEX calibration strategy foresees the use of these algorithms for the retrieval/refinement of spectral response function (SRF) shape as well as band centre and bandwidth (11,12). Retrieval and refinement of spatial characterization will be applied using a method for spatial misregistration detection (13) and correction (6). Currently, scene-based calibration/characterization cannot fully replace laboratory calibration but it can supplement and validate them as well as possibly increase instrument "up time" in between intensive full laboratory calibration/characterization campaigns.

THE APEX CALIBRATION AND CORRECTION PARAMETERS

Several sets of data are acquired during the calibration/characterization phase in order to get the highest knowledge of the APEX system. The automatic calibration concept is a pioneer in the field of the calibration of hyperspectral sensors, in the sense that the saved time in performing the traditional procedures will be used to measure other parameters. The amount of calibration data can be large; a coarse estimation indicates that such data will be around half a terabyte. Thus, a dedicated software (e.g. parallel computing) and/or hardware (e.g. cluster or grid) strategy becomes compulsory, as a common CPU will not be able to process this amount of data in an acceptable short timeframe. Parallelization (14) of the data processing scheme will be used for APEX in order to satisfy the high computational power demand. These issues of processing setup and computing architectures are however not further elaborated in this paper. Our main objective will be to describe the calibration parameters that will be retrieved by processing calibration/characterization data.

Therefore the parameters issued out of the laboratory facility are described hereafter. The first point we take care of is related to the classical radiometric calibration, i.e. the passage from the raw digital numbers to physical units (e.g. radiance units). The radiometric calibration itself allows determining the relationship between these two entities, taking into account both the dark current level and the instrument exposure time; usually this step ends by identifying the gain coefficient and the dark current baseline for every pixel of the two APEX sensors (i.e. the VNIR detector and the SWIR detector). Non-linear behaviour with both time and light intensity is also here investigated, and a dedicated parameterization of the radiometric equation will take these effects into account; this will avoid, for instance, any kind of unfruitful use of the acquired data when we operate close to the saturation detector limit.

The spectral calibration, due to the automatic strategy, can be performed at several spatial locations and at several spectral channels with sub-pixel precision. The first advantage is that the interpolation between measurements, necessary to determine the centre wavelengths of the unconsidered pixels, will be much more precise; furthermore possible non-linear behaviour in the relationship between band number and wavelength will be better identified. It is worth to mention that in the classical approach the spectral calibration is performed in only a few spectral (1) channels. The second advantage is related to the fact that the same measurement is performed in several spatial (i.e. across-track angles) positions; the current baseline approach foresees 9 different spatial locations. It means that spectral misregistration, also called smile, can be detected, and eventually correct for. The last benefit is due to the sub-pixel precision; the SRF shapes will be known and help to understand how the incoming light signal is dispersed along the pixel in terms of spectral resolution, where the spectral resolution equals to the FWHM of the response function, if a Gaussian-like shape is assumed.

The geometric calibration consists essentially of measuring both the across-track and along-track line spread function (LSF). Even in this case, several spatial positions and several spectral channels will be investigated at sub-pixel level. Determining the LSF is necessary in order to retrieve both the across-track and along-track point spread function (PSF). By knowing the PSF at different CCD locations, we are able to identify spatial misregistration in both spatial dimensions. Nevertheless, changes of the PSF shapes can be used to identify possible variations of the spatial resolution and eventually correcting for it by degrading (smoothing) the image selectively to the broadest PSF within one dimension (5).

The parameters issued of the spectral and of the geometric calibration can be used to correct for misregistration artefacts. If one wants to correct for each of them step by step, the data loss will not be negligible, and the value of such a scheme would be doubtful. A potential strategy would be to combine, for every pixel, all these coefficients together, in order to get a unique weighting value for a unique pixel; by doing so the correction can be performed in only one step. This will reduce drastically the amount of information that is going to be lost. On the other side, such a correction is not strictly necessary if the instrument characterization reveals that the APEX instrument meets the demanded requirements in terms of performances (e.g. spectral resolution and spatial resolution). Nevertheless, questions arise if we look for spatial and/or spectral uniformity, that is, uniformity of the response functions along the spectral direction or spatial direction respectively; it could imply that some of the corrections can be omitted. However, the corrections for the along-track artefacts shall be keep separated from the spectral/across-track coefficients as the shape of the along-track response function depends on the chosen integration time.

Straylight measurements will take place during the laboratory phase. Straylight from inside the field of view (FOV) and spectral straylight data can be processed in a way that a correction coefficient can be retrieved for each one of them. These two coefficients can be eventually combined together in order to generate for every pixel a unique straylight coefficient. Straylight from outside the FOV is also measured but this value cannot be used for correction because it is extremely scene-dependent, but it will be used for characterization. In reality, the other straylight coefficients are also scene-dependent but their influence is constantly affecting the pixel light conditions even in presence of a ghost image as, for instance, a cloud.

A set of different polarizing filters is also used in order to identify polarization influences but these data will be used for characterization only, as the polarization is drastically scene-dependent. From the hardware point of view, APEX could be equipped with two removable scramblers in order to reduce such an influence. They will be used if priority has to be given to spectral or spatial resolution respectively; otherwise no scrambler is mounted. The polarization measurement ends the procedures to be performed in the CHB.

The IFC facility allows another series of measurements. We already described the stability of radiometric and spectral parameters over time in a previous section. Other measurements are related to the co-registration artefact. A set of different detector frames will be acquired at different altitude, because our aim is to investigate how the detector system behaves at different pressures and temperatures. As the external temperature and pressure vary exponentially with flight altitude we might expect a similar dependency of the co-registration coefficients on altitude. The co-registration will be measured along the three dimensions of the hyperspectral cube. A combination of these three coefficients can be created in order to correct for such an artefact in only one step. A fourth type of co-registration that does not require a direct measurement concerns the overlapping region between the VNIR and the SWIR detector. In fact, the last few bands of the VNIR spectral region coincide with the first spectral channels of the SWIR spectral range; a dedicated analysis of the acquired scenes will identify the amount of mismatch between the two CCD's, and a correction scheme will be applied.

Finally, scene-based algorithms will be applied to the acquired data in order to identify spectral curvature (10), spatial misregistration (6), and to retrieve SRF shape (11,12) and centre wavelength. In some cases, these procedures will generate absolute coefficients that can eventually be used to improve the correction and/or to refine the characterization of the detector. Vertical or rotational misalignments between the optical parts of the APEX system can be identified by analysing results of these methods (6). Therefore, if these misalignments are considerable, then a review of the optical system will be suggested to the optical team.

By using a calibration/characterization strategy as described above, several parameters will be generated (cf. Table 1). The three dimensions of the hyperspectral cube (i.e. along-track, across-track, and spectral dimensions) are indicated by x , y , and z respectively, with indexes i , j , and k . Spectral bands are also indicated by λ , and across-track angles by θ . Subscripts indicate in which dimension we operate while the superscripts indicate whether the coefficients vary along one or two directions. The coefficients miss the superscript i because we assume their values are constant over the along-track direction. Straylight from outside the FOV as well as polarization coefficients cannot be determined for every pixel and therefore a pixel-wise correction cannot be applied. By processing all the acquired raw calibration data, these parameters will be generated, and used to calibrate the real scene and correct for potential artefacts and/or non-linearities.

Table 1: List of the generated calibration/characterization parameters.

Coefficient	Notation	Coefficient	Notation
Radiometric gain	$G^{j,k}$	Polarization Measurement	-
Dark current	$D^{j,k}$	Non-Linearity with Time	$n_t^{j,k}$
Centre Wavelength	λ^j	Non-Linearity with Intensity	$n_I^{j,k}$
SRF shape	$\sigma_\lambda^{j,k}$	Spectral co-registration	$c_\lambda^{j,k}$
PSF shape Across-Track	$\sigma_\theta^{j,k}$	Across-Track co-registration	$c_\theta^{j,k}$
PSF shape Along-Track	$\sigma_x^{j,k}$	Along-Track co-registration	$c_x^{j,k}$
Spectral Misregistration	$\lambda_i^{j,k}$	Centre Wavelength Stability	$\lambda_i^{j,k}$

Spatial Misregistration Across-Track	$m_g^{j,k}$	Radiometric Gain Stability	$G_t^{j,k}$
Spatial Misregistration Along-Track	$m_x^{j,k}$	Spectral Curvature (Scene-Based)	$m_{\lambda S}^{j,k}$
Straylight from inside FOV	$S_I^{j,k}$	Spatial Misregistration (Scene-Based)	$m_{gS}^{j,k}$
Straylight from outside FOV	-	SRF retrieval (Scene-Based)	$\sigma_{\lambda S}^{j,k}$
Spectral Straylight	$S_S^{j,k}$		

CONCLUSIONS

The APEX instrument establishes the basis for a new characterization/calibration concept based on automatic procedures and correction scheme. This strategy relies on the CTM, an advanced software/hardware equipment able to independently control the instrumentation and to process online or offline the large amount of data required to characterize such a sophisticated instruments. The advantage of such an approach is twofold: first it allows a drastic reduction of the time to be spent in the laboratory and secondly it allows to measure more parameters than with classical calibration/characterization approaches. If several pixels in all the three hyperspectral dimensions are analyzed, then it is obvious that the whole sensor system can be more accurately characterized. The measured data, once processed by the master processor, will generate several coefficients that in turn will feed the processing and archiving facility (PAF). Therefore, the PAF will be able to calibrate the acquired scenes and, if needed, to correct for artefacts, non-linearities, and non-uniformities. Eventual upgrades to the CTM system could consist of (a) automatic application of the scene-based algorithms, which currently need to be supervised and (b) parallelization on a grid or cluster of CPUs (15).

REFERENCES

1. T. G. Chrien, R. O. Green, and M. L. Eastwood, "Accuracy of the Spectral and Radiometric Laboratory Calibration of the Airborne Visible/Infrared Imaging Spectrometer (AVIRIS)," in *Imaging Spectroscopy of the Terrestrial Environment*, G. Vane, ed., Proc. SPIE 1298, 37-49 (1990)
2. D. Schlöpfer, M. Schaepman, S. Bojinsk, and A. Börner, "Calibration and Validation Concept for the Airborne PRISM Experiment (APEX)," in *Canadian Journal of Remote Sensing* (February 2000)
3. Stenz, K., T.Szeredi, and J. Schwarz, "ISDAS - A System for Processing/Analyzing Hyperspectral Data", Technical Note, *Canadian Journal of Remote Sensing*, Vol. 24, No.2, 1998, pp. 99-113.
4. Nieke, J., Schlöpfer, D., Dell'Endice, F., Brazile, J., and Itten, K., "Uniformity of imaging spectrometry data products - the APEX approach", *Remote Sensing of Environment*, 2007, in review
5. D. Schlöpfer, J. Nieke, and K.I. Itten, "Spatial PSF non-uniformity effects in airborne pushbroom imaging spectrometer data," in *IEEE Transaction on Geoscience and Remote Sensing*, 45(2), 458-468 (2007)
6. F. Dell'Endice, J. Nieke, D. Schlöpfer, and K.I. Itten, "A scene based method for spatial misregistration detection in hyperspectral imagery," in *Applied Optics*, Vol. 46 N. 15, pp 1-14 (20 May 2007)
7. B. Suhr, P. Gege, P. Strobel, J.W. Kaiser, J. Nieke, K.I. Itten, G. Ulbrich, "Calibration Home Base for the Airborne Imaging Spectrometer APEX", in *Proc. Of 4th EARSeL Workshop on Imaging Spectroscopy*, Warsaw, 27-29 April 2005

8. B.C. Gao, M.J. Montes, C.O. Davis, "A curve-fitting technique to improve wavelength calibrations of imaging spectrometer data", in Proc. of the 11th JPL Airborne Earth Science Workshop, volume 03-4, pp. 99-105, 2002
9. B.C. Gao, M.J. Montes, C.O. Davis, "Refinement of wavelength calibrations of hyperspectral imaging data using a spectrum-matching technique", in Remote Sensing of Environment, Vol.90, pp.424-433, 2004
10. R.A. Neville, L. Sun, and K. Staenz, "Detection of spectral line curvature in imaging spectrometer data", in S. Shen, P. Lewis editors, SPIE Algorithms and Technologies for Multispectral Hyperspectral and Ultraspectral Imagerz IX, Vol. 5093, pp 144-154, Orlando
11. Brazile, J., Neville, R. A., Staenz, K., Schläpfer, D., Sun, L., and Itten, K.I., "Scene-based spectral response function shape discernibility for the APEX imaging spectrometer", IEEE Geoscience and Remote Sensing Letters, 3:414-418, 2006
12. Brazile, J., Neville, R. A., Staenz, K., Schläpfer, D., Sun, L., and Itten, K. I., "Toward scene-based retrieval of spectral response functions for hyperspectral imagers using fraunhofer features", Canadian Journal of Remote Sensing, 2006, in review
13. R. A. Neville, L. Sun, K. Staenz, "Detection of keystone in imaging spectrometer data," in Algorithms and Technologies for Multispectral, Hyperspectral, and Ultraspectral Imagery X, S. Shen and P. Lewis, Proc, SPIE 5425, 208-217 (2004)
14. J. Brazile, J.W. Kaiser, D. Schläpfer, J. Nieke. M. Schaepman, and K.I. Itten, "Parallelization of APEX Airborne Imaging Spectrometer Product Generation", in Proc. Of the 4th EARSeL Workshop in Imaging Spectroscopy, Warsaw, 27-29 April 2005
15. Brazile, J., Schläpfer, D., Kaiser, J., Schaepman, M. E., and Itten, K. I., "Cluster versus grid for large-volume hyperspectral image preprocessing", In SPIE Atmospheric and Environmental Remote Sensing Data Processing and Utilization: an End-to-End System Perspective, volume 5548, pages 48-58, 2004

5.5 Calibration cube

The calibration and the characterization approach, described in the previous paragraphs, lead to the generation of a considerable amount of calibration coefficients (i.e. centre wavelengths, radiometric gain and offset, smile and frown profile, point spread function across-track and along-track, straylight from inside and outside FOV). The CTM generates these coefficients for all detector array pixels. Therefore, a new data structure that groups all these parameters for all the detector pixels has been introduced and called *calibration cube* (Figure 11). A calibration cube is a three-dimensional promptly accessible data structure, whose first dimension corresponds to the number of detector across-track pixels, the second dimension corresponds to the number of spectral bands, and third dimension is equal to the number of retrieved calibration and characterization coefficients. Every layer of the calibration cube (i.e. spectral and spatial dimension) has a number of cells that is equal to the number of pixels in the detector (e.g. CCD or CMOS).

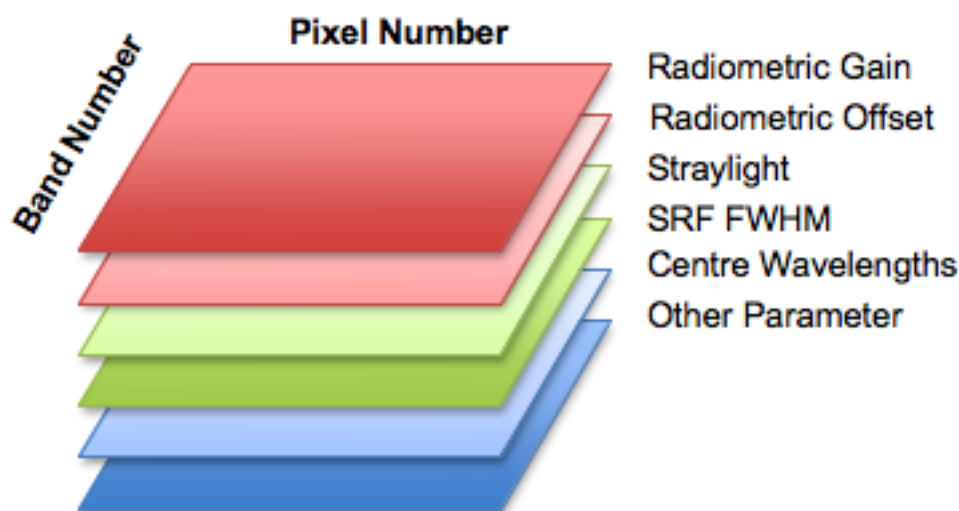


Figure 11: The calibration cube.

The calibration cube provides users with an additional insight into the instrument performance and gives the chance to compute the measurement uncertainty budget in a more precise manner. Generally, imaging spectroscopy images come with text files containing radiometric coefficients, centre wavelength, and spectral response function characteristics that are assumed constant for all across-track pixels. The calibration cube, instead, provides these and other parameters for every across-track pixels. The drawback is that user deals with a larger volume of information but a relevant advantage is the possibility of tracking products anomalies back to instrument performances.

The calibration and characterization coefficients can be used, for example, for correction algorithms, for selection of the most responsive pixels, for definition of consistent and reliable detector regions, as well as for the uncertainty assessment of imaging spectroscopy methods and products.

5.6 A case study: the Airborne Prism Experiment (APEX)

The calibration concept, presented above, has been tested on APEX (Airborne Prism Experiment), the airborne pushbroom imaging spectrometer, built by a joint Swiss-Belgian consortium, and financed through the ESA-PRODEX (European Space Agency – Program for experience development) (Itten

et al. 2008). The first test flight campaign has been carried out in Summer 2009 and its operational phase will start in Spring 2010 under the coordination of the Remote Sensing Laboratories (RSL) and the Flemish Institute of Technological Research (VITO).

The APEX calibration and characterization strategy has been implemented to reach these general objectives:

- Absolute radiometric accuracy better than 3%
- Spectral accuracy of 0.1 nm
- Geometrical accuracy of 0.049 mrad

Several characterization procedures were implemented in order to measure non-uniformities and achieve the above goals. The APEX laboratory calibration and characterization procedures and main results are described and discussed in the next publication.

5.7 Laboratory calibration and characterization of APEX

Dell'Endice, F., Alberti, E., Schaepman, M., & Malenovsky, Z. (2009). Laboratory Calibration and Characterization Results of the APEX Airborne Pushbroom Imaging Spectrometer. *Applied Optics, in review*

Laboratory Calibration and Characterization of the Airborne Pushbroom Imaging Spectrometer APEX

Francesco Dell'Endice^{1,*}, Edoardo Alberti¹, Michael E. Schaepman¹, Zbyněk Malenovský¹

¹ *Remote Sensing Laboratories, University of Zurich, Winterthurerstrasse 190*

Zurich, CH-8057, SWITZERLAND

**Corresponding author: francesco.dellendice@geo.uzh.ch*

Recent imaging spectroscopy applications make use of continuous spectral features of interest, to investigate the biochemical, structural and physical characteristics of natural and man-made Earth targets. These analyses require high spectral and radiometric measurement accuracy, and thus precision in the calibration and characterization process of the sensing optical device. The laboratory is optimal for the calibration of an imaging spectrometer and, when necessary, it is also an ideal environment to characterize system non-uniformities, instabilities, and uncertainty sources. The present study describes calibration and characterization of the Airborne Prism Experiment (APEX) pushbroom imaging spectrometer, performed at a specifically designed Calibration Home Base (CHB) laboratory. The main objective is to verify the following predefined APEX technical specifications: (1) an absolute radiometric uncertainty of 3%, (2) a spectral uncertainty of 0.1 nm, and (3) a geometric uncertainty of 0.049 mrad. The APEX spectral, radiometric, geometric, and general performance achieved in the laboratory, along with related uncertainty, is discussed. Lastly, the concept of the calibration cube is established as a promptly accessible and logically structured data source of calibration and characterization parameters.

OCIS codes: 040.0040, 040.1520, 110.3000, 110.4234, 120.0280, 120.4800, 120.6200, 230.5480, 280.4788, 300.6190.

Introduction

Imaging spectroscopy measurements of various spectral and spatial resolutions are nowadays used to retrieve geo- and bio-physical properties of natural targets from the scale of leaves up to the scale of ecosystems and biomes [1-4]. Physically based approaches implementing advanced modeling algorithms of radiative transfer in natural but also man-managed environments [5-7] are applied on air-/space-borne spectral image data, in order to reveal the spatial distribution of physical, structural and biochemical variables of the Earth's surface [8]. Operational examples include vegetation products of the MODIS instrument [9-11] and products of MERIS onboard the ENVISAT satellite [12]. The uncertainty of these retrieved remote sensing (RS) products depends directly on the accuracy and uncertainty behind the input measurements [13]. Hence, accurate, consistent, and standardized RS products require consistent high quality input data. The most accurate means of assessing the spectrometer measurement uncertainty lies within the laboratory calibration and characterization [14-17]. The fully controlled measuring conditions and procedures ensure the most accurate assessment of the system's optical properties and non-uniformities. Within this framework, the term *calibration* refers to determining the relationships between detector readouts (e.g. digital counts or digital numbers) and radiance units, along with the measurement uncertainty and accuracy [18], while the term *characterization* is defined as the influence of sensor parameters (e.g. pixel location, integration time, temperature, pressure) on the spectral, geometric, and radiometric properties of the sensor, determined during the calibration procedures. This case study presents the results of the Airborne Prism Experiment (APEX) [19] imaging spectrometer calibration and characterization, which was performed in a dedicated Calibration Home Base (CHB) laboratory [20]. The major objective of all the measurements is to verify the performance of APEX, namely: (1) an absolute radiometric uncertainty of 3%, (2) a spectral calibration uncertainty of 0.1 nm, and (3) a geometric calibration uncertainty of 0.049 mrad. Secondly, an assessment of the amount of incoming straylight and polarization sensitivity of the sensor is also given.

The APEX sensor design and technical specifications are first introduced. Subsequently, the laboratory calibration and characterization equipment and methodologies are described, followed by the results and discussion on sensor measurement performance including the assessment of complementary uncertainties. In conclusion, some improvements of the APEX laboratory calibration and characterization strategy are discussed.

APEX imaging spectrometer

APEX is an airborne dispersive pushbroom spectrometer that measures the incident spectral radiance between 380 and 2500 nm with two main spectral channels (see [21] for radiance and reflectance terminology used) [22, 23]. It comprises (1) a Visible-Near-Infrared (VNIR) channel, with a charge-coupled-device (CCD) light sensitive detector [24] covering the wavelength range from 380 to 1000 nm, and (2) a Short-Wavelength-Infrared (SWIR) channel, with a complementary-metal-oxide-semiconductor (CMOS) [25] chip covering the wavelength range between 940 and 2500 nm. The two detectors share the same foreoptics while having 1000 across-track pixels Field-Of-View (FOV) of $\pm 14^\circ$. The VNIR channel receives photons amongst 335 spectral bands that can be binned and re-configured accordingly to specific user application requirements [26], while the SWIR detector records reflected radiance over 199 spectral bands. The default configuration foresees 115 binned spectral bands in the VNIR. Signals of both

detectors are sampled and converted with 14 bits resolution. The system is equipped with an in-flight characterization facility (IFC) that monitors the sensor's spectral and radiometric stability during airborne operations [27]. A built-in scrambler can also be inserted into the incoming light path to reduce the effect of polarization interferences.

Calibration and characterization equipment

The CHB laboratory provides the following calibration possibilities: (1) calibrated light stimuli that are directly traceable to standardized radiance units, (2) remote control of all the instrumentation, and (3) the possibility of directing the light stimuli into the sensor FOV by means of a automated folding mirror assembly. CHB equipment is calibrated by recognized laboratories and certified by manufacturer specifications (e.g. integrating spheres or monochromator). Therefore, an uncertainty evaluation of Type B [28] can be conducted. The remote control permits the implementation of automatic procedures that, when compared to the classical calibration approach, cumulatively reduce the time invested, and this allows for a more extensive system characterization. A dedicated application called Calibration Test Master (CTM) has been developed [29] in order to satisfy the operational needs of: (1) the interfacing APEX with CHB, (2) driving the acquisition of the calibration data in an automatic way, and (3) processing the numerous measurements and generating the results. The light stimuli are provided by: (1) a Czerny Turner monochromator, (2) a lamp-slit-collimator assembly (i.e. a panchromatic beam), (3) two radiance standards, namely a secondary standard small-size integrating sphere, and (4) a large-size field standard integrating sphere.

Light sources and additional material

The monochromator (ORIEL MS 257) is equipped with three turret-holding gratings (UV-VIS, VIS-NIR, SWIR), four neutral density filters (0.01%, 1%, 10%, 50%), and a set of manually and motor driven slits. The slits are used to adjust the output stimulus, generated by a 150 W Quartz-Tungsten-Halogen (QTH) lamp, to the required spectral and spatial amplitudes. The first two gratings (covering the VNIR spectral region) have a resolution of $1200 \text{ lines}\cdot\text{mm}^{-1}$ and a reciprocal dispersion of about $3.1 \text{ nm}\cdot\text{mm}^{-1}$, while the third one resolves $600 \text{ lines}\cdot\text{mm}^{-1}$ with a reciprocal dispersion of $6.2 \text{ nm}\cdot\text{mm}^{-1}$.

The APEX spatial properties are measured using the lamp-slit-collimator (LSC) assembly. The panchromatic beam of a 100 W intensity tunable QTH lamp illuminates a very narrow slit (chosen between six different motor driven slits), and its' image is projected in the APEX FOV through a collimator with 120 mm aperture and 750 mm focal length.

The small-size integrating sphere (0.50 m in diameter) is used as a secondary calibration standard and is traceable to the primary reference at the German Institute of Standards (PTB). The sphere is equipped with four 100W QTH lamps with constantly monitored light intensity, achieving a radiometric stability of the radiant exitance of 2439 Wm^{-2} with deviations lower than 0.1% (after 45 min of warming-up). The light stimulus covers the whole APEX spectral wavelength range.

Since the exit door of the small-size integrating sphere covers only less than a fifth of the APEX FOV, the large-size integrating sphere (1.65 m in diameter) is needed to transfer the secondary standards to the instrument covering the full swath. The light stimulus that covers the whole APEX spectral range is supplied with a combination of 18 QTH lamps producing light intensities

ranging from 45 to 1200 W. The stimulus non-homogeneity at the exit port was measured to be lower than 1% (1σ) with stability deviations lower than 0.6%.

Additional experimental material includes a large series of neutral density (ND) filters (with transmissions ranging from 0.1% to 99%), three polarizing filters (VIS-500, IR-1300, IR-2000), and four homogeneous spectral targets with reflectance of 2%, 50%, 75%, and 99%.

Calibration and characterization methodologies

A pushbroom sensor is an imaging system which acquires a series of one-dimensional samples orthogonal to the platform line of flight with the along-track spatial dimension constructed by the forward motion of the platform. The spectral component is acquired by dispersing the incoming radiation onto an area array. Since area arrays are used as focal planes in these systems, the uniform calibration of the detector response is critical. However, in a combined analysis of SNR, uniformity, and stability, pushbroom scanners might not necessarily outperform whiskbroom systems even though they have a longer integration time [30]. Several specific procedures have therefore been defined for APEX and its CHB, described in Table 1, and were performed in this sense using CTM capabilities.

Table 1: APEX calibration and characterization procedures. The columns designate the type of procedure, the light source adopted and additional accessories respectively (left to right).

PROCEDURE TYPE	LIGHT STIMULUS	OTHER MATERIALS
Spectral calibration	Monochromator	ND Filters
Smile characterization	Monochromator	ND Filters
Across-track PSF calibration	LSC	-
Along-track PSF calibration	LSC	-
Keystone characterization	LSC	-
Straylight from inside FOV characterization	Monochromator	ND Filters
Straylight from outside FOV characterization	Large integrating sphere	Reflectance targets
Radiometric calibration	Small integrating sphere	ND Filters
Polarization characterization	Small integrating sphere	Polarizing filters
Irradiance distribution over FOV (i.e. vignetting)	Large integrating sphere	-
Noise Equivalent Delta Radiance	Small integrating sphere	-

APEX temporal noise and bad pixels map

The inherent detector properties, particularly bad pixels and temporal noise T , are first determined in order to prevent misinterpretation of the calibration and characterization results. A large number of frames are recorded by the sensor during its placement over the exit port of the large-size integrating sphere, emitting different levels of uniform and stable light intensities, which allows for the statistical analysis of the 14-bits dynamic range of all the CCD and CMOS pixels. All frames are dark current corrected and the pixels that diverge more than 2σ from the average behavior are assigned as bad pixels. The temporal noise, T , is assessed by calculating the standard deviation of the detector digital output, with respect to the different uniform and stable input light intensities. T incorporates several detector noise sources [31], spatial noise, and also the lamp instability. In relation to the input light intensity, T can be considered as the noise-

equivalent-delta-radiance of the system ($Ne\Delta L$) [32]. The relationship between $Ne\Delta L$ and the input radiance L is expressed as (eq. 1):

$$Ne\Delta L = c\sqrt{L} [W/(nm\ m^2\ sr)] \quad (1)$$

Where the constant c is determined by fitting the radiometrically corrected data sets (L) - expressed in physical units - applying a least square method (LSM).

Spectral Properties

The APEX spectral properties [13, 33, 34] are determined using the monochromator coupled with a folding mirror that enlightened selected pixels of the FOV. The procedure purposes are to: (1) define the spectral response function (SRF) [35] along with its center wavelength (λ_C), (2) verify if the SRF can be correctly approximated using a Gaussian function characterized by the λ_C and subsequently allowing to derive the full-width-at-half-maximum (FWHM), and (3) determine the spectral misregistration (or smile) [36, 37] affecting the instrument's performance. The exit and entrance slits of the monochromator are set so that the image of the monochromator output covers an area of nine pixels (independently from the spectral range under investigation) at the APEX focal plane. The light spot was automatically aligned onto APEX through the CTM, and the light intensity level was optimized to cope with the APEX dynamic range by changing ND filters and integration time. The spectral scans below 600 nm are conducted in steps of 0.2 nm and, above this wavelength, in steps of 0.5 nm, representing 1/10th or less of a spectral sampling interval. They are executed in unbinned mode at almost 400 detector spatial and spectral locations and were distributed in a way to ensure proper characterization of detector non-uniformities [38] (e.g. smile effect).

The APEX wavelength-dependent spectral uncertainty was computed as the root-square-sum (RSS) of the monochromator's spectral uncertainty (u_{MONO}) and the uncertainty of a spline algorithm (u_{SPL}) was used to identify the center wavelength of spectral pixels, which were not directly measured (eq. 2):

$$u_{SPEC}(\lambda) = \sqrt{u_{MONO}^2(\lambda) + u_{SPL}^2(\lambda)} \text{ [nm]} \quad (2)$$

Geometric properties

The across- and along-track point-spread function (PSF) is measured with the LSC (lamp-slit-collimator) assembly. The QTH white light illuminates a 1 μm wide slit creating a beam, which after collimation and projection by the CHB folding mirror, corresponds to 1/10th of an APEX spatial pixel. As the light beam simultaneously illuminates all sensor spectral channels, a line-spread function (LSF) is generated together with the PSF corresponding to the monochromatic section of LSF. This allows assessing the spatial co-registration consistency of the VNIR and SWIR detector, particularly in the overlapping spectral region between 940 and 1000 nm. The optimization and alignment of the APEX response with respect to the input stimulus are

automatically performed collecting 20 scans for every pixel. The across-track LSF is measured by keeping the CHB image slit fixed while moving the CHB folding mirror in small steps. In the case of the along-track LSF, the forward movement of a real sensor carrier is simulated by keeping the mirror in a steady position while rotating the collimator slit in small steps. Placing the sensor at 1 m above the basement plane resulted in an overall pointing resolution of the folding mirror assembly of 0.36 arcsec and an uncertainty of 1.5 arcsec. These PSF non-uniformities [38, 39] and keystone profile [40, 41] measurements are repeated every 1° of the APEX across-track FOV.

The APEX geometric uncertainty for a given spatial location (eq. 3, $u_{GEO}(s)$), is computed as the root-square-sum (RSS) of the folding mirror assembly pointing uncertainty (u_{CHB_MIRROR}), the uncertainty contribution due to the folding mirror assembly pointing resolution and the uncertainty of a spline algorithm (u_{SPL}) used to identify the angular position of the pixels that were not directly measured:

$$u_{GEO}(s) = \sqrt{u_{CHB_MIRROR}^2 + \left(\frac{r_{CHB_MIRROR}}{\sqrt{3}}\right)^2 + u_{SPL}(s)^2} \text{ [arcsec]} \quad (3)$$

Radiometric properties

Radiometric calibration is carried out in order to convert: (1) the numerical coefficients of the acquired spectra expressed in digital numbers (DN) into radiances [21] [W/(m² nm sr)], and (2) the traceability of the APEX radiometric accuracy to the primary standard. APEX is placed on top of a small-size integrating sphere that produces a stable light beam covering 5° of the APEX FOV. A set of ten ND filters are then placed between the sphere exit door and the APEX entrance window to cover the whole APEX dynamic range, and more than 500 frames are recorded. The LSM fitting applied to the 11 dark current corrected data sets reveals, after spectral convolution of the certified PTB spectral bands and radiances to the APEX spectra bands and to the ND transmissivity profiles, the radiometric coefficients. The radiometrically-calibrated frames are used to compute relative and absolute radiometric accuracy. The procedure is then repeated for almost 500 pixels by positioning the sphere at the edges of the APEX FOV. APEX is then placed over the large-size integrating sphere and the irradiance distribution (i.e. vignetting) is measured for the total 28° FOV. Remaining radiometric coefficients are indirectly determined through a scaling approach using the following radiometric equation (eq. 4):

$$L(s,b) = \frac{1}{v(s,b)} \cdot \left[g(s,b) \cdot \frac{(D(s,b) - D_D(s,b))}{t} + c(s,b) \right] \quad (4)$$

where s is the spatial location, b is the spectral location, v is the scaling vignetting coefficient, g and c are the gain and the dark current coefficients, t is the integration time, D are the measured DN, D_D is the dark level associated with the APEX integration time (IT), and L is the unknown radiance level.

Characterization of APEX non-linearities, with respect to integration time and input intensity, leads to the assessment of the wavelength-dependent absolute radiometric uncertainty (u_{ABS}). It is expressed as the RSS of: (1) APEX uncertainty (u_{APEX}) due to its instability, (2) APEX relative uncertainty (u_{REL}) with respect to the small-size sphere output, (3) the sphere instability (u_{SIN}), and (4) the sphere traceability error (u_{PTB}):

$$u_{ABS}(\lambda) = \sqrt{u_{APEX}^2(\lambda) + u_{REL}^2(\lambda) + u_{SIN}^2(\lambda) + u_{PTB}^2(\lambda)} \quad [\%] \quad (5)$$

The APEX uncertainty is considered equal to the $Ne\Delta L$.

Straylight properties

Straylight [42-44] refers to unwanted or misbinned photons generated by sources inside or outside the APEX FOV that reach the detectors of the sensor optical system. Straylight originating from within the FOV was assessed from two measurement data sets acquired for a 3x3 pixel spot illuminated with the monochromator. The first data set corresponds to signal levels close to the APEX saturation limit, but still within its linear region. The second data set was recorded by placing a 1% ND filter in front of the APEX entrance window. A circle of 35 pixels in radius is drawn and averaged around the most illuminated pixel of each recorded frame. The straylight coefficient is computed as the ratio between the irradiance measured within the S_A circle (coming from the almost saturated frame) and the irradiance of the S_B circle, extracted from the average frame corresponding to the 1% of ND data set. The measurement is repeated at several angles and wavelengths to provide a complete detector characterization.

An assessment of straylight originating from outside FOV is carried out through an experimental setup with the large-size integrating sphere. Four reflectance targets are consecutively placed on the sphere bottom in such a way so that they are detectable from a few spatial pixels around the APEX nadir position, and several frames are recorded and dark current corrected. The four measured data sets are then averaged and a LSM approach is applied to extrapolate the instrument response at 0% reflectance, which is considered a qualitative estimate of the worst-case scenario for the APEX straylight originating from outside the FOV.

Polarization properties

The APEX polarization sensitivity [45] is tested by installing the system on top of the small-size integrating sphere with three polarizers ('VIS-500' covering wavelengths ranging from 475 to 650 nm, 'IR-1300' for the region between 650 and 1600 nm, and 'IR-2000' covering the remaining spectral range) in-between. Each filter is rotated in steps of 11.5° from 0° to 135°, and frames are recorded for each angle. The measurements are repeated once again with the APEX scrambler in place. The measured points are then interpolated using a sine function and the polarization sensitivity P is calculated as (eq. 6):

$$P(\lambda) = \frac{I_{\max}(\lambda) - I_{\min}(\lambda)}{I_{\max}(\lambda) + I_{\min}(\lambda)} \quad (6)$$

Finally, the wavelength-dependent maximum and minimum responses, I , are derived from the function fitting of the radiances.

Calibration and characterization data structure

The CTM produces an extensive series of calibration and characterization coefficients that are grouped into an $S \times B \times N$ matrix, where S represents the number of across-track pixels, B is the number of spectral bands in the unbinned configuration, and N indicates the number of measured parameters. This entity, defined as an APEX *calibration data cube* (CDC), is produced for both the VNIR and the SWIR channel. The purpose of all CDC layers (Figure 1) is to provide, pixel wise, a complete collection of the instrument calibration parameters.

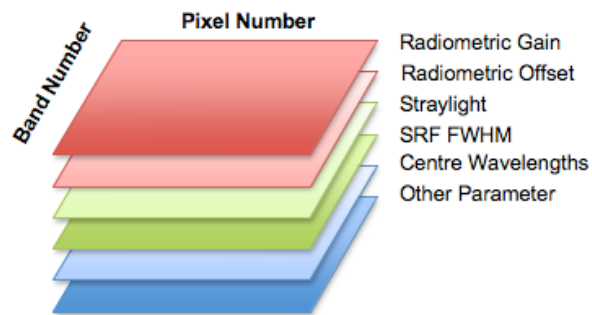


Figure 1: Example of layers of an APEX calibration cube. (NB: ‘Centre’ above needs to be spelt as ‘Center’ – American spelling)

Results and Discussion

APEX temporal noise and bad pixels map

Processing the frames acquired with the integrating spheres reveals that the SWIR channel is affected from 0.43% of bad pixels, while the VNIR CCD functions without any bad pixels. The percentage of bad pixels is a time-dependent function of sensor ageing, particularly in the case of the CMOS channel, where an increasing number of cooling cycles will reduce pixel sensitivity. This quantity is expected to grow at a rate of +0.05% bad pixels per flight campaign, which means that a new bad pixel map must be constantly generated and reconsidered during data calibration and characterization. Data processing and correction schemes (e.g. radiometric calibration, geo-correction, interpolation, atmospheric-correction, etc.) [33, 46, 47] significantly benefit from such a map, because they reduce the generation of artifacts that would otherwise influence the results or products. Interpolation techniques might be applied in future to replace missing pixels' values [39, 48].

It is anticipated that the temporal noise will depend on the level of input radiance (Figure 2), mainly because of the photon noise. Figure 2 illustrates that the $Ne\Delta L$ is higher in the VNIR binned region (i.e. below 630 nm), due to the broad bandwidths, and in the last 250 nm of the

SWIR channel, because of a different gain setting and different uncertainty given by the small-size integrating sphere.

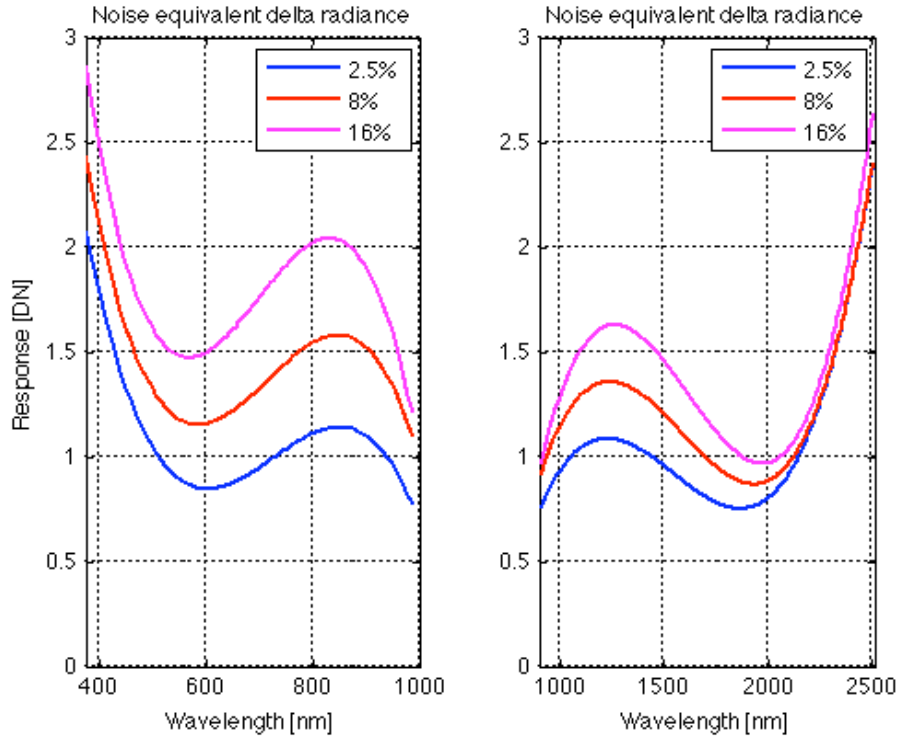


Figure 2: APEX Noise equivalent delta radiance plotted as a function of the input light intensity. Radiance levels were simulated by placing three neutral density filters (2.5%, 8%, and 16%) in front of the small-size integrating sphere’s exit door.

According to Figure 3, showing the $Ne\Delta L$ for an expected average level of input radiance during an airborne mission, the VNIR detector and the SWIR channel suffer, on average, from a temporal noise of 0.21% and of 0.19% of the input radiance, respectively. Looking at all the measured scenarios, it was noticed that the $Ne\Delta L$ never exceeded the value 0.5%, which can be considered as the APEX radiometric detection limit. The low detector noise implies that radiance differences between spectra of the same target can then be attributed to target non-homogeneities. Moreover, users can obtain a qualitative merit figure for the signal-to-noise-ratio (SNR) by dividing the measured radiance with the worst case of 0.5% signal $Ne\Delta L$. The SNR value then indicates the expected performance of each spectral pixel.

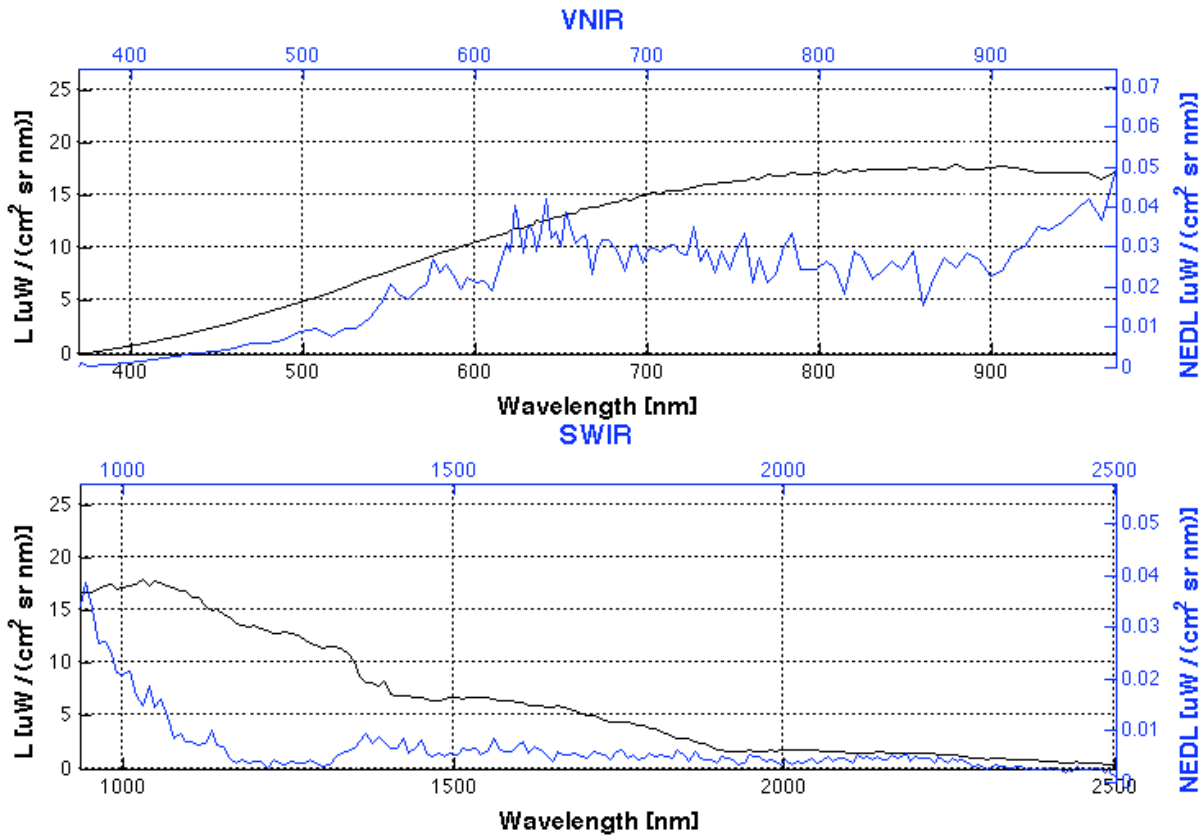


Figure 3: APEX *NeAL* (blue curve) for an expected average radiance input (black curve).

Low values of temporal noise suggest a high APEX radiometric stability under constant laboratory conditions, which also allows for the identification of possible light source instabilities.

Spectral Properties

The APEX wavelengths are determined experimentally at almost 400 locations along the spectral and spatial domains, and were used to compute the SRF properties of the remaining positions with a spline function. The per-wavelength monochromator spectral uncertainty depends on the spectral resolution, uncertainty and error repeatability of the monochromator that is directly linked to the characteristics of the gratings (Table 2).

Table 2: Uncertainty indicators of the spectral calibration.

Spectral Region [nm]	u_{MONO} [nm]	u_{SPL} [nm]	u_{SPEC} [nm]
380 – 560	0.084	≈ 0	0.084
560 – 1000	0.104	≈ 0	0.10
1000 -2500	0.178	≈ 0	0.18

The VNIR detector is spectrally calibrated to within the predefined measuring requirement of 0.1 nm, while the SWIR detector is calibrated to within an accuracy of 0.18 nm, mainly due to the low resolution of the monochromator grating used in this spectral region.

Figure 4 shows that the spectral smile of both detectors is smaller than 0.25 pixels, with the variable spectral sampling interval (SSI) between 0.15 and 2.5 nm. Our results confirm the previously published finding that the smile profile follows a quadratic law with respect to the across-track dimension [41]. This characterization is positive for applications using variations in positions of specific absorption features as indicators of the target optical and/or chemical properties [49]. In fact, smile correction can be applied. This is an advantage when compared with smile correction based on flight data, where an estimation of the most accurate channel (the one to be used as a reference [37]) can be determined with vicarious calibration techniques [50].

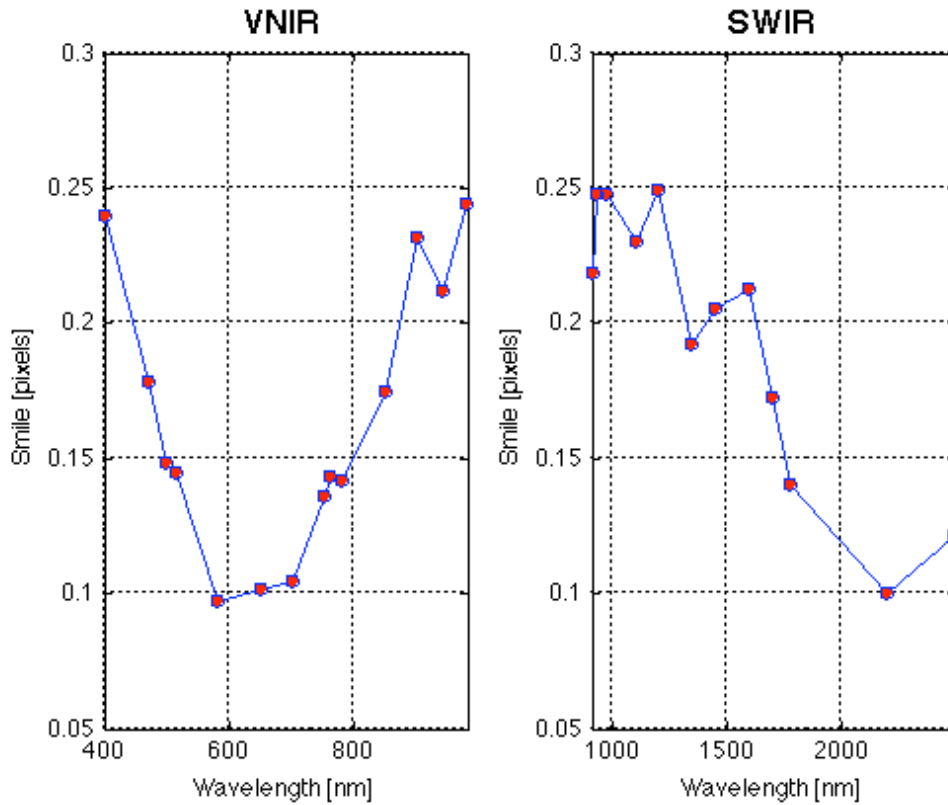


Figure 4: The APEX spectral smile profile for the Visible-Near-Infrared channel (VNIR) and for the Short-Wave-Infrared (SWIR) channel.

The calculated APEX spectral resolution (Figure 5) is assumed to be, on average, equal to the spectral sampling interval, because the system undersamples the spectral domain (i.e. SSI is lower than the spectral bandpass [51]). The spectral resolution for the VNIR channel was found to be between 0.5 and 8 nm in unbinned mode, while for the SWIR channel it is between 6 and 9 nm. The customized binning patterns could be implemented for specific spectral regions of interest of the VNIR detector [26], which would change the spectral resolution accordingly. An example given for the default VNIR binning pattern in Figure 5 shows how the spectral resolution was reduced in the range up 620 nm (i.e. higher spectral sampling interval) to improve SNR.

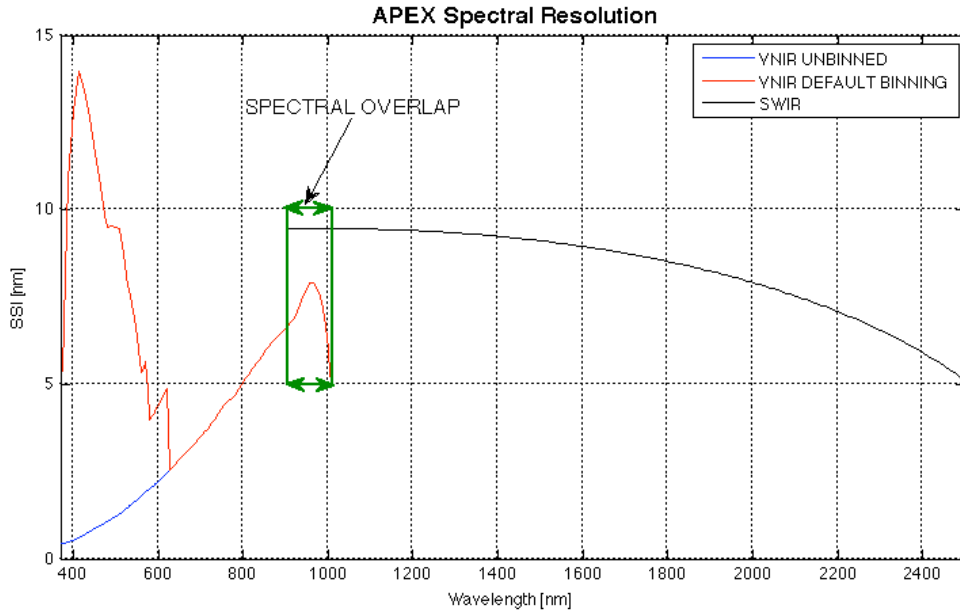


Figure 5: APEX spectral resolution for (a) VNIR in unbinned mode (335 bands), (b) VNIR in default binning (115 bands), and (c) SWIR channel. The spectral overlap region is highlighted.

Geometric properties

It was observed that the FWHM of the PSF across-track was always less than 1.5 times of the instantaneous-field-of-view (IFOV) in the VNIR and less than 1.8 times in the SWIR channel. Regarding the along-track direction, the FWHM of the PSF was less than 1.0 times IFOV in case of the VNIR and about 1.1 times IFOV in the SWIR region. Nevertheless, the PSF along-track depends on integration time, which varies per flight operation. The PSF non-uniformities [38, 39] computed per spectral channel identify the FWHM PSF variation in all the corresponding spatial pixels (i.e. 1000) as less than 5%. As the CHB folding mirror uncertainty is 1.5 arcsec (i.e. less than a $1/10^{\text{th}}$ of an APEX pixel), the calibration objective of $0.49 \cdot 10^{-1}$ mrad was achievable.

The average spatial misregistration (or keystone) [36] was determined to be about 0.2 spatial pixels for VNIR and 0.4 for SWIR channel. The keystone correction suffers from a similar lack of reference as the smile effect [40, 41], with the suggestion that the value at the nadir can be a best candidate for this purpose.

Finally, the average error made in resolving the same spatial target simultaneously in the VNIR and in the SWIR wavelengths (i.e. spatial co-registration error) was less than 0.62 pixels between -14° and -6° of FOV, and less than 0.46 pixels between -6° and $+14^{\circ}$ of FOV.

Radiometric properties

The radiometric gain (Figure 6) varies in VNIR wavelengths due to the quantum efficiency and optical transmission. The spectral region between 380 and 650 nm is influenced by the applied default-binning pattern, higher binning means lower gain, but higher sensitivity. The SWIR

radiometric gain, apart from the first 80 and last 250 nm, can be considered constant, given the constant quantum efficiency of the CMOS detector. In order to improve SNR, the last 50 rows of the SWIR channel are configured with a different capacitance value (30 fF) than the first part (130 fF), which explains the abrupt decrease of gain in this region. By observing Figure 6, it can be noted that the two detectors have an overlapping spectral region of about 70 nm, however, the final images will be delivered to users as one continuous spectral dataset. The optimization of this region will be automatically performed in the APEX Processing and Archiving Facility (PAF) [47] during production of the Level 1C data.

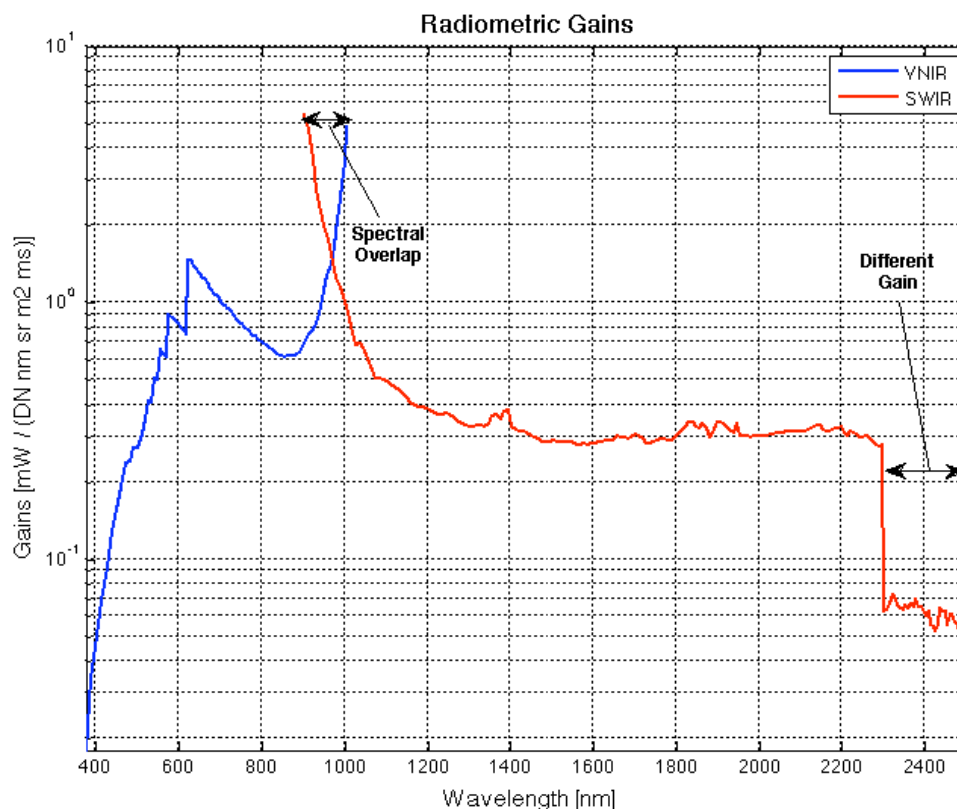


Figure 6: APEX Radiometric gains for pixel 500 (i.e. NADIR position) in the VNIR (standard binning) and SWIR channels.

The vignetting profiles, retrieved for the VNIR and SWIR detector separately, were found to match better than 0.2%. The nadir spatial pixel (i.e. pixel no. 500) is used as the reference to evaluate the irradiance distribution variation. The mean attenuation is 4.46% between -14° and $+13.44^\circ$ ($\sigma = 4.97\%$) and 32.1% in the last 0.56° (i.e. last 20 pixels) of the FOV ($\sigma = 7.6\%$). A vignetting compensation has also been implemented in the processing chain, with the consequence that the radiometric coefficients are spatially scaled using these values.

The radiometric uncertainty range was thus calculated (Figure 7) to assess the APEX traceability to the PTB primary standard.

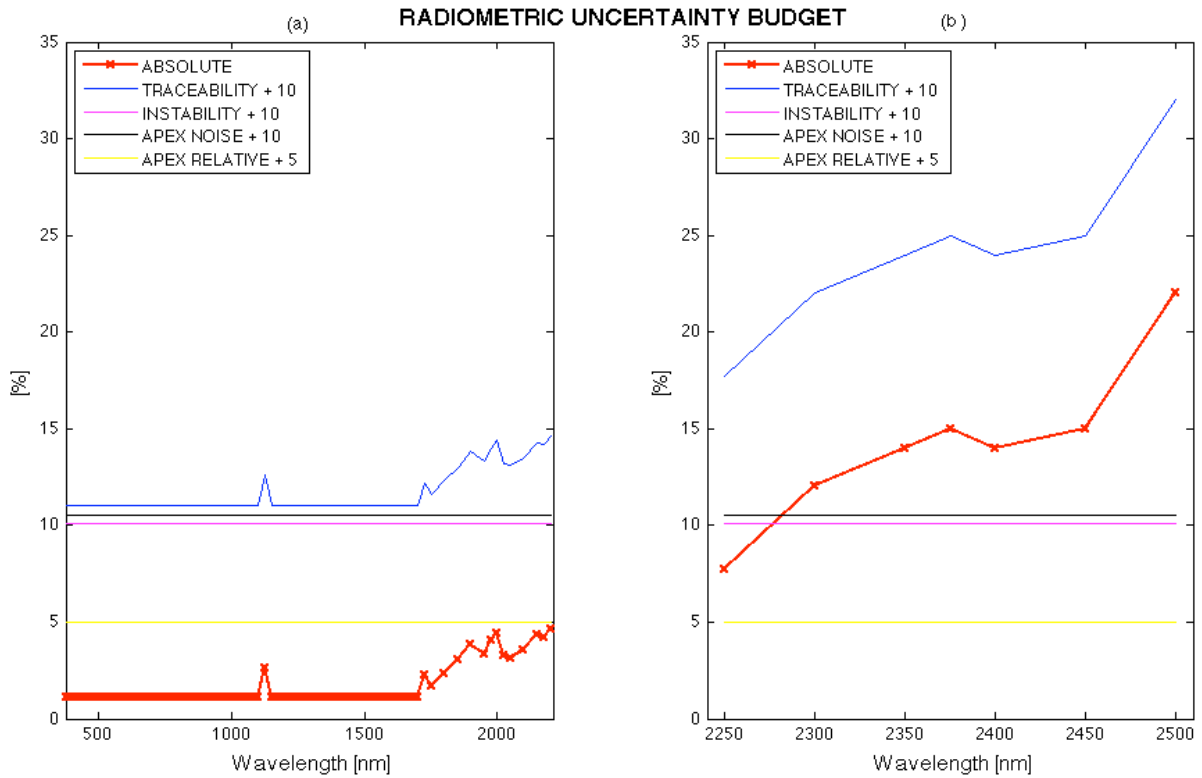


Figure 7: APEX radiometric uncertainty budget, evidencing (a) the radiometric traceability error contribution between 380 and 2250 nm, (b) radiometric traceability error contribution between 2250 and 2500 nm. (The contributions have been offset to improve readability).

The APEX temporal stability was assumed being equal to the worst possible case of $NeAL$, which means equal to 0.5% for all wavelengths. The APEX relative accuracy was determined by calibrating spectra of the certified integrating sphere using the retrieved radiometric coefficients with a relative error less than 0.01% (constant for all wavelengths). The sphere instability was known to be of 0.1% (constant for all wavelengths). The traceability error, as certified from the PTB, was generally 1% up to 1700 nm, averaging 3% between 1700 and 2250 nm, and averaging 14% for the last 50 rows of the SWIR detector (2250-2500 nm). Other uncertainty sources are negligible when compared with the radiometric traceability. The radiometric requirement (3% of absolute radiometric calibration accuracy) is fulfilled from 380 until 1700 nm. In the region between 1700 and 2250 nm, an average uncertainty of 3.54% exists (slightly above the goal), and an average of 14.25% is obtained for the remaining spectral range. The extent of this large error is mainly driven by the traceability error of the integrating sphere uncertainty. In addition, the weak radiance levels of the sphere lamp, between 2250 and 2500 nm, induces a very low SNR of the calibrating device (i.e. calibration between sphere and primary standard) leading to a high uncertainty.

Straylight properties

APEX straylight originating from inside the FOV was assessed to be better than 2% in the VNIR channel and better than 6% in the SWIR channel, while no relevant straylight contribution from external sources could be identified. This confirms the APEX optimal optical design. Yet, the straylight outside the FOV was detected as the result of a qualitative assessment so the real response of the system might be different when used in an actual observational scenario.

Polarization properties

The polarization sensitivity was measured to be between 2% and 5% and between 2% and 6% for the VNIR detector and the SWIR channel, respectively. When the scrambler is inserted in the incoming light path, the polarization sensitivity is reduced to 1% in both channels. However, the scrambler slightly modifies the acquisition spatial properties (i.e. the FWHM of the across- and along-track PSF becomes larger, about 15%), therefore its use is traded off against the reduced spatial resolution of the system. Consequently, such a configuration is recommended to be used mainly for highly polarized and highly uniform observational targets (e.g. water bodies).

Calibration and characterization data structure

The large amount of calculated calibration and characterization parameters of both channels generates a high number of layers for the APEX calibration cubes. In spite of this, the actual CDC provides all relevant parameters related to the most relevant system properties (i.e. spectral, radiometric, geometric performance), allowing full reproducibility of the above calibration steps. APEX calibration and characterization are regularly scheduled twice per year. Updates of the calibration cubes are additionally conducted whenever a significant change in the instrument performance or hardware design appears. The dimensionality of the CDC allows proper estimation of instrument related effects on future data products.

Conclusions

The results of the APEX laboratory calibration and characterization revealed that the characterization of the optical performance of a pushbroom imaging spectrometer is, to a very large extent, pixel related, meaning that each spatial pixel must be considered as an independent radiometer that needs calibration. The calibration and characterization objectives can be performed for the APEX instrument, for the VNIR channel and the SWIR channel. The reduced SWIR channel accuracy resulted from a lower resolution of the monochromator grating and from a low SNR of the light stimulus (i.e. small-size integrating sphere) between 2250 and 2500 nm. Therefore, future enhancements of the measurement setup should include an investigation of alternative lamp sources for short wave near infrared and for UV spectral regions, where an APEX-CHB optimization effort has been conducted and reasonable SNR levels attained. In this context, a stability monitoring methodology, which could possibly induce the prediction of the calibration and characterization coefficients with a timestamp [27], is currently being developed. Additionally, we have demonstrated the use of the CTM and introduced the concept of using a calibration cube as a data structure that can support users in computing the accuracy of their RS

products. In addition, the calibration cube allows users to reconstruct the original measurement data, eventually being used to implement own calibration routines.

The achieved laboratory calibration and characterization results demonstrated the measurement capabilities of the APEX imaging spectrometer. The influence of non-uniformities (i.e. smile of 0.25 pixels, average keystone of 0.3 pixels, and average straylight from inside FOV of 4%) were assessed with the required uncertainty. The APEX data and ancillary ground spectral measurements, acquired during a flight campaign in June 2009, will now be used jointly with vicarious calibration efforts allowing to describe the performance of the instrument under laboratory conditions as well as during in-flight. However, due to the multi-dimensional problem of characterizing imaging spectrometer data during in-flight, further advanced calibration procedures will significantly profit from simultaneous assessment of all influencing parameters.

References

1. S. L. Ustin, A. A. Gitelson, S. Jacquemoud, M. Schaepman, G. P. Asner, J. A. Gamon, and P. Zarco-Tejada, "Retrieval of foliar information about plant pigment systems from high resolution spectroscopy," *Remote Sensing of Environment* **113**, S67-S77 (2009).
2. M. E. Martin, L. C. Plourde, S. V. Ollinger, M. L. Smith, and B. E. McNeil, "A generalizable method for remote sensing of canopy nitrogen across a wide range of forest ecosystems," *Remote Sensing of Environment* **112**, 3511-3519 (2008).
3. R. F. Kokaly, G. P. Asner, S. V. Ollinger, M. E. Martin, and C. A. Wessman, "Characterizing canopy biochemistry from imaging spectroscopy and its application to ecosystem studies," *Remote Sensing of Environment* **113**, S78-S91 (2009).
4. M. E. Schaepman, S. L. Ustin, A. J. Plaza, T. H. Painter, J. Verrelst, and S. Liang, "Earth system science related imaging spectroscopy--An assessment," *Remote Sensing of Environment* **113**, S123-S137 (2009).
5. D. Huang, Y. Knyazikhin, R. E. Dickinson, M. Rautiainen, P. Stenberg, M. Disney, P. Lewis, A. Cescatti, Y. H. Tian, W. Verhoef, J. V. Martonchik, and R. B. Myneni, "Canopy spectral invariants for remote sensing and model applications," *Remote Sensing of Environment* **106**, 106-122 (2007).
6. S. Jacquemoud, W. Verhoef, F. Baret, C. Bacour, P. J. Zarco-Tejada, G. P. Asner, C. Francois, and S. L. Ustin, "PROSPECT plus SAIL models: A review of use for vegetation characterization," *Remote Sensing of Environment* **113**, S56-S66 (2009).
7. J. L. Widlowski, M. Taberner, B. Pinty, V. Bruniquel-Pinel, M. Disney, R. Fernandes, J. P. Gastellu-Etchegorry, N. Gobron, A. Kuusk, T. Lavergne, S. Leblanc, P. E. Lewis, E. Martin, M. Mottus, P. R. J. North, W. Qin, M. Robustelli, N. Rochdi, R. Ruiloba, C. Soler, R. Thompson, W. Verhoef, M. M. Verstraete, and D. Xie, "Third Radiation Transfer Model Intercomparison (RAMI) exercise: Documenting progress in canopy reflectance models," *Journal of Geophysical Research-Atmospheres* **112**, - (2007).
8. Z. Malenovsky, K. B. Mishra, F. Zemek, U. Rascher, and L. Nedbal, "Scientific and technical challenges in remote sensing of plant canopy reflectance and fluorescence," *J. Exp. Bot.*, erp156 (2009).
9. N. V. Shabanov, D. Huang, W. Z. Yang, B. Tan, Y. Knyazikhin, R. B. Myneni, D. E. Ahl, S. T. Gower, A. R. Huete, L. E. O. C. Aragao, and Y. E. Shimabukuro, "Analysis and optimization of the MODIS leaf area index algorithm retrievals over broadleaf forests," *Ieee Transactions on Geoscience and Remote Sensing* **43**, 1855-1865 (2005).
10. Y. Knyazikhin, J. V. Martonchik, R. B. Myneni, D. J. Diner, and S. W. Running, "Synergistic algorithm for estimating vegetation canopy leaf area index and fraction of absorbed photosynthetically active radiation from MODIS and MISR data," *J. Geophys. Res.* **103**.

11. W. Z. Yang, B. Tan, D. Huang, M. Rautiainen, N. V. Shabanov, Y. Wang, J. L. Privette, K. F. Huemmrich, R. Fensholt, I. Sandholt, M. Weiss, D. E. Ahl, S. T. Gower, R. R. Nemani, Y. Knyazikhin, and R. B. Myneni, "MODIS leaf area index products: From validation to algorithm improvement," *Ieee Transactions on Geoscience and Remote Sensing* **44**, 1885-1898 (2006).
12. N. Gobron, B. Pinty, O. Ausedat, M. Taberner, O. Faber, F. Mélin, T. Lavergne, M. Robustelli, and P. Snoeij, "Uncertainty estimates for the FAPAR operational products derived from MERIS -- Impact of top-of-atmosphere radiance uncertainties and validation with field data," *Remote Sensing of Environment* **112**, 1871-1883 (2008).
13. R. O. Green, "Spectral calibration requirement for Earth-looking imaging spectrometers in the solar-reflected spectrum," *Appl. Opt.* **37**, 683-690 (1998).
14. C. Davis, J. Bowles, R. Leathers, D. Korwan, T. V. Downes, W. Snyder, W. Rhea, W. Chen, J. Fisher, P. Bissett, and R. A. Reisse, "Ocean PHILLS hyperspectral imager: design, characterization, and calibration," *Opt. Express* **10**, 210-221 (2002).
15. T. G. Chrien, R. O. Green, and M. L. Eastwood, "Accuracy of the spectral and radiometric laboratory calibration of the Airborne Visible/Infrared Imaging Spectrometer," in *Imaging Spectroscopy of the Terrestrial Environment*, (SPIE, 1990), 37-49.
16. M. A. Folkman, J. Pearlman, L. B. Liao, and P. J. Jarecke, "EO-1/Hyperion hyperspectral imager design, development, characterization, and calibration," in (SPIE, 2001), 40-51.
17. M. E. Schaepman and S. Dangel, "Solid Laboratory Calibration of a Nonimaging Spectroradiometer," *Appl. Opt.* **39**, 3754-3764 (2000).
18. JCGM/WG2, *International vocabulary of metrology - Basic and general concepts and associated terms (VIM)*, 3rd Edition (Bilingual E/F) ed. (2008).
19. K. I. Itten, F. Dell'Endice, A. Hueni, M. Kneubuehler, D. Schläpfer, D. Odermatt, F. Seidel, S. Huber, J. Schopfer, T. Kellenberger, Y. Bühler, P. D'Odorico, J. Nieke, E. Alberti, and K. Meuleman, "APEX - the Hyperspectral ESA Airborne Prism Experiment," *Sensors*, 25 (2008).
20. P. Gege, J. Fries, P. Haschberger, P. Schötz, H. Schwarzer, P. Strobl, B. Suhr, G. Ulbrich, and W. J. Vreeling, "Calibration Facility for airborne imaging spectrometers," *ISPRS Journal of Photogrammetry & Remote Sensing* (accepted for publication) (2009).
21. G. Schaepman-Strub, M. E. Schaepman, T. H. Painter, S. Dangel, and J. V. Martonchik, "Reflectance quantities in optical remote sensing--definitions and case studies," *Remote Sensing of Environment* **103**, 27-42 (2006).
22. M. E. Schaepman, K. I. Itten, D. R. Schlaepfer, J. W. Kaiser, J. Brazile, W. Debruyn, A. Neukom, H. Feusi, P. Adolph, R. Moser, T. Schilliger, L. D. Vos, G. M. Brandt, P. Kohler, M. Meng, J. Piesbergen, P. Strobl, J. Gavira, G. J. Ulbrich, and R. Meynart,

- "APEX: current status of the airborne dispersive pushbroom imaging spectrometer," in (SPIE, 2004), 202-210.
23. M. E. Schaepman, L. d. Vos, and K. I. Itten, "APEX-airborne PRISM experiment: hyperspectral radiometric performance analysis for the simulation of the future ESA land surface processes earth explorer mission," in (SPIE, 1998), 253-262.
 24. G. Amelio, M. Tompsett, and G. Smith, "Experimental verification of the charge coupled device concept," *Bell Syst. Tech. Journal* **79**, 593 - 600 (1970).
 25. P. Chorier and P. M. Tribolet, "High-performance HgCdTe SWIR detectors for hyperspectral instruments," in *Sensors, Systems, and Next-Generation Satellites V*, (SPIE, 2001), 328-341.
 26. F. Dell'Endice, J. Nieke, B. Koetz, M. Schaepman, and K. I. Itten, "Improving Radiometry of Imaging Spectrometers by using Programmable Spectral Regions of Interest," *IPSRS Journal of Photogrammetry & Remote Sensing*, in press (2009).
 27. P. D'Odorico, E. Alberti, F. Dell'Endice, J. Nieke, and K. I. Itten, "Tracking Spectral Accuracy of Hyperspectral Data by means of an In-Flight Calibration Facility (IFC)," in *Proceedings of 6th EARSeL Workshop on Imaging Spectroscopy*, 2009), 9.
 28. P. De Bièvre, "The 2007 International Vocabulary of Metrology (VIM), JCGM 200:2008 [ISO/IEC Guide 99]: Meeting the need for intercontinentally understood concepts and their associated intercontinentally agreed terms," *Clinical Biochemistry* **42**, 246-248 (2009).
 29. F. Dell'Endice, J. Nieke, J. Brazile, D. Schläpfer, A. Hueni, and K. I. Itten, "Automatic Calibration and Correction Scheme For APEX (Aiborne Prism EXperiment)," in *Proceedings of 5th EARSeL Workshop on Imaging Spectroscopy*, 2007), 9.
 30. M. E. Schaepman, "Imaging Spectrometers," in *The SAGE Handbook of Remote Sensing*, T. A. Warner, M. D. Nellis, and G. M. Foody, eds. (SAGE, London (UK), 2009), pp. pp. 166-178.
 31. J. Nieke, M. Solbrig, and A. Neumann, "Noise Contributions for Imaging Spectrometers," *Appl. Opt.* **38**, 5191-5194 (1999).
 32. D. Schläpfer and M. Schaepman, "Modeling The Noise Equivalent Radiance Requirements of Imaging Spectrometers Based On Scientific Applications," *Appl. Opt.* **41**, 5691-5701 (2002).
 33. L. Guanter, R. Richter, and J. Moreno, "Spectral calibration of hyperspectral imagery using atmospheric absorption features," *Appl. Opt.* **45**, 2360-2370 (2006).
 34. O. D. D. Soares and J. L. C. Costa, "Spectrophotometer Spectral Bandwidth Calibration with Absorption Bands Crystal Standard," *Appl. Opt.* **38**, 2007-2013 (1999).

35. L.-P. Boivin, "Study of Bandwidth Effects in Monochromator-Based Spectral Responsivity Measurements," *Appl. Opt.* **41**, 1929-1935 (2002).
36. P. Mouroulis, R. O. Green, and T. G. Chrien, "Design of Pushbroom Imaging Spectrometers for Optimum Recovery of Spectroscopic and Spatial Information," *Appl. Opt.* **39**, 2210-2220 (2000).
37. R. A. Neville, L. Sun, and K. Staenz, "Detection of spectral line curvature in imaging spectrometer data," in *Algorithms and Technologies for Multispectral, Hyperspectral, and Ultraspectral Imagery IX*, (SPIE, 2003), 144-154.
38. J. Nieke, D. Schläpfer, F. Dell'Endice, J. Brazile, and K. I. Itten, "Uniformity of Imaging Spectrometry Data Products," *IEEE Transactions on Geoscience and Remote Sensing* **46**, 11 (2008).
39. D. Schlapfer, J. Nieke, and K. I. Itten, "Spatial PSF Nonuniformity Effects in Airborne Pushbroom Imaging Spectrometry Data," *Geoscience and Remote Sensing, IEEE Transactions on* **45**, 458-468 (2007).
40. R. A. Neville, L. Sun, and K. Staenz, "Detection of keystone in imaging spectrometer data," in *Algorithms and Technologies for Multispectral, Hyperspectral, and Ultraspectral Imagery X*, (SPIE, 2004), 208-217.
41. F. Dell'Endice, J. Nieke, D. Schläpfer, and K. I. Itten, "Scene-based method for spatial misregistration detection in hyperspectral imagery," *Applied Optics* **46**, 14 (2007).
42. K. W. Busch, O. O. Soyemi, D. Rabbe, and M. A. Busch, "Determination of the Stray Light Levels in a Dispersive Near-Infrared Spectrometer with Trichloromethane," *Appl. Spectrosc.* **54**, 1759-1766 (2000).
43. H. S. Coleman, "Stray Light in Optical Systems," *J. Opt. Soc. Am.* **37**, 434-448 (1947).
44. Y. Zong, S. W. Brown, B. C. Johnson, K. R. Lykke, and Y. Ohno, "Simple spectral stray light correction method for array spectroradiometers," *Appl. Opt.* **45**, 1111-1119 (2006).
45. U. Böttger, J. Nieke, and D. Schläpfer, "Assessing polarization effects for the Airborne imaging spectrometer APEX," *Adv. Radio Sci.* **4**, 323-328 (2006).
46. B.-C. Gao, M. J. Montes, Z. Ahmad, and C. O. Davis, "Atmospheric Correction Algorithm for Hyperspectral Remote Sensing of Ocean Color from Space," *Appl. Opt.* **39**, 887-896 (2000).
47. A. Hueni, J. Biesemans, K. Meuleman, F. Dell'Endice, D. Schlaepfer, S. Adriaensen, S. Kempenaers, D. Odermatt, M. Kneubuehler, and J. Nieke, "Structure, Components and Interfaces of the APEX Processing and Archiving Facility," *Transactions on Geoscience and Remote Sensing* (2008).

48. M. E. Winter, P. G. Lucey, T. Williams, and M. Wood, "Calibration of the University of Hawaii's airborne hyperspectral imager," in *Imaging Spectrometry IX*, (SPIE, 2003), 370-379.
49. R. F. Kokaly, G. P. Asner, S. V. Ollinger, M. E. Martin, and C. A. Wessman, "Characterizing canopy biochemistry from imaging spectroscopy and its application to ecosystem studies," *Remote Sensing of Environment* **In Press, Corrected Proof**(2009).
50. P. Koepke, "Vicarious satellite calibration in the solar spectral range by means of calculated radiances and its application to Meteosat," *Appl. Opt.* **21**, 2845-2854 (1982).
51. G. A. Swayze, R. N. Clark, A. F. H. Goetz, T. G. Chrien, and N. S. Gorelick, "Effects of spectrometer band pass, sampling, and signal-to-noise ratio on spectral identification using the Tetracorder algorithm," *J. Geophys. Res.* **108**(2003).

Binning patterns for spectral regions of interest

6 Binning patterns for spectral regions of interest

Optimization of instrument settings is an important task that has to be performed in order to ensure the best acquisition performance. Optimization has to be applied in laboratory as well as in flight mode. The laboratory scenario includes the combined optimization of instrument parameters (e.g. APEX settings) and equipment parameters (e.g. CHB parameters). The flight scenario, instead, implies that the optimization of instrument parameters is performed against the target properties. Laboratory optimization has been tackled in the previous chapter while this one focuses on the flight mode, i.e. image acquisition.

Imaging spectroscopy data provide spatial information in several bands, usually covering the range between 400 and 2500 nm. However, specific remote sensing products are derived using only a small portion of the available spectral range. Thus, we introduce the concept of *spectral region of interest (SROI)*. Generally, a remote sensing product is associated with a particular SROI.

In order for this product to be successfully retrieved, the corresponding SROI must respond to defined spectral and radiometric requirements as, for instance, spectral sampling interval, noise-equivalent-delta-radiance ($Ne\Delta L$), and signal-to-noise ratio (SNR). Imaging spectrometers are conceived and operated in a way that reasonable spectral, geometric and radiometric performances are guaranteed over the entire spectral range (usually between 400 and 2500 nm). The spectral bands of an imaging spectrometer are usually selected using a target-dependent approach: for every spectral region the requirements are driven by the most performance-demanding target (Schlöpfer and Schaepman 2002). A statistical band selection strategy has been also used (Price 1994), which is based on specific system response functions.

Nevertheless, specific products might need spectral and radiometric requirements that differ from the default instrument performances; for instance, a product may require only a portion of the available spectral range and have requirements that differ from the ones of the default mission. One might wonder whether the instrument settings might be changed in such a way that these additional requirements can be achieved.

Modern imaging spectrometers, as APEX (Itten et al. 2008), offer the possibility of reprogramming the detector spectral domain by means of field-programmable-gate-arrays (FPGA) (Kuusilinna et al. 1999).

Moved by this idea, the chance of modifying instrument settings applying *on-chip spectral binning* was investigated. A software tool called BinGO (Binning patterns Generator and Optimizer) optimizes the spectral and radiometric instrument variables and generates specific spectral binning patterns. These patterns are customized for specific SROIs and are uploaded into the sensor-controlling unit before a mission takes place. This way, the sensor flexibility can be used to sense different targets with different acquisition settings aiming at ensuring optimal performance.

The optimization process consists of a series of trade-off discriminations between spectral resolution, spectral uncertainty and SNR; for a particular centre wavelength, the best choice is the one that provides the lowest spectral sampling interval (i.e. the lowest spectral uncertainty) with the highest SNR.

BinGO is built around several instrument parameters (e.g. well-depth, bit-resolution, noise contributions, quantum efficiency, optical transmission, saturation levels). If these variables are not known, they can be assessed or guessed indirectly using an instrument model.

Spectral reprogramming may be of high interest for the spectroscopy community users because imaging spectroscopy products are generated by using the information contained in specific SROIs.

The description of the BinGO optimization process, as well as its advantages and drawbacks, are presented in the next publication in order to discuss the following research question:

How can high quality products be generated by optimizing the data acquisition for specific spectral regions of interest?

6.1 Improving Radiometry by using Programmable Spectral Regions of Interest

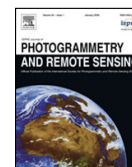
Dell'Endice, F., Nieke, J., Koetz, B., Schaepman, M.E., & Itten, K. (2009). Improving radiometry of imaging spectrometers by using programmable spectral regions of interest. *ISPRS Journal of Photogrammetry and Remote Sensing*, 64, 632-639



Contents lists available at ScienceDirect

ISPRS Journal of Photogrammetry and Remote Sensing

journal homepage: www.elsevier.com/locate/isprsjprs



Improving radiometry of imaging spectrometers by using programmable spectral regions of interest

Francesco Dell'Endice^{a,*}, Jens Nieke^b, Benjamin Koetz^{a,c}, Michael E. Schaepman^{a,d}, Klaus Itten^a

^a Remote Sensing Laboratories, Department of Geography, University of Zurich, Winterthurerstr. 190, 8057 Zurich, Switzerland

^b ESA-ESTEC, Keplerlaan, 2200 AG Noordwijk, The Netherlands

^c ESA-ESRIN, via Galileo Galilei, Casella Postale 64, 00044 Frascati, Italy

^d Wageningen University, 6700 AA Wageningen, The Netherlands

ARTICLE INFO

Article history:

Received 5 September 2008

Received in revised form

25 May 2009

Accepted 27 May 2009

Available online 21 June 2009

Keywords:

Calibration

Algorithms

Pushbroom

Radiometric

Imaging spectrometer

ABSTRACT

Programmable imaging spectrometers can be adjusted to fit specific application requirements that differ from the instrument initial spectral design goals. Sensor spectral characteristics and its signal-to-noise ratio (SNR) can be changed by applying customized online binning patterns.

We present a software utility that generates application driven spectral binning patterns by using an SNR dependent sensor model. The utility, named BinGO (Binning patterN Generator and Optimiser), is used to produce predefined binning patterns that either (a) allow an existing imaging spectrometer to optimize its spectral characteristics for a specific application, (b) allow an existing imaging spectrometer to spectral and/or spatially emulate another instrument, or (c) design new multispectral or imaging spectrometer missions (i.e. spaceborne, airborne, terrestrial). We present a variety of BinGO case studies, including the simulation of airborne (APEX) [Itten, K.I. et al., 2008. APEX – The hyperspectral ESA Airborne Prism Experiment. *Sensors* 8(1), 1–25], spaceborne (SENTINEL III) [Nieke, J., Frerick, J., Stroede, J., Mavrocordatos, C., Berruti, B., 2008. Status of the optical payload and processor development of ESA's Sentinel 3 mission. In: *Proceedings of the Geoscience and Remote Sensing Symposium IGARSS 2008*, pp. 427–430], as well as scientific and performance optimized approaches. We conclude that the presented approach can successfully be used to increase the efficiency of spectral information retrieval by using imaging spectroscopy data and to simulate various missions and requirements, finally supporting proper trade-off decisions to be made between performance optimization and scientific requirements. In addition, if specific sensor parameters are known, BinGO can also model other imaging spectrometers.

© 2009 International Society for Photogrammetry and Remote Sensing, Inc. (ISPRS). Published by Elsevier B.V. All rights reserved.

1. Introduction

Pushbroom based imaging spectrometers (e.g. APEX [Itten et al., 2008], CHRIS [Barnsley et al., 2004], HYSPEX [Baarstad et al., 2005], PHILLS [Davis et al., 2002], Hyperion [Folkman et al., 2001], Casi-3 [Babey and Anger, 1993]) are currently used for Earth Observation purposes to identify spectral signatures of a broad range of surface properties and materials in the solar reflected range of the electromagnetic spectrum. These instruments are designed to fulfil a large variety of application requirements, usually with highest performance requirements. Various application driven requirements have been successfully translated into radiometric performance requirements for imaging spectrometers [Schläpfer and Schaepman, 2002]. The inherent challenge is that multiple

applications will pose different performance requirements on the same spectral band as well as all applications jointly will require a contiguous coverage of the whole spectral range. The latter again has led to a series of scientific requirements (REQ), formulated in terms of spectral resolution [Green, 1998; Mouroulis et al., 2004; Schläpfer and Schaepman, 2002] (Fig. 1), signal-to-noise ratio (SNR), noise equivalent delta radiance [Schläpfer and Schaepman, 2002] ($Ne\Delta L$), or spatial resolution. To achieve optimal performance over the whole instrument spectral range, a default configuration is usually defined as a mission standard. Traditionally, the mission standard is based on a trade-off between mission costs and scientific requirements and always includes compromises from either side.

Nevertheless, specific applications might not require full spectral coverage or may allow relaxation of spectral resolution requirements in certain portions of the covered wavelength range. Accounting for this increased flexibility of requirements, we introduce the concept of spectral ranges of interest (SROI). SROI are

* Corresponding author. Tel.: +41 (0) 44 63 55149; fax: +41 (0) 44 63 56846.

E-mail address: francesco.dellendice@geo.uzh.ch (F. Dell'Endice).

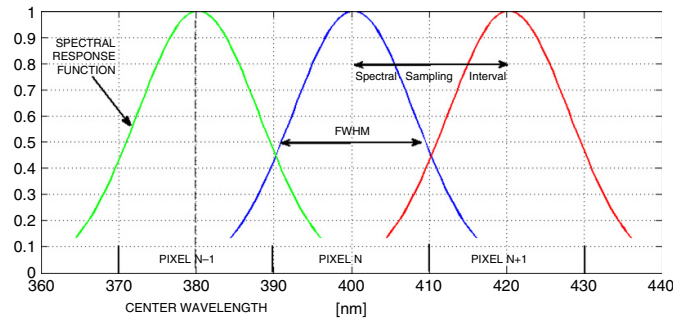


Fig. 1. Spectral parameters. *Spectral response function (SRF)*: the pixel response curve to a spectral stimulus as a function of wavelength; the width of the SRF at half of its peak is the *FWHM (Full-Width-at-Half-Maximum)* (nm), which corresponds to the spectral resolution of the corresponding spectral channel. The *Spectral Sampling Interval (SSI)* (nm) is the distance between two adjacent centre wavelengths.

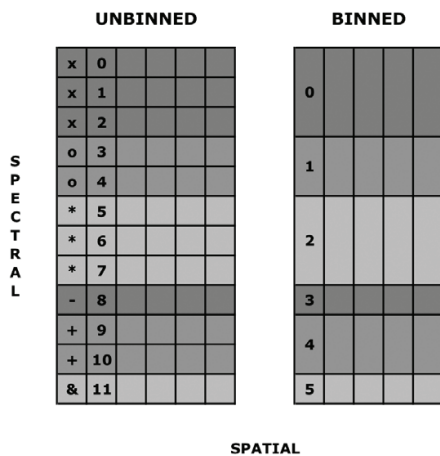


Fig. 2. Online Spectral Binning Scheme. Two or several adjacent detector spectral rows are summed up together in order to form a single *binned* channel. For instance, the unbinned bands from 0 to 2 (left figure) are read together in order to form the binned band 0 (right figure).

focusing of application requirements, such as pigment retrieval in vegetation (Ustin et al., 2006), or equivalent water thickness (EWT) in canopies (Clevers et al., 2008). While the first SROI would be focusing on high spectral resolution in the pigment region (mainly Chl absorption) in the VIS/NIR range of the spectrum, the latter SROI would be located in the NIR and SWIR regions. However EWT retrievals consist already of dual application requirements, namely the inherent separation of canopy and atmospheric water absorption features.

We propose using spectral binning for the definition of application specific SROI, along with specific SNR requirements and spectral resolution. The aforementioned applications are examples of case studies that could be implemented using spectral binning.

Currently only two concepts of SROI have so far been implemented in imaging spectrometers. MERIS (Rast et al., 1999) is using the concept of SROI for post-launch calibration adjustments to compensate pre- and post-launch calibration differences (Delwart et al., 2007). CHRIS (Barnsley et al., 2004) on PROBA uses predefined application sets of SROI, however usually at the cost of being a trade-off between spatial and spectral resolution.

Current imaging spectrometers like APEX (Itten et al., 2008) allow us to efficiently re-program electronic (e.g. gain, integration time) and optical settings using field programmable gate arrays (FPGA) (Kuusilinna et al., 1999). The re-programming of spectral

configuration is a mandatory requirement for BinGO to be applied successfully.

We discuss in this paper the flexible use of SROI depending on variables such as spectral range, SNR, spectral binning and spectral resolution.

2. Method

Pushbroom imaging spectrometers offer several narrow and contiguous spectral bands (Gomez, 2002; Itten et al., 2008). We assume that P spectral bands are recorded when those sensors are operated in full spectral mode, i.e. when all spectral channels are read out without any reduction.

Spectral binning, also called spectral windowing, consists of reading two or more adjacent spectral pixels together in order to form a unique spectral band (Fig. 2); therefore the reading configuration of the P spectral bands can be changed to adjust the sensor spectral range to the requested SROIs. If spectral binning is done by hardware during image acquisition then it is called *on-chip binning*, otherwise when performed by software in data post-processing it is then called *off-chip binning*. Binning can also be applied in any spatial dimension but in this research we mainly focus on online spectral binning.

Imaging spectrometer acquired data can be represented using a three-dimensional structure, also referred to as *data cube*, that has M across-track pixels, L along-track pixels and P spectral pixels (Dell'Endice et al., 2007). The plane formed by the across-track and the spectral pixels, whose dimensions are $M \times P$, is called *frame*. If online spectral binning is applied then the data structure will preserve its spatial dimensions (i.e. M and L) but will have a number B of spectral bands that are less than P .

Pushbroom imaging spectrometers (a typical imaging scanner is shown in Fig. 3) are delivered to the scientific community with a standard binning pattern, consisting of B spectral channels, that fulfils the requirements of several SROIs identified during the instrument design phase. Whenever different SROIs have to be investigated and their corresponding spectral requirements (e.g. spectral resolution and SNR) fulfilled, the standard binning pattern shall be re-programmed and implemented into the instrument electronic reading board by means, for instance, of FPGA cards.

The primary interest of online spectral binning resides on the fact that spectral resolution and SNR can be adjusted, within certain limits, to specific needs and possibly increased.

The signal-to-noise ratio of an imaging spectrometer can be approximated using Eq. (1) for a single spectral band (cf., Nieke et al. (1999)):

$$SNR = \frac{S}{N} \propto \frac{\frac{L \cdot A \cdot S^2 \cdot \tau \cdot \eta \cdot \lambda \cdot \Delta \lambda \cdot t}{h \cdot c}}{\sqrt{N_{dark}^2 + N_{amp}^2 + N_{read}^2 + N_{ADC}^2 + N_{phot}^2 + N_{other}^2}} \quad (1)$$

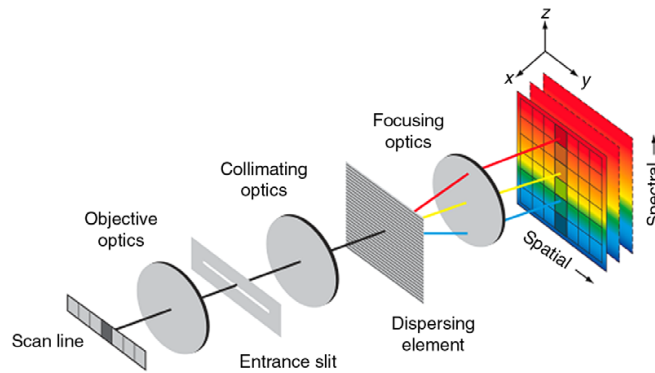


Fig. 3. Optical chain of a common pushbroom imaging spectrometer. The light back scattered from ground targets enters the pushbroom sensors through an entrance slit. The beam is therefore decomposed into its wavelength components by using a dispersive element (usually a grating or a prism). A focusing optics is then imaging the quasi-monochromatic beams onto a matrix detector (e.g. a CCD or a CMOS detector).

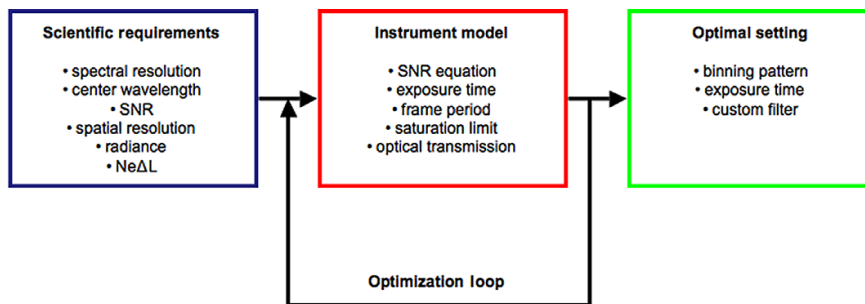


Fig. 4. BinGO logical model. A specific application is formulated in terms of spectral resolution, centre wavelengths, SNR, and other parameters; those are the input *scientific requirements* for the *Instrument model*. The instrument model is described by using its SNR equation that includes relevant sensor parameters (e.g. integration time, frame period, quantum efficiency). An optimization process generates an *optimal configuration* (e.g. binning pattern, integration time, customized filters) that allows the sensors to satisfy the demanded scientific needs.

Shortly, the main advantage of spectral binning is a noise reduction resulting in an increased SNR (Eq. (1)). In order to outline the consequences of online spectral binning on the SNR ratio, let us consider the case where R adjacent spectral channels are binned together. The signal level increases because (a) the photons (represented by the radiance term L in Eq. (1)) collected by the R bands are summed together and (b) the resulting spectral bandwidth $\Delta\lambda$ is larger. On the noise side, photon noise (N_{phot}) (proportional to the square root of the number of collected photons) and dark noise (N_{dark}) increase while amplifier noise (N_{amp}), read-out noise (N_{read}) and ADC converter noise (N_{ADC}) remain unchanged because the charge transfer/reading phase is done only once for all the R binned bands. Therefore the SNR of the binned channel gets higher at the expenses of a worse spectral resolution, i.e. a larger $\Delta\lambda$. The exposure time t can be also used to increase the SNR ratio, nevertheless without falling in detector saturation. Offline binning does not provide the same increase on SNR because every binned spectral pixel will bring along its noise contribution; it means that the noise term of Eq. (1) does not fall off. Nevertheless SNR slightly rises because of the larger bandwidth. A more detailed explanation of the optimization working flow is given in the following paragraphs and the extension to other imaging spectrometers than APEX is also discussed.

Any imaging spectrometer can be modelled into BinGO if the following parameters are known: (1) overall optical transmission (τ), (2) quantum efficiency (η), (3) number of allowed electrons in unbinned mode, (4) number of allowed electrons in binned mode, (5) allowed exposure time range, (6) read-out noise as

number of electrons, (6) amplifier noise as number of electrons, (8) ADC noise as number of electrons, (9) dark noise as number of electrons per second, (10) instrument optical aperture (A), (11) spatial sampling interval (i.e. instantaneous field of view expressed in meters), (12) centre wavelengths of the unbinned spectral axis, and (13) FWHM of the unbinned spectral bands. Additionally other noise sources might be modelled and implemented into the scheme. Once all those parameters are known Eq. (1) can be optimized. The BinGO software utility generates customized binning patterns by optimizing the SNR. An instrument model is introduced based on noise sources (i.e. dark noise, amplifier noise, read-out noise, photon noise), transmission of optics and chip quantum efficiency, unbinned configuration of the chip (only Charge Coupled Device (CCD) (Amelio et al., 1970) and Complementary Metal Oxide Semiconductor (CMOS) (Hendry and Massingham, 1992) architectures are considered here) in terms of both bandwidth and corresponding centre wavelength, and other parameters (i.e. flight altitude, field-of-view (FOV)). Such a model holds for both airborne and spaceborne imaging spectrometers (IS).

The optimization algorithm is a trade-off analysis between number of binned spectral pixels, integration time, saturation and spectral resolution: the objective is to create that spectral channel that satisfies the most the needs of the wished SROI. The problem model is presented in Fig. 4.

Users shall specify their application requirements defining (1) the radiance levels (expressed as $W/nm^2/sr$) and (2) the corresponding centre wavelengths along with (3) the corresponding

Table 1

Simulation for APEX Median Radiance requirements. Comparison between requirements (subscript *R*) and BinGO results (subscript *C*). A customized filter is necessary for bands 780 and 850 nm in order to avoid detector saturation. The $Ne\Delta L$ are expressed in $W/nm/sr/m^2$.

λ_R (nm)	λ_C (nm)	SSI_R (nm)	SSI_C (nm)	GSD_R (m)	GSD_C (m)	SNR_R	SNR_C	$Ne\Delta L_R$	$Ne\Delta L_C$	<i>F</i>
380	387.73	15	16.30	3.65	3.65	314	716.35	2.23e-4	0.98e-4	-
400	400.55	15	8.80	3.65	3.65	681	692.27	1.32e-4	1.30e-4	-
470	469.85	10	8.97	3.65	3.65	484	924.07	2.41e-4	1.27e-4	-
500	500.53	10	9.92	3.65	3.65	737	897.31	1.44e-4	1.18e-4	-
515	515.59	9	9.59	3.65	3.65	901	879.91	1.14e-4	1.17e-4	-
580	581.77	5	4.06	3.65	3.65	554	557.14	1.69e-4	1.68e-4	-
650	650.89	5	2.86	3.65	3.65	436	444.64	1.87e-4	1.83e-4	-
700	698.83	5	3.51	3.65	3.65	313	450.99	2.19e-4	1.52e-4	-
750	749.61	5	4.27	3.65	3.65	197	604.96	4.98e-4	1.63e-4	-
780	781.45	5	4.76	3.65	3.65	186	623.29	6.44e-4	1.54e-4	0.80
850	850.98	10	5.89	3.65	3.65	134	629.56	1.21e-3	1.57e-4	0.61
900	901.81	10	6.73	3.65	3.65	138	590.81	8.56e-4	1.99e-4	-
940	937.16	10	7.30	3.65	3.65	118	239.08	3.12e-4	1.54e-4	-
980	983.54	10	8.04	3.65	3.65	156	176.11	5.38e-4	4.75e-4	-
1000	1000	10	8.29	3.65	3.65	121	78.89	6.53e-4	1.01e-3	-

FWHM, (4) the desired *SNR* levels. The noise equivalent delta radiance for a specific band might be derived from the ratio between the radiance and the *SNR* at that band. The radiance levels must be converted into number of electrons in order to run the model.

The main criterion for the optimization of Eq. (1) consists of retrieving a spectrally binned band that provides the highest *SNR* with the lowest spectral sampling interval; this choice has been made considering the fact that the narrower the spectral band the higher the chance to resolve spectral features. The optimization process is performed in the following way: (a) one requirement is selected from the user list; (b) the instrument unbinned band whose centre is the closest to the one selected in (a) is also selected; (c) *SNR* is calculated for this channel at different exposure times; (d) if none of the calculated *SNR* values satisfies the requirement then additional unbinned bands are added to the band selected in (b) and a new set of *SNR* values is calculated; (e) the optimization goes then in a loop until the desired level of *SNR* has been found.

The selection of the additional bands in (d) is performed in such a way that the centre wavelength of the resulting binned band is as close as possible to the centre wavelength of the required spectral band; therefore, the bandwidth is increased taking simultaneously bands at the right and at the left of the band selected in (b).

It might happen that increasing the bandwidth of the binned band does not lead to the wished results because of detector limitation as, for instance, saturation; in this case the band combination that results in the highest *SNR* (without incurring into saturation) must be selected. High integration times cannot be always used because this will originate spatial pixels extremely rectangular; this might be sources of error for other data processing step. The optimization is done for several requirements at the same time: the best binning pattern is the one that optimizes the highest number of user requirements (Itten et al., 2008).

As has been mentioned earlier, specific spectroscopy applications have their one SROI; this would mean that two or more applications whose SROI are similar or do not bring to overlapping and counteracting requirements can be implemented at the same time into BinGO, that leading to a unique optimal binning pattern for all of them.

3. Case studies and results

In order to outline the multiple functionalities of BinGO several case studies have been analysed. The BinGO instrument model has been constructed upon APEX (Itten et al., 2008) optical and electrical parameters.

APEX (Itten et al., 2008), the ESA Airborne Prism Experiment is a flexible imaging spectrometer simulator and calibrator for existing and upcoming or planned future space missions. Operating

between 380 nm and 2500 nm with about 500 freely configurable bands (335 unbinned bands in the VNIR and 199 in the SWIR), this pushbroom scanner offers a 28° FOV and 1000 spatial pixels. Variable frame rates and integration times allow adjusting to specific flying heights, speeds and patterns. APEX allows choice of predefined or user defined programmable binning patterns, thanks to a dedicated algorithm in the FPGA card.

The case studies are the following:

- 3.1 *Standard mission*: An optimal spectral binning pattern is generated for all the APEX SROIs specified during the instrument design phase.
- 3.2 *Application driven*: A binning pattern is created for a set of spectral/*SNR* requirements of a typical vegetation application.
- 3.3 *Minimal performance*: The sensor is tuned upon a customized binning pattern in order to ensure minimal spectral resolution and *SNR* performances over the whole available spectral range.
- 3.4 *Sensor emulation*: A specific binning pattern is applied to APEX in order to reproduce the spectral bands of the OLCI instrument, embedded into the SENTINEL III satellite.

Results are shown mainly through tables; the subscript *R* stands for requirements while the *C* stands for calculated. The presented case studies have been applied only to the APEX VNIR channel.

3.1. Standard mission

The general APEX requirements are illustrated in Table 1. The optimal calculated integration time is of 38 ms.

The centre wavelength requirements (λ_R) are all met with an error less than 3%, as is shown in column 2 of Table 1. The deviation error of the spectral sampling interval (*SSI*) is always negative; it means that BinGO has generated spectral channels that satisfy the *SNR* requirement by using a narrower bandwidth, i.e. with an increased spectral resolution.

The noise equivalent delta radiance ($Ne\Delta L$) requirement is not fulfilled at 780, 850 and 1000 nm. At 780 and 850 nm the target input median radiance causes saturation in the shift registers of the CCD for 38 ms of integration time; therefore a dedicated attenuation filter is designed in order to reduce the signals of 20% and 39% respectively (i.e. the filter value is indicated in the column labelled *F*). At 1000 nm the *SNR* requirement is not satisfied (i.e. 78.89 instead of 121) because this is the last available unbinned channel in the APEX VNIR detector; the *SNR* could be matched at the expenses of spectral resolution.

A very positive error deviation has been observed for the *SNR*, meaning that the *SNR* would be higher than the requirements; this is certainly an advantage because it allows distinguishing between

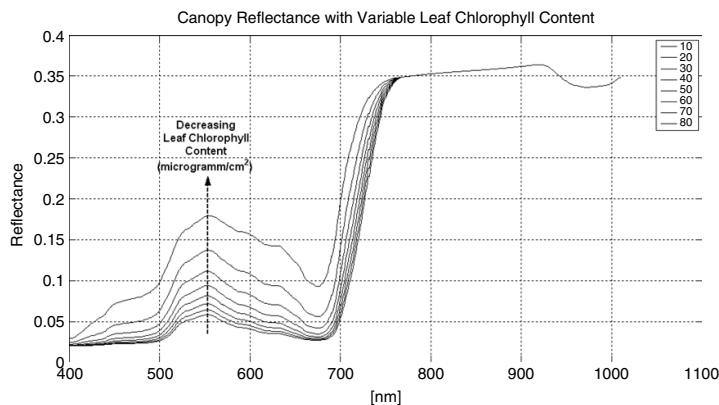


Fig. 5. Canopy Reflectances with variable Leaf Chlorophyll Content. Reflectance profiles of canopy with variable leaf chlorophyll content ($\mu\text{g}/\text{cm}^2$) are shown. Between 400 and 770 nm, the lower the chlorophyll content the higher the curve on the diagram; starting from 770 nm the leaf chlorophyll does not influence the shape of the reflectance spectra.

Table 2

Binning pattern for the APEX Median Radiance requirements. Example of generated binning pattern: the unbinned detector bands (indexes in the second and third row) are summed up together for the binned channels to be formed.

R	1	2	3	4	5	6	7	8	9	10	11	12	13	14	15
First	1	35	132	160	172	214	243	258	271	278	291	299	304	310	312
Last	34	50	140	167	178	215	243	258	271	278	291	299	304	310	312

radiance levels that might differ e.g. only for a few percent of chemical contents.

The suggested binning pattern for this scenario is indicated in Table 2; the second and the third row contain the indexes of the first and last unbinned bands that have to be summed in order to create the customized binning pattern. For instance, the binned band one will be the sum of the bands comprised between band 1 and band 34 of the unbinned configuration.

By using 38 ms as integration time, 80% of the requirements are fulfilled without applying any filtering while 93% with customized filter.

3.2. Application driven: Chlorophyll/Red-Edge

This case study illustrates how BinGO can produce customized binning patterns for specific science application. Let us assume that it is necessary to identify the chlorophyll content of a vegetation canopy with an absolute accuracy of 2 ($\mu\text{g}/\text{cm}^2$), based on the bidirectional reflectance factor (BRF) (cf., (Schaeppman-Strub et al., 2006)) in the visible–near-infrared spectral region. The goal of this simulation is to create a specific binning pattern that will allow the APEX instrument to satisfy such a request.

BRF profiles corresponding to a range of chlorophyll content between 10 $\mu\text{g}/\text{cm}^2$ and 80 $\mu\text{g}/\text{cm}^2$ are shown in Fig. 5. (The coupled models PROSPECT (Jacquemoud et al., 2006) and SAIL (Verhoef, 1984) have been used to generate those curves in step of 2 $\mu\text{g}/\text{cm}^2$ leaf chlorophyll content.) If a vegetation canopy has more than 60 $\mu\text{g}/\text{cm}^2$ chlorophyll content, it becomes very difficult to distinguish the variations in reflectance because of the saturated absorption – a well-known process; therefore only curves up to 60 $\mu\text{g}/\text{cm}^2$ of chlorophyll have been considered. The reflectance curves have been transformed into at-sensor radiance by using MODO (Schläpfer, 2001) the graphical user interface to MODTRAN (Schläpfer, 2001).

A median radiance level is retrieved averaging the highest curve (20% chlorophyll) with the lowest curve (i.e. 60% chlorophyll).

In order to run the BinGO model the application driven requirements must be created. The scientist would like to

distinguish between radiance spectra that differ of about 2 $\mu\text{g}/\text{cm}^2$ in chlorophyll content; this requirement can be formulated by imposing a minimal wavelength dependent precision uncertainty for the radiance, also called noise equivalent delta radiance ($Ne\Delta L$). To this purpose, the most relevant SROI is located between 680 and 750 nm (Fig. 5), i.e. the vegetation red edge; in order to detect the slope of the edge, 4 spectral channels have been selected in this region with a spectral resolution of 5 nm. A few additional adjacent bands with a spectral resolution of 10 nm have been also chosen. The median radiance requirement is defined by averaging the maximum radiance curve with the minimum radiance curve. Therefore, the SNR requirement is the ratio between the medium radiance level and the $Ne\Delta L$. Requirements are shown in Table 3.

For an integration time of 31 ms, the centre wavelengths as well as the spectral resolution requirements have been met with a maximum error less than 5%. The suggested binning pattern generates SNR values that are much higher than what requested from this application, which translates in a $Ne\Delta L$ one magnitude order smaller. In other words, within the limits of the applicability of a linear assumption, this instrument is potentially able to distinguish chlorophyll content with an accuracy of better than 0.2 $\mu\text{g}/\text{cm}^2$. This observation is valid for the studied value range (up to 60 ($\mu\text{g}/\text{cm}^2$)) and assuming no other disturbing effects, such as uncertainties due to an atmospheric correction.

3.3. Minimal performance

The purpose of this case study is to use BinGO in order to generate a spectral binning pattern allowing APEX to ensure a minimal level of performances for the all VNIR spectral region, given a set minimal radiance levels (L_R column in Table 4). The minimal performances consist of spectral channels of about 15 nm resolution and able of providing an SNR of at least 100.

For an integration time of 24 ms, 73% of the requirements have a SNR greater than 100; the deviation about centre wavelength is about 1% while the deviation about the spectral bandwidth is less than 15%. The latter requirements (i.e. from 900 nm to 1000 nm)

Table 3

Vegetation (Chlorophyll Content – Red Edge) requirements. Comparison between requirements (subscript *R*) and BinGO results (subscript *C*). The generated SNRs are much higher than the requested one. The $Ne\Delta L$ are expressed in $W/nm/sr/m^2$.

λ_R (nm)	λ_C (nm)	SSI_R (nm)	SSI_C (nm)	GSD_R (m)	GSD_C (m)	SNR_R	SNR_C	$Ne\Delta L_R$	$Ne\Delta L_C$	<i>F</i>
400.2	405.1	10	10.35	3.65	3.65	404	745	1e-4	6.7e-5	-
450.4	445.8	10	9.89	3.65	3.65	70	931	8e-4	6.0e-5	-
499.9	504.3	10	10.18	3.65	3.65	45	831	11e-3	5.9e-5	-
550.9	552.6	5	5.17	3.65	3.65	37	578	18e-3	1.1e-4	-
559.9	603.4	10	9.10	3.65	3.65	31	803	16e-3	6.0e-5	-
650.9	650.9	5	2.86	3.65	3.65	30	403	12e-3	8.7e-5	-
681.7	681.7	5	3.28	3.65	3.65	31	399	10e-3	7.6e-5	-
702.4	702.4	5	3.57	3.65	3.65	29	414	16e-3	1.2e-4	-
728.9	728.9	5	3.96	3.65	3.65	84	483	7e-4	1.2e-4	-
749.6	749.6	5	4.27	3.65	3.65	551	552	2e-4	1.9e-4	-

Table 4

Minimal spectral and radiometric requirements. Comparison between requirements (subscript *R*) and BinGO results (subscript *C*). In order to increase the SNR for most of the channels, the sensor shall be operated with an integration time of 85 ms. The *L* are expressed in $W/nm/sr/m^2$.

λ_R (nm)	SSI_R (nm)	L_R	SNR_R	SNR_C (24 ms)	SNR_C (85 ms)
380	15	3.78e-2	100	257	560
400	15	3.24e-2	100	345	719
470	15	2.29e-2	100	316	666
500	15	1.91e-2	100	280	602
515	15	1.78e-2	100	274	590
580	15	1.52e-2	100	262	569
650	15	9.97e-3	100	232	512
700	15	7.37e-3	100	183	421
750	15	5.05e-3	100	124	306
780	15	4.97e-3	100	128	314
850	15	4.54e-3	100	117	293
900	15	4.00e-3	100	63	161
940	15	2.74e-3	100	33	101
980	15	4.00e-3	100	22	69
1000	15	4.00e-3	100	8	25

are not met because of both the low input radiance and the low detector quantum efficiency. The SNR levels between 380 nm and 700 nm are twice higher than requested; it means that low levels of chemical constituents can be identified for specific application because of the low value $Ne\Delta L$.

In order to reach a higher SNR between 900 and 1000 nm, the integration time has been raised to 85 ms; at 980 and 1000 nm, the SNR is lower than 100 and this is mainly due to the low CCD quantum efficiency and low optical transmission in this region of the detector (between 15% and 20%). Increasing the integration time means high flight altitudes or lower platform speeds. Higher integration times could also easily bring channel saturation, especially when flying over bright targets. Therefore this parameter has to be traded-off with operational platform variables.

3.4. Sensor emulation: SENTINEL 3

In the frame of the Global Monitoring for Environment and Security programme (GMES), ESA is undertaking the development of the Sentinel-3 (Nieke et al., 2008), a polar orbiting satellite system for the provision of operational marine and land monitoring services. These services include products in the area of land and ocean colour measurements, sea and land surface temperature, vegetation products, sea and land surface topography. The Sentinel-3 spacecraft will observe the Earth from a sun-synchronous orbit with a mean altitude of 815 km. The launch of the first platform is expected for 2012. The lifetime of one platform is 7.5 years in-orbit aiming to an overall service duration of 20 years with several satellites. The satellite will carry optical and infrared instruments and a topography package routinely observing ocean and land over long term and in continuous fashion with a consistent quality and

a very high level of availability. The Ocean and Land Colour Instrument (OLCI) is a pushbroom instrument with 5 camera modules sharing the field-of-view (FOV); each camera has an optical grating to provide the minimum baseline of 16 spectral bands required by the mission together with the potential for optional bands for improved atmospheric corrections. A set of 21 spectral requirements is presented in Table 5.

The BinGO results are shown in Table 5 for an optimal integration time of 51 ms. The centre wavelengths deviation is less than 5% for 92% of the requirements. The OLCI band at 1020 cannot be granted because the APEX VNIR channel goes up to 1000 nm. The requirements on the Spectral Sampling Interval are met for 47% of the selected bands; this is because (a) saturation occurs if adjacent bands are binned and used with 55 ms of integration time (b) the APEX unbinned bands are larger than the requirement, or (c) the OLCI required bands are much smaller than a single unbinned APEX band. In order to satisfy more OLCI spectral requirements, additional binning can be applied in post-processing. The spatial sampling interval of APEX is much smaller than that of OLCI; therefore the SNR requirements, not mentioned in this simulation, can be met by binning the APEX across-track and along-track pixels in post-processing.

4. Discussion

Spectral binning pattern can be applied to imaging spectrometers in order to modify spectral resolution and SNR. The read-out process of CCD and CMOS detectors can be re-programmed by means of an FPGA card in such a way that the group of adjacent spectral lines are summed up and read out at once. Online spectral binning usually leads to a higher SNR at the expenses of spectral resolution; nevertheless, SNR can be increased online also by using a longer exposure time but, in this case, detector saturation might occur. In fact, the well depth of the detector shift registers is a constraint to the number of spectral rows that can be eventually binned.

The BinGO software utility optimizes the SNR of every spectral band by trading off between spectral resolution and exposure time. Theoretically, the ideal result of such an optimization would be the narrowest bandwidth with the highest SNR; a higher spectral resolution is more favourable in order to identify target details. On the other side, some SROIs would be better sensed if the instrument could provide as much SNR as possible. Nevertheless, the algorithm tries to minimize the spectral bandwidth; a high number of binned bands would mean a lower spectral resolution. On the other side, the exposure time cannot be increased beyond a certain limit because of detector saturation and because a long integration time would generate very rectangular pixels when the platform moves. Nevertheless, the resulting SNR of the binned band depends as well on both (1) the quantum efficiency and (2) the optical transmission profiles.

Table 5

OLCI/SENTINEL III Bands emulation. Comparison between requirements (subscript R) and BinGO results (subscript C). The band at 764.38 nm cannot be reproduced because APEX does not have such a small band in this spectral region.

REQ	λ_R (nm)	λ_C (nm)	$\Delta\lambda$ (%)	SSI_R (nm)	SSI_C (nm)	ΔSSI (%)
1	400	400.49	0.12	15	14.82	-1.21
2	412.5	417.33	1.17	10	10.31	3.14
3	442.5	442.97	0.11	10	10.47	4.75
4	490	485.79	-0.86	10	10.07	0.73
5	510	505.64	-0.86	10	10.27	2.69
6	560	555.29	-0.84	10	10.49	4.99
7	620	622.63	0.42	10	10.02	0.21
8	665	665.78	0.12	10	3.05	-69.40
9	681.25	681.73	0.07	7.5	3.27	-56.30
10	708.75	709.69	0.13	10	3.67	-63.26
11	753.75	753.95	0.03	7.5	4.34	-42.17
12	761.25	762.83	0.21	2.5	4.47	78.97
13	764.38	-	-	3.75	-	-
14	773.75	771.99	-0.23	5	4.62	-7.65
15	781.25	783.87	0.34	10	9.61	-3.90
16	862.5	863.06	0.07	15	6.09	-59.39
17	872.5	875.55	0.35	5	6.29	25.92
18	885	881.95	-0.34	10	6.40	-35.99
19	900	901.81	0.20	10	6.73	-32.72
20	940	937.16	-0.30	20	7.30	-63.48
21	1020	983.79	-3.55	40	40.21	-0.52

There are cases where the BinGO optimization process does not lead to satisfying results; therefore alternative solutions must be investigated. If, for instance, the target emitted radiance is too high to cause an early saturation in the sensor, then an *ad hoc* density filter can be designed and implemented into the system in order to reach a higher integration time; this solution is cost expensive and requires the scanner to be built for such an eventuality. When the system parameters can be varied only within a limited range then an offline spectral binning pattern can be applied in post-processing of the data; the increase in SNR is low compared to the one that can be obtained by applying online binning.

5. Conclusion

This study focused on the optimization of programmable imaging spectrometers for specific spectral regions of interest (SROIs) using the BinGO software. Results showed the potential and flexibility of programmable spectrometers to improve the performance of scientific applications as well as to define and simulate various optical spectral band configurations. BinGO has been applied to several case studies in order to demonstrate the use of spectral binning: the first case study shows how a default and generic binning pattern can be generated for a standard imaging spectrometer; in the second one a customized binning pattern has been created for a specific science application, i.e. the discrimination of different levels of leaf chlorophyll content within a vegetation canopy; in the third scenario the possibility of generating a spectral binning pattern that lets the instrument ensure a minimal level of performance over its full spectral range in terms of SNR (i.e. about 100) and spectral bandwidth (i.e. about 15 nm) has been investigated; the last case shows how BinGO can re-program the bands of imaging spectrometers in order to simulate the bands of another sensor and allow inter-sensors comparison.

BinGO bases its optimization process on online spectral binning. The continuation of the study will include the possibility for offline binning patterns in both the spectral and spatial dimensions. The BinGO code, implemented supporting the APEX spectrometer, is available for research institutions and universities. BinGO can be easily customized for imaging spectrometers different from APEX if all instrument parameters as specified in the method section, are known. The routines are written in MATLAB and a simple Graphical User Interface (GUI) is also available.

Acknowledgements

This work has been supported by ESA/ESTEC contract No. 14906/00/NL/DC. We acknowledge F. Seidel for supporting MODTRAN calculations. O. Mykhailova is acknowledged for commenting on an early draft of the manuscript. We thank the anonymous reviewers for helpful suggestions and comments.

References

Amelio, G., Tompsett, M., Smith, G., 1970. Experimental verification of the charge coupled device concept. *Bell System Technical Journal* 49 (4), 593–600.

Baarstad, I., L. ke, T., Kaspersen, P., 2005. ASI – A new airborne hyperspectral imager. In: *Proceedings of the 4th EARSeL Workshop on Imaging Spectroscopy*, Warsaw, Poland.

Babey, S.K., Anger, C.D., 1993. Compact airborne spectrographic imager (CASI): A progress review. In: *Imaging Spectrometry of the Terrestrial Environment. Proceedings of the SPIE 1937*, Orlando, FL, USA, pp. 152–163.

Barnsley, M.J., Settle, J.J., Cutter, M.A., Lobb, D.R., Teston, F., 2004. The PROBA/CHRIS mission: A low-cost smallsat for hyperspectral multiangle observations of the earth surface and atmosphere. *IEEE Transactions on Geoscience and Remote Sensing* 42 (7), 1512–1520.

Clevers, J.G.P.W., Kooistra, L., Schaepman, M.E., 2008. Using spectral information from the NIR water absorption features for the retrieval of canopy water content. *International Journal of Applied Earth Observation and Geoinformation* 10 (3), 388–397.

Davis, C., et al., 2002. Ocean PHILLS hyperspectral imager: Design, characterization, and calibration. *Optics Express* 10 (4), 210–221.

Dell'Endice, F., Nieke, J., Schläpfer, D., Itten, K.I., 2007. Scene-based method for spatial misregistration detection in hyperspectral imagery. *Applied Optics* 46 (15), 2803–2816.

Delwart, S., et al., 2007. MERIS in-flight spectral calibration. *International Journal of Remote Sensing* 28 (3), 479–496.

Folkman, M.A., Pearlman, J., Liao, L.B., Jarecke, P.J., 2001. EO-1/Hyperion hyperspectral imager design, development, characterization, and calibration. In: William, L.S., Yoshifumi, Y. (Eds.), *Proceedings of the SPIE 4151*, pp. 40–51.

Gomez, R.B., 2002. Hyperspectral imaging: A useful technology for transportation analysis. *Optical Engineering* 41 (9), 2137–2143.

Green, R.O., 1998. Spectral calibration requirement for Earth-looking imaging spectrometers in the solar-reflected spectrum. *Applied Optics* 37 (4), 683–690.

Hendry, D.C., Massingham, J.W., 1992. CMOS/ECL circuits with reduced power dissipation. *Technology and Application of Combined Bi-Polar and CMOS Semiconductor Processes, IEEE colloquium*, pp. 5/1–5/5.

Itten, K.I., et al., 2008. APEX – The Hyperspectral ESA Airborne Prism Experiment. *Sensors* 8 (1), 1–25.

Jacquemoud, S., et al., 2006. PROSPECT+SAIL: 15 Years of Use for Land Surface Characterization. In: *Proceedings of the International Geoscience and Remote Sensing Symposium, IGARSS 2006*, pp. 1992–1995.

Kuusilinnä, K., Hamalainen, T., Saarinen, J., 1999. Field programmable gate array-based PCI interface for a coprocessor system. *Microprocessors and Microsystems* 22 (7), 373–388.

Mouroulis, P., et al., 2004. Trade studies in multi/hyperspectral imaging systems, final report.

- Nieke, J., Frerick, J., Stroede, J., Mavrocordatos, C., Berruti, B., 2008. Status of the optical payload and processor development of ESA's Sentinel 3 mission. In: Proceedings of the Geoscience and Remote Sensing Symposium, IGARSS 2008, pp. 427–430.
- Nieke, J., Solbrig, M., Neumann, A., 1999. Noise contributions for imaging spectrometers. *Applied Optics* 38 (24), 5191–5194.
- Rast, M., Bezy, J.L., Bruzzi, S., 1999. The ESA medium resolution imaging spectrometer MERIS a review of the instrument and its mission. *International Journal of Remote Sensing* 20 (9), 1681–1702.
- Schaepman-Strub, G., Schaepman, M.E., Painter, T.H., Dangel, S., Martonchik, J.V., 2006. Reflectance quantities in optical remote sensing: Definitions and case studies. *Remote Sensing of Environment* 103 (1), 27–42.
- Schläpfer, D., 2001. MODO: An interface to MODTRAN for the simulation imaging spectrometry at-sensor signals. In: Proceedings of the 10th annual JPL airborne earth science workshop, JPL, Pasadena, USA, pp. 343–350.
- Schläpfer, D., Schaepman, M., 2002. Modeling the noise equivalent radiance requirements of imaging spectrometers based on scientific applications. *Applied Optics* 41 (27), 5691–5701.
- Ustin, S.L., et al., 2006. Retrieval of quantitative and qualitative information about plant pigment systems from high resolution spectroscopy. In: Proceedings of the Geoscience and Remote Sensing Symposium, IGARSS 2006, pp. 1996–1999.
- Verhoef, W., 1984. Light scattering by leaf layers with application to canopy reflectance modeling: The SAIL model. *Remote Sensing of Environment* 16 (2), 125–141.

Synopsis

7 Synopsis

7.1 Main findings

The main objective of the thesis was to provide calibration and characterization techniques that reduce the measurement uncertainty of pushbroom imaging spectrometers. In fact, low measurement uncertainty leads to the generation of selected reliable imaging spectroscopy products. The general research questions were outlined in §1 and discussed in more detail in §3-§6, where possible answers were given through the annexed publications

The main findings of each publication in this dissertation are summarized in this chapter. The results of every proposed technique are then combined to calculate an updated measurement uncertainty budget. Possible improvements to every single research question as well as to the general measurement uncertainty problem are given.

More specifically, the publications dealt with the following issues:

1. Uniformity of imaging spectrometry data products. The research questions discussed in this publication are:
 - a. Which impact do instrument factors have on the quality of imaging spectroscopy measurements and products?
 - b. Is it possible to quantify the overall uncertainty of imaging spectroscopy products (see §3)?
2. Scene-based method for spatial misregistration detection in imaging spectrometers. The research question discussed in this publications is:
 - a. How can data non-uniformities be identified directly from the measured data? Is it possible to implement correction schemes based on this information (see §4)?
3. Laboratory calibration and characterization strategy. The research questions developed in the conference proceeding and the first-authored publications are:
 - a. How can the calibration and characterization process reduce the uncertainty of imaging spectroscopy products (see §5)?
 - b. How can an imaging spectrometer be calibrated such that the measurement quality/fidelity is improved?
 - c. ? How can calibration and characterization techniques reduce the measurement uncertainty?
4. Improving radiometry of imaging spectrometers by using programmable spectral regions of interest. The research question discussed in this publication is:
 - a. How can high quality products be generated by optimizing the data acquisition for specific spectral regions of interest (see §6)?

The main findings related to questions above are summarized in the following sections.

7.1.1 Uniformity of Imaging Spectrometry Data Products

The publication §3 aimed at estimating the uncertainty budget in imaging spectroscopy data and product. It was shown (see §3) how the acquired raw data and related retrieved products are affected by high acquisition and processing errors, as well as how correction schemes might reduce their impact. Nevertheless, the residual intrinsic error after corrective measures can still be as high as 10% (Nieke et al. 2008) and compromise the product quality, if alternative calibration/characterization strategies or assimilation models are not used. Therefore, it was recommended to adopt calibration and characterization strategies that tackle instrument non-uniformities, detect them, measure them, and provide the basis for data correction. However, calibration and characterization uncertainties related to other phenomena (e.g. radiometry, polarization, straylight) were not considered in the overall budget. Considering these additional calibration and characterization procedures, as well as uncertainties introduced from data processing schemes, the total uncertainty can be as high as 27% (see §1, Table 2). Thus, improved calibration and characterization strategies should be adopted, as well as detection algorithms for non-uniformities.

7.1.2 Scene-based method for spatial misregistration detection in hyperspectral imagery

The publication in §3 suggested that non-uniformities of pushbroom imaging spectrometers have to be characterized in more precise manner. The publication in §4 describes a scene-based technique for the detection of spatial misregistration, a special kind of non-uniformity.

Spatial misregistration was detected by means of an edge-detection algorithm and compared with a model established around the root causes of this effect, i.e. optical aberrations and misalignments of components. The method has been tested on several pushbroom imaging spectrometers (PHILLS, HYPERION, CASI-3, HYSPEX, AISA, and CHRIS) and one whiskbroom (AVIRIS). The processor identified edges on the spatial domain using a high contrast band and measured the relative angular shift of the edge in the various spectral channels (Dell'Endice et al. 2007b).

It was concluded that spatial misregistration (or keystone) is the result of a quadratic optical aberration and misalignments between the system optical and mechanical components (e.g. entrance slit, lenses, mirrors, prisms).

It has been demonstrated that:

- Keystone varies over detector focal plane in a quadratic manner with respect to band number and in a linear way with respect to across-track pixels, i.e. FOV of the sensor.
- Misalignments can cause translations of the spatial-misregistration profile.
- Whiskbroom scanners are spatial-misregistration free because one spatial pixel is acquired at time.
- Correction schemes may be implemented based on the results of scene-based procedure.

Since this method is based on edge detection, the presence of relevant spatial features in the sensed image is of prime importance for the success of the algorithm. How can non-uniformities be measured if edges are not recognizable in the sensed scene? Laboratory calibration/characterization can solve these issues and additionally serves as the most accurate approach to tackle the data quality problem. The results of this methodology are discussed in the next paragraph.

7.1.3 Laboratory calibration and characterization strategy

Laboratory calibration/characterization is the most accurate technique for quantifying the distribution of non-uniformities and assessing the measurement acquisition error budget more precisely. This paragraph describes the advantages of the laboratory calibration and characterization approach discussed in §5.

A software/hardware utility, called Calibration Test Master (CTM) (Dell'Endice et al. 2007a), was implemented and serves at the interface between APEX and the Calibration Home Base (CHB) (see Figure 12), which is composed of a suite of highly automated equipment.

It was demonstrated that the CTM (Dell'Endice et al. 2007a) was able to (1) independently control the laboratory instrumentation (e.g. monochromators, integrating spheres, collimator), (2) acquire measurements and (3) produce calibration/characterization results, which were stored in a logical data structure called *calibration cube*. The CTM and the non-classical calibration approach were extensively tested on the APEX instrument in several occasions, and it was demonstrated that a full characterization and calibration campaign can be performed in less than 10 days including data processing.



Figure 12: APEX campaign in the CHB (DLR, Munich).

It was shown that the automated laboratory calibration approach can considerably increase non-uniformities characterization of pushbroom sensors, therefore significantly reducing the uncertainty of the calibration process (Dell'Endice et al. 2009a). By virtue of the automatic measurement and processing chain, several detector elements could be characterized and, therefore, a detailed map of non-uniformities could be created and used for correction schemes. The proposed laboratory

calibration methodology also faced the trade-off optimization process between instrument parameters (e.g. integration time, capacities) and light stimuli setup (e.g. power, source stability, custom neutral density filters): a proper tuning is extremely important for acquiring reliable measurement and retrieving meaningful results. The non-uniformities affecting the APEX instrument were documented in (Dell'Endice et al. 2009a). Because of the calibration strategy used and because of the well-certified laboratory equipment (e.g. accuracy, repeatability error, instability), the following calibration quality figures were achieved for the APEX imaging spectrometer:

- Relative radiometric accuracy is better than 3%
- Absolute radiometric accuracy is better than 2%
- Spectral accuracy is better than 0.1 nm
- Geometric accuracy is better than 0.0028°

This result has a direct impact on the overall data uncertainty budget because it implies that laboratory calibration/characterization allows a proper estimation of data non-uniformities and their correction.

Optimization of the instrument settings was a critical task to be performed in the laboratory environment. However, the results of an optimization of the instrument settings for image acquisition, i.e. flight mode, are discussed in the next paragraph.

7.1.4 Improving radiometry of imaging spectrometers by using programmable spectral regions of interest

The optimization of sensor acquisition parameters can increase the information retrieval in specific spectral regions of interest. The application of such a process during image acquisition were described in §6 and summarized here.

It was demonstrated how the radiometric and spectral resolution of an imaging spectrometer can be modified to fulfill the requirements of spectral regions of interest. Online binning can be efficiently used (Dell'Endice et al. 2009b) to re-program the detector spectral configuration for specific scientific mission. It was shown how online spectral binning, applied to sensors equipped with FPGA technology, can allow (a) optimization of spectral performance for specific applications, (b) spectral emulation of other instruments and (c) the design of new multispectral or imaging spectrometer airborne/spaceborne missions.

The APEX unbinned spectral configuration was considered the baseline, and an optimization algorithm was used to generate specific spectral binning patterns for several case studies.

However, the optimization process included several parameters and the sensor electrical properties constrained the upper limit of the process. Specifically, saturation, noise sources, and bandwidth can limit the improvement that such a method can bring; in fact, these parameters can limit the expected SNR levels.

7.2 Discussion and conclusions

The main findings of this work have been outlined in the previous paragraph. Discussion and conclusions on the result is given in this paragraph.

Research question: *Uniformity of imaging spectrometry data products.*

The first research question aimed at quantifying the uniformity of imaging spectroscopy products. Therefore, the data quality problem was described in §1.4 and it was concluded (see §1.5) that imaging spectroscopy data are affected by an intrinsic measurement uncertainty of about 27%. As calibration and characterization related issues accounted for 25% of this budget, it was suggested that optimization of laboratory techniques, developed to characterize the instrument non-uniformities, can considerably reduce this error.

The main objective of this thesis was then fixed: implementing calibration and characterization techniques aiming at reducing the measurement uncertainty from 25% to 5%. Measurement uncertainty was the focus throughout the dissertation while data processing uncertainty was considered only when related to algorithms based on calibration and characterization parameters (i.e. atmospheric and geometric correction have not been discussed here). Environmental disturbances contribute to the acquisition uncertainty as well but their nature does not allow a systematic approach involving modelling and subsequent reduction of their uncertainty contribution.

Starting from the estimation of the uncertainty budget (Nieke et al. 2008) (see §3), a series of scene-based (Dell'Endice et al. 2007b) and laboratory (Dell'Endice et al. 2009a) techniques were proposed, which were the focus of two research questions: (a) quantifying non-uniformities by means of scene-based methodologies and (b) quantifying and correcting for non-uniformities by means of laboratory equipment.

Research question: *Scene-based method for spatial misregistration detection in imaging spectrometers*

Scene-based assessment of non-uniformities is useful whenever laboratory measurements of the system properties are not feasible (e.g. for spaceborne sensors after launch). However, the accuracy of these methods is not high (approx. 5%), because of the absence of absolute references. Nevertheless, it remains a valid approach in defining a qualitative measure of certain system non-uniformities (e.g. smile and spatial misregistration). The lack of an absolute reference implies that correction schemes cannot be easily implemented because they suffer from a bias effect. However, effort can be put into defining the most suitable reference, and the intrinsic error of such a methodology can be reduced.

Research question: *Laboratory calibration and characterization strategy for more accurate non-uniformities characterization.*

Instead, laboratory calibration and characterization methodologies offer a higher degree of accuracy and lead to the proper assessment of system non-uniformities. More particularly, a measurement strategy focusing on the quantitative assessment of non-uniformities distributions over the focal plan can bring the uncertainty budget from 25% to less than 5%.

It was shown (Dell'Endice et al. 2009a) how this goal was achieved for the APEX instrument. Nevertheless, the achievement of such an objective highly depends on (1) the quality of the laboratory

instrumentation and (2) the optimization of sensor and laboratory equipment parameters.

Laboratory instrumentation for the calibration and characterization of imaging spectrometers between 250 nm and 2500 nm has to exhibit a high degree of reliability, stability and error reproducibility error across the spectral range. The characterization of system non-uniformities at subpixel level can be attained only if the laboratory instrumentation and the measurement procedure together generate a measurement error lower than the desired measurement accuracy. Light sources need to provide an intensity level that can be measured from the system with an SNR level that allows separation of the instrument noise from the lamp noise. For example, this could not be done for APEX between 380 nm and 430 nm, and between 2250 nm and 2500 nm. The measurement of the APEX properties in these regions was instead made possible by adopting customized system configurations (e.g. high integration times, spectral binning patterns). Improvement of the calibration facility might include (1) the use of different light sources, such as white LED, Hg or Xe-Hg lamps, or (2) the implementation of customized neutral density filters.

Another issue concerns the traceability of the laboratory equipment to primary standards. If high absolute radiometric and spectral calibration accuracies are needed then it should be verified that laboratory instrumentation has a traceability error that is at least half of the calibration goal. This problem was faced during APEX calibration/characterization, for instance, when the absolute radiometric accuracy between 2250 nm and 2500 nm in the SWIR channel had to be validated. In fact, the traceability error of the integrating sphere (i.e. the secondary standard) was higher than 12% in this spectral region. The calibration objective of 3% could not be achieved here because of such large error (e.g. weak intensity of the light source). This implies that the APEX radiometric performance could not be verified between 2250 and 2500 nm and this further justifies the use of a different light source in future laboratory campaign.

The radiometric calibration of image data must ensure the proper integration of calibration/characterization information into the measured spectra. An imaging flight, either airborne or spaceborne, might induce deviations in the instrument properties because of environmental disturbances (e.g. temperature, pressure, vibrations). Furthermore, the system behaviour also changes with time because of degradation issues. This implies that laboratory calibration/characterization data only cannot guarantee the spectral consistency of the measured spectra. Hence, an additional approach must be implemented in order to monitor and to identify the drifts in the instrument properties. In fact, the radiometric calibration of APEX image data was conceived such that most calibration/characterization performance coefficients are retrieved from a number of independent sources. First, a partial laboratory calibration/characterization campaign is performed after a flight season in order to assess the permanent shifts of the instrument properties, mostly due to degradation issues. Second, an on-board characterization facility (IFC) monitors the influence of environmental parameters on the instrument properties during the imaging flight itself and generates stability coefficients.

Additionally, images can be directly used to identify artefacts and data inconsistencies. All these data are merged together into a unique calibration cube that represents the best estimate of the calibration and characterization coefficients such that consistent radiometrically corrected spectra can be retrieved. Hence, the calibration/characterization data of a flight campaign (i.e. pre- and post-flight laboratory, IFC, and scene-based coefficients) are fed into an assimilation scheme whose goal is (1) to store the instrument performance at different times and (2) to predict calibration/characterization coefficients for the future campaign. It must be noted that an instrument refurbishment most likely will cause an

abrupt change in the instrument properties, possibly requiring a new assimilation scheme shall be started from that point onwards.

The quality data problem was quantified in terms of required accuracies and a calibration/characterization strategy was proposed such that low measurement uncertainties can be reached. Such a concept requires the use of automated procedures that demand a complex interface between the sensor and the laboratory equipment. This effort is needed when spectral high consistency of the imaging spectroscopy data needs to be guaranteed. Other laboratory calibration/characterization approaches (Chrien et al. 1990; Chrien et al. 1994; Barnes et al. 1998; Folkman et al. 2001; Davis et al. 2002; Murakami et al. 2003; Winter et al. 2003; Kohler et al. 2004; White et al. 2004) are valid alternatives that guarantee an acceptable average performance. However, they cannot be considered representative of the pixel-level behavior, in particular for pushbroom imaging spectrometer. For instance, a precise smile characterization is crucial for the success of algorithms that correlate the spectral position of an absorption feature to other biochemical parameters of the target. In order to correctly quantify the required calibration/characterization effort, one needs to (1) quantify the envisaged product accuracies and uncertainties, and (2) derive the corresponding calibration/characterization requirements, also taking into account the interferences of other data correction/processing schemes (e.g. atmospheric correction, geometric correction). This inverse approach will ultimately fill the gap between sensor development and product generation. However, imaging spectroscopy data serve several research communities at the same time (e.g. vegetation studies, limnology studies, atmospheric studies) and the aforementioned process shall be carried out for the most demanding applications of every domain. This multiple sensitivity analysis will then lead to a quantification of the calibration/characterization effort such that all domains are covered.

Optimization of sensor and calibration equipment settings is a fundamental step in the proper assessment of instrument properties in the laboratory environment. However, optimization of sensor settings may help enhancing the performance during imaging flights.

Research question: ***Improving radiometry of imaging spectrometers by using programmable spectral regions of interest***

In fact, the possibility of improving radiometry of imaging spectrometers by using programmable spectral regions of interest was investigated.

In §6, it was demonstrated how on-chip spectral binning can optimize the acquisition performance of the sensor in specific spectral regions of interest to ensure application-driven SNR levels. The optimization of the sensor acquisition parameters can be accomplished using the spectral, radiometric, and geometric requirements of the targets. This approach might be most useful in defining the best acquisition configurations for specific applications, but it can be problematic if the optical properties of targets are completely unknown or only partly known. In the latter cases, the optimal approach would be to ensure a reasonable level of SNR accompanied by the highest spectral resolution. The detector technology (e.g. quantum efficiency, optical transmissivity) can further limit the number of optimization possibilities and this cannot be neglected when developing a sensor model.

Generally, the proper understanding of the sensor optical performances provides scientific users with the optimal system background needed to correctly interpret imaging spectroscopy results.

7.2.1 Updated measurement uncertainty budget

The series of calibration and characterization techniques proposed in this dissertation aimed at reducing the measurement uncertainty of pushbroom imaging spectrometers. Acquisition uncertainty is reduced also by using programmable spectral regions, i.e. on-chip binning because SNR and spectral resolution are specialized for particular applications.

In summary, the following results were achieved:

1. A scene-based method for the detection of spatial misregistration. The assessment of the spatial misregistration distribution allows the implementation of a correction scheme that can be applied to image data.
2. A laboratory calibration and characterization approach aiming at quantifying the measurement uncertainty. A radiometric uncertainty of less than 3% was achieved for large part of the APEX spectral region.
3. An optimization of instrument parameters for enhancing the acquisition performances during the imaging flight. Higher level of SNR and higher spectral resolution allow a better retrieval of imaging spectroscopy products.

In §1, the intrinsic sensor acquisition error budget due to calibration and data non-uniformity factors was estimated around 25%. The improvements due to the proposed techniques, whose results are listed above, reduce this error to less than 5%, how it is depicted in Figure 13. This result suggests that instrument properties of imaging spectrometers have to be assessed and investigated at pixel level. In other words, every pixel should be considered as an independent spectroradiometer. The bi-dimensional technology of pushbroom imaging spectrometers causes cross contamination between neighbouring detector pixels. However, when the optical components are integrated with electronic components then a series of defect, artefacts, and anomalies appear and this may give pixels an independent behaviour. In other words, the response function of every pixel might differ from the ones of adjacent pixels. These anomalies need to be properly identified during calibration and characterization because this increases the measurement accuracy and prevents the retrieval of physically meaningless imaging spectroscopy products.

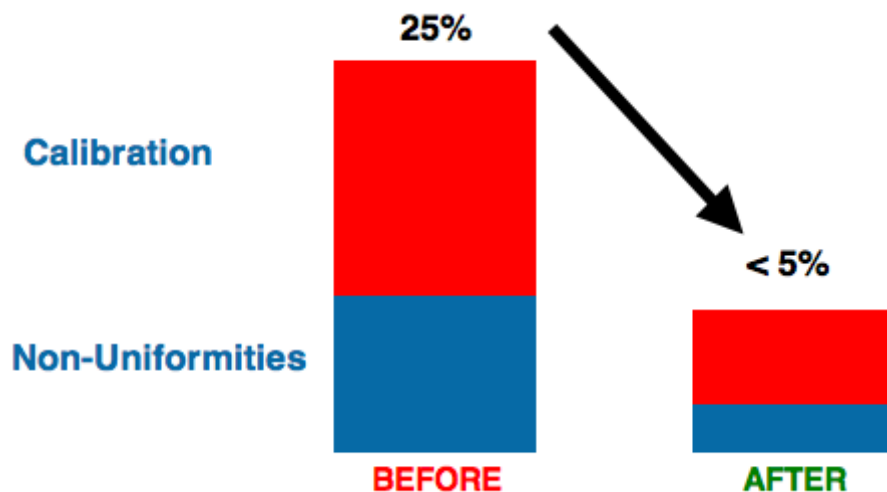


Figure 13: Updated measurement uncertainty budget.

7.3 Future perspectives

The main findings of this dissertation have been presented and discussed in the previous sections of this chapter. A series of characterization/calibration as well as optimization techniques have been proposed such that the measurement uncertainty can be reduced to 5%. However, specific applications may require higher accuracy.

An overview of possible improvements to the research questions that have been addressed in this work and to the general development of the data quality problem is given hereinafter. These improvements may ultimately lead to a measurement uncertainty of about 3%.

7.3.1 Sensitivity analysis and calibration with respect to environmental parameters

Environmental disturbances are generally unpredictable. Some can be measured to a certain extent but not completely. This implies that the significance of such variables on data acquisition and data quality is an intricate and problematic question. Models as well as specific observation approaches need to be developed and tested such that the environmental influence on uncertainty can be determined, and a correction scheme might be implemented.

Alternatively, calibration and characterization with respect to environmental disturbances can be performed in laboratory. However, this approach maybe expensive (e.g. a thermal chamber would be needed for assessing the influence of temperature on the calibration coefficients) but may lead to improvement of the measurement accuracy.

7.3.2 Sensitivity analysis of data processing schemes

Imaging spectroscopy data undergo several data processing steps, from acquisition to generation of quantitative products. Examples include raw data segregation, calibration to obtain radiances, calibration to obtain reflectances, geometric correction, and retrieval algorithms. Each of these processing schemes is associated with uncertainties and assumptions, and errors are systematically introduced into the final products. Customized error propagation models would be needed to quantify the sensitivity of the imaging spectroscopy measurements to the data processing. Spectral consistency of the data must be preserved, and the mechanisms preventing the realization of such a goal must be understood and ultimately eliminated. For example, a detailed sensitivity analysis on atmospheric modelling variables might reveal unknown mechanisms and dependencies between parameters. Spatial distributions of atmospheric parameters need to be coupled with the atmospheric correction models. This possible input might suggest new calibration approaches and precise measurement of quantities that otherwise need to be predicted or assumed as being uniformly distributed over the region of interest.

7.3.3 Quality flags

Imaging spectroscopy data contain a huge volume of information that can serve numerous remote sensing communities in the form of specific products. As such, quality flags should be routinely provided, as a way of giving users important information about the spectral region of interest. Defining a quality flag for a distinct spectral band should include indications about the radiometric, spectral, and geometric measurement uncertainties. A quality flag could indicate the suitability of a spectral band for specific applications. However, quality is an application-specific quantity: some products will tolerate spectral measurement with higher uncertainty than others. Quality flags might include

also recommendations about sensor anomalies and any kind of metadata that can be relevant to the user.

7.3.4 On-chip binning

Spectral binning for spectral regions of interest represents one of the latest applications in imaging spectroscopy data processing. The upcoming imaging spectroscopy instrumentation should be implemented with on-chip binning capabilities. The online application of binning patterns can considerably increase the SNR level and ensure a better discrimination and measurement of quantitative remote sensing variables. The development of online smart binning algorithms might support specific applications, such as sensors network, change detection, or in-flight optimization of the data acquisition processes. Given a series of tuneable electrical system parameters and relevant sample measurements, an instrument should be capable of optimizing its observational configuration for a specific target.

7.3.5 Validation of spectral measurements

The validation of the spectral measurements is a pre-requisite for the assessment of the product quality. Laboratory calibration and characterization provide the most accurate means of assessing the performance of imaging spectrometers. However, as described earlier in §1.3, the in-flight image acquisition is influenced by a series of disturbances that introduce additional uncertainty. In order to validate the data with respect to ground-truths, the in-flight imagery data need to be atmospherically corrected. Problems may arise in defining the ground-truths for targets that are not homogenous and have a three-dimensional structure (e.g. forest, cities). These targets may have a heterogeneous spectral and spatial behaviour that is difficult to model.

Effort is needed in implementing in-field measurement procedures that could lead to the generation of reference pixels representative of in-flight image pixels, in terms of radiometric, spectral and geometric properties.

7.3.6 Assimilation techniques for radiometric calibration

Performing a laboratory calibration and characterization experiment (Dell'Endice et al. 2009a) before a flight campaign is not sufficient for defining the best estimates of (1) the radiometric coefficients used in transforming the measured raw spectra in radiance values, and (2) the centre wavelengths of the spectral channels. The flight environment introduces disturbances that cannot be evaluated in laboratory, in particular if they temporarily modify the instrument performance (e.g. effects of pressure, temperature, vibrations). Spectral, radiometric and geometric shifts might then occur, compromising the data quality.

Consequently, the most appropriate calibration coefficients (necessary for the radiometric calibration) may differ from the ones determined in laboratory. Thus, additional information sources are required to evaluate such drift. An assimilation and prediction model is being developed for the APEX imaging spectrometer (Itten et al. 2008) and it consists of feeding a prediction model with instrument performance data generated through:

1. Laboratory experiments carried out at different times (e.g. before and after a flight campaign).
2. Flight stability data provided by means of an on board characterization lamp (D'Odorico et al. 2009).
3. Scene-based assessment of spatial, spectral, and geometric non-uniformities (Dell'Endice et al. 2007b).

4. Correlation between acquired images and meta-data (e.g. temperature of the sensors, differential pressure, power supply instabilities).

The various aspects of the proposed model aim at reducing the data uncertainties caused by flight conditions and thus at further improving the calibration of the APEX data. All these steps are carried out in the processing and archiving facility (Hueni et al. 2008). These techniques might additionally indicate instrument configuration parameters for the optimal sensing of spectral regions of interest (Dell'Endice et al. 2009c).

References

References

- Amelio, G., Tompsett, M., & Smith, G. (1970). Experimental verification of the charge coupled device concept. *Bell Syst. Tech. Journal*, 79, 593 - 600
- Ångström, A. (1930). On the Atmospheric Transmission of Sun Radiation. II. *Geografiska Annaler*, 12, 130-159
- Asner, G.P., Jones, M.O., Martin, R.E., Knapp, D.E., & Hughes, R.F. (2008). Remote sensing of native and invasive species in Hawaiian forests. *Remote Sensing of Environment*, 112, 1912-1926
- Asner, G.P., & Martin, R.E. (2008). Spectral and chemical analysis of tropical forests: Scaling from leaf to canopy levels. *Remote Sensing of Environment*, 112, 3958-3970
- Asner, G.P., Wessman, C.A., Schimel, D.S., & Archer, S. (1998). Variability in Leaf and Litter Optical Properties: Implications for BRDF Model Inversions Using AVHRR, MODIS, and MISR - a summary review. *Remote Sensing of Environment*, 63, 243-257
- Aspinall, R.J., Marcus, W.A., & Boardman, J.W. (2002). Considerations in collecting, processing, and analysing high spatial resolution hyperspectral data for environmental investigations. *Journal of Geographical Systems*, 4, 15-29
- Babey, S.K., & Anger, C.D. (1993). Compact airborne spectrographic imager (CASI): a progress review. In *Imaging Spectrometry of the Terrestrial Environment* (pp. 152-163). Orlando, FL, USA: SPIE
- Barnes, W.L., Pagano, T.S., & Salomonson, V.V. (1998). Prelaunch characteristics of the Moderate Resolution Imaging Spectroradiometer (MODIS) on EOS-AM1. *Geoscience and Remote Sensing, IEEE Transactions on*, 36, 1088-1100
- Barnsley, M.J., Settle, J.J., Cutter, M.A., Lobb, D.R., & Teston, F. (2004). The PROBA/CHRIS mission: a low-cost smallsat for hyperspectral multiangle observations of the Earth surface and atmosphere. *Geoscience and Remote Sensing, IEEE Transactions on*, 42, 1512-1520
- Biggar, S.F., Thome, K.J., Holmes, J.M., Kuester, M.A., & Schowengerdt, R.A. (2001). In-flight radiometric and spatial calibration of EO-1 optical sensors. In *Geoscience and Remote Sensing Symposium, 2001. IGARSS '01. IEEE 2001 International* (pp. 305-307 vol.301)
- Böttger, U., Nieke, J., & Schläpfer, D. (2006). Assessing polarization effects for the Airborne imaging spectrometer APEX. *Adv. Radio Sci.*, 4, 323-328
- Bowles, J.H., Maness, S.J., Chen, W., Davis, C.O., Donato, T.F., Gillis, D.B., Korwan, D., Lamela, G., Montes, M.J., Rhea, W.J., & Snyder, W.A. (2005). Hyperspectral imaging of an inter-coastal waterway. In *Remote Sensing for Environmental Monitoring, GIS Applications, and Geology V* (pp. 59830F-59838). Brugge, Belgium: SPIE
- Brazile, J., Neville, R.A., Staenz, K., Schlapfer, D., Lixin, S., & Itten, K.I. (2006). Scene-based spectral response function shape discernibility for the APEX imaging spectrometer. *Geoscience and Remote Sensing Letters, IEEE*, 3, 414-418

References

- Brown, H.E., Diuk-Wasser, M.A., Guan, Y., Caskey, S., & Fish, D. (2008). Comparison of three satellite sensors at three spatial scales to predict larval mosquito presence in Connecticut wetlands. *Remote Sensing of Environment*, *112*, 2301-2308
- Brown, S.W., Eppeldauer, G.P., & Lykke, K.R. (2006). Facility for spectral irradiance and radiance responsivity calibrations using uniform sources. *Appl. Opt.*, *45*, 8218-8237
- Brown, S.W., Johnson, B.C., Michae, E.F., Yarbrough, M.A., Flora, S.J., Lykke, K.R., & Clark, D.K. (2003). Stray-light correction algorithm for spectrographs. *Metrologia*, S81
- Busch, K.W., Soyemi, O.O., Rabbe, D., & Busch, M.A. (2000). Determination of the Stray Light Levels in a Dispersive Near-Infrared Spectrometer with Trichloromethane. *Appl. Spectrosc.*, *54*, 1759-1766
- Carlson, R.C., Hayden, A.F., & Telfair, W.B. (1988). Remote observations of effluents from small building smokestacks using FTIR spectroscopy. *Appl. Opt.*, *27*, 4952-4959
- Chang, C.-C., & Lee, H.-N. (2008). On the estimation of target spectrum for filter-array based spectrometers. *Opt. Express*, *16*, 1056-1061
- Chorier, P., & Tribolet, P.M. (2001). High-performance HgCdTe SWIR detectors for hyperspectral instruments. In, *Sensors, Systems, and Next-Generation Satellites V* (pp. 328-341). Toulouse, France: SPIE
- Chrien, T.G., Green, R.O., & Eastwood, M.L. (1990). Accuracy of the spectral and radiometric laboratory calibration of the Airborne Visible/Infrared Imaging Spectrometer. In, *Imaging Spectroscopy of the Terrestrial Environment* (pp. 37-49): SPIE
- Chrien, T.G., Kopp, G., Green, R.O., Chovit, C., Eastwood, M., Holbrook, J., Johnson, H., Hajek, P., Raney, J., & Sarture, C. (1994). Improvements to the Airborne Visible/Infrared Imaging Spectrometer (AVIRIS) calibration system. In, *Geoscience and Remote Sensing Symposium, 1994. IGARSS '94. Surface and Atmospheric Remote Sensing: Technologies, Data Analysis and Interpretation., International* (pp. 2293-2294 vol.2294)
- Clark, R.N., Boardman, J., Mustard, J., Kruse, F., Cindy, O., Pieters, C., & Swayze, G.A. (2006). Mineral Mapping and Applications of Imaging Spectroscopy. In, *Geoscience and Remote Sensing Symposium, 2006. IGARSS 2006. IEEE International Conference on* (pp. 1986-1989)
- Clevers, J.G.P.W., de Jong, S.M., Epema, G.F., van der Meer, F., Bakker, W.H., Skidmore, A.K., & Addink, E.A. (2001). MERIS and the red-edge position. *International Journal of Applied Earth Observation and Geoinformation*, *3*, 313-320
- Coleman, H.S. (1947). Stray Light in Optical Systems. *J. Opt. Soc. Am.*, *37*, 434-448
- Coops, N.C., Smith, M.L., Martin, M.E., & Ollinger, S.V. (2003). Prediction of eucalypt foliage nitrogen content from satellite-derived hyperspectral data. *Geoscience and Remote Sensing, IEEE Transactions on*, *41*, 1338-1346

- D'Odorico, P., Alberti, E., Dell'Endice, F., Nieke, J., & Itten, K.I. (2009). Tracking Spectral Accuracy of Hyperspectral Data by means of an In-Flight Calibration Facility (IFC). In, *Proceedings of 6th EARSeL Workshop on Imaging Spectroscopy* (p. 9). Tel Aviv
- Datt, B., & Paterson, M. (2000). Vegetation-soil spectral mixture analysis. In, *Geoscience and Remote Sensing Symposium, 2000. Proceedings. IGARSS 2000. IEEE 2000 International* (pp. 1936-1938 vol.1935)
- Davis, C., Bowles, J., Leathers, R., Korwan, D., Downes, T.V., Snyder, W., Rhea, W., Chen, W., Fisher, J., Bissett, P., & Reisse, R.A. (2002). Ocean PHILLS hyperspectral imager: design, characterization, and calibration. *Opt. Express*, 10, 210-221
- Dell'Endice, F., Alberti, E., Schaepman, M., & Malenovsky, Z. (2009a). Laboratory Calibration and Characterization of the APEX Airborne Pushbroom Imaging Spectrometer. *Applied Optics*, in review
- Dell'Endice, F., Nieke, J., Brazile, J., Schläpfer, D., Hueni, A., & Itten, K.I. (2007a). Automatic Calibration and Correction Scheme For APEX (Aiborne Prism EXperiment). In, *Proceedings of 5th EARSeL Workshop on Imaging Spectroscopy* (p. 9). Bruges
- Dell'Endice, F., Nieke, J., Koetz, B., Schaepman, M., & Itten, K.I. (2009b). Improving Radiometry of Imaging Spectrometers by using Programmable Spectral Regions of Interest. *IPSRS Journal of Photogrammetry & Remote Sensing*, in press
- Dell'Endice, F., Nieke, J., Schläpfer, D., & Itten, K.I. (2007b). Scene-based method for spatial misregistration detection in hyperspectral imagery. *Applied Optics*, 46, 14
- Dell'Endice, F., Nieke, J., Schläpfer, D., & Itten, K.I. (2007c). Spatial Misregistration Detection For Hyperspectral Sensor Using In-Flight Data. In, *Proceedings of SPIE Defence and Security Systems* (p. 12). Orlando
- Desclotres, J., Sohlberg, R., Owens, J., Giglio, L., Justice, C., Carroll, M., Seaton, J., Crisologo, M., Finco, M., Lannom, K., & Bobbe, T. (2002). The MODIS rapid response project. In, *Geoscience and Remote Sensing Symposium, 2002. IGARSS '02. 2002 IEEE International* (pp. 1191-1192 vol.1192)
- Doyle, W.M., McIntosh, B.C., & Clarke, W.L. (1980). Refractively Scanned Interferometers for Fourier Transform Infrared Spectrophotometry. *Appl. Spectrosc.*, 34, 599-603
- Du, H., & Voss, K.J. (2004). Effects of Point-Spread Function on Calibration and Radiometric Accuracy of CCD Camera. *Appl. Opt.*, 43, 665-670
- Duca, R., & Del Frate, F. (2008). Hyperspectral and Multiangle CHRIS's PROBA Images for the Generation of Land Cover Maps. *Geoscience and Remote Sensing, IEEE Transactions on*, 46, 2857-2866
- Ewing, G.E. (1972). Infrared Spectroscopy. *Annual Review of Physical Chemistry*, 23, 141-164
- Fetterman, M.R. (2005). Fourier-transform infrared derivative spectroscopy with an improved signal-to-noise ratio. *Opt. Lett.*, 30, 2311-2313

References

- Folkman, M.A., Pearlman, J., Liao, L.B., & Jarecke, P.J. (2001). EO-1/Hyperion hyperspectral imager design, development, characterization, and calibration. In L.S. William & Y. Yoshifumi (Eds.) (pp. 40-51): SPIE
- Foster, J.R., Townsend, P.A., & Zganjar, C.E. (2008). Spatial and temporal patterns of gap dominance by low-canopy lianas detected using EO-1 Hyperion and Landsat Thematic Mapper. *Remote Sensing of Environment*, 112, 2104-2117
- Galeazzi, C., Sacchetti, A., Cisbani, A., & Babini, G. (2008). The PRISMA Program. In, *Geoscience and Remote Sensing Symposium, 2008. IGARSS 2008. IEEE International* (pp. IV - 105-IV - 108)
- Gambhir, B.L., & Erives, H. (2006). Scene statistics based calibration of remote sensing instruments. *Geoscience and Remote Sensing Letters, IEEE*, 3, 178-182
- Gao, B.-C., Goetz, A.F.H., & Wiscombe, W.J. (1993). Cirrus Cloud Detection from Airborne Imaging Spectrometer Data Using the 1.38 micro;m Water Vapor Band. *Geophys. Res. Lett.*, 20
- Gomez, R.B. (2002). Hyperspectral imaging: a useful technology for transportation analysis. *Optical Engineering*, 41, 2137-2143
- Goodenough, D.G., Dyk, A., Niemann, K.O., Pearlman, J.S., Hao, C., Han, T., Murdoch, M., & West, C. (2003). Processing Hyperion and ALI for forest classification. *Geoscience and Remote Sensing, IEEE Transactions on*, 41, 1321-1331
- Govaerts, Y.M., Jacquemoud, S., Verstraete, N.M., & Ustin, S.L. (1995). Modeling plant leaf bidirectional reflectance and transmittance with a 3-D ray tracing approach. In, *Geoscience and Remote Sensing Symposium, 1995. IGARSS '95. 'Quantitative Remote Sensing for Science and Applications', International* (pp. 1460-1462 vol.1462)
- Gower, J.F.R., Borstadt, G.A., Gray, L.H., & Edel, H.R. (1988). The Fluorescence Line Imager: High-Resolution Imaging Spectroscopy Over Water and Land. In, *Spectral Signatures of Objects in Remote Sensing*. Aussois (France)
- Green, R.O. (1998). Spectral calibration requirement for Earth-looking imaging spectrometers in the solar-reflected spectrum. *Appl. Opt.*, 37, 683-690
- Gross, M.F., & Klemas, V. (1986). The use of airborne imaging spectrometer (AIS) data to differentiate marsh vegetation. *Remote Sens. Environ.*, 19, 97-103
- Guanter, L., Alonso, L., & Moreno, J. (2005). First results from the PROBA/CHRIS hyperspectral/multiangular satellite system over land and water targets. *Geoscience and Remote Sensing Letters, IEEE*, 2, 250-254
- Guanter, L., Richter, R., & Moreno, J. (2006). Spectral calibration of hyperspectral imagery using atmospheric absorption features. *Appl. Opt.*, 45, 2360-2370
- Haboudane, D., Miller, J.R., Pattey, E., Zarco-Tejada, P.J., & Strachan, I.B. (2004). Hyperspectral vegetation indices and novel algorithms for predicting green LAI of crop canopies: Modeling and validation in the context of precision agriculture. *Remote Sensing of Environment*, 90, 337-352

- Haboudane, D., Tremblay, N., Miller, J.R., & Vigneault, P. (2008). Remote Estimation of Crop Chlorophyll Content Using Spectral Indices Derived From Hyperspectral Data. *Geoscience and Remote Sensing, IEEE Transactions on*, 46, 423-437
- Hall, D.K., Key, J.R., Casey, K.A., Riggs, G.A., & Cavalieri, D.J. (2004). Sea ice surface temperature product from MODIS. *Geoscience and Remote Sensing, IEEE Transactions on*, 42, 1076-1087
- Hall, D.K., Riggs, G.A., Salomonson, V.V., & Scharfen, G.R. (2000). Early results from the Moderate resolution Imaging Spectroradiometer (MODIS) global snow and ice cover products. In, *Geoscience and Remote Sensing Symposium, 2000. Proceedings. IGARSS 2000. IEEE 2000 International* (pp. 1763-1765 vol.1764)
- Hao, C., Wu, S., & Xu, C. (2008). Comparison of some vegetation indices in seasonal information. *Chinese Geographical Science*, 18, 242-248
- Hayat, M.M., Torres, S.N., Armstrong, E., Cain, S.C., & Yasuda, B. (1999). Statistical Algorithm for Nonuniformity Correction in Focal-Plane Arrays. *Appl. Opt.*, 38, 772-780
- Hendry, D.C., & Massingham, J.W. (1992). CMOS/ECL circuits with reduced power dissipation. Technology and Application of Combined Bi-Polar and CMOS Semiconductor Processes. In, *IEEE colloquium* (pp. 5/1 - 5/5)
- Hollander, J.M., & Shirley, D.A. (1970). Chemical Information from Photoelectron and Conversion-Electron Spectroscopy. *Annual Review of Nuclear Science*, 20, 435-466
- Hopey, J.A., Fuller, K.A., Krishnaswamy, V., Bowdle, D., & Newchurch, M.J. (2008). Fourier transform infrared spectroscopy of size-segregated aerosol deposits on foil substrates. *Appl. Opt.*, 47, 2266-2274
- Hueni, A., Biesemans, J., Meuleman, K., Dell'Endice, F., Schlaepfer, D., Adriaensen, S., Kempenaers, S., Odermatt, D., Kneubuehler, M., & Nieke, J. (2008). Structure, Components and Interfaces of the APEX Processing and Archiving Facility. *Transactions on Geoscience and Remote Sensing*
- ISO (1993). *Guide to the expression of uncertainty in measurement*. [Geneva] :
- Itten, K.I., Dell'Endice, F., Hueni, A., Kneubuehler, M., Schläpfer, D., Odermatt, D., Seidel, F., Huber, S., Schopfer, J., Kellenberger, T., Bühler, Y., D'Odorico, P., Nieke, J., Alberti, E., & Meuleman, K. (2008). APEX - the Hyperspectral ESA Airborne Prism Experiment. *Sensors*, 25
- Jacquemoud, S., Verhoef, W., Baret, F., Zarco-Tejada, P.J., Asner, G.P., Francois, C., & Ustin, S.L. (2006). PROSPECT+SAIL: 15 Years of Use for Land Surface Characterization. In, *Geoscience and Remote Sensing Symposium, 2006. IGARSS 2006. IEEE International Conference on* (pp. 1992-1995)
- Janesick, J., & Putnam, G. (2003). DEVELOPMENTS AND APPLICATIONS OF HIGH-PERFORMANCE CCD AND CMOS IMAGING ARRAYS. *Annual Review of Nuclear and Particle Science*, 53, 263-300

References

- Jarecke, P., Yokoyama, K., & Barry, P. (2001). On-orbit radiometric calibration the Hyperion instrument. In, *Geoscience and Remote Sensing Symposium, 2001. IGARSS '01. IEEE 2001 International* (pp. 2825-2827 vol.2826)
- Kacenjar, S., & Honvedel, M. (2004). Atmospheric characterization using space-based hyperspectral imaging systems. In, *Geoscience and Remote Sensing Symposium, 2004. IGARSS '04. Proceedings. 2004 IEEE International* (pp. 4199-4202 vol.4196)
- Kaufmann, H., Segl, K., Chabrillat, S., Hofer, S., Stuffer, T., Mueller, A., Richter, R., Schreier, G., Haydn, R., & Bach, H. (2006). EnMAP A Hyperspectral Sensor for Environmental Mapping and Analysis. In, *Geoscience and Remote Sensing Symposium, 2006. IGARSS 2006. IEEE International Conference on* (pp. 1617-1619)
- Kavaldjiev, D., & Ninkov, Z. (2001). Influence of nonuniform charge-coupled device pixel response on aperture photometry. *Optical Engineering, 40*, 162-169
- King, M.D., Kaufman, Y.J., Menzel, W.P., & Tanre, D. (1992). Remote sensing of cloud, aerosol, and water vapor properties from the moderate resolution imaging spectrometer (MODIS). *Geoscience and Remote Sensing, IEEE Transactions on, 30*, 2-27
- Koepke, P. (1982). Vicarious satellite calibration in the solar spectral range by means of calculated radiances and its application to Meteosat. *Appl. Opt., 21*, 2845-2854
- Kohler, D., Bissett, W., Steward, R., & Davis, C. (2004). New approach for the radiometric calibration of spectral imaging systems. *Opt. Express, 12*, 2463-2477
- Kokaly, R.F., & Clark, R.N. (1999). Spectroscopic Determination of Leaf Biochemistry Using Band-Depth Analysis of Absorption Features and Stepwise Multiple Linear Regression. *Remote Sensing of Environment, 67*, 267-287
- Kotchenova, S.Y., & Vermote, E.F. (2007). Validation of a vector version of the 6S radiative transfer code for atmospheric correction of satellite data. Part II. Homogeneous Lambertian and anisotropic surfaces. *Appl. Opt., 46*, 4455-4464
- Kotchenova, S.Y., Vermote, E.F., Levy, R., & Lyapustin, A. (2008). Radiative transfer codes for atmospheric correction and aerosol retrieval: intercomparison study. *Appl. Opt., 47*, 2215-2226
- Kotchenova, S.Y., Vermote, E.F., Matarrese, R., & Klemm, J.F.J. (2006). Validation of a vector version of the 6S radiative transfer code for atmospheric correction of satellite data. Part I: Path radiance. *Appl. Opt., 45*, 6762-6774
- Koziana, J., Ahmad, S., Leptoukh, G., Sharma, A.K., & Serafino, G. (2001). MODIS atmospheric data products at the Goddard Earth Sciences DAAC. In, *Geoscience and Remote Sensing Symposium, 2001. IGARSS '01. IEEE 2001 International* (pp. 1708-1710 vol.1704)
- Krüger, G., Erzinger, J., & Kaufmann, H. (1998). Laboratory and airborne reflectance spectroscopic analyses of lignite overburden dumps. *Journal of Geochemical Exploration, 64*, 47-65

- Kruse, F.A., & Taranik, D.L. (1989). Mapping Hydrothermally Altered Rocks with the Airborne Imaging Spectrometer (ais) and the Airborne Visible/infrared Imaging Spectrometer. In, *Geoscience and Remote Sensing Symposium, 1989. IGARSS'89. 12th Canadian Symposium on Remote Sensing., 1989 International* (pp. 952-956)
- Kuusilinna, K., Hamalainen, T., & Saarinen, J. (1999). Field programmable gate array-based PCI interface for a coprocessor system. *Microprocessors and Microsystems, 22*, 373-388
- le Maire, G., François, C., Soudani, K., Berveiller, D., Pontailier, J.-Y., Bréda, N., Genet, H., Davi, H., & Dufrêne, E. (2008). Calibration and validation of hyperspectral indices for the estimation of broadleaved forest leaf chlorophyll content, leaf mass per area, leaf area index and leaf canopy biomass. *Remote Sensing of Environment, 112*, 3846-3864
- Li, L., Cheng, Y.B., Ustin, S., Hu, X.T., & Riaño, D. (2008). Retrieval of vegetation equivalent water thickness from reflectance using genetic algorithm (GA)-partial least squares (PLS) regression. *Advances in Space Research, 41*, 1755-1763
- Lobb, D.R. (1994). Theory of concentric designs for grating spectrometers. *Appl. Opt., 33*, 2648-2658
- Low, F.J., Rieke, G.H., & Gehrz, R.D. (2007). The Beginning of Modern Infrared Astronomy. *Annual Review of Astronomy and Astrophysics, 45*, 43-75
- Lucas, K.L., & Carter, G.A. (2008). The use of hyperspectral remote sensing to assess vascular plant species richness on Horn Island, Mississippi. *Remote Sensing of Environment, 112*, 3908-3915
- Makisara, K., Meinander, M., Rantasuo, M., Okkonen, J., Aikio, M., & Sipola, K. (1993). Airborne imaging spectrometer for applications (AISA). In, *Geoscience and Remote Sensing Symposium, 1993. IGARSS '93. Better Understanding of Earth Environment., International* (pp. 479-481 vol.472)
- Marchand, E.W. (1964). Derivation of the Point Spread Function from the Line Spread Function. *J. Opt. Soc. Am., 54*, 915-919
- Martin, M.E., Plourde, L.C., Ollinger, S.V., Smith, M.L., & McNeil, B.E. (2008). A generalizable method for remote sensing of canopy nitrogen across a wide range of forest ecosystems. *Remote Sensing of Environment, 112*, 3511-3519
- Moorthy, I., Miller, J.R., & Noland, T.L. (2008). Estimating chlorophyll concentration in conifer needles with hyperspectral data: An assessment at the needle and canopy level. *Remote Sensing of Environment, 112*, 2824-2838
- Mouroulis, P., Green, R.O., & Chrien, T.G. (2000). Design of Pushbroom Imaging Spectrometers for Optimum Recovery of Spectroscopic and Spatial Information. *Appl. Opt., 39*, 2210-2220
- Mouroulis, P., & McKerns, M.M. (2000). Pushbroom imaging spectrometer with high spectroscopic data fidelity: experimental demonstration. *Optical Engineering, 39*, 808-816
- Mouroulis, P., Thomas, D.A., Chrien, T.G., Duval, V., Green, R.O., Simmonds, J.J., & Vaughan, A.H. (2004). Trade Studies in Multi/Hyperspectral Imaging Systems Final Report. In

References

- Muller, A., Richter, R., Habermeyer, M., Dech, S., Segl, K., & Kaufmann, H. (2005). Spectroradiometric requirements for the reflective module of the airborne spectrometer ARES. *Geoscience and Remote Sensing Letters, IEEE*, 2, 329-332
- Murakami, H., Tanaka, K., Kurihara, S., Okamura, Y., Inoue, J., Nieke, J., Asanuma, I., Yatagai, H., Mitomi, Y., Yoshida, M., Higuchi, R., Kawamoto, S., Isono, K., & Senga, Y. (2003). GLI early calibration results for oceanographic applications. In J.F. Robert, D.G. Gary & P. Delu (Eds.) (pp. 73-82): SPIE
- Neville, R.A., Sun, L., & Staenz, K. (2003). Detection of spectral line curvature in imaging spectrometer data. In *Algorithms and Technologies for Multispectral, Hyperspectral, and Ultraspectral Imagery IX* (pp. 144-154). Orlando, FL, USA: SPIE
- Neville, R.A., Sun, L., & Staenz, K. (2004). Detection of keystone in imaging spectrometer data. In *Algorithms and Technologies for Multispectral, Hyperspectral, and Ultraspectral Imagery X* (pp. 208-217). Orlando, FL, USA: SPIE
- Nieke, J., Aoki, T., Tanikawa, T., Motoyoshi, H., Hori, M., & Nakajima, Y. (2003). Cross-calibration of satellite sensors over snow fields. In L.B. William (Ed.) (pp. 406-414): SPIE
- Nieke, J., Frerick, J., Stroede, J., Rebhan, H., Mavrocordatos, C., & Berruti, B. (2009). ESA's Sentinel 3 mission: Overview on optical payload and processor development. *Proceedings of SPIE*
- Nieke, J., Schläpfer, D., Dell'Endice, F., Brazile, J., & Itten, K.I. (2008). Uniformity of Imaging Spectrometry Data Products. *IEEE Transactions on Geoscience and Remote Sensing*, 46, 11
- Nieke, J., Solbrig, M., & Neumann, A. (1998). Signal-to-noise ratio reduction due to image smear concerning spaceborne imaging spectrometers for remote sensing of the Earth. In L.B. William (Ed.) (pp. 492-502): SPIE
- Nieke, J., Solbrig, M., & Neumann, A. (1999). Noise Contributions for Imaging Spectrometers. *Appl. Opt.*, 38, 5191-5194
- Nieke, J., Solbrig, M., Suemnich, K.-H., Zimmermann, G., & Roeser, H.-P. (2000). Spaceborne spectrometer calibration with LEDs. In L.B. William (Ed.) (pp. 384-394): SPIE
- Pignatti, S., Cavalli, R.M., Cuomo, V., Fusilli, L., Pascucci, S., Poscolieri, M., & Santini, F. (2009). Evaluating Hyperion capability for land cover mapping in a fragmented ecosystem: Pollino National Park, Italy. *Remote Sensing of Environment*, 113, 622-634
- Piterman, A., & Ninkov, Z. (2002). Subpixel sensitivity maps for a back-illuminated charge-coupled device and the effects of nonuniform response on measurement accuracy. *Optical Engineering*, 41, 1192-1202
- Price, J.C. (1994). Band selection procedure for multispectral scanners. *Appl. Opt.*, 33, 3281-3288
- Ramsey, I.E., A., R., G., N., R., E., & K., M. (2005). Generation and validation of characteristic spectra from EO1 Hyperion image data for detecting the occurrence of the invasive species, Chinese tallow. *International Journal of Remote Sensing*, 26, 1611-1636

- Rieke, G.H. (2007). Infrared Detector Arrays for Astronomy. *Annual Review of Astronomy and Astrophysics*, 45, 77-115
- Ruyten, W. (1999). Smear correction for frame transfer charge-coupled-device cameras. *Opt. Lett.*, 24, 878-880
- Schaepman, M.E. (2009). Imaging Spectrometers. In T.A. Warner, M.D. Nellis & G.M. Foody (Eds.), *The SAGE Handbook of Remote Sensing* (pp. pp. 166-178). London (UK): SAGE
- Schaepman-Strub, G., Schaepman, M.E., Painter, T.H., Dangel, S., & Martonchik, J.V. (2006). Reflectance quantities in optical remote sensing--definitions and case studies. *Remote Sensing of Environment*, 103, 27-42
- Schlapfer, D., Biesemans, J., Hueni, A., & Meuleman, K. (2008). Evaluation of the atmospheric correction procedure for the APEX level 2/3 processor. In, *Remote Sensing of Clouds and the Atmosphere XIII* (pp. 710709-710712). Cardiff, Wales, United Kingdom: SPIE
- Schlapfer, D., Nieke, J., & Itten, K.I. (2007). Spatial PSF Nonuniformity Effects in Airborne Pushbroom Imaging Spectrometry Data. *Geoscience and Remote Sensing, IEEE Transactions on*, 45, 458-468
- Schläpfer, D., & Schaepman, M. (2002). Modeling The Noise Equivalent Radiance Requirements of Imaging Spectrometers Based On Scientific Applications. *Appl. Opt.*, 41, 5691-5701
- Seidel, F., Nieke, J., Schlapfer, D., Holler, R., von Hoyningen-Huene, W., & Itten, K. (2005). Aerosol retrieval for APEX airborne imaging spectrometer: a preliminary analysis. In, *Remote Sensing of Clouds and the Atmosphere X* (pp. 59791W-59710). Brugge, Belgium: SPIE
- Seidel, F., Schläpfer, D., Nieke, J., & Itten, K.I. (2008). Sensor Performance Requirements for the Retrieval of Atmospheric Aerosols by Airborne Optical Remote Sensing. *Sensors*, 8, 1901--1914
- Seon Joo, K., & Pollefeys, M. (2008). Robust Radiometric Calibration and Vignetting Correction. *Pattern Analysis and Machine Intelligence, IEEE Transactions on*, 30, 562-576
- Soares, O.D.D., & Costa, J.L.C. (1999). Spectrophotometer Spectral Bandwidth Calibration with Absorption Bands Crystal Standard. *Appl. Opt.*, 38, 2007-2013
- Suhr, B., Gege, P., Nieke, J., Itten, K., & Ulbrich, G. (2005). Calibration facility for airborne imaging spectrometers. In, *Sensors, Systems, and Next-Generation Satellites IX* (pp. 59780R-59789). Brugge, Belgium: SPIE
- Tanzi, C.P., & Aben, I. (1999). Polarization measurements of the Global Ozone Monitoring Experiment. In, *Optical Remote Sensing of the Atmosphere* (p. RWB2): Optical Society of America
- Thenkabail, P.S., Enclona, E.A., Ashton, M.S., Legg, C., & De Dieu, M.J. (2004). Hyperion, IKONOS, ALI, and ETM+ sensors in the study of African rainforests. *Remote Sensing of Environment*, 90, 23-43
- Townsend, P.A., Foster, J.R., Chastain, R.A., Jr., & Currie, W.S. (2003). Application of imaging

References

- spectroscopy to mapping canopy nitrogen in the forests of the central Appalachian Mountains using Hyperion and AVIRIS. *Geoscience and Remote Sensing, IEEE Transactions on*, 41, 1347-1354
- Ustin, S.L., Asner, G.P., Gamon, J.A., Huemmrich, K.F., Jacquemoud, S., Schaepman, M., & Zarco-Tejada, P. (2006). Retrieval of Quantitative and Qualitative Information about Plant Pigment Systems from High Resolution Spectroscopy. In, *Geoscience and Remote Sensing Symposium, 2006. IGARSS 2006. IEEE International Conference on* (pp. 1996-1999)
- Ustin, S.L., Roberts, D.A., Gamon, J.A., Asner, G.P., & Green, R.O. (2004). Using Imaging Spectroscopy to Study Ecosystem Processes and Properties. *BioScience*, 54, 523-534
- Vane, G., Green, R.O., Chrien, T.G., Enmark, H.T., Hansen, E.G., & Porter, W.M. (1993). The airborne visible/infrared imaging spectrometer (AVIRIS). *Remote Sensing of Environment*, 44, 127-143
- Verrelst, J., Schaepman, M.E., Koetz, B., & Kneubühler, M. (2008). Angular sensitivity analysis of vegetation indices derived from CHRIS/PROBA data. *Remote Sensing of Environment*, 112, 2341-2353
- Vora, P.L., Farrell, J.E., Tietz, J.D., & Brainard, D.H. (2001). Image capture: simulation of sensor responses from hyperspectral images. *Image Processing, IEEE Transactions on*, 10, 307-316
- Vural, K. (1987). Mercury cadmium telluride short- and medium-wavelength infrared staring focal plane array. *Optical Engineering*, 26, 201-208
- Walsh, S.J., McCleary, A.L., Mena, C.F., Shao, Y., Tuttle, J.P., González, A., & Atkinson, R. (2008). QuickBird and Hyperion data analysis of an invasive plant species in the Galapagos Islands of Ecuador: Implications for control and land use management. *Remote Sensing of Environment*, 112, 1927-1941
- Wang, S.-W., Xia, C., Chen, X., Lu, W., Li, M., Wang, H., Zheng, W., & Zhang, T. (2007). Concept of a high-resolution miniature spectrometer using an integrated filter array. *Opt. Lett.*, 32, 632-634
- White, H.P., Khurshid, K.S., Hitchcock, R., Neville, R., Lixin, S., Champagne, C.M., & Staenz, K. (2004). From at-sensor observation to at-surface reflectance - calibration steps for Earth observation hyperspectral sensors. In, *Geoscience and Remote Sensing Symposium, 2004. IGARSS '04. Proceedings. 2004 IEEE International* (pp. 3241-3244 vol.3245)
- Wilson, R., & Boksenberg, A. (1969). Ultraviolet Astronomy. *Annual Review of Astronomy and Astrophysics*, 7, 421-472
- Winter, M.E., Lucey, P.G., Williams, T., & Wood, M. (2003). Calibration of the University of Hawaii's airborne hyperspectral imager. In, *Imaging Spectrometry IX* (pp. 370-379). San Diego, CA, USA: SPIE
- Wright, R., & Pilger, E. (2008). Satellite observations reveal little inter-annual variability in the radiant flux from the Mount Erebus lava lake. *Journal of Volcanology and Geothermal Research*, 177, 687-694

- Zarco-Tejada, P.J., Miller, J.R., Morales, A., Berjón, A., & Agüera, J. (2004). Hyperspectral indices and model simulation for chlorophyll estimation in open-canopy tree crops. *Remote Sensing of Environment*, *90*, 463-476
- Zarco-Tejada, P.J., Rueda, C.A., & Ustin, S.L. (2003). Water content estimation in vegetation with MODIS reflectance data and model inversion methods. *Remote Sensing of Environment*, *85*, 109-124
- Zong, Y., Brown, S.W., Johnson, B.C., Lykke, K.R., & Ohno, Y. (2006). Simple spectral stray light correction method for array spectroradiometers. *Appl. Opt.*, *45*, 1111-1119

Appendixes

Appendixes

Acknowledgements

This work was carried out in the framework of the ESA PRODEX-sponsored APEX project, in particular ESA/ESTEC contracts 16298/02/NL/US and 15449/01/NL/Sfe.

I am very grateful to my supervisor Prof. Dr. Klaus Itten for providing me research independence, freedom and real friendship.

I would like to thank the PhD committee for reviewing this work and the external reviewer, Prof. Karl Staenz , for his inputs. I would like to thank all colleagues at RSL and all industry partners that gave me precious inputs throughout the preparation of this manuscript. I am very grateful to my friends, family and all people that supported me during this thesis.

A special thanks goes to Olya for continuously supporting me anyhow and anywhere.

Authored and Co-Authored Publications

Dell'Endice, F., Nieke, J., Schläpfer, D., & Itten, K.I. (2007b). Scene-based method for spatial misregistration detection in hyperspectral imagery. *Applied Optics*, 46, 14

Dell'Endice, F., Nieke, J., Koetz, B., Schaepman, M.E., & Itten, K. (2009c). Improving radiometry of imaging spectrometers by using programmable spectral regions of interest. *ISPRS Journal of Photogrammetry and Remote Sensing*, In Press

Dell'Endice, F., Alberti, E., Schaepman, M., & Malenovsky, Z. (2009a). Laboratory Calibration and Characterization of the APEX Airborne Pushbroom Imaging Spectrometer. *Applied Optics*, in review

Hueni, A., Biesemans, J., Meuleman, K., Dell'Endice, F., Schläpfer, D., Adriaensen, S., Kempenaers, S., Odermatt, D., Kneubuehler, M., & Nieke, J. (2008). Structure, Components and Interfaces of the APEX Processing and Archiving Facility. *Transactions on Geoscience and Remote Sensing*

Itten, K.I., Dell'Endice, F., Hueni, A., Kneubuehler, M., Schläpfer, D., Odermatt, D., Seidel, F., Huber, S., Schopfer, J., Kellenberger, T., Bühler, Y., D'Odorico, P., Nieke, J., Alberti, E., & Meuleman, K. (2008). APEX - the Hyperspectral ESA Airborne Prism Experiment. *Sensors*, 25

Nieke, J., Schläpfer, D., Dell'Endice, F., Brazile, J., & Itten, K.I. (2008). Uniformity of Imaging Spectrometry Data Products. *IEEE Transactions on Geoscience and Remote Sensing*, 46, 11

Conference Proceedings

D'Odorico, P., Alberti, E., Dell'Endice, F., Hueni, A., & Schaepman, M. (2009a). Spectral Stability Monitoring of an Imaging Spectrometer with Onboard Sources. In, *IEEE International Geoscience and Remote Sensing Symposium (IGARSS '09)*. Cape Town (South Africa)

D'Odorico, P., Alberti, E., Dell'Endice, F., Nieke, J., & Itten, K.I. (2009b). Tracking Spectral Accuracy of Hyperspectral Data by means of an In-Flight Calibration Facility (IFC). In, *Proceedings of 6th EARSeL Workshop on Imaging Spectroscopy* (p. 9). Tel Aviv

Dell'Endice, F., Nieke, J., Brazile, J., Schläpfer, D., Hueni, A., & Itten, K.I. (2007a). Automatic Calibration and Correction Scheme For APEX (Airborne Prism EXperiment). In, *Proceedings of 5th EARSeL Workshop on Imaging Spectroscopy* (p. 9). Bruges

Dell'Endice, F., Nieke, J., Schläpfer, D., & Itten, K.I. (2007c). Spatial Misregistration Detection For Hyperspectral Sensor Using In-Flight Data. In, *Proceedings of SPIE Defence and Security Systems* (p. 12). Orlando

Dell'Endice, F. (2008). Improving the performance of hyperspectral pushbroom imaging spectrometers for specific science applications. In, *Proceedings of ISPRS*. Beijing

Dell'Endice, F., Itten, K.I., & Team, A. (2009b). Sensing Earth Surface with the APEX Airborne Imaging Spectrometer. In, *Proceedings of 6th EARSeL Workshop on Imaging Spectroscopy* (p. 9). Tel Aviv

Dell'Endice, F. (2009). Calibration Algorithms for an Imaging Spectrometer. In, *IEEE International Geoscience and Remote Sensing Symposium (IGARSS '09)*. Cape Town

Itten, K.I., Meuleman, K., Schaepman, M., Alberti, E., Bomans, B., Dell'Endice, F., D'Odorico, P., Hueni, A., Kneubhueler, M., Nieke, J., Schlaepfer, D., & Ulbrich, G. (2009). First Results of the Airborne Dispersive Pushbroom Imaging Spectrometer APEX. In, *Proceedings of 6th EARSeL Workshop on Imaging Spectroscopy* (p. 9). Tel Aviv

Nieke, J., Dell'Endice, F., Hüni, A., Kneubühler, M., Schläpfer, D., Kötz, B., Schopfer, J., Itten, K.I., & Plaza, A. (2007). Calibration and Validation Activities in the Scopy of Hyper-I-Net: The RSL Approach. In, *IEEE International Geoscience and Remote Sensing Symposium (IGARSS '07)* (p. 2). Barcelona

Schläpfer, D., Nieke, J., Dell'Endice, F., Hüni, A., Biesemans, J., Meuleman, K., & Itten, K.I. (2007). Optimized Workflow for APEX Level 2/3 Processing. In, *Proceedings of 5th EARSeL Workshop on Imaging Spectroscopy* (p. 11). Bruges

Curriculum

Present Address
 Remote Sensing Laboratories
 Winterhurerstrasse 190
 8057 Zurich – Switzerland
 +41446355149

FRANCESCO DELL'ENDICE
 June 23, 1979 Andria (BA) - ITALY
francesco.dellendice@geo.uzh.ch
www.rsl.ch



EDUCATION

10/2005 – 10/2009	PhD Remote Sensing University of Zurich (www.uzh.ch). Faculty of Mathematics and Natural Science. Thesis title: Improving Accuracy of Imaging Spectroscopy Data.
07/2005	Master and Bachelor in Aerospace Engineering Politecnico di Milano (www.polimi.it) - Italy
09/2004	Graduate Certificate in Applied Science and Space Studies University of South Australia (www.unisa.edu.au), Adelaide (Australia)
06/2004 – 08/2004	Summer School Program (SSP04) International Space University (www.isunet.edu) held in Adelaide (Australia)
09/2003	Diplôme Ingénieur (Bachelor) SUPAERO (Ecole de l'Aéronautique et de l'Espace), Toulouse, France (www.supaero.org)
05/2001	T.I.M.E. (Top Industrial Manager for Europe) Program (www.time-association.org) This program consists of a Double Degree in Engineering. Home University: Politecnico di Milano. Host University: SUPAERO.
09/1993 - 07/1998	High school diploma (Mathematics, Physics and Computer Science) at Liceo Scientifico "R.Nuzzi" Andria (Ba), Italy

WORKS

2006 - Present	Project Leader – University of Zurich (www.rsl.ch) Leading the development of the CTM software for automatic calibration of the APEX instrument (MATLAB, IDL).
2006 – Present	Project Leader - University of Zurich (www.rsl.ch) Leading the development of the BINGO software for the optimal selection of spectral regions of interest for airborne imaging spectrometers (MATLAB).
10/2005 - Present	Calibration Scientist – University of Zurich (www.apex-esa.org , www.rsl.ch) Developing calibration strategy for the Airborne Prism Experiment Imaging Spectrometer (APEX).
09/2007 – 05/2008	Teacher of mathematics and physics - Gasser Learning Center (www.gasserlearningcenter.com)
06/2007 – 07/2008	Software analyst - SVOX Zurich (www.svox.com) Improving performance of speech recognition software for car navigation systems.
08/2004	Project STREAM member - University of Adelaide – Australia (www.unisa.edu.au) Using space-based remote sensing technologies for freshwater resource management.
04/2003 – 09/2003	Internship – CESR (Research center on astrophysics and planetology) – Toulouse - France Performance studies of a detector for the exploration of Mercury (GEANT, C++)
05/2002 – 07/2002	Satellite Data Analyst – SUPAERO (www.supaero.org) and MIT University (web.mit.edu) Create a database (Visual Basic) for HETE-2 Satellite data ground station.
03/2002 – 05/2002	Project TREX member – ONERA, Toulouse, France (www.onera.fr) Experiments in the wind tunnel to improve the performances of a Ferrari Formula 1.
07/2001	Phone marketing agent - RICAGNI SPA – Milan, Italy – (www.ricagni.it) Sales and marketing for home air conditioning systems.
03/1999 – 06/1999	CAD Technician - Politecnico di Milano – Italy (www.polimi.it) Reproduction of airplanes with AutoCAD.
Several summers	General Manager assistant - Confezioni DIENNE – Andria – Italy Supporting sales, marketing, design of new collection in a textile company specialized in polos.

SOFTWARE

Operating Systems	Unix, Mac OS, Windows 95/98/ME/NT/2000/XP
Programming Languages	C, C++, Fortran, Visual Basic, Java, SQL, Tcl
Programming Libraries	MATLAB, Simulink, IDL, ENVI, Maple, Fluent, Gambit, Visual Studio, Eclipse, Cinema 4D
Web and Design Tools	HTML, Front Page, XML
Software Packages	AutoCAD, MSOffice, OpenOffice, Adobe Tools, EndNote

LANGUAGES

English	Fluent
French	Fluent
German	Level A2/B1. Currently following German classes.
Spanish	Good level of understanding and writing.
Russian	Medium level of understanding and writing.
Italian	Mother Tongue

HONORS AND PRIZES

2008	Best Paper from Young Author from ISPRS, presented in Beijing (China).
2004	European Space Agency (ESA) fellowship for ISU summer school.
2003	Mention for the project of end of studies.
2001	Student financial assistance for the program T.I.M.E. from European Community.

EXTRACURRICULAR

Traveling, 10+ years piano, Soccer, Tennis, Swimming.

REFERENCES

References are available upon request.

